Improving Surface Finish of Metallic Powder Bed Fusion Additive Manufactured Components by Multi-Step Electrochemical Polishing

By

Haitao Zhu

A dissertation submitted to

Lancaster University

for the degree of

DOCTOR OF PHILOSOPHY

School of Engineering

Lancaster University

April 2023

Abstract

Metallic powder bed fusion additive manufactured components have been extensively applied in the fields of aerospace, mobility, construction, etc. However, poor surface quality owing to residual powder, stair-step structure, un-melted track, etc. hinder its application in the market. Electrochemical polishing (EP) is a promising method for smoothing metal surfaces without inducing extra mechanical damage to the product while some disadvantages appeared when being applied on the Laser-Powder Bed Fusion components including low polishing efficiency, poor geometry control, and high cost of the experiment investigation. To solve the problems, this thesis investigated the EP effect of L-PBF 316L stainless steel (316L SS) and TC4 (Ti-6Al-4V) utilising the methods of numerical simulation, experiment, and machine learning. Firstly, a novel 2-dimensional EP model based on the Finite Element Method utilising the Spatial Frequency Method was proposed to simulate the viscous layer formation process with the consideration of the high surface roughness. In addition, the effect of parameters including diffusion coefficient, inlet velocity, inter-electrode distance, and more importantly, the surface textures on the thickness and uniformity of the viscous layer formation were investigated. Based on the simulation parameters, the EP effect of the current density ranging between 250 - 2000 mA/cm^2 on the surface roughness, morphology, weight loss, and geometry changes was investigated, and a two-step EP process was proposed for optimisation. The experiment results were adopted to machine learning with six algorisms including the Adaptive Boosting algorithm, Random Forest, Multilayer Perceptron Regression, Ridge Regression, Support Vector Regression, and Classification and Regression Trees. Simulation results showed that the diffusion coefficient should be smaller than 1.0×10^{-7} m^2/s to generate the viscous layer. The conditions of 0 mm/s inlet velocity, at least 3 mm inter-electrode distance, and small and short peak features of the sample surface are preferable to generate a uniform viscous layer with moderate thickness for L-PBF components with initial surface roughness ranging between 10 μm - 20 μm. Experiment results showed that the two-step EP method could improve the polishing effect, especially for L-PBF TC4 whose roughness reduction was 70.8 % ± (7.4 %, 11.5 %) more than 66.6 % ± (14.3 %, 10.6 %) and 66.5 % ± (7.8 %, 9.1 %) for one-step EP methods with NaCl solutions and A2 electrolytes. Finally, the Multilayer Perceptron Regression and Random Forest algorithms have optimal prediction accuracy and stability, respectively. The corresponding mean and variance of the coefficient of determination values were 0.85 ± (0.08, 0.11) and 0.0017. This simulation-experiment-prediction procedure can also be applied to guide the EP process of other metals or electrolytes to improve polishing efficiency and reduce the experiment cost.

Acknowledgements

This PhD research was made possible by the sponsorship and support of Lancaster University and the Royal Society. Most experiments were carried out in Lab 24, School of Engineering and the characterisation facilities were provided by the School of Engineering and the Chemistry Department at Lancaster University. School of Engineering also provided me with a 3-year student stipend covering my living cost/tuition fee, which guarantees a relaxing research life without consideration of my economic problem. The Royal Society, one of the oldest and most prestigious scientific research institutions in the United Kingdom, aims to promote the development and study of science and to make contributions to the welfare of humanity.

I express my sincere gratitude to my academic supervisors, Dr Yingtao Tian, Prof Allan Rennie and Prof Jianqiao Ye for their invaluable guidance and support throughout my project research. Although Dr Yingtao Tian resigned from my third-year PhD study, he has helped a lot in guiding the establishment of my experiment system, academic writing, etc. Dr Yingtao also provides help for my life in the United Kingdom such as house rental, tourism, etc. Even after resigned, he still guides me on my research by email. Prof Allan Rennie and Prof Jianqiao Ye are willing to be my first and second supervisors later and their affirmation of my progress encourages me to finish the thesis. Being my first supervisor, Prof Allan Rennie is always ready to give me help, no matter how busy he is. I am grateful that Prof Allan Rennie can provide resources and opportunities to me when he finds anything related to my research. I would like to thank Prof Ruifeng Li of Jiangsu University of Science and Technology, who provided the experiment samples for my research.

I would like to thank the technicians in the School of Engineering and the Chemistry Department. Jess Fisher, Ashley Jones, and Agata Makas would always provide help when I had any technical problems in the chemical lab. Andrew Steventon helped with the experiment tools and cut the experiment sample. I also would like to thank Sara Baldock, the experimental officer in the Chemistry Department, for helping me finish the SEM test.

I am also very grateful to my parents, sister, and my girlfriend who gave physical and mental support to motivate me to complete my PhD studies.

Declaration

Lancaster University

Faculty of Science and Technology

School of Engineering

Signed Declaration on the submission of a dissertation.

I declare that this project/dissertation is my own work and has not been submitted in substantially the same form towards the award of a degree or other qualification. Acknowledgement is made in the text of assistance received, and all major sources of information are properly referenced. I confirm that I have read and understood the publication Guidance on Writing Technical Reports published by the School of Engineering.

Signed:

Date:

Publications

Journals

- **Zhu, H**., Rennie, A., Li, R., & Tian, Y. (2022). Two-Steps Electrochemical Polishing of Laser Powder Bed Fusion 316L Stainless Steel. ***Surfaces and Interfaces***, 102442.
- Lu, Y., **Zhu, H**., Zaman, A. M., Rennie, A. E., Lin, H., Tian, Y., & Degl'Innocenti, R. (2023). Contactless 3D surface characterization of additive manufactured metallic components using terahertz time-domain spectroscopy. ***Optical Materials Express***, 13(9), 2513-2525.

Book Chapter

- **Zhu, H**., Rennie, A, Tian, Y. Chapter 2: An Overview of Post-Processing Technologies in General Practice, *in the book: Handbook of Post-Processing in Additive Manufacturing: Requirements, Theories, and Methods*, 1st Edition, 2023, CRC Press, ISBN 9781003276111, doi: https://doi.org/10.1201/9781003276111

Conferences

- **Zhu, H**., Tian, Y., & Rennie, A. E. (2022, November). Viscous Layer Formation in Electrochemical Polishing Laser-Powder Bed Fusion Parts with Different Surface Profiles. In *Casablanca International Conference on Additive Manufacturing* (pp. 219-228). Cham: Springer Nature Switzerland.
- **Zhu, H**., Tian, Y., Rennie, A., Multi-Step Electrochemical Polishing of Additively Manufacturing 316L Stainless Steel Components, *In 41st MATADOR Conference on Advanced Manufacturing*, 2021
- Lu, Y., **Zhu, H**., Zaman, A. M., Lin, H., Degl'Innocenti, R., & Tian, Y. (2022, August). Surface Roughness Measurement of 3D-Printed 316L Stainless Steel Surface using Terahertz Time-Domain Spectroscopy. In *2022 47th International Conference on Infrared, Millimeter and Terahertz Waves (IRMMW-THz)* (pp. 1-2). IEEE.

Contents

List of Figures

List of Tables

Chapter 1 Introduction

This chapter covers the research background, the tasks of the research, and the layout of the thesis. A brief introduction of laser powder bed fusion metals with their main surface limitations is given. The type and product mechanism of surface texture and the methods to remove these barriers are discussed.

1.1 Laser Powder Bed Fusion (L-PBF)

Additive Manufacturing (AM), which may be known by names like 3D printing, layer manufacturing, or freeform fabrication[1], was defined in 2009 by an ASTM standard. Laser Powder Bed Fusion (L-PBF) was amongst the primary commercialised and remains one of the most versatile AM techniques [2]. This technology uses Powder Bed Fusion to create complex components layer by layer from a computer model, without the need for part-specific tooling. Compared with the subtractive manufacturing process, AM technologies provide advantages of less material waste, support of complex structures, improved mechanical properties, etc. A general AM process is as follows[3]:

- CAD modelling
- conversion to STL files
- Transfer to AM machine and STL file manipulation
- Machine setup
- Manufacturing process
- Removal from the working platform

- Post-Processing
- Application

Laser Powder Bed Fusion (L-PBF) is one of a class of AM technologies developed at the University of Texas at Austin, USA[2]. L-PBF processes are normally composed of one or more powder sources and a controlling system to fuse powder particles layer-by-layer. Figure 1 shows the composition of the L-PBF systems[2]. Two powder cartridges are located on opposite sides of the system to hold the material powder. A cartridge piston lifts the powder to allow adequate delivery and coating to the chamber surface of the part constructed by the levelling roller. In the part-building chamber, the top surface of the powder undergoes laser scanning and subsequently solidifies into a solid once melted, with the amount of powder and the exact size of the part in the vertical direction being regulated by the piston and levelling rollers. Through the laser melt pool, the layer is merged by melting the top layer into the previous layer, as it penetrates deeper than the powder layers.

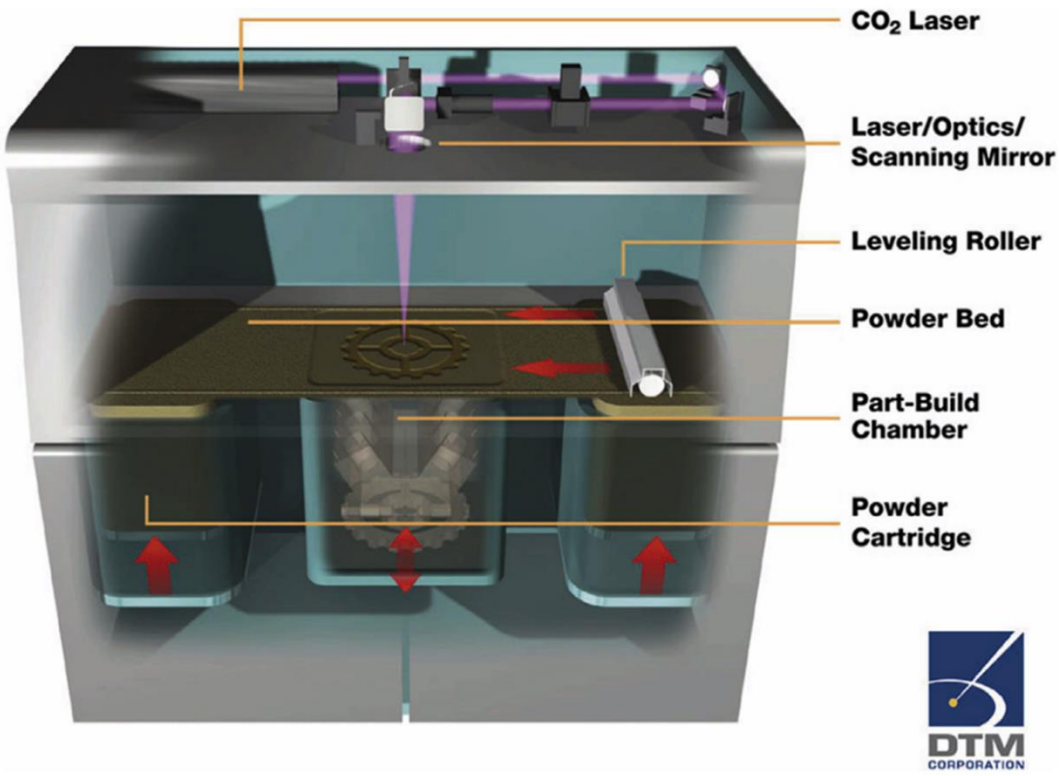

Figure 1 Schematic of the first commercial L-PBF system sold to the public. Courtesy of DTM Corporation[2].

1.2 Surface Limitation of L-PBF Components

Since the metallic L-PBF AM process uses a highly-focused laser or electron beam to fuse thin layers of metal powder spreading across the working area layer-by-layer, this technology

will inevitably cause undesirable surface texture features such as stair-step structure, spattering, attachment of partially melted particles, undesired melted pool causing the morphology of the single solidified laser track, and neighbouring tracks interacting, etc[2–4]. These defects would lead to high surface roughness and thus poor aesthetic, mechanical and biocompatibility properties. Typical surface topographies measured by optical focus variation technologies are shown in Figure 2[5].

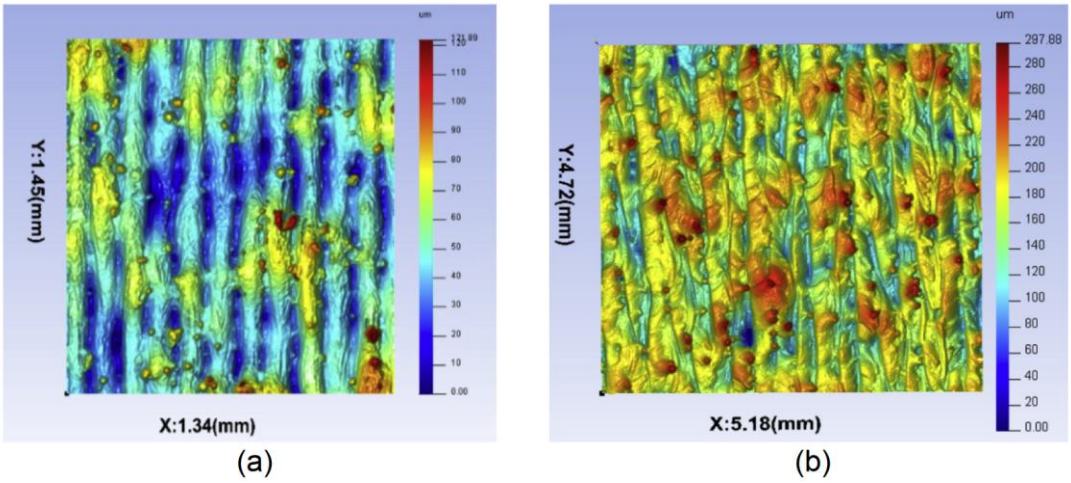

Figure 2 PBF surface topographies measured by optical focus variation technique (a) an SLM surface and (b) an EBM surface[5].

1.2.1 Stair-Step Phenomena

Stair-step structure is a common phenomenon and the main reason for the low surface quality of L-PBF components, which cannot be eliminated since L-PBF manufactures components layer-by-layer. Figure 3 shows the stair-step structure during the modelling and slicing process[6]. Products with a model having a greater layer thickness would have a more evident stair-step structure.

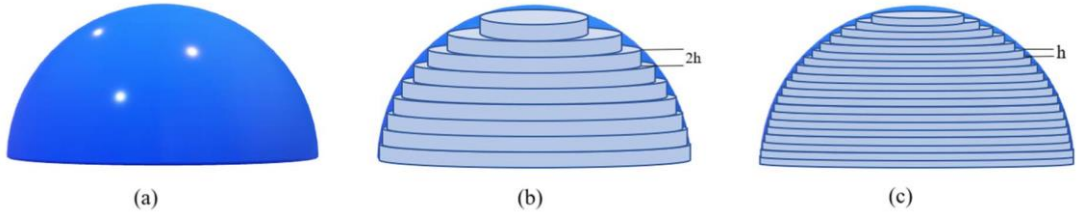

Figure 3 The stair-step effect in AM parts: (a) 3D design, (b) AM parts with a layer thickness of 2 h, and (c) AM parts with a layer thickness of h[6].

Other factors during the manufacturing process include the powder size, material composition and properties, laser beam spot size, energy deposition, scan speed, atmosphere, material homogeneity, linear track separation, vertical step height, powder re-use, part geometry,

scanning strategy and errors caused due to motion & energy deposition[7]. Figure 4 and Figure 5 show the sample manufactured via direct metal laser sintering (DMLS) technology with different building orientations, and the stair-step structure values change. Figure 4 (a) and (b) showed the scanning direction and as-built conditions of samples after manufacturing, where *t* represents layer thickness (μm), *n* represents the layer number, and x_n represents the coordinate values in the X direction (x-axis was the direction that the laser moved). Therefore, the equations for calculating the waviness values are as follow[8]:

$$W_{TJ} = \frac{1}{2}\left(\frac{t}{2} + \frac{t}{2}cos\left(arctan\left(\frac{x_{n+1}-x_n}{t}\right)\right)\right) \quad (1)$$

The result showed that the waviness values were predictable and decreased with the building inclination angles.

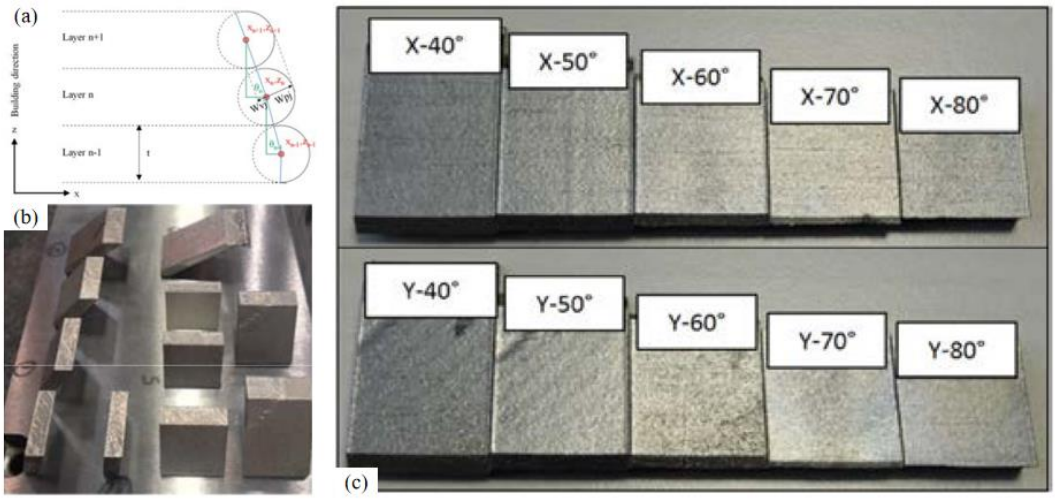

Figure 4 (a) Schematic for scanning direction (b) as-built conditions on the working plate (c)Surface conditions of Sample parts for X & Y axis with angle values indicated above[8].

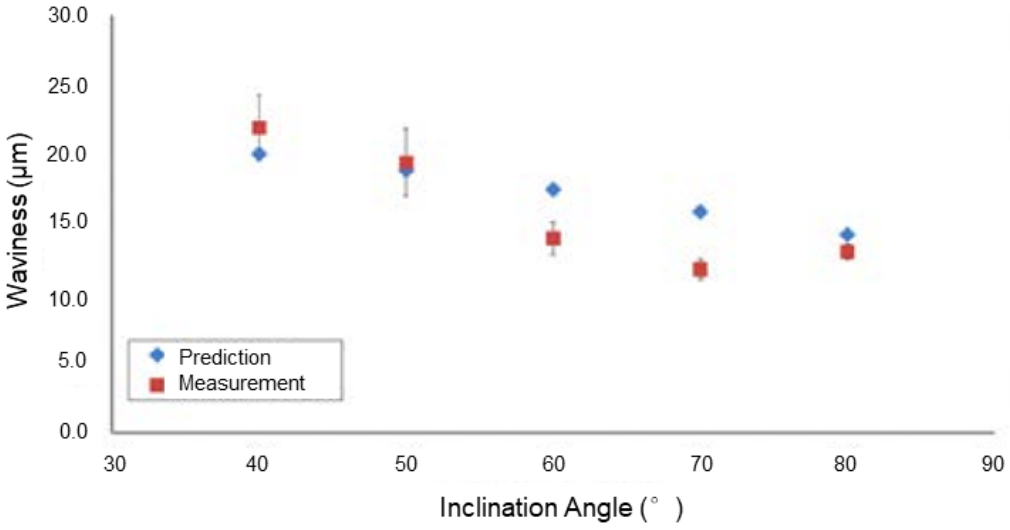

Figure 5 Comparison of measured waviness and predicted waviness values. Error bars represent a 95% confidence interval[8].

1.2.2 Spattering

Spatter causes defect formation, powder redistribution and contamination in the L-PBF process, which can be categorised into five groups: Solid spatter, metallic jet, powder agglomeration spatter, entrainment melting spatter and defect-induced spatter[9]. Figure 6 shows the formation mechanism of all types of spatters and all of them were formed mainly because of the interaction with the laser beam. When the laser beam moves and melts the powders, a large amount of vapour jet is generated and forces the spatter of un-melted powder particles. These un-melted particles re-distributed on the sample surface are called solid spatter[10]. If the powders were melted into liquids and then ejected out from the melt pools, they are called metallic jet spatter[11]. If un-melted powder particles are carried by gas flow into the laser beam and melted but ejected out by the vapour jet again, they are called entrainment melting spattering. Powder agglomeration spatter refers to those with a large size that are formed by liquid-liquid or liquid-powder agglomeration[12]. Finally, if the powder bed distribution is not uniform and severe defect exists, liquid spatter would be serious at the point, and this is called defect-induced spatter.

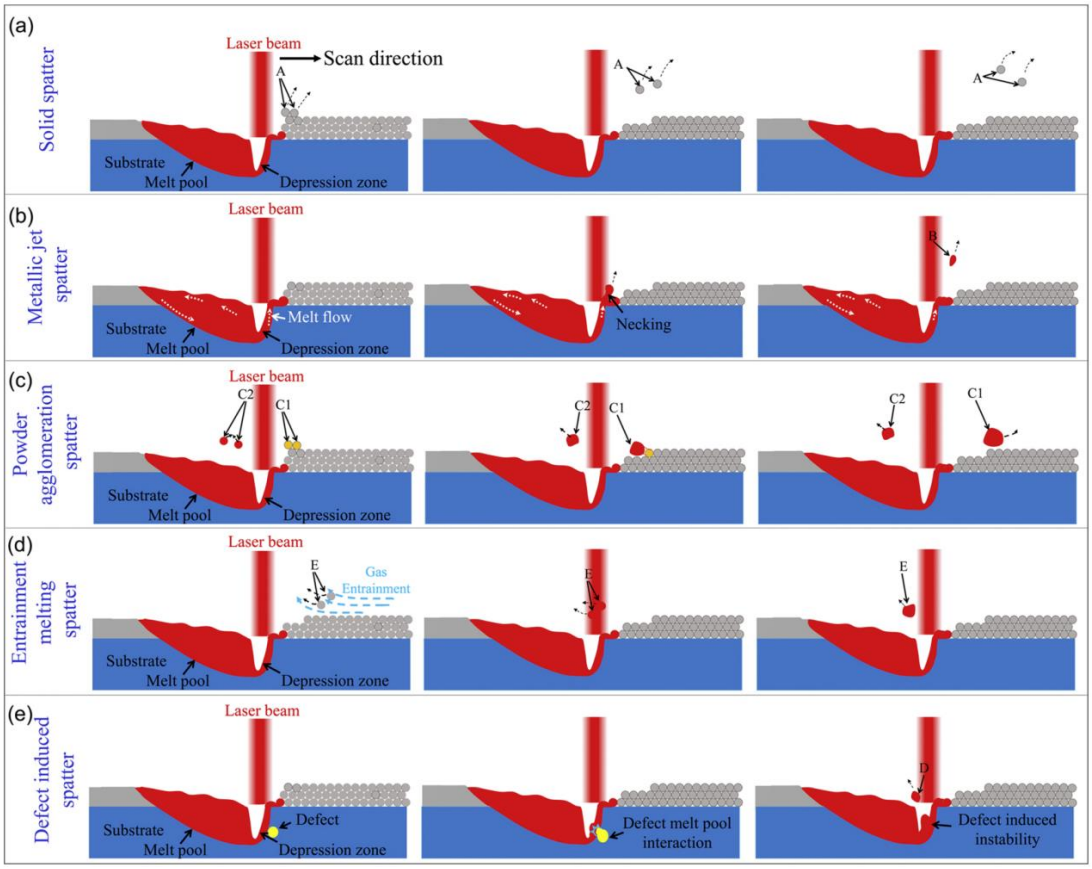

Figure 6 Schematic showing the formation of spatter[9].

The spatter features (type, size and quantity) are directly dependent on the manufacturing parameters such as laser power, scan speed, build orientation, atmosphere and pressure.

1.2.3 Attachment of Residual Particles

Attachment of residual particles including excess independent powder, partially melted powder and bonded powder is another factor influencing the surface quality. These particles will distribute on any manufacturing surfaces, holes, cavities and other geometric features. In the vast majority of situations, most of the excess independent powder can be removed using brushes, compressed airflow and/or sandblasting, or for significant residues, removal using advanced cleaning methods such as pressure washing, ultrasonic cleaning, plasma cleaning, chemical cleaning, etc. However, partially melted and bonded powder is firmly fixed on the sample surface and requires machining to remove it. Figure 7 shows the internal surface morphologies of a Selective Laser Melting (SLM) 304 stainless steel, where a large amount of residual powder particles adhere[13]. They were bonded to the laser tracks on the sample surface, which can only be removed by machining such as shot blasting, electrochemical machining, laser machining, etc., and would severely increase surface roughness.

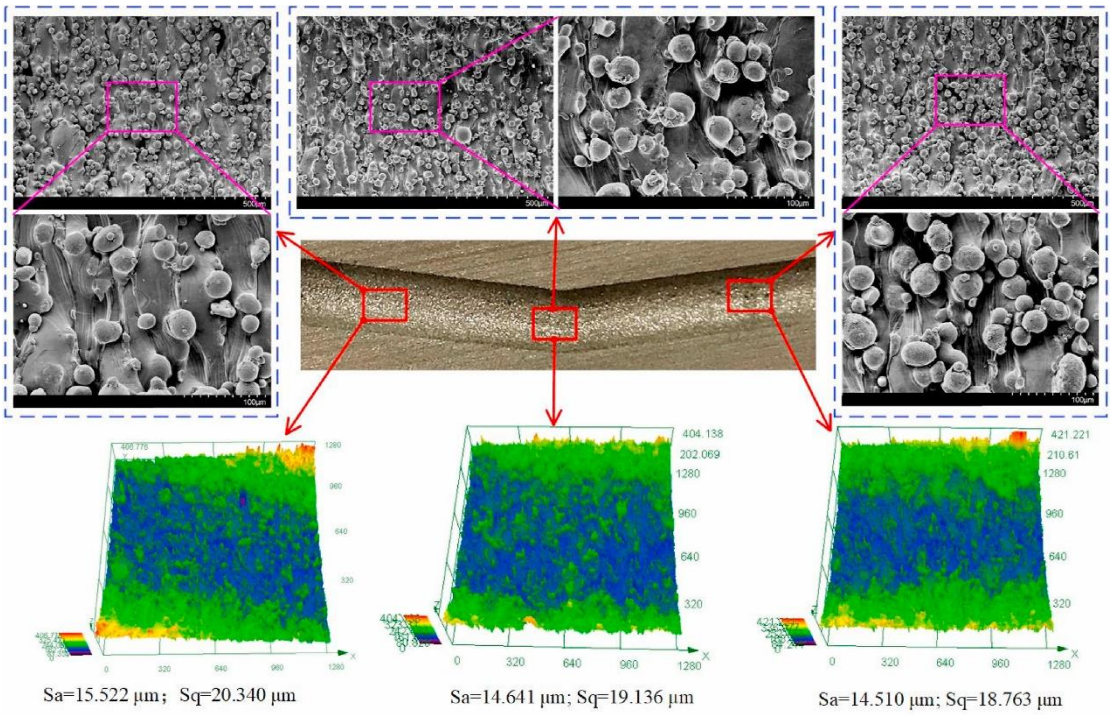

Figure 7 Pristine curving internal hole of a 304 stainless steel tunnel created by AM[13].

1.2.4 Melt-Pool Phenomena

The liquid metal part with a certain geometry formed on the base component during the fusion process is called the melt pool. Although this is not surface texture, it is the basis of the PBF process and will determine the morphology of the solidified laser track and influence the final surface quality[14]. Factors of power properties (source power and geometry), scanning

speed, scan pattern, etc., could influence the quality of the melt pool and the temperature distribution[15,16]. Figure 8 shows the classical cross-sectional melt pool morphologies under different laser power and scanning speeds[17]. Figure 8 (b) to (e) shows the undesirable geometry of the melt pool and therefore would cause pores, spatters, and denudation zones when melting flows and interacts with peripheral powder particles. Figure 9 (a) shows the elongated flow liquid ejected out due to high vapour flux and formed spatter (metallic jet spatter, entrainment melting spattering or powder agglomeration spatter). Figure 9 (b) and (c) show the lateral and open pores formed during the melt flow process, and these pores would cause more defects in the subsequent layers[18]. Additionally, raw powder composition is another crucial factor influencing melt pool shape because it will cause different viscosity and influence the flow behaviour during melting[19].

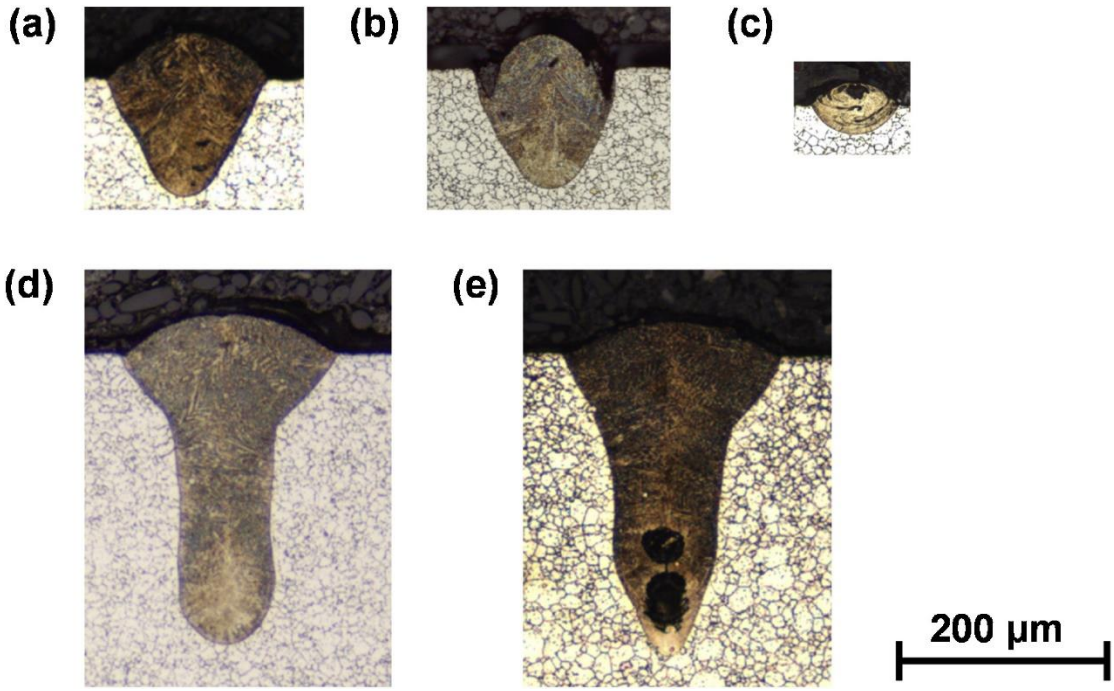

Figure 8 Cross-sectional melt pool morphologies. (a) desirable (285 W, 960 mm/s), (b) balling (370 W, 1200 mm/s), (c) under-melting (100 W, 1000 mm/s), (d) severe keyholing (250 W, 400 mm/s), and (e) keyholing porosity (150 W, 200 mm/s) [17].

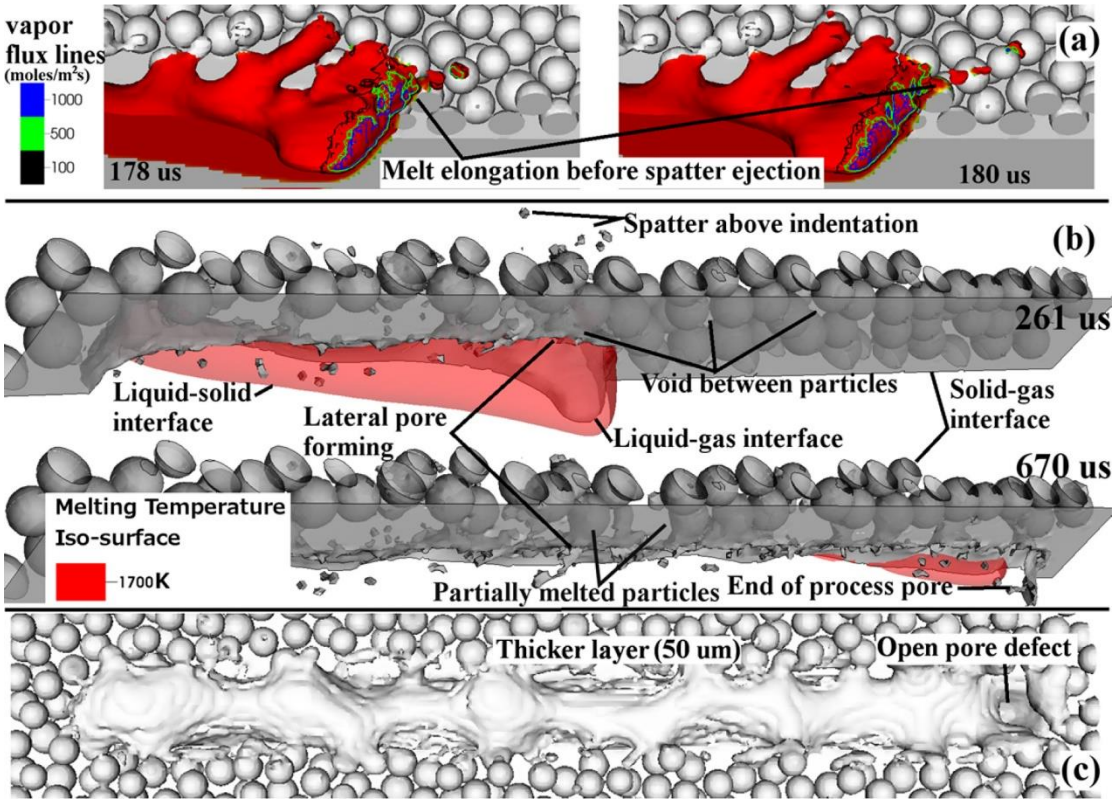

Figure 9 Formation of pores and spatter (laser power 200 W, scan speed 1500 mm/s) [18].

1.2.5 Morphology of the Single Solidified Laser Track

The powder particle will be melted and solidified during the L-PBF process, where the manufacturing parameters will influence the speed and stability of the melting and solidification. For example, Table 1 listed the parameters including the laser power, beam radius and scanning used for building a single laser track of Inconel 718, and their corresponding morphologies were shown in Figure 10[20]. The width, amplitude and profile of the laser track will govern the surface quality of the final components.

Table 1 Process parameters considered[20].

Sample track	Parameters		
	Power (W)	Radius (μm)	Scanning speed (mm/s)
Track 1	100	25	700
Track 2	100	35	700
Track 3	100	48	700
Track 4	100	25	1000
Track 5	100	25	1300

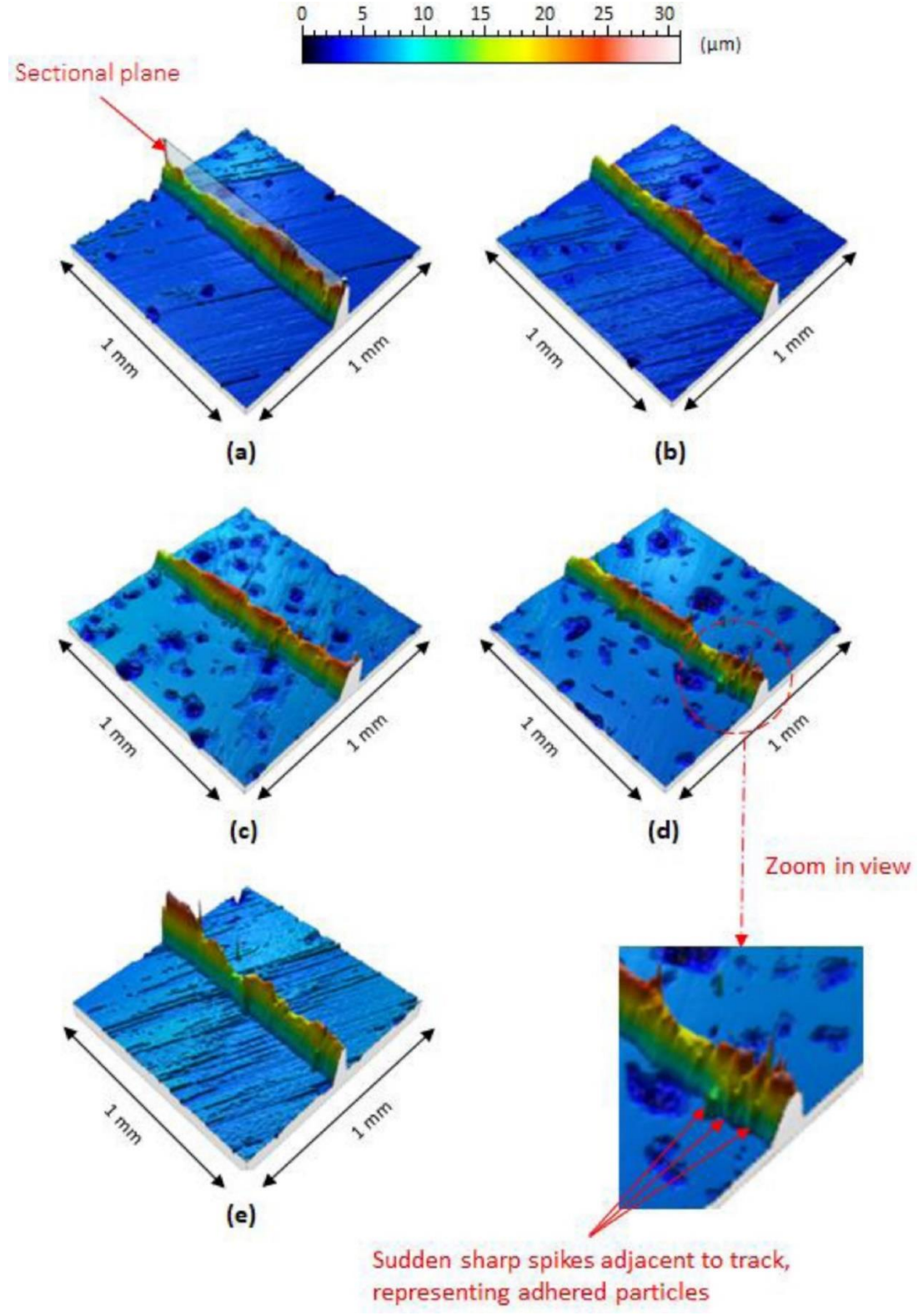

Figure 10 View of the built tracks as obtained by optical profilometry (a) Track 1 (b) Track 2 (c) Track 3 (d) Track 4 and (d) Track 5[20].

1.2.6 Neighbouring Tracks Interact

Melt pool would flow around and mainly from the top region to the bottom region on the laser track due to the gravity during the manufacturing process, leading to track overlap and thus particular surface texture and sometimes defects such as regular and irregular voids, etc. Figure 11 and Figure 12 show the surface textures of SLM 316L SS after the laser tracks interacted with each other in the x-y and y-z planes[21]. The track width was different from the diameter of the laser beam because of the overlap and some pores can be easily found, especially in the direction of the tracks. These defects will seriously increase the surface roughness and influence the mechanical properties of the components. Many factors will cause porosity such as source power, scan speed, etc. According to the works done by Zhang et al and Khairallah et al, the main reason causing the porosity was the rapid evaporation of the metal powder. The metal gas will remove the powder around the laser track and strong recoil pressure will push the surrounding melt liquid downward[18,22].

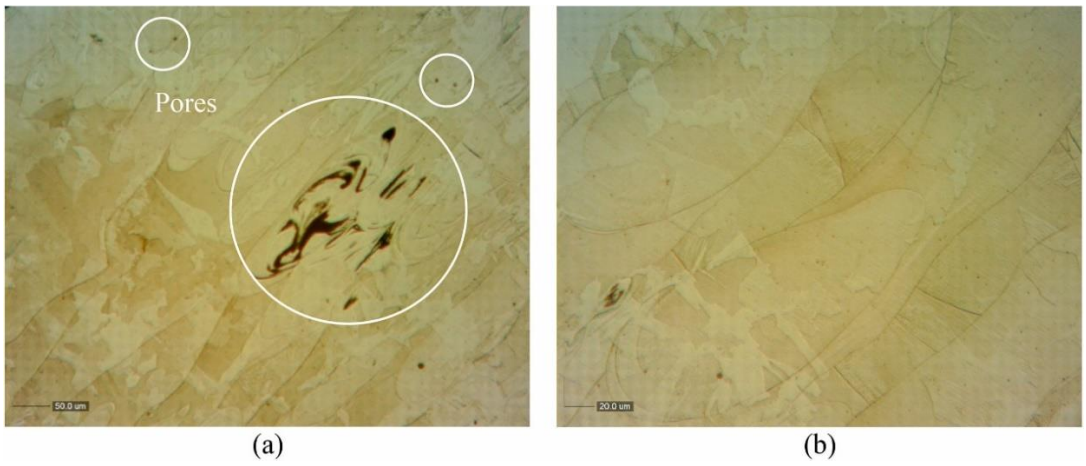

Figure 11 Parallel tracks of the SLM manufactured sample of 316L SS in the x-y plane, observed by an optical microscope with a) 1450, and b) 3625 magnifications[21].

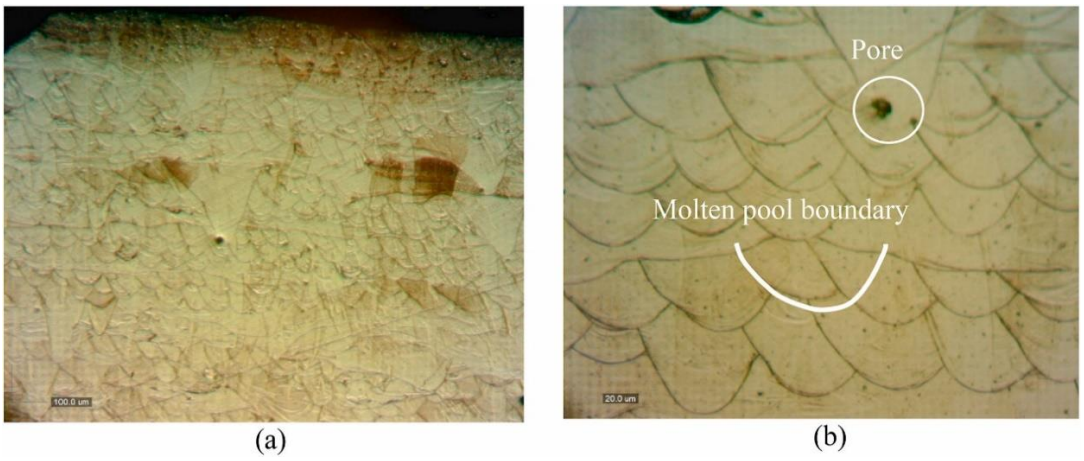

Figure 12 Parallel tracks of the SLM manufactured sample of 316L SS in the y-z plane, observed by an optical microscope with a) 1450, and b) 3625 magnifications.

1.3 Post-Processing Technologies

The technologies applied after the component removal from the working platform are known as post-processing, as mentioned in section 1.1, which play a fundamental role and constitute between 4 % - 13 % of the cost of the whole AM process[23]. Post-processing technologies can be categorised into primary and secondary post-processing, where the former is a mandatory process while the latter is optional to satisfy the functional, geometrical and/or dimensional requirements of final products or costumer's requirements. The impact of post-processing technologies on improving the surface properties of as-built AM parts is depicted in Figure 13, as reported in previous research[24]. The results demonstrate significant differences in properties such as tensile residual stress, surface roughness, microhardness, composition, porosity, and wear.

As discussed in section 1.2, the surface roughness of the AM components is high due to various complicated surface textures including stair-step structure, residual powder, laser tracks, pores, etc. These defects cannot be controlled, are not eliminated by adjusting the manufacturing parameters, and generally, the surface roughness would still be higher than traditional machined products. Figure 14 depicts the impact of manufacturing parameters, such as laser power, scan speed, and scan space, on surface roughness[25]. In general, the surface roughness of the L-PBF products removed from the working platform would be larger than 10 µm which is too high for the requirement of most applications. Therefore, surface finishing can be categorised as the primary post-processing due to the inherent problem of poor surface quality in AM products.

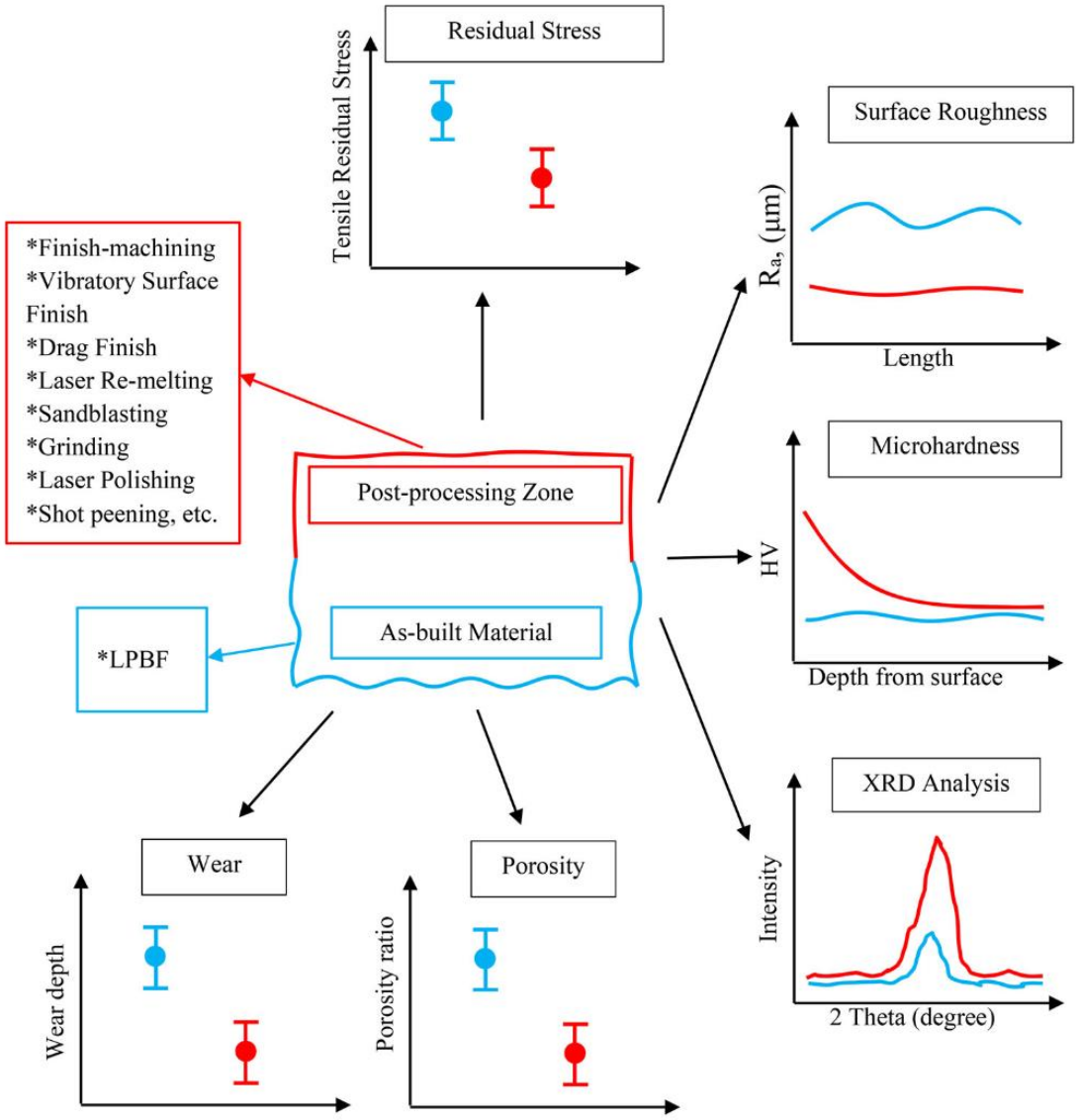

Figure 13 Schematic representation of the effect of post-processing operation on the surface characteristics of the as-built AM parts[24].

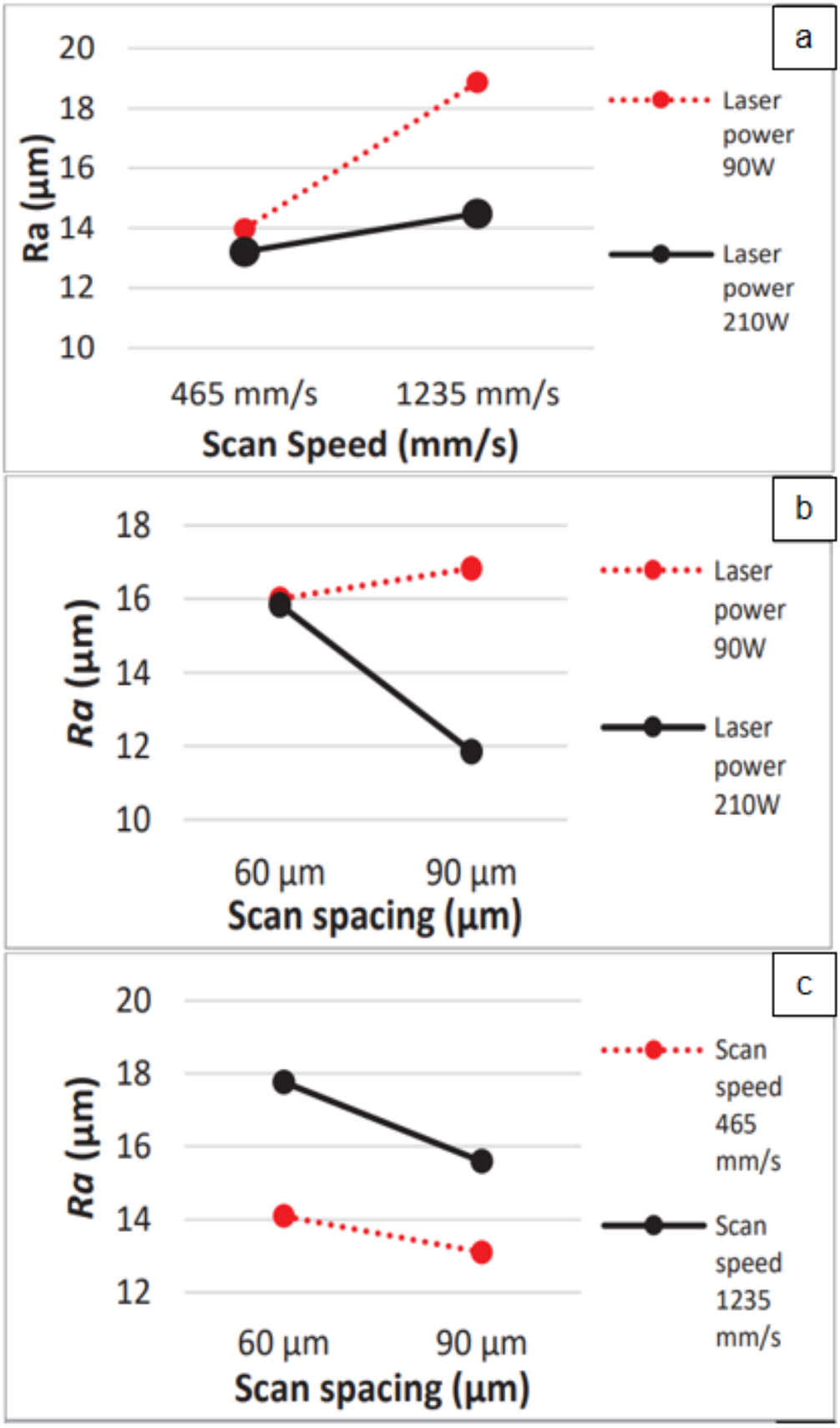

Figure 14 Roughness measurement in terms of Ra for different (a) scan speeds and laser power, (b) scan spaces and laser power, and (c) scan speeds and scan spaces[25].

1.4 Aims and Scope of this Research

As summarised in section 1.2, the surface morphology of the AM components is quite complicated including stair-step structure, residual powder, varied textures caused by single and interacted laser track, etc., typically ranging from a few tens of microns to hundreds of microns. Consequently, the surface roughness of AM parts is larger than 10 μm. For example, the waviness and roughness of components manufactured by DMLS with different orientations range from 10 μm to 25 μm, as shown in Figure 5. The surface roughness of AM components manufactured under different laser powers, scan speeds, and scan space ranges from 10 μm to 20 μm. The unfavourable surface quality restricts the integration of metal AM technology into the production chain[26].

Currently, most machining technologies such as mechanical machining, electrochemical machining, laser machining, etc. and other processing technologies have been proven to be effective in improving the surface and bulk properties of the AM components. Traditional mechanical polishing methods are simple and widely used for the post-processing of L-PBF metal components but they are time-consuming, costly and remain difficult to access the undercut or internal surface of complex-shaped components[27]. The chemical polishing method can polish all surfaces that come into contact with electrolytic solutions, but they are also time-consuming, and in many instances, hazardous materials such as hydrofluoric acid are needed[28,29]. The electrochemical polishing (EP) method is a highly-efficient method to greatly reduce the roughness of the surfaces where the counter electrode can reach without mechanical damage and is not dependent on the electrolyte composition[30–32]. Additionally, It can enable high productivity by processing a large surface area or a large number of components at the same time. Therefore, the EP method has become one of the most promising polishing methods for L-PBF-based metal AM parts in recent years.

A typical EP system includes a power source, an anode (workpiece), a cathode (tool electrode) and electrolytes[33]. With the increased of the current density, the anodic EP process can be divided into 4 steps: etching, passivating, polishing (limiting current density plateau region), and transpassive regions. During the polishing process, a uniform viscous layer forms on the anode surface causing a current density difference between the peak and valley regions on the anode surface. Finally, the surface becomes smooth gradually because the materials removal rate is proportional to the current density according to Faraday's law[34]. However, the current density in the polishing region of the acid solutions, including phosphoric acid, sulphuric acid and perchloride acid is normally below 100 mA/cm^2 at ambient temperature[35–39]. Most of the investigations using the electrolytes focused on the surface with an initial roughness of approximately 1 μm or at a nanometre scale. In contrast, L-PBF components usually have a

roughness approximately in the order of 15 μm or greater[5,36–40], meaning that the polishing efficiency would be low or the polishing time would be long for polishing AM components at the low limiting current density with the electrolytes. Additionally, the dimensional accuracy and component shape could deteriorate when the polishing time is too long because of the large materials removal rate and the subsequent impact of the edge effect[41–43].

The transpassive region on the polarisation curve is where the viscous layer starts to be broken down and many side reactions happen. The EP process can be carried out at a high current density to reduce polishing duration at the region, for instance, it can take 300s to smooth 316L SS from the roughness of 13.88 to 3 μm through an EP process using a mixture of phosphoric and sulphuric acids under 104 °C, 800 mA/cm^2 and 200 rmp magnetic stirring[44]. However, the electrolysis of water at the high current density could generate oxygen bubbles on the anode surface, which might cause pitting corrosion due to the 'broken bubble tunnelling effect'[45]. Recently, Han *et al* proposed an eco-friendly non-aqueous NaCl-based electrolyte, which had a better polishing effect than the H_3PO_4 – H_2SO_4 mixture for the nanometre-scale steel surface[39]. However, the polishing effect of the electrolyte for the rough AM steel surface in the transpassive region is still unknown.

Other parameters including the electrolyte viscosity, inter-electrode distance, electrolyte flowing mode and the impact of the L-PBF sample surface profile on the polishing effect still need to be investigated. Since the EP process is too complicated and the parameters have an influence on each other, a large number of experimental attempts need to be carried out when a new type of metal or electrolyte is introduced. Therefore, many researchers started to focus on modelling, simulating and predicting the polishing process and roughness changes using Finite Element Method (FEM) and Machine Learning[46–49]. FEM could provide the relationship between polishing parameters and roughness changes, particularly for observing the process changes with time, while Machine Learning could predict the roughness changes for large amounts of polishing parameter sets in a short time. In some engineering fields, researchers adopted the FEM method to generate data and then input them into machine learning models for prediction to save time[50,51].

The main aim of this research is to successfully reduce and control the surface roughness of L-PBF samples. Since the surface texture of the L-PBF components is different from the machine sample, the characterisation method should also be adjusted. The materials selected for the experiment have different polishing characteristics: 316L SS and L-PBF TC4 (Ti6Al4V). Regarding 316L SS, many salt and acid electrolytes can be used for polishing and thus the critical issue is to identify the suitable polishing windows to reduce the surface roughness with the least materials removal amount[36,52–55]. Regarding TC4, common acid solutions might not work as the oxide layer on the surface is too dense to be removed[31,56,57].

Therefore, the critical issue is to identify a suitable combination of electrolyte and metal for polishing. Regarding the prediction, since experiments usually have errors for the same set of samples, and the collection of data takes time, an accurate and stable algorithm should be identified to predict small-scale samples.

To achieve the targets listed above, this research needs to complete the following objectives:

- Surface characterisation: The surface texture of the L-PBF ranges from sub-microns to hundreds of microns, while the ISO standard does not define how to distinguish and measure the surface roughness of the L-PBF samples. Generally, a primary surface can be divided into waviness and roughness surfaces, which have a specific distinct cut-off value. Many researchers considered the texture with a wavelength smaller than the laser track width as the roughness features while those textures with a wavelength larger than the laser track width also contribute to the poor surface quality. Therefore, identifying a method to evaluate the surface quality is necessary.
- Modelling and simulation of the EP system. The EP process involved many parameters including the polishing current density, polishing time, electrolyte type, electrolyte flow mode, inter-electrode distance, sample surface texture, etc. To reduce the experiment workload, an appropriate Finite Element Analysis (FEA) EP simulation model is necessary. The model should have a similar surface profile and roughness to the practical sample and the results should reflect the polishing effect.
- EP L-PBF samples: The 316L SS and TC4 with initial roughness above 10 μm should be polished with the simulated parameters and the roughness, weight and height changes should be investigated. How to improve the polishing effect such as further reducing the roughness or the materials removal amount, and how is the effect of the combination of different polishing parameters should be investigated.
- Prediction model selection and setup: Many models can be applied for carrying the prediction, like numerical simulation (FEM, Monte-Carlos, etc), machine learning (Neural Network, Random Forest, etc), etc. Numerical simulation can reduce the experiment workload and provide the details of the polishing process and results while this method takes time. Machine Learning could give a fast response, but a large amount of data is needed. In this thesis, this simulation will be discussed, and a moderate method adopted for prediction.

1.5 Methodology of this Thesis

In this thesis, the following research methodologies were adopted:

- The sample polarisation curve will be measured by a potentiostat in a three-electrodes electrochemical system. The curve will be analysed to primarily evaluate the polishing effect of the electrolytes and confirm the range of the polishing current density (mA/cm^2).
- The gaussian filter will be introduced to divide the primary surface of the L-PBF sample into waviness surface and residual surface based on the wavelength of the laser track. Profiles with different cut-off values will be investigated to guarantee the signal integrity of all types of surface textures.
- The Spatial Frequency Method was employed to model rough L-PBF surfaces, and the simulated surface roughness was compared with the measured results. FEM was introduced to model the viscous layer formation process during the EP process. The surface roughness and the uniformity of the viscous layer were calculated in MATLAB software.
- The 316L SS and TC4 samples will be polished based on the simulation parameters with different current densities and polishing times. Each experiment will be repeated three times to minimise random error. A two-step EP process will be proposed and carried out based on the one-step polishing effect.
- The neural network and random forest will be introduced to train and predict data obtained in the experiment. The prediction accuracy of the model will be improved using the hyperparametric optimisation method.

1.6 Thesis Layout

- Chapter 1 covers the research background, tasks, methodologies, and layout of this PhD research.
- Chapter 2 provides a literature review of technologies and studies relevant to surface finishing and measurement methods, including traditional mechanical polishing, abrasive-based polishing, thermal-based polishing, and chemical and electrochemical polishing.
- Chapter 3 introduces the measurement technologies including electrochemical analysis and surface characterisation. The initial characterisation and analysis of the polarisation curve and division of the surface texture were presented.
- Chapter 4 numerically simulates the viscous layer growth process on the anode surface during the EP process. The polishing parameters including diffusion coefficient, inlet velocity, inter-electrode distance, and height and wavelength distribution are investigated numerically concerning the thickness and geometry of the viscous layer.

- Chapter 5 investigated four types of electrolytes for their effectiveness in polishing 316L SS and TC4. The electrolyte included 65 % H_3PO_4, 85 % H_3PO_4, a mixture solution of 1M sodium chloride (NaCl), ethylene glycol (EG), and 10% ethanol, and an aqueous commercial electrolyte A2. The effects of high current densities on the surface roughness, materials removal weight, and thickness reduction were evaluated, along with the morphological characteristics of the polished surfaces.
- Chapter 6 proposes a two-step EP process method by using the NaCl-EG-10% Ethanol and A2 electrolyte with different polishing times and current densities. The one-step and two-step experiment parameters and results were adopted for future prediction using machine learning.
- Chapter 7 details some important conclusions of this research and future work to improve the polishing efficiency of the rough AM surface and the prediction accuracy.

Chapter 2 Literature Review

This chapter provides a literature review concerning EP technology. Firstly, the basic knowledge including the system setup, materials removal mechanism, polarisation curve, theory development, materials and processing factors in general EP process are presented. Then the application of EP technology in polishing L-PBF components and its limitations are summarised.

2.1 Fundamental Aspects of Electrochemical Polishing

EP technology is a process of removing materials from component surfaces for the aim of polishing, passivating, and deburring[58,59]. Although the EP process was initially discovered in the nineteenth century, it is still a promising method to machine metals as it has no damage on the surface, unlike the mechanical method. In recent years, laser manufacturing, AM, and biomedical devices developed rapidly, which further provided high requirements on surface conditions obtained by EP technologies.

EP technology is a complex process that involves several simultaneous mechanisms, including chemical reactions, electron exchange, ion transfer, and electric-thermal exchange. The process is influenced by various factors, such as current density, voltage, electrolyte composition, temperature, agitation, inter-electrode distance, etc. Currently, there is no mature theory able to explain the EP process and mechanism perfectly. Therefore, understanding the fundamental aspect is essential for researchers or practitioners before carrying out simulations or experiments.

2.1.1 Electrochemical System

EP systems can be classified into two types: two-electrode and three-electrode systems, as depicted in Figure 15. In the two-electrode system, the workpiece serves as the anode, or working electrode, and is connected to the positive side of the power source. The other electrode, the cathode or counter electrode, is connected to the negative side of the power source. Both electrodes are immersed in a tank filled with electrolyte[33]. When the power source is turned on, current flows through the direction of the positive - working electrode - electrolyte - counter electrode - negative, and the metal dissolved occurs on the anode surface[34,60]. Usually, the dissolved metals would transform into metal oxide or hydroxide, and some by-product may be generated on the anode and cathode surface depending on the polishing parameters. Regarding a specific EP system, there should exist an optimal region of current density and potential for achieving the desired polishing effect. Nevertheless, it should be noted that the potential difference between the anode and cathode may be influenced by the surface conditions of the counter electrode. Consequently, the optimal polishing parameters may optimal polishing parameters might be varied slightly each time.

Figure 15 (b) depicts the three-electrode EP system, which includes an additional reference electrode in addition to the two electrodes in the two-electrode system. In this system, the applied voltage is the potential difference between the working electrode and the reference electrode. As the potential of the reference electrode is insensitive to changes in the environment, the voltage values remain stable. Therefore, the optimal polishing parameters and better polishing effect are easier to obtain. However, the reference electrode usually has restrictions on the applied voltage, pH, electrolyte composition, etc., or it would be destroyed.

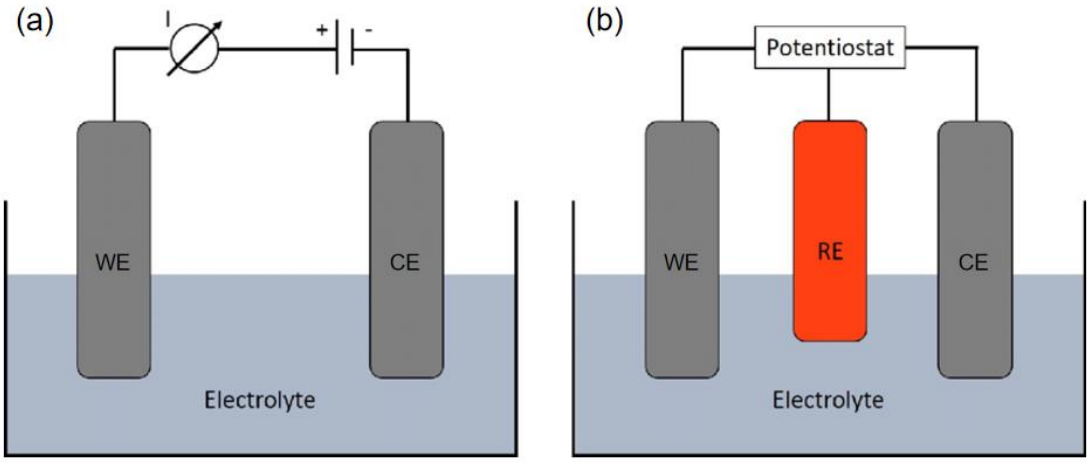

Figure 15 Typical setup of EP system (a) two-electrodes system and (b) three electrodes system (WE: working electrode, RE: reference electrode, CE: counter electrode).

2.1.2 Materials Removal Mechanism

During the EP process, electrons will be transferred from the anode to the cathode via the external circuit, and from the cathode to the anode within the electrolyte. This will result in the loss of electrons and oxidation of metal elements situated on the anode surface. Simultaneously, the metal ions will transport toward the cathodic side and possibly be reduced depending on the potential. If the solution contains hydrogen ions, the cathode surface will generate hydrogen as a result of the low reaction potential.

Figure 16 (a) illustrates an example of chemical reactions in the EP process. The reaction can be expressed as the oxidisation of metal and oxygen ions, and the reduction of hydrogen ions on the anode and cathode surface, respectively.

$$Me \rightarrow Me^{+}$$

$$O^{2-} \rightarrow O_2$$

$$H^{+} \rightarrow H_2$$

where M_e represents one type of metal. However, sometimes the generation of gas bubbles cannot be observed during the EP process because a compact salt film will form on the anode surface during the EP process.

Figure 16 (b) illustrates the 'sharp effect' of the electrons, which is one of the factors for surface flattening. More electrons prefer gathering at the sharp regions and therefore, the current density at the region will be higher than in the flat region. According to Faraday's first law:

1. The amount of material (ions) oxidised or reduced at the electrodes during electrolysis is directly proportional to the amount of electrical charge that is passed through the electrolytic solution or molten electrolyte.

$$m = zFIt \qquad (2)$$

where m is the mass of substance deposited or dissolved, z is the number of moles of electrons involved in the reaction, F is the Faraday constant (96485 C/mol), I is the current flowing through the electrolyte, and t is the time. Therefore, the peak region will have a larger materials removal amount than the flat region in the same polishing time. Additionally, Faraday's second law can also be applied to describe the materials removal process, as shown below as 2.

2. When the same amount of electrical charge is passed through different electrolytes containing ions of different elements, the amount of material (ions) that is oxidised or reduced at the electrodes is directly proportional to the chemical equivalent weight of the element.

$$m = \frac{MIt}{nF}[g] \quad (3)$$

where M is the molar mass of the material being dissolved, I is the current flowing through the electrolyte, t is the time of EP process, n is the number of moles of electrons involved in the reaction, and F is the Faraday constant. Noticeably, the number of coulombs of electricity required to oxidise or reduce 1 M of a particular element during the EP process can be expressed as *nF/M*.

With a workpiece material density of ρ, the volume of material V removed during the EP process based on the current I, time t and the fundamental principles of electrochemistry can be expressed as equation *(4)*.

$$V = \frac{MIt}{nF\rho}[mm^3] \quad (4)$$

However, mass transport of the dissolved metals, acceptors, etc. will also restrict the current density. Detailed discussion will be presented in the following sections.

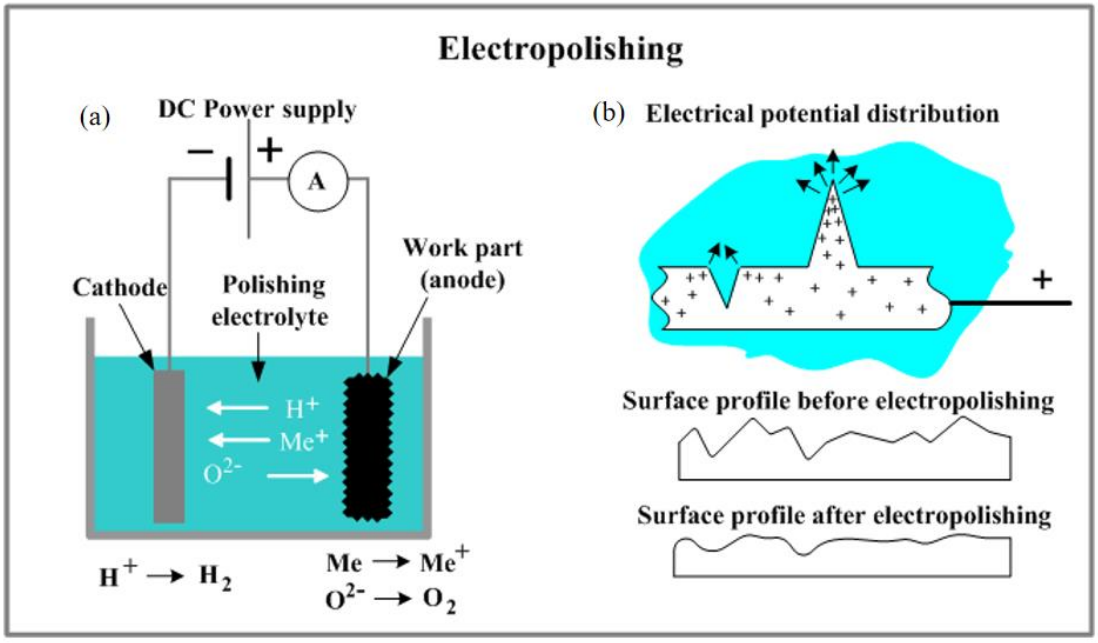

Figure 16 Materials removal mechanism in a two-electrodes EP system (source: www.substech.com)

2.1.3 Anodic Polarisation Curve

Generally, the anodic polarisation curve is the voltage-current density curve measured in a three-electrode EP system, which can present the surface processes status on the anode surface under different voltage or current densities. Figure 17 shows three types of polarisation curves measured in the electrochemical systems with different electrode materials and electrolyte compositions). Curve 1 implied that only the etching process happened in the

electrochemical system with the increasing current density. In this system, the grain boundary on the anode surface will be electrochemically corroded and no other behaviour will occur in the electrolyte, leading to the generation of an uneven surface. Curve 2 implied the polishing process with high efficiency could happen in the electrochemical system where three sub-regions were divided. Etching still occurred in region (i) because the fundamental anodic layer was still not generated on the anode surface. With the increase of current density, the layer was generated and stable, polishing behaviour occurred in region (ii). The polishing process in region (ii) was mass transport controlled and the thickness of the layer would be increased with the increased voltage. However, the anodic layer because unstable and even broken when the current density enters the region (iii). A large amount of gas bubble would also be generated on the anode surface, leading to pitting corrosion. Curve 3 implied the passivation process happened and affected the polishing efficiency in the electrochemical system. Region (i) is also the etching process as curve 2 while a passive oxide layer would form on the anode surface when current density enters region (ii). The current density had an evident drop because the resistance of the oxidised layer was high, leading to a low rate of metal dissolution. In region (iii), the passive oxidise layer would be destroyed and the transpassive phenomenon occurred that the dissolution became uniform, leading to a smooth but not polished surface.

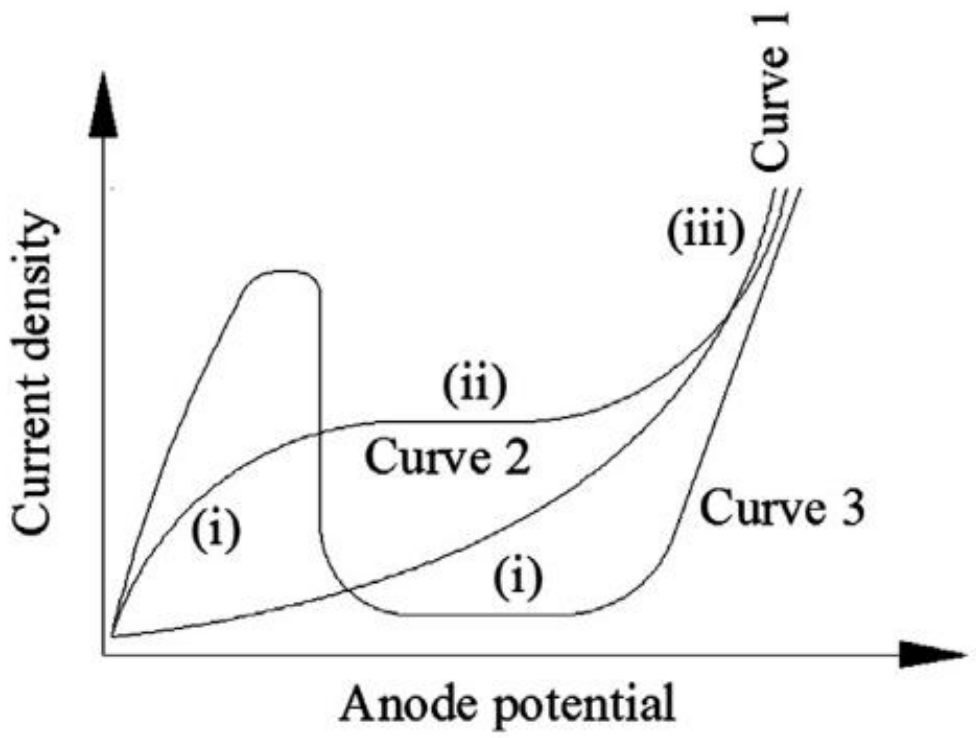

Figure 17 Anode potential–current density polarization curves [61].

In general practice, the polarisation curve in the EP system might not be as ideal as curve 2, but it would be more similar to one between curve 2 and curve 3. Figure 18 shows a classical polarisation curve of an EP system, including the regions of etching, passivating, polishing (limiting current density plateau region), and transpassive (gas evolution). The etching, passivating, and polishing phenomena would occur at the same time while the polishing was the domination at the limiting current density plateau region.

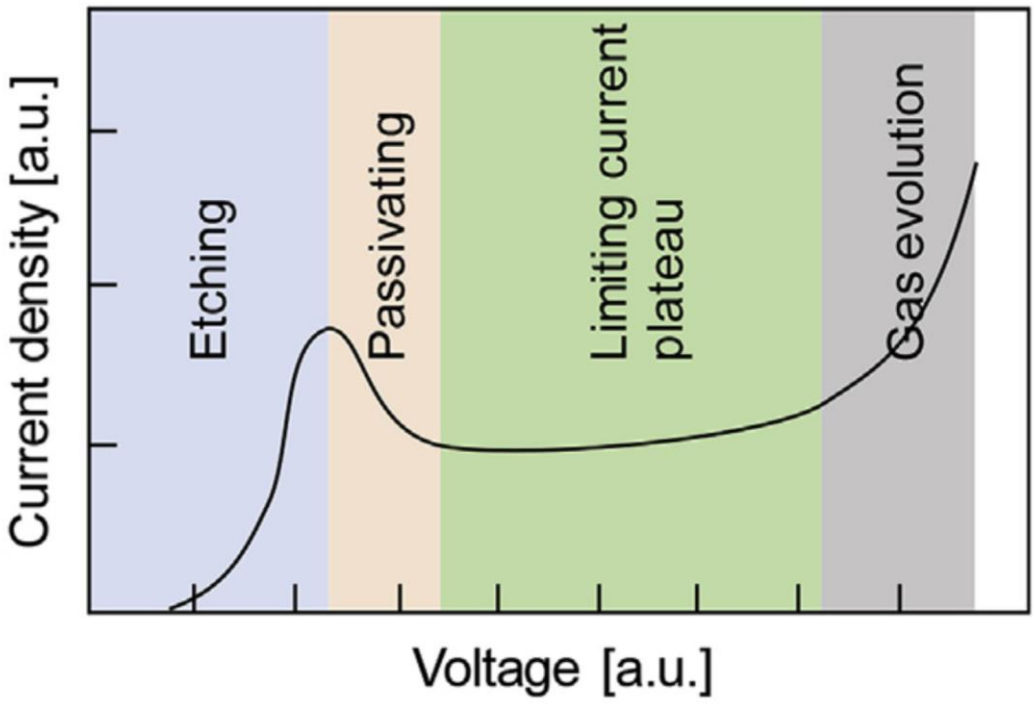

Figure 18 The current density-voltage curve of EP process[34].

2.1.4 Electrochemical Polishing Theory

As the metal continues to dissolve, a viscous layer is generated on the anode surface, causing the metal ion concentration to decrease from the surface towards the bulk electrolyte. Despite the numerous theories that have been proposed to explain the nature of the viscous layer, the materials removal mechanism, and other aspects of the process, no single theory can fully explain the complexities of electrochemical polishing (EP). However, these theories have contributed to a better understanding of the EP mechanism. For example, Jacquet's and Hoar's theories provide insight into the surface smoothing mechanism, while Elmore's, Halfaway's and Rowland's theories help to explain EP efficiency[62–66].

- Viscous layer theory

Jacquet pioneered the systematic study of the EP process through brightening copper surfaces in aqueous orthophosphoric acid and proposed the 'viscous layer theory' in 1935 and 1936[62,67].

As shown in Figure 19, a viscous layer with high ohmic resistance was generated on the anode surface because of the diffusion of the electrolyte and dissolved metals. Under the assumption that the viscous layer boundary adjacent to the bulk electrolyte was flat, the viscous layer thickness at the valley regions was larger than that of the peak regions on the anode surface. Therefore, the current density would be higher at the peak regions than that of the valley regions. As the materials removal rate is proportional to the charges flowing through the system according to Faraday's law, metal at the peak regions would have a more rapid dissolution rate. Finally, the surface became smooth gradually.

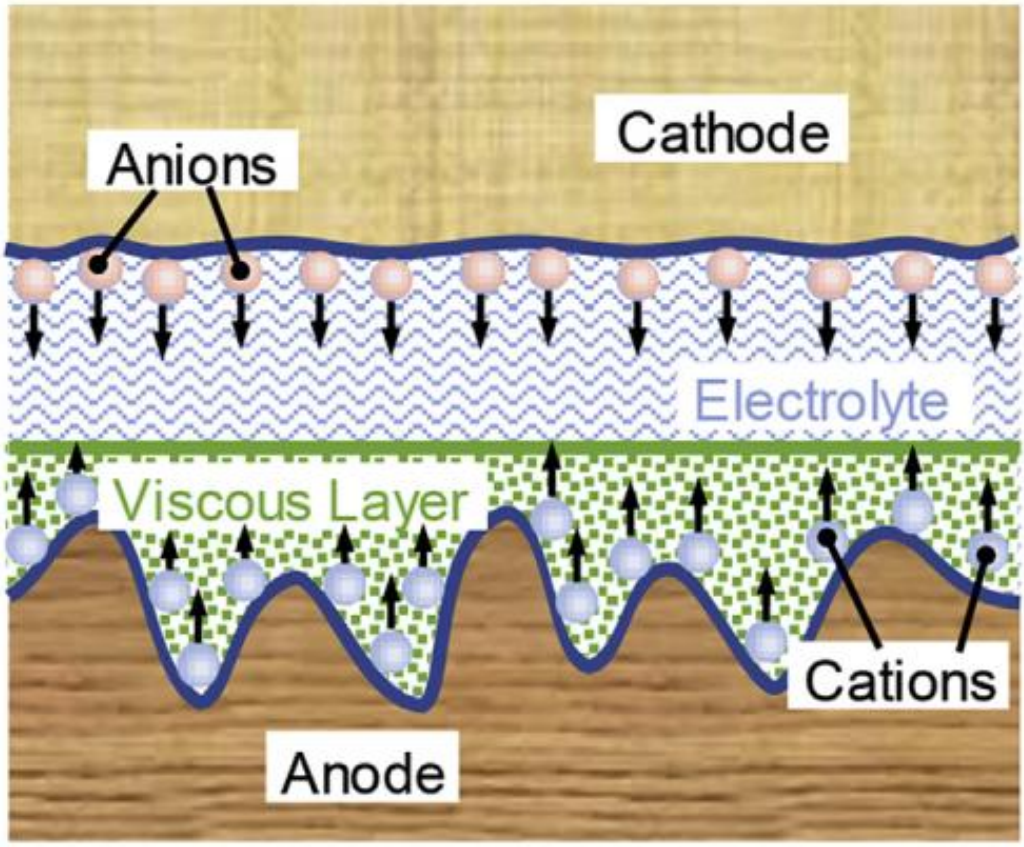

Figure 19 Schematic diagram of 'viscous layer theory'[34].

The viscous layer was experimentally observed later in 1942 and 1950 by Gilbertson and Francis *et al* on polishing a silver surface in a cyanide bath with direct and cycle current[68,69]. In the same year 1950, Walton *et al* studied the effect of viscosity and conductivities of aqueous phosphoric acid and phosphoric acid-glycerol-ethylene glycol mixtures on the anode layer during the EP process. They concluded that the polishing effect would deteriorate if the anode layer was destroyed, and the effective thickness of the anode layer was estimated to be 100 μm.

However, the description of the theory at that time was somewhat obscure and too simple to explain some common phenomena during the process. For example, why is the existence of the limiting current density plateau region, and why some external parameters such as temperature, agitation, inter-electrode distance and electrolyte viscosity could influence the polishing effect and efficiency? Hickling and Higgins also found the reverse relationship between the metal dissolution rate and electrolyte viscosity in 1953 which cannot be explained by the viscous layer theory at that time. However, The theory indeed provides a new horizon for explaining the EP process and is still widely adopted for guiding the experiment nowadays[70–73].

- Passivation theory

In 1950, Hoar *et al* proposed the 'passivation theory', where the characteristics of the compact solid film generated on the anode surface during the EP process were similar to the anodic passivity oxidise film[63]. They conducted nickel anodic in the solution of aqueous sulfuric acid and found the potential had a sharp increase before the polishing occurred. The result was compared with the passivation experiment of nickel in low-concentration acid conducted by Muller *et al*[74]. However, the thickness of the compact solid film was the order of a few Angstroms and would be difficult to grow thick because the metal oxidise was dissolved into the bulk electrolyte as fast as it was formed anodically from the metal[63]. Later, Hoar *et al* proved the existence of the presence of the compact solid film by EP copper and α-brass anodes in the aqueous orthophosphoric acid in 1952[75]. Droplets of mercury on EP copper or alpha brass become fixed and then become wet in a small area with the flow of anodic current without spreading, indicating the creation of a successively formed and dissolved dense solid film in the polished area.

In Hoar's theory, the valley region preferred to be oxidised than the peak region on the anode surface because of the thicker and more stable transient flowing layer of the electrolytes. Therefore, the valley region would have more serious polarised, driving the current gathering at the peak region. However, Rowland *et al* reported that Hoar's result could not be confirmed in 1953 and Williams *et al* reported the detection of the copper phosphate film but not copper oxidise by electron diffraction later, which conflicted with Hoar's theory[66,76]. Therefore, the composition of the film generated on the anode surface still needs further investigation.

- Diffusion theory

In 1939 and 1940, Elmore proposed that the concentration gradient on the anode surface alone controls the rate of solution[64,65]. He made two assumptions: (1) the concentration of copper reached its maximum at the anode surface and decreased toward the bulk electrolyte, limiting the dissolution and transport of the copper; (2) the concentration gradient at the peak regions

was larger than that of the valley regions, and therefore the surface became smooth gradually. According to the Nernest equation as follows:

$$i = \frac{nFD(C_s - C_b)}{\delta} \quad (5)$$

where δ is the diffusion layer thickness, i is the current density, n is the total amount of ions in the EP system, F is the Faraday constant, D is the diffusion coefficient of the rate-limiting species, C_s is surface concentration and C_b is the bulk concentration of the ions. As the diffusion layer thickness at the peak region is thinner than that at the valley region, the current density at the peak regions would be higher and thus a higher materials removal rate. Additionally, Elmore also established the relationship between the current density and the time required for the diffusion layer growth. The equation was as follows[65]:

$$r = \frac{t_0}{i_0 t_0^{\frac{1}{2}} C_m A F \sqrt{\pi D}} \quad (6)$$

where i_0 is the current, t_0 is the period to generate the stable diffusion layer, C_m is the dissolution ability of metal in the electrolyte, A is the polishing area, F is the Faraday constant and D is the diffusion coefficient of dissolved anode materials.

In 1956, Williams and Barrett confirmed Elmore's theory by experimentally polishing copper in aqueous phosphoric acid. The composition of copper phosphate was observed by electron diffraction technology and the assumption that copper ions had a dissolution limitation in phosphoric acid was proved. Currently, the diffusion theory is one of the most acceptable mechanisms for explaining the EP process, especially in the rate determination process. However, it did not count the electrolyte viscosity, and therefore, the problems of why the electrolyte must be the viscous solution, and why the changes of viscosity or temperature could influence the polishing efficiency cannot be solved by the theory.

- Acceptor theory

Elmore's theory considered the metal ions to be the limiting factor while Kolthoff and Miller found the limiting current density for anodic dissolution of mercury also emerged when the limiting ions were anions such as SCN^-, etc[77]. In 1951, Halfaway proposed that the anions also contribute to the dissolution of metals on the anode surface, and this theory was developed by Edwards in 1953[78–80]. Firstly, Halfaway tested Elmore's equations by polishing copper in the aqueous phosphoric acid and concluded that the process is diffusion-controlled while the assumption that the onset EP coincided with the attainment of the solubility limit of copper in the electrolytes was incorrect. Then Halfaway studied the polishing process on a composite anode surface with peak and valley regions insulated from each other and found that the surface smoothing mode in the EP process was solely related to the concentration gradient within the diffusion layer. Specifically, the polishing effect was governed by the

acceptor including the anions and molecules. Figure 20 shows the concentration distribution of the acceptor from anode surface to the bulk electrolyte, where the limiting current density would be reached when the acceptors on the anode surface was totally consumed.

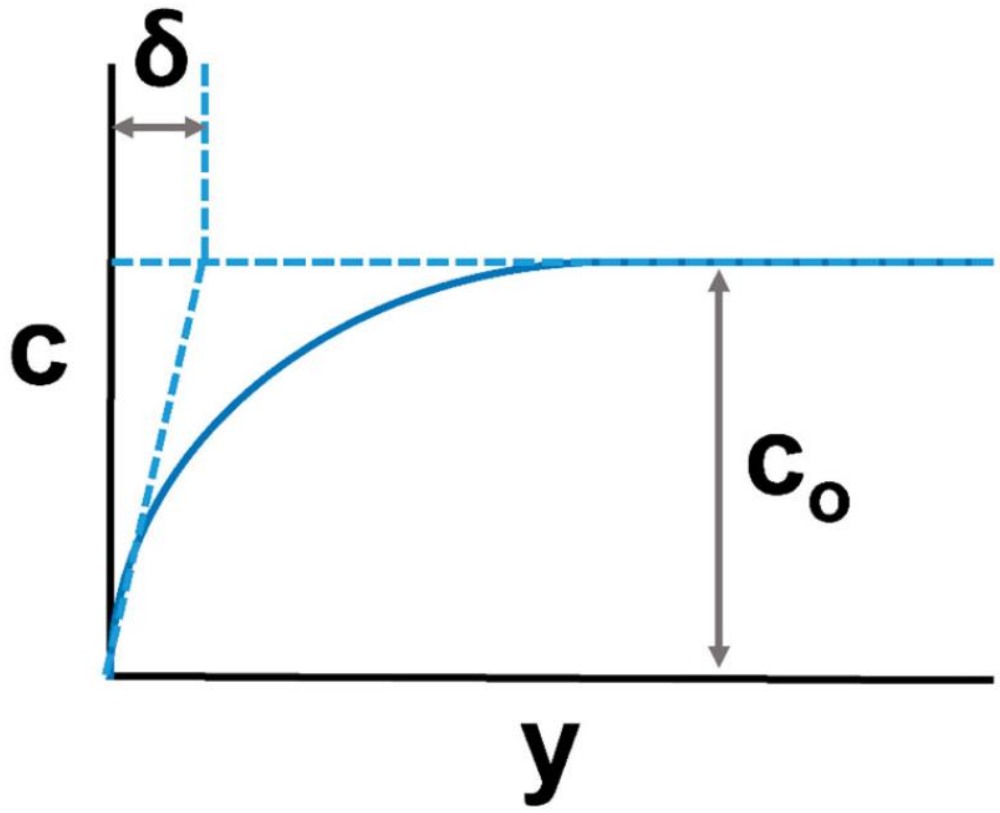

Figure 20 Concentration distribution of the acceptor to the anode surface[60]

➢ Ionic adsorption theory

In 1950, Darmois *et al* proposed the 'ionic adsorption theory' that anions would be adsorped on the anode surface and formed an ionic layer[81]. This theory was established based on Rowland's findings that some metals could be polished in molten chloride[66]. As the oxides would be chlorides at a high temperature, the oxide film formed on the anode surface during the polishing process became impossible.

2.2 Electrode and Electrolyte

Most metals can be polished by electrochemical method while suitable electrolytes should be identified as the electrochemical reaction may be varied according to the electrode and electrolyte materials.

2.2.1 Anode Materials

Electrode-related Variables contain the materials, shape, initial surface conditions of two electrodes and surface size of the anode.

Initially, EP was mainly applied for finishing stainless steel, which was being utilised to smooth the surface and improve the anti-corrosion until now. At present, EP materials have been extended mainly on the following metals[82]: aluminium, antimony, beryllium, bismuth, cadmium, chromium, cobalt, copper, germanium, gold, hafnium, indium, iron (including alloy steels, carbon steels, cast iron, ferrosilicon, stainless steels), lead, magnesium, manganese, molybdenum, nickel, niobium, palladium, platinum, silver, tantalum, thorium, tin, titanium, tungsten, uranium, vanadium, zinc, and zirconium. This development is because of its various advantages, such as uniform finish, removal of burrs and sharp edges, improved cleanliness, precise material removal, ability to smooth complex components, etc. In this part, 316L SS and TC4 were selected as examples because (1) stainless steel is the most common metal in the manufacturing industry and (2) TC4 are promising material used widely in many fields, especially medical devices while polishing by EP is still difficult.

- 316L SS

The polishing of stainless-steel mainly consists of three steps[83], pre-treatment, EP process and characterisation, as shown in Figure 21. The specimen is first grounded to remove macro-defects such as scratches, etc., and to obtain an expected initial surface roughness. Then the anodic polarisation curve is measured to confirm the EP potential and current density. Typically, the EP process is carried out at the limiting current density plateau region where the current density and the corresponding potential are low. Other parameters, such as the inter-electrode distance, agitation rate, polishing duration, etc., are adjusted in the experiment process. After polishing, several methods will be used to measure its polishing efficiency and final surface quality. Electrochemical impedance spectroscopy can be adopted to investigate the resistive and capacitive properties of the EP system and could provide valuable insights into the anodic dissolution process of SS under the mass transport process[84]. X-ray photoelectron spectroscopy can be used to analyse the composition of the surface oxide film to compare anti-corrosion ability before and after polishing[83]. For example, the increase of the Cr element in the surface oxide film can offer a significant improvement in corrosion resistance and pitting potential[4]. Several types of microscopes introduced in section 2.4.2 can be applied to primary surface roughness[62,85–87].

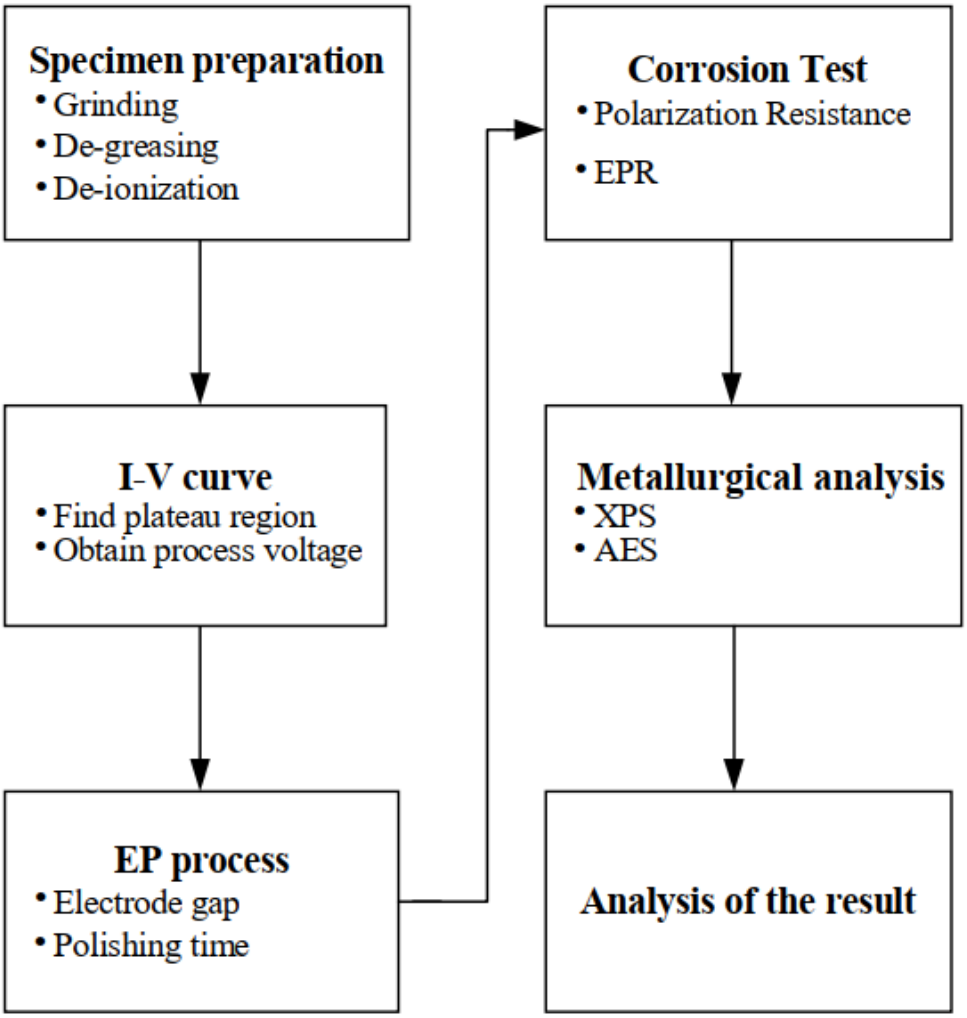

Figure 21 Flow chart of EP stainless-steel[83]

➢ TC4

Ti and its alloy are currently in high demand in the industry due to their versatility and capability with a wide range of applications, including aerospace[88], medical applications[89], goods storage[90], and medical devices. etc. The surface of Ti alloys naturally forms a stable oxide layer under ambient conditions, which imparts excellent corrosion resistance, biocompatibility, and excellent mechanical properties to these materials[91–93]. EP technique has been proven to effectively eliminate surface unevenness, residual stress, etc., and produce a thin, well-defined TiO_2 layer that serves as a protective barrier[94]. However, Ti alloys, especially pure Ti, are commonly polished in HF or perchloric acid solution because of the highly stable oxide thin layer on the surface[95,96]. These species are highly hazardous and could cause several accidents if not used with extreme care. Two methods have been taken to solve this issue, including developing new electrolytes and using pulse-reverse current.

Zhang *et al*[27] polished Ti-6Al-4V using a mixture electrolyte of ethylene glycol, magnesium chloride, and a small amount of deionized water. Figure 22 (left) shows that a levelled and brightened surface with lower roughness (Ra = 2.52 μm and 1.13 μm) and weight loss was attained when the chloride concentration is 0.3 or 0.4 mol/L. This means that chloride ions can promote the dissolution of Ti alloys and improve the polishing effect. However, when chloride concentration is 0.5 mol/L, a rough and dark surface was observed, which may be caused by the continuous metal dissolution process or over-corrosion during the EP process. Figure 22 (right) shows the effect of adding ethanol into sodium chloride electrolyte to polish pure titanium, and successfully obtaining a smooth and brighten surface after 50 min[56].

Taylor developed a versatile pulse-reverse waveform to smooth passive metals[97]. The anodic forward pulse is adjusted to augment anion movement toward the anode. Throughout the reverse pulse stage, the cathodic pulse is activated, possessing the ability to de-passivate the surface, thus eliminating the necessity for chemical additives such as hydrofluoric acid or alternative oxides. Subsequently, an OFF period might be implemented to enable the restoration of reactive species and the expulsion of by-products and heat. Compared to the traditional EP system with a DC output, the pulse reverses EP process can provide a more flexible combination between the workpiece and electrolytes, and a high materials removal rate because of the high instantaneous positive current density.

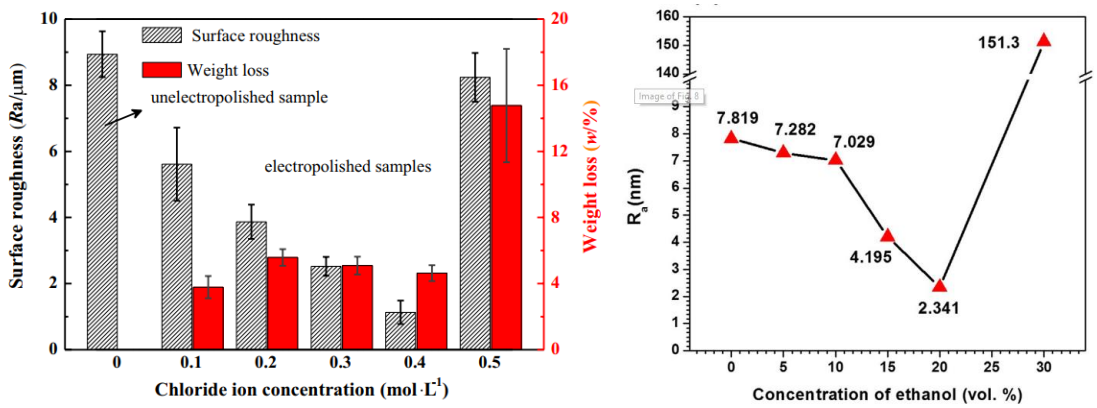

Figure 22 Influence of chloride concentrations on the surface roughness of Ti–6Al–4V for EP at 25°C, a current density of 0.5 A/cm and a polishing time of 10min (left) Ra values of the EP Ti substrates, as determined with AFM: as a function of the concentration of ethanol added when a constant 20V is applied (right)[27,56]

2.2.2 Cathode and Reference Electrode Materials

The common cathodes are as follows: platinum, graphite, titanium, brass, silver, stainless steel, and copper, which are required to have high stability, not to react with electrolytes and good electrical conductivity[98–100]. The additional reference electrode is an electrode that has a stable and well-known electrode potential such as the standard hydrogen electrode, normal

hydrogen electrode, and saturated calomel electrode. Such electrodes are used as a reference potential to measure the voltage-current curve of the anode/electrolyte interface or electrolyte or electrolyte/cathode interface to speculate potential physical/chemical reactions[101–103].

2.2.3 Other Electrode-Related Parameters

➢ Electrode shape

Shapes of the cathode should be designed according to the anodic structure to form a stable and average electric distribution field. The cylindrical tool can be used for polishing the inner surface of holes, and the cuboid tool is for a flat surface. Regarding complex-shaped components, several large-sized plates can be introduced and connected to surrounding workpieces[104,105]. Hocheng *et al* designed several different forms of tools to smooth holes and found that an electrode with a helical flute can further improve surface roughness, meaning that more form-details optimisation can lead to a better polishing effect[106]. Additionally, differently shaped tools can change the electric distribution between anode and cathode, resulting in different size accuracy after processing[107]. The region that could not be covered by the cathode will have little current density flow through and therefore, a low materials removal rate.

➢ Initial surface condition

The initial surface condition is another critical factor influencing the final polishing effect. First oils and greases should be washed by the process of degreasing and pickling, promoting electrolyte contact with the anode surface[108]. Second, initial surface roughness should be controlled to obtain expected results because of the limited polishing ability of the EP process. Maciag *et al* electropolished several samples with different initial pre-treatment methods (mechanical polishing with different sandpapers, sandblasting, brushing)[109]. Results showed that these samples reached their respective optimal surface quality under the same time, voltage, and current density conditions, but with different roughness values. Figure 23 illustrates the impact of initial surface roughness on the EP of nitinol surfaces using an acid electrolyte[110]. The results show that, on one hand, with an initial roughness of 1 μm, the surface roughness was rapidly reduced to below 0.5 μm within 50 s during the EP process, and there was no signification improvement in surface roughness beyond this point. On the other hand, with an initial roughness of 2 μm, the surface roughness was gradually reduced to 0.98 μm after 300 s EP process, and no apparent improvement was observed beyond this point. The findings highlight the importance of carefully considering the initial surface roughness of the workpiece to achieve a fast and effective EP process because the maximum polishing capability of the EP process is limited. At the same time, cathodic surface quality

can influence the polishing effect for the anode because micro-peak and valley can affect the distribution of the electric field, leading to etching, not polishing, or other defects.

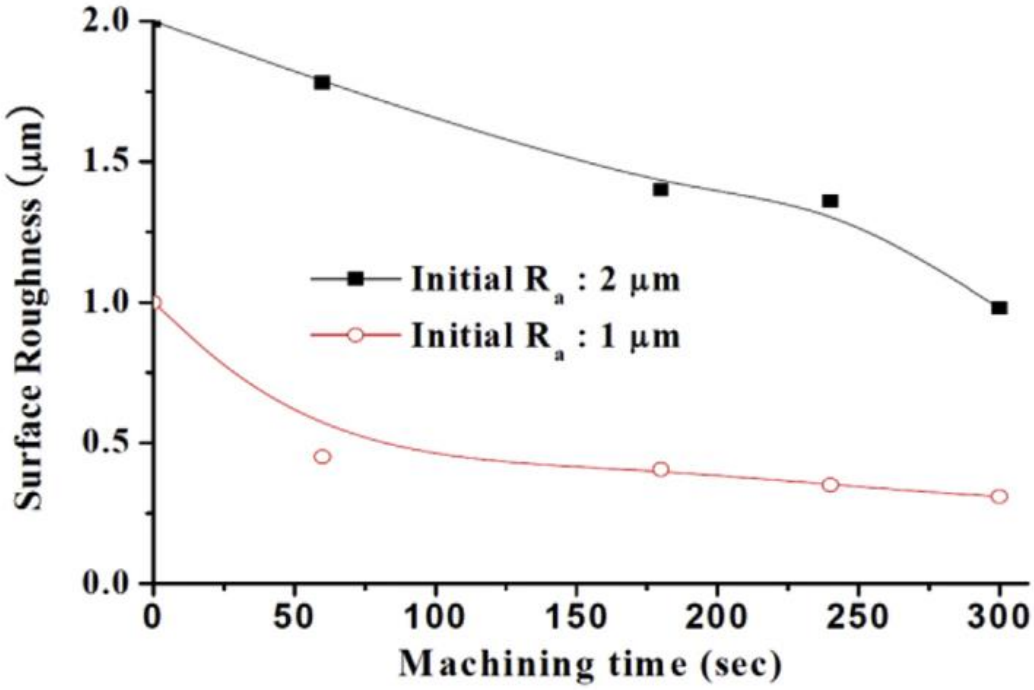

Figure 23 Characteristics of initial anode surface roughness according to the variation of machining time[110]

➢ Polished surface size

Anodic surface size is essential to calculate current density combined with the average output current of the power source. Current density is a primary parameter reflecting chemical reaction rate, and its equation can be expressed as follow[111].

$$i = \frac{I_{ave}}{S} = \frac{I_{on} \times t_{on}}{S \times (t_{on} + t_{off})} \quad (7)$$

where I_{ave} is the average current density, S is the anodic surface size for polishing, and I_{on}, t_{on}, and t_{off} are the current density and time of the pulse on and off.

2.2.4 Electrolytes

A desired electrolyte contains three parts: electroactive species, additives, and solvent. As a result of the unique characteristics of metals, particular solution compositions should be designed for polishing different metals, leading to a large number of electrolyte types. The conventional electrolytes used to electropolish metals are acid solutions: hydrogen fluoride[112], perchloric acid[31], sulfuric acid[113–115], phosphoric acid[113,114,116,117], or hydrochloric acid[118] because they can react with metals and remove materials effectively. However, some of them are toxic or explosive, and some are concentrated acids, which can damage the human body

and environment. Some researchers try to use other solutions such as sodium hydroxide but do not obtain an ideal result[32,37]. Recently, the neutral salt electrolyte was proved to have a similar polishing effect as the acid electrolytes in the EP process. For example, sodium chloride[119–121] and sodium nitrate[106,113,120,122–130] can be used to electropolish stainless steel. Table 2 and Table 3 summarise the electrolytes used for polishing steel materials in the previous studies. These chemical materials have their characteristics and can be mixed to improve the polishing effect.

Additives are another important species added to the electrolyte for diverse purposes[131]. Some additives are used to reduce the electrolyte resistance to improve polishing efficiency[132]. Others may be added to reduce surface tension, improve the wetting of the metal surface, maintain the pH of the electrolyte, control the rate of metal dissolution, or optimise the chemical, physical or technical properties of the surface[133–135]. These properties include corrosion resistance, texture, hardness, friction resistance, wear resistance, reflectivity, surface energy, ductility and solderability. Sometimes additives can be used as the solvent instead of water[136,137]. Some additives used in the literature included Ethylene glycol, glycerol, diethylene glycol monobutyl ether, Isopropyl alcohol, triethanolamine, triethylamine, ethanolamine, diethanolamine, etc[31,56,114–117,138–143].

The volume ratio of each species also plays a critical role in the EP process of various materials. Inorganic chemical species, such as acids or salts, act as carriers of current, heat, and reaction products during the EP process. For instance, when polishing copper, an increase in acid concentration has been shown to improve the polishing effect, as evidenced by a decrease in average surface roughness[144]. Similarly, when pure Ti alloys are polished using the electrolyte of the sulfuric acid-ethanol, anodic polarisation behaviour recorded at a constant temperature of 253 K reveals that the limiting current density increases with decreasing H_2SO_4 concentration, reaching a maximum at 1M electrolytes, as shown in Figure 24[115]. This trend is consistent with the findings reported by Chen *et al*[145] and Fushimi *et al*[146], who demonstrated that current density decreases with increasing sulfuric acid volume ratio in phosphoric-sulfuric mixed acid. The decrease in current density suggests that the SO_4^{2-} ion is not a significant factor in mass transport during the limiting current plateau region. These findings emphasise the importance of carefully controlling the volume ratio of each species to optimise the EP process for a given material.

Table 2 Electrolytes used for polishing stainless steel

Type of electroactive materials/electrolyte	Function
NaCl[119–121]	➢ Enhanced metal dissolution and improved conductivity ➢ Increased risk of corrosion if the concentration of NaCl is too high and difficulty in achieving a uniform finish
$NaNO_3$[83,104,118,120,122,122–130,147,148]	➢ Used for high chromium steel[149] ➢ Reduced hydrogen gas evolution and environment-friendly ➢ Low material removal rate, increased risk of surface pitting, and difficulty in achieving a high degree of brightness
NaOH [118,147]	➢ Increased materials removal rate and enhanced brightness ➢ Potential damage to equipment and limited compatibility
$NaNO_2$[147,150]	➢ Enhanced brightness, and reduced risk of surface pitting ➢ Limiting compatibility, increased risk of hydrogen gas evolution, and potential environment concerns
H_2SO_4[118,147]	➢ Enhanced material removal rate, improve the polishing effect ➢ Corrosive, limited combability and environment concerns
H_3PO_4[151]	➢ Low corrosive but low polishing efficiency
$NaClO_3$[147]	➢ High removal rates and close tolerances while the removal rate may be reduced if the anode being polished contains high levels of chromium.
$H_3PO_4 + H_2SO_4$[116,147,152]	/
KNO_3[147]	/
$NaNO_3 + Na_2SO_4$[153]	/
NaCl + $NaNO_3$[120,154,155]	/
HCl[156]	/
Na_2SiO_3[157]	➢ Passivating electrolyte
$H_3PO_4 + H_2SO_4 + CrO_3$[158]	/
ChCl + Ethylene glycol[159]	/
H_3PO_4 + Glycerol[117,151]	/
ChCl + Ethylene glycol + $(COOH)_2$[160]	➢ Oxalic acid could improve the properties of the liquid formed

Table 3 Electrolytes used for polishing Ti alloys

Type of electroactive materials/electrolyte	Function
$HF + H_2SO_4 + HNO_3$[161] $AlCl_3 + ZnCl_2 + EtOH + IPA$[95,162–165] $AlCl_3 + ZnCl_2 + EtOH + nBuOH$[162,166] $HClO_4 + CH_3COOH$[95,167,168,168,169] $HClO_4 + CH_3COOH + C_2H_5OH$[169–171] $HF + CH_3COOH + H_2SO_4$[172] $NaCl + C_2H_4(OH)_2$[56,173,174] $C_2H_4(OH)_2 + MgCl_2 + H_2O$[27] $HClO_4 + CH_3COOH + H_2O$[167] $C_5H_{14}ClNO + C_3H_8O_2$[175] $H_2SO_4 + CH_3OH$[134,176] $HClO_4 + C_2H_5OH$[177]	➢ Acid solution is corrosive while can remove materials at a fast speed. Some acid solution is hazardous and not recommended to use such as HF and $HClO_4$. ➢ Salt electrolyte (NaCl, $AlCl_3$, $ZnCl_2$, $NaNO_3$, etc.) is environment friendly while having a low material removal rate, and the polishing quality is worse than acid solution. ➢ Organic solution can de-stabilise the passive film in an anhydrous environment and is environment friendly, while the material removal rate is low[162].

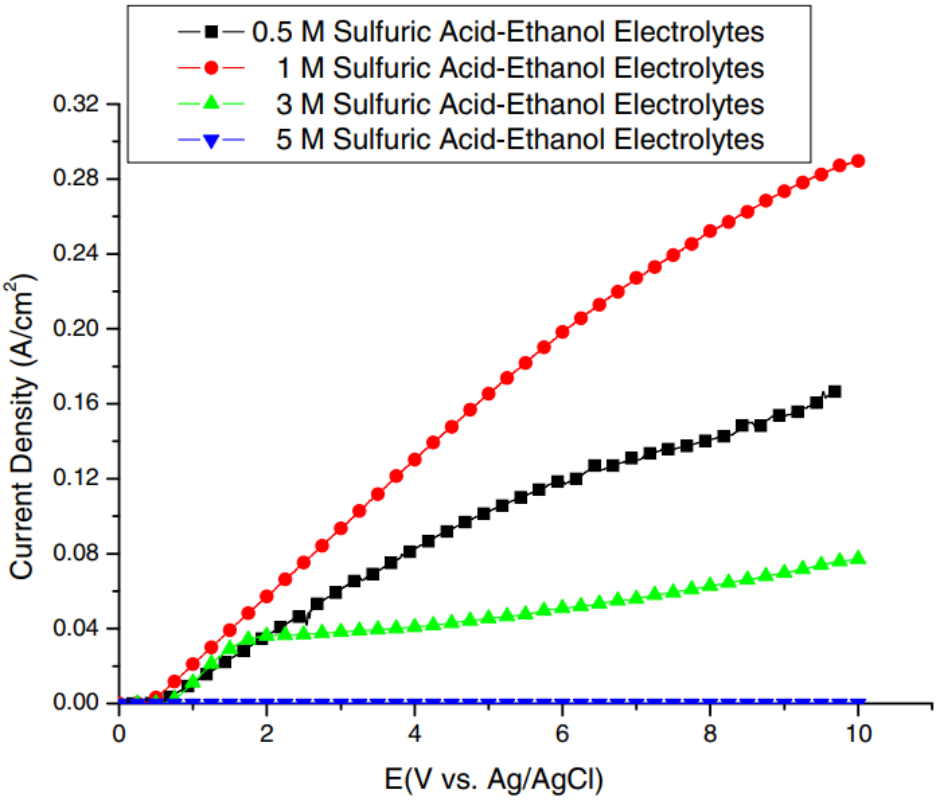

Figure 24 Anodic polarization behaviour of the Ti at a rotation speed of 100 rpm in 0.5, 1, 3 and 5 M sulfuric acid–ethanol electrolytes[115]

2.3 Factors in Polishing Process

Other than the electrode and solution-related variables that will affect the electrode reaction rate, there are still many other factors, as shown in Figure 25. Common factors include temperature, polishing duration, potential, current density and mass transfer mode.

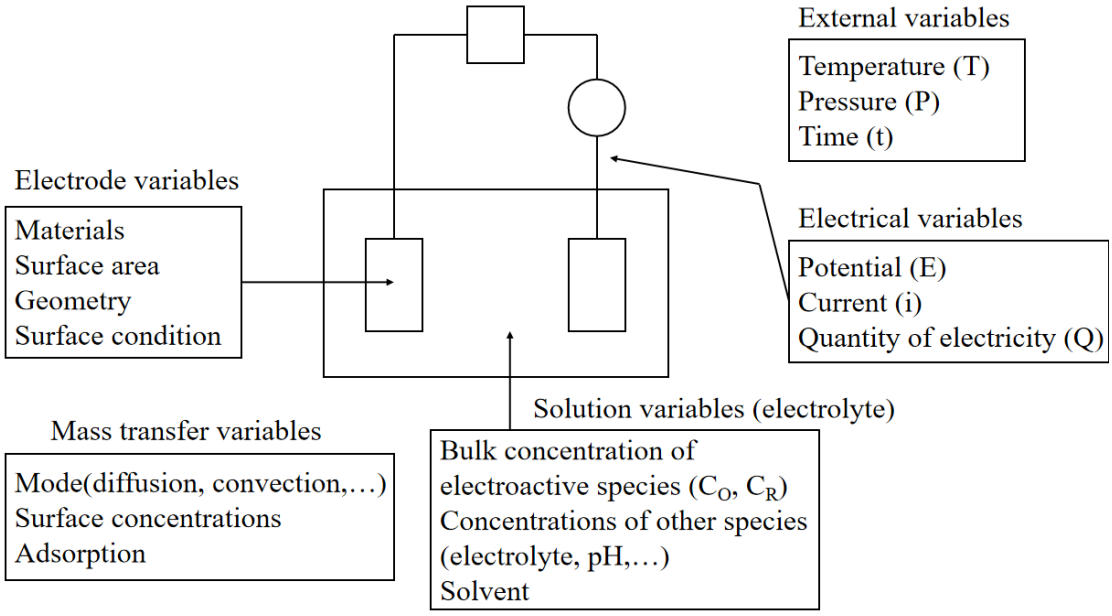

Figure 25 Variables affecting the rate of an electrode reaction[178].

2.3.1 Electrical Variables

As shown in Figure 26, three types of power supply are commonly used in EP: direct current, pulse current and pulse-reverse current. The conventional EP process is typically performed with direct current, in which case only electrical parameters of potential and current density need to be considered[72,179–182]. However, traditional electrolytes usually have high viscosity or low conductivity to increase the potential gradient between the protruded and depressed parts. Consequently, a large amount of heat was generated during the EP process and damaged the viscous layer, leading to a deteriorating polishing effect[60]. For example, in Pawan's experiment, the temperature of the electrolyte can be around 75 ℃, and even a value higher than 100 ℃ can be observed in his previous research[33]. This phenomenon cannot be avoided even if adding a cooling-down device during the EP process.

Soon after, it was found that pulse reverses waveform of the current can be employed, and it can provide an expected polishing effect. Although the average current density and the electrolyte flow rate were low the instantaneous current density was high enough to remove the passive layer adherent on the anode surface[60,152,183,184]. Moreover, the EP system will be

controlled at a low temperate because of the low average current density. For example, Hye-Jin *et al* successfully polished steel at room temperature using pulsed electric current[185]. In this case, extra parameters of pulse width (t_{on} and t_{off}) and duty cycle ($t_{on}/(t_{off}+t_{off})$) can also contribute to the polishing effect. However, this kind of current still cannot finish titanium, which is easily passivated in most electrolytes without concentrated acid[31].

Tayler proposed surface finishing techniques using the pulse-reverse current density, reducing the dependence of the EP system on the types of electrolytes[186]. Figure 26 (c) shows a general pulse-reverse waveform used for the EP process, which can be divided into three stages[60,97,187,188]. At the region of the positive pulse (pulse-time t_F and peak current I_F), the anode dissolved, and the cations moved to the cathode in the electrolyte. At the region of the negative pulse, the anode surface was de-passivated, meaning that the passive layer was reduced. Consequently, the necessity of strong acids such as perchloride acid and hydrofluoric acid was eliminated. At the period of pulse off, the by-product in the electrolyte, heat generation and more importantly, the electrochemical product that accumulates on the anode surface can be removed. Noticeably, the control of the duty cycle is crucial because the continuous pulse current is the basis for generating the stable viscous layer on the anode surface during the polishing process.

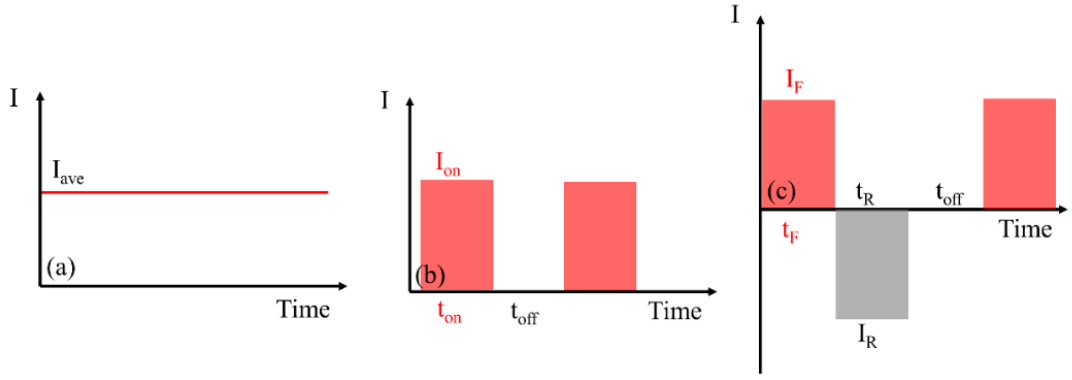

Figure 26 Types of power supply used for EP.

In general, current density controls the electrochemical reaction rate while the potential controls the type of the electrochemical reaction. Figure 27 shows the pourbaix diagram for the valence state of iron in solutions with different pH values and potential. When the anode potential is below line 1, in the acid solution the iron will keep a solid state of Fe. When the anode potential increases to above the dotted line of the hydrogen reduction (where the hydrogen was generated, such as around line 2), iron will be dissolved into Fe^{2+} and Fe^{3+} in acid solutions. Additionally, according to the anodic polarisation curve of steels, as shown in Figure 18, etching, passivating, polishing, and pitting should also be controlled by adjusting the potential difference between the electrodes.

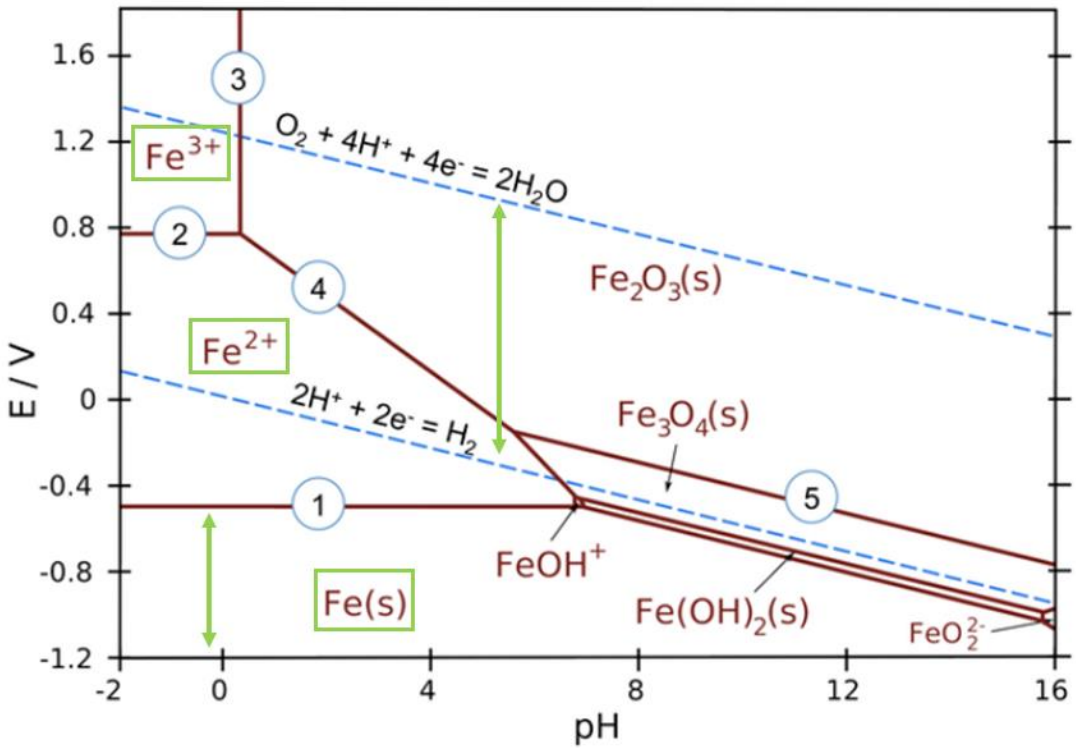

Figure 27 Pourbaix diagram for iron at ionic concentrations of 1.0 mM

2.3.2 Mass Transfer Variables

Mass transfer can be divided into three groups: diffusion, convection and migration, where the mechanisms are concentration gradient, external force and potential difference.

The driving force of diffusion is the thermal motion of molecules, leading to dynamic equilibrium of concentration distribution. As the concentration of dissolved metals reaches the maximum on the anode surface and decreases towards the bulk electrolyte during the EP process, dissolved metals will move along the concentration gradient. Similarly, the anions from the electrolyte will move from the electrolyte to the anode surface.

The mass transfer caused by convection was due to the motion of the solution, and therefore, external forces should be applied such as agitation, flow electrolyte, etc. Figure 28 shows the anode behaviour of 316L SS in the 1M NaCl-Ethylene glycol electrolyte with different stirrer rate[38]. As the EP process at the limiting current density was determined by the mass transport and the agitation could promote the mass transfer, the limiting current density increased with the increasing stirrer rate. Additionally, the passivation and viscous layer could be thinner under the higher stirrer rate, and therefore, the potential range of etching increased.

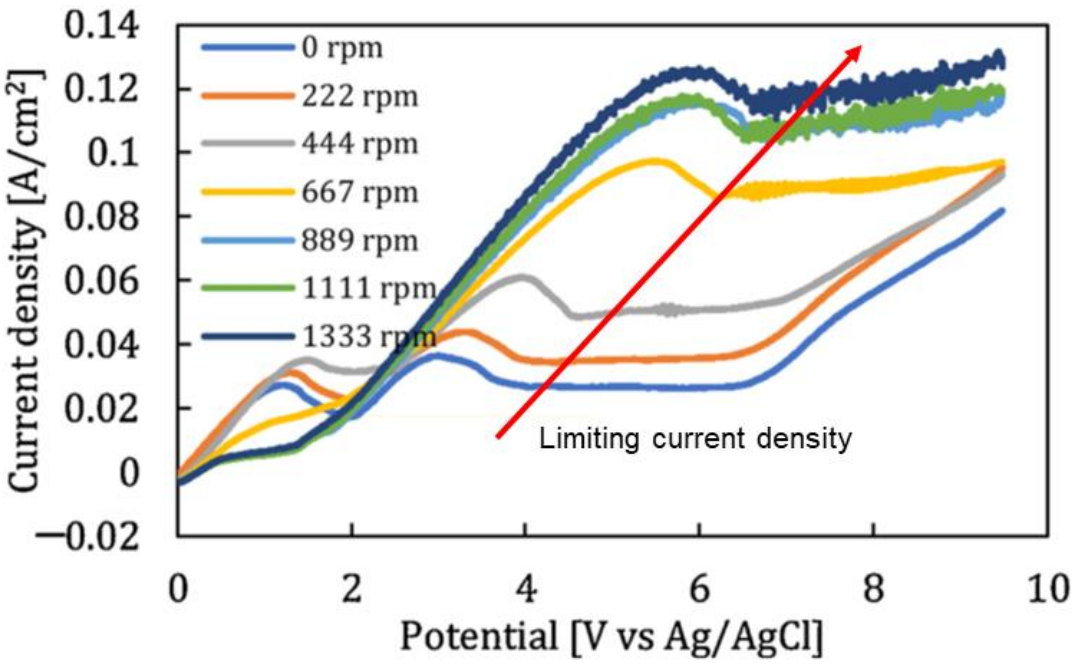

Figure 28 Polarisation curves of 316L SS measured in the NaCl-Ethylene glycol electrolyte at ambient temperature with different stirrer speed[38]

2.3.3 External Variables

Pressure, temperature, and polishing time are three regular parameters being considered during the process. However, pressure usually keeps ambient because of the open polishing system.

Temperature is a crucial factor affecting the motion of molecules and some additives content, which may significantly influence the final surface roughness. According to Chi-Cheng. research, weak intermolecular force and adsorbed ability caused the formation of a noncompact anodic shield (vicious layer), meaning that some regions were shielded, and some were not[189]. This phenomenon resulted in abnormal current density distribution, leading to uneven surface or pitting corrosion. However, the low temperature can reduce the molecular mobility, including the viscous layer formation and the ions transfer, which can have additional effects on reducing the current density and lowering the EP efficiency[190].

EP process of porous austenitic SS in phosphoric-sulfuric mixed acid was studied using current density-voltage curves at temperatures of 60°C, 70°C, and 80°C[145]. The results indicated that current density increases with temperature, leading to a high material removal rate, as shown in Figure 29. Similar findings were obtained by Eliaz and Nissan[191] during their EP process of 316L SS, as the data presented in Figure 29. These results underscore the

importance of carefully controlling the temperature during the EP process to optimise surface finish and achieve superior performance in a variety of applications.

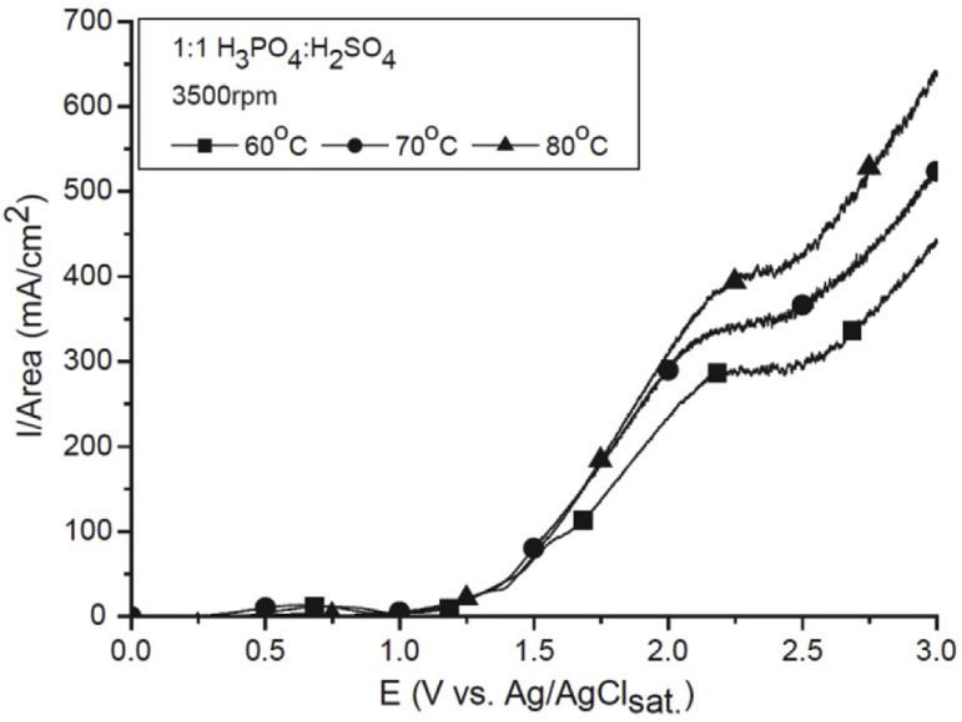

Figure 29 The current density-voltage curve of porous authentic stainless steel at temperatures of 60, 70 and 80 ℃[145]

Each electrolyte has a limited polishing capability, meaning that surface roughness will reach a constant after a long-time EP process. This capability depends on the electrolyte composition, electrical parameters, and temperature. As shown in Figure 30, 316L SS polished using electrolyte with lower water concentration (0%) had a lower final surface roughness, which reaches the lowest value at approximately 10 mins and then keeps constant[39]. Materials removal rate decreases and reaches the lowest value at the same time but not zero, meaning that the workpiece will continue dissolving after the surface roughness reaches the lowest, and this will affect the size accuracy of components.

Combining initial anodic surface and polishing time, the surface roughness parameters Ra can be approximated by the following parametric dependence on time t[192]:

$$Ra = Ae^{\frac{-t}{\tau}} + C \qquad (8)$$

where A is the maximum decrease in roughness, τ is the time constant, C is the minimum achievable roughness, and t is the processing time.

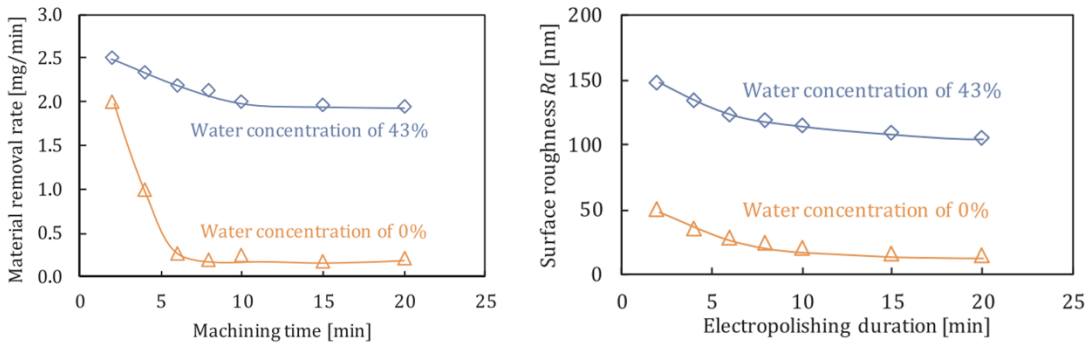

Figure 30 Material removal rates (left) and surface roughness Ra (right) of the EP processes with the water concentrations of 0 % and 43 %[39]

2.4 Electrochemical Polishing L-PBF Components

As mentioned in sections 1.2 and 1.4, the surface morphologies of the L-PBF components are complicated and the capability of the EP process is limited. According to the impact factors discussed in sections 2.2 and 2.3, this can be owing to the inappropriate selection of the electrolyte and the polishing parameters. Additionally, the polishing results may be varied using the same polishing setup and parameters in different literature because the characterisation method is not the same, leading to non-meaningful results.

Brent *et al* studied the polishing effect of the EP duration, temperature, agitation and electrolyte composition on the 316L SS. The surface roughness can reduce from 7.389 ± 0.106 µm to 1.996 ± 0.126 µm, and the corresponding roughness reduction rate was 63 %[193]. The electrolyte of phosphoric acid and sulfuric acid are widely used to polish steel materials while the current efficiency is somewhat low nowadays and the high temperature of 104 ℃ will also cause unstable current density. Rotty also used a mixture of acid electrolytes to polish the steel while the roughness they focus on is approximately and below 1 µm[194]. Although the ratio of phosphoric acid and sulfuric acid is different, the difference in the roughness scale is too large. Rotty *et al* also found a deep eutectic solvent containing choline chloride and ethylene glycol used for polishing 316L SS, which showed a better polishing effect than the acid electrolyte they used before[52]. Later, many researchers used the mixture electrolytes of acid, methanol, ethylene glycol, etc to polish steel while the polishing effect was not satisfied, e.g., from 10.3 µm to 6.14 µm and the characterisation methods were not unified[30,44,195,196].

Ti and its alloys are difficult to polish in general acid solution because a stable oxidise layer will form on the anode surface and hinder the polishing process during EP. The industry uses hydrofluoric acid and perchloric acid as electrolytes they are quite harmful to human bodies

and the environment[96]. Longhitano *et al* tried to polish Ti-6Al-4V alloy with 5 % perchloric acid (60 %) in acetic acid and compared it with the blasting, chemical etching and combination methods[169]. However, the roughness of the Ti-6Al-4V increased to approximately 7.8 μm from 6.4 μm after the EP process, which might be because of the unsuitable concentration of the perchloric acid. Urlea *et al* use the 6 % perchloric acid in glacial acetic acid and successfully reduce the roughness of Ti-6Al-4V from approximately 22.68 μm to 2.52 μm, which is quite noble[95]. Dong *et al* tried to use a salt electrolyte composed of ethanol, n-butyl alcohol, hydrated aluminium chloride and zinc chloride anhydrous[166]. Although the roughness reduction was not evident, e.g., from 10.314 μm to 3.309 μm, the electrolyte did not contain a harmful composition. Later, a new salt electrolyte composed of ethylene glycol, magnesium chloride and water was proposed. The roughness reduction was a little better than the result obtained in Dong's work, corresponding to 75 % and 67 %, respectively. Noticeably, the influence of the Cl^- on the polishing effect was investigated and a new TiO_2 layer formation and materials removal process was proposed, as shown in Figure 31.

In addition, using high polishing current density can dramatically increase the material removal rate according to Faraday's Law. However, H_2O electrolysis will be serious at high current density and oxygen bubbles will be generated on the anode surface. The bubble will move from the viscous layer to the electrolyte while the viscosity difference could cause the bubble to break, and then the vacancy will be filled with the electrolyte which has a higher fluidity than the viscous layer. Therefore, the current density at the vacancy will be higher than other positions and the pitting hole is generated eventually. This phenomenon was called the 'Broken Bubble Tunnelling Effect'[45].

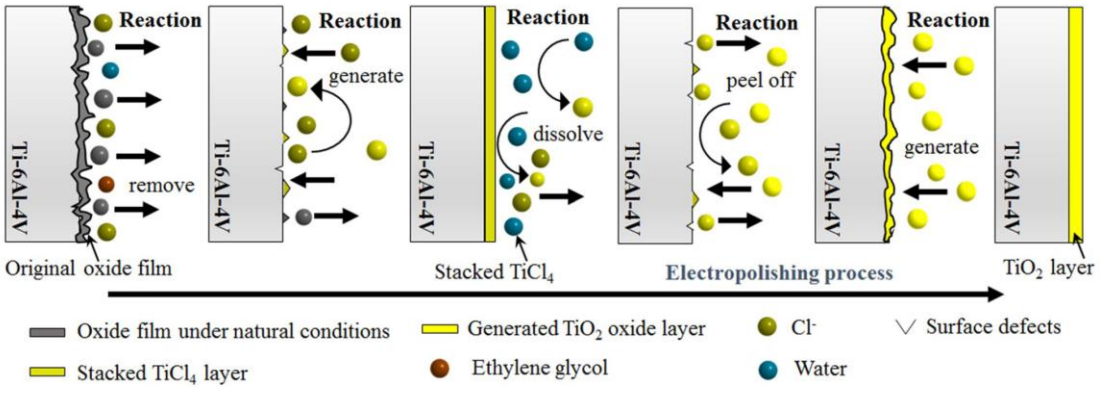

Figure 31 Formation process of TiO_2 oxide film on the surface of Ti-6Al-4V alloy[27]

2.5 FEM Modelling of the EP process

The viscous layer formation and growth process are essential for the polishing effect of L-PBF components since they have rough surface features with a height and wavelength range of several hundred microns, which differs from the surface finish at the micro/nanometre level. However, because of the electrolyte obstruction and the complexity of the EP process, direct observation of the viscous layer with in-situ methods is difficult, restricting its application in guiding the determination of the polishing window[197]. Many researchers adopted Taguchi methods to determine the polishing potential, inter-electrode distance, electrolyte composition, stirring, etc., which are time-consuming and resource inefficient[113,198,199]. Although voltammetry can reflect surface reaction indirectly and benefit the potential/current density selection, the determination of other parameters still requires a large number of experimental attempts. Moreover, since no matured theory can be applied for guidance and the EP process is sensitive to the environment, the process parameters selected in the previous studies are varied[27,166,169,170,178,200,201].

The FEM is extensively employed in electrochemistry to solve the constituent partial differential equations, which can simulate the growth mechanism of the viscous layer during the EP process [202]. Jemmely *et al* first modelled the growth of the viscous layer and assumed that the layer thickness varied linearly with the charge transmitted through the system [203]. However, the assumed linearity exponent exclusively correlated with the metal oxidation while other ions from the electrolyte were neglected[38]. Lee *et al* modelled and predicted the thickness and uniformity of the viscous layer in convection and diffusion modes, where multi-ions were considered as an assembly with an concentration of 1 on the anode boundary[204]. Tang *et al* indicated that the electrolyte flow field directly influenced the polishing quality of the workpiece surface[205]. Tailor *et al* modelled and simulated the thickness and uniformity of the viscous layer by varying diffusion coefficient, inter-electrode distance, inlet velocity and surface roughness [46]. The simulation process and parameters were then improved and applied in the electrochemical buffing experiment[206]. Increasing studies have been reported on simulating the electrochemical machining process to determine the electrolyte flow mode, inter-electrode distance, rotational speed, etc.[207–212]. However, most of them on EP were carried out on smooth surfaces or flat surfaces, ignoring the influence of the surface profile on viscous layer thickness and geometry. For instance, the surface profile in Tailor's work was assumed to be ideal equilateral triangles, which can introduce deviation from the practical components[46]. Moreover, the height difference of the L-PBF sample surfaces can exceed 100 μm, which has a non-negligible influence on the viscous layer.

2.6 Machine Learning for EP

Machine Learning has progressed over the past two decades and can be defined as the research field of enabling computers to learn without being explicitly programmed[213,214]. It can assist in handling complicated data more efficiently than humans and developing software for computer vision, robot control, data optimisation, natural language processing and other applications[213]. Common types of machine learning methods can be divided into supervised learning, unsupervised learning, semi-supervised learning, reinforcement learning, transduction, and learning to learn[215].

Regarding the field of predicting the surface roughness of samples obtained by AM techniques, grinding, turning, multi-jet polishing etc., the researcher established the physical model by investigating the relationship between the parameters and results and then solving the mathematical equations before the widespread of the machine learning[216]. The model is meaningful and explainable but it is difficult to realise when the model involves complicated physical fields and parameters. Numerical simulation such as the finite element method, finite differentiate method, etc. can simulate the physical process and provide fundamental understandings of the micro process with the assistance of the computer[217]. However, reasonable assumptions are necessary during the modelling process which will bring deviations in the simulation results and the simulation time will also be long when the simulation model is complicated or the mesh amount is large. Machine learning can also be applied to train and predict the experiment results, which can produce accurate fitting results in a short time. Brezocnik et al. proposed the genetic programming approach to predict surface roughness based on cutting parameters. The final developed model showed very good training and testing results. In addition to the genetic programming approach, many algorithms can also be applied to train and test the surface roughness such as classification and regression tress, random vector functional link network, ridge regression, support vector regression, random forest, AdaBoost, etc. Li et al. compared and combined these algorithms to predict the surface roughness in extrusion-based additive manufacturing polylactic acid. The ensemble learning algorithm showed more accurate predicting results than the separated algorithms[218]. Later, Wang et al applied ensemble learning with a genetic algorithm in the multi-jetting polishing process. This method showed improved prediction results and superior robustness to the ensemble strategy and genetic algorithms[219]. The difference is that the ensemble learning method in Li's work involved six separated algorithms while Wang's work involved five separated algorithms. In addition, many other algorithms and machine learning methods can be adopted such as deep learning, neural network, Bayesian, etc.

2.7 Characterisation Techniques

Generally, EP is a technique employed to enhance the surface finish of metals by rendering them anodic within an appropriate solution[220]. Anodic levelling or smoothing is commonly described in the literature, with surface brightening used as a distinguishing factor. Anodic levelling generally refers to the removal of surface textures larger than 1 μm, resulting in a flat but dull surface. On the contrary, anodic brightening involves eliminating textures smaller than 1 μm, subsequently producing a mirror-like surface[221]. This phenomenon can be explained by the wavelength of visible light perceived by the human eyes, which ranges between 400 and 700 nm. A mirror-like surface is achievable when surface textures are maintained within or below this wavelength spectrum. Edwards et al[222] later introduced a classification of macro and micro smoothing, based on the dissolution mechanisms during the electropolishing process. Macro smoothing encompasses the process wherein the impact of surface defects and crystallographic orientation on metal dissolution is suppressed. Conversely, micro smoothing is characterised by metal dissolution being governed by concentration gradients and the tip-effect of electrical influences. As a result, diverse evaluation methods are necessitated for assessing polishing surface finishes across varying size scales. Stylus profilometry serves as the initial surface characterisation instrument, with microscopic techniques progressively employed to obtain surface profiles, textures, and additional information. Early 20th-century research by Jacquet utilised microscopic approaches to examine the surface conditions of copper post-polishing[223,224]. More recently, the application of microscopic techniques such as scanning electron microscopy (SEM), transmission electron microscopy (TEM), and atomic force microscopy (AFM) for evaluating surface conditions has become increasingly prevalent. Microscopy techniques are indispensable diagnostic tools for assessing surface quality after the EP process. This review offers a comprehensive examination of microscopic evaluation methods for EP techniques, with a particular emphasis on the two fundamental forms of smoothing attainable through EP technique: macroscopic and microscopic smoothing.

2.7.1 Stylus profilometry

The initial surface profilometry techniques can date back to the early 20th century when one of the earliest techniques was stylus profilometry[225]. The technique involves the use of a stylus or probe, typically made of diamond or other hard material, that is brought into contact with the surface being measured. The stylus is then moved along the surface, and the vertical displacement of the stylus is recorded to create a profile of the surface topography.

Modern stylus profilometers typically use a motorised stage to move the sample and stylus probe, enabling fast and accurate measurements. The stylus is usually mounted on a cantilever beam, which can deflect in response to the surface topography. The deflection of the stylus is measured using a displacement sensor, such as a piezoelectric transducer or an interferometer, which can detect sub-nanometre deflections[226].

Stylus profilometry has the advantage of being a relatively simple and inexpensive technique that can measure surface topography over a wide range of length scales, from a few nanometres to millimetres. It is also capable of measuring surfaces with a wide range of materials, including metals, ceramics, polymers, and semiconductors. However, stylus profilometry has some limitations. One major limitation is the potential for the stylus to damage or alter the surface being measured, especially at high contact forces or on soft or delicate surfaces. Another limitation is the inability of the stylus to measure surface features that are smaller than the stylus tip radius, typically on the order of a few nanometers[227]. Additionally, the technique is not well-suited for measuring surfaces with complex geometries, such as those found in microfluidic channels or rough surfaces. Despite these limitations, stylus profilometry remains a valuable technique for many applications, including quality control in manufacturing, surface roughness measurement in tribology, and surface analysis in materials science. Recent advances in stylus profilometry include the integration of multiple measurement modalities, such as optical and confocal microscopy, for more comprehensive surface characterization. Additionally, the use of machine learning algorithms for data analysis is becoming increasingly common in stylus profilometry, enabling faster and more accurate measurement of surface topography[228].

2.7.2 Optical Microscope

The optical microscope, sometimes also called a light microscope, is one of the oldest and most widely used tools in the field of the microscope. It can provide high-quality, three-dimensional images of samples without causing mechanical damage to the sample surfaces. At the initial discovery of the electrolysis phenomenon, the optical microscope was adopted by Jacquet for evaluating the surface brightness and the crystal grains of the anode before and after the EP process[223,224]. Later, Edwards *et al* designed an anode composed of copper alloys, which had the evident geometrical structure of peak and valley regions on the surfaces and the regions were isolated from each other. The polishing effect can be obtained from an optical microscope by comparing the surface conditions between the peak and valleys, and thus the EP smoothing efficiency can be calculated[222].

There are many types of optical microscopes including the compound microscope, stereo microscope, polarising microscope, fluorescence microscope, and confocal microscope can be employed to observe surface conditions. Although most of them cannot be used for measuring surface textures at the nano scale, they can be used as the pre-processing for the electron microscope. For instance, R. D. Schoone et al evaluated the sample quality obtained after the EP process utilising an optical microscope to justify if the sample can be used for the TEM observation. By combining the microscopies, they found that dislocation and stacking layers would appear in the electropolished cobalt under the particular polishing environment, while Fe-Ni alloys would have a structure of fine and tiny grains[229].

Although optical microscopes have the advantages of simple sample preparation and low cost, the resolution and magnification are restricted because of the interference phenomenon of visible light[230]. In contrast, an electron microscope uses a beam of electrons that has a shorter wavelength, allowing for high-resolution imaging with the ability to resolve structures down to the atomic level (below 0.1 nanometres). Therefore, evaluating surface conditions of samples in different scales should combine the employment of the optical microscope and electron microscope.

2.7.3 Electron Microscope

Owing to the limitations imposed by light diffraction, a conventional optical microscope is inadequate for assessing surface features that are below the threshold of light diffraction. Nevertheless, substituting the lamp with a higher-energy alternative can lead to a corresponding reduction in the irradiation wavelength. Consequently, electron microscopes have emerged as indispensable tools for detecting structures considerably smaller than the light diffraction limit[230]. Enhanced beam energy can further diminish the wavelength to the sub-nanometre range. For example, a 5 KeV electron source in an electron microscope can generate 0.248 nm electron irradiation and even atomic-resolution images using a sub-50 pm electron probe[231]. Two kinds of electron microscopes are commonly employed to evaluate electropolishing finishes: scanning electron microscopy (SEM) and transmission electron microscopy (TEM).

The principle of SEM is to utilise a beam of high-energy electrons concentrated on the sample surface, inducing the emitting of secondary electrons. Then, these electrons are captured and utilised to produce visual images of the sample surface. SEM is particularly useful for the visualisation of microstructures and defects and can also be combined with Energy Dispersive X-ray Spectroscopy (EDS) for elemental analysis[232–235]. TEM, on the other hand, works by transmitting a beam of high-energy electrons through a thin sample, which interacts with the

atoms in the sample, causing scattering and absorption of the electrons. The transmitted electrons are then focused onto a fluorescent screen or detector, generating an image of the internal structure, defects, and composition of materials, as well as allowing for the visualisation of individual atoms and molecules[236]. Currently, TEM has become an essential instrument for directly correlating the internal structure of materials such as metals, semiconductors, ceramics, polymers and biomaterials with macro properties. To allow electron transmission, metal specimens for TEM must be carefully prepared to achieve a thickness of a few hundred nanometres or less[237,238]. The quality of the thin metal samples greatly influences the success of TEM analysis. Although there are mechanical polishing techniques available to prepare thin TEM samples, ensuring sample quality can be difficult[239,240]. Various literature has indicated that electrochemical polishing is a crucial step in preparing qualified TEM samples[229,239,241,242]. Thin TEM specimen preparation typically consists of three stages: (a) manufacturing a sample with a thickness of below 2 mm, (b) machining the sample to ensure a thickness of approximately 0.2 mm, and (c) further reducing the thickness of the sample to the nanometre scale to allow for adequate electron beam penetration[243].

Regarding the application of the Microscope in the EP component, critical parameters such as potential, current density, agitation, inter-electrode distance, electrolyte composition, temperature, polishing time, and electrolyte flowing must be meticulously optimised to obtain a qualified TEM sample for consistent characterisation. Necip[244] produced aluminium samples with high quality for TEM characterisation using a double-jet EP technique, providing valuable suggestions for minimising failure during TEM workpiece preparation with optimal EP parameters. In addition to pure metals, understanding alloy microstructures is crucial for comprehensively understanding and reasoning their macro physical and chemical properties. For instance, the two-phase TiAl alloy, which possesses exceptional specific mechanical properties, has significant potential for aerospace applications. Consequently, considerable research has focused on investigating the influence of the microstructure on the mechanical performance of TiAl. A. Couret *et al*[245] prepared thin TEM samples utilising a jet EP method with an electrolyte containing perchloric acid and methanol. Because of the suitable EP parameters and procedure, the quantitative relationship between the microstructure and the macro performance can be calculated based on the TEM characterisation. Sulaiman *et al*[246] prepared a TEM replica workpiece of P91 SS utilising a combination of advanced techniques, region-specific replication, and EP process and conducted quantitative microstructure analysis on the P91 steel workpiece.

Although the TEM can determine thin specimen microstructures, it cannot assess sample surface morphology. Therefore, other techniques, such as SEM, are required for evaluating

the surface morphology of samples after the EP process. SEM employs a high-energy electron beam to scan the workpiece surface, with electron detectors probing the electrons that carry workpiece structural information, revealing the surface structure. In 2012, the impact of the EP process on copper foil in an H_3PO_4 electrolyte at high temperatures was investigated by Didier Pribat and his colleagues[247]. The polished workpiece surfaces were analysed using a JEOL JSM-7600F field emission SEM, and the electron backscattering diffraction (EBSD) images were used to assess the grain growth process on the workpiece surfaces. Their findings revealed that copper foil polished at approximately 65 °C in a 2.17 M H_3PO_4 electrolyte had a greater grain size in comparison to samples treated under different conditions. Similarly, in 2016, the removal process of the tarnishing and surface roughness of copper using the EP technique was investigated by Dahy et al[248]. The SEM with an energy-dispersive X-ray (EDX) spectroscopy was introduced to analyse the surface conditions including the residual elements and morphologies of the copper foil. In addition, the SEM was employed to investigate the nano-crystallinity of the oxide layer on the 304 SS surface at high temperatures in hydrogenated water by Sander *et al*[249]. Results showed that the chromite-based crystals (ranging between 10 and 26 nm) were smaller than those produced by the machining techniques such as cold-worked. Therefore, the expected smooth and brighten surface conditions were obtained by the EP techniques because the surface micro-strain generated in the cold-working process was eliminated. In a separate study on the EP of AlSl-314 SS, Biaggio *et al*[250] utilised SEM at 1000x magnification to evaluate the polished surface structure. The SEM results revealed that the opaque, semi-bright, and bright AISI-314 SS samples exhibited different surface textures.

2.7.4 Atomic Force Microscope

Although SEM can determine micromorphological features, it can only provide two-dimensional and qualitative information about the surface finish. To achieve a comprehensive understanding of the height profile or roughness of an electropolished component, AFM is sometimes employed. Different from optical microscopy and SEM, AFM uses no optical/electron lenses or light/electron radiation. Instead, the AFM technique uses a sharp tip (approx. 10 nm in diameter), which was attached to a cantilever, to collect information by the interaction between the tip and the surface profile of the workpiece. The deflection of the cantilever is detected by a laser beam that is reflected off the back of the cantilever onto a position-sensitive photodetector and then the signal from the cantilever deflection is transformed into an electrical signal, which is processed by software to generate a surface morphology. AFM offers many advantages compared to microscopic technologies. Firstly,

because of the sharp tip, AFM can achieve sub-nanometre resolution, allowing for the imaging of individual atoms and molecules. Secondly, because AFM only requires the tip to interact with the surface of the sample, without the need for coating, or staining, it will not damage the sample. Thirdly, AFM can generate 3D images, providing a more comprehensive view of the sample[36,251].

A significant application of AFM in assessing electropolished metal surfaces is to provide direct information on sample surface roughness, which cannot be accomplished by electron microscopes. For instance, in 2012, Chi-Chang Hu *et al*[252] investigated the polishing effect of the 304 SS under different electrolyte temperatures and polishing duration using the EP process in a mixture of electrolyte containing the H_3PO_4, $H2_SO_4$, and glycerol. The roughness changes of the workpiece surface were characterised and calculated utilising the AFM techniques. The results indicated that the electrolyte temperature and polishing duration were two critical parameters that influenced the polishing quality of the SS materials. Later, the EP parameters were optimised for polishing the 304 SS by Chi-Chang Hu *et al*[36] and it was found that the surface roughness of the workpiece can be reduced to below 45 nm in the same electrolyte with surface roughness calculated with the AFM technique[36]. In 2016, Dahy *et al*[248] optimised EP parameters of the current density, polishing duration, electrolyte temperature, and electrolyte viscosity during the polishing of commercial copper samples to remove stains and improve surface smoothness. The surface roughness was also characterised and calculated utilising the AFM technique. In 2013, Zak *et al*[253] investigated the EP conditions of Ni-Ti alloy and evaluated the surface quality of the alloy after polishing using AFM techniques.

Additionally, AFM is also a valuable technique for characterising metal surface morphology after polishing. For example, the ordered nano-scale surface textures generated on the aluminium obtained by the EP process were characterised using the AFM technique by Metzger *et al*[87]. Muhammad Aslam *et al*[254] also utilised porous anodic alumina pre-treated by the EP process, generating random features between 100 and 150 nm (4 nm - 5 nm amplitude), and nano-strips of 50 nm at different EP potentials, which were validated by AFM characterisation.

2.8 Surface Metrology

The initial profile measurement was initially carried out on the 2-dimensional aspect since the first profilometry was invented in the 1930s. The areal texture measurement was realised in the 1980s when white light interferometers and 3D profilometers appeared. Then, the standardisation of the surface tools and characterisation indexes began with the related

programmes starting in Europe. However, the areal surface texture was still in the research progress and the recognition of characterising the L-PBF surfaces still lacking.

2.8.1 Profile parameters

Profile parameters can be divided into three groups: primary parameters, waviness parameters and roughness parameters. After obtaining a raw measured surface profile, the primary profile and parameters can be obtained by introducing a low pass filter with a cut-off value of λs. Then, the roughness profile can be obtained by applying a high-pass filter with a cut-off value of λc to the primary profile. The waviness profile can be obtained by applying a filter with cut-off values of λf and λc to the primary profile. The relationship between the profiles is shown in Figure 32.

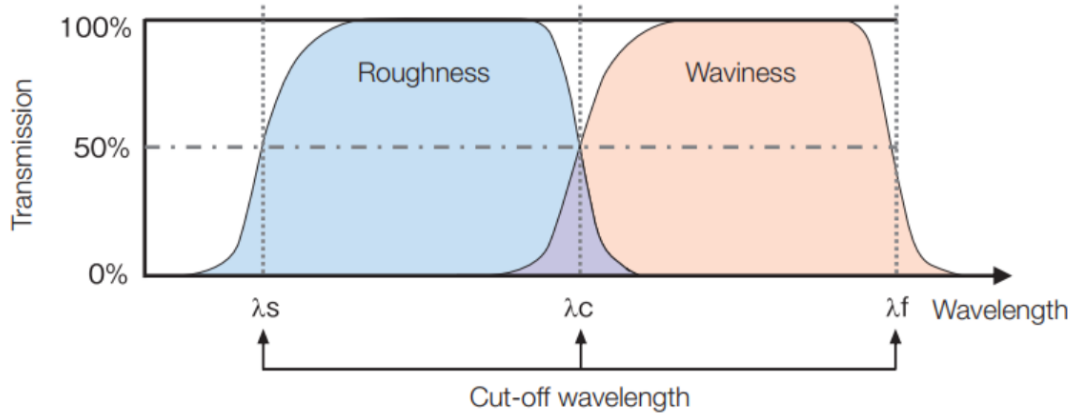

Figure 32 conceptual drawing of the filtration method

To avoid the noise and improve the repeatability of the characterisation, concepts of evaluation length and sampling length were introduced for calculating the average, as shown in Figure 33. ISO 4288 regulated that the selection of the sampling and evaluation length can be based on the surface features and roughness values. Table 4 and Table 5 show the criteria for selecting the sampling and evaluation lengths for the non-periodic and periodic profiles, where *Sm* was the element length of the periodic profiles defined in ISO 4287/1.

ISO 4287 also defined the terms for roughness parameters, which are summarised in Table 6, where $Z(x)$ was the height at the point x, $Z(Rp)_i$, $Z(Rp)_i$, $Z(Rt)_t$ were the maximum, minimum and total height of the *i*th sampling length, *l* and *ln* were sampling length and evaluation length, and $Ml(c)_i$ was the materials length of the profile element for the section height level c. The waviness and primary parameters shared similar equations and definitions, and the expression of R was replaced with W and P, respectively. For example, the arithmetic means deviation of the roughness, waviness and primary profiles were Ra, Wa, and Pa, respectively. The ISO 4287 standard was partly replaced and modified in ISO 21920 later. Noticeably, the

sampling length was renamed as section length, and some height parameters were categorised as peak-to-valley parameters (features parameters). Other changes referred to the new standard documents.

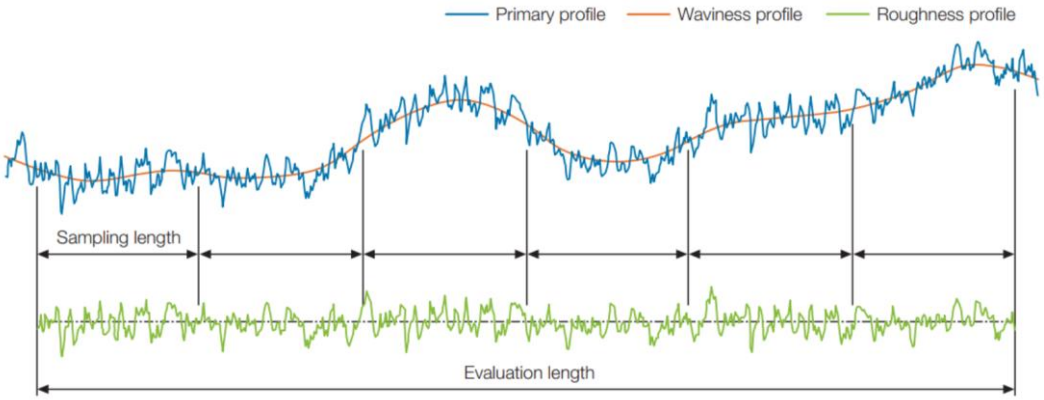

Figure 33 conceptual drawing of the sampling method

Table 4 Sampling and evaluation lengths for the measurement of non-periodic profiles

Ra (μm)	Sampling length (mm)	Evaluation length (mm)
0.006-0.02	0.08	0.4
0.02-0.1	0.25	1.25
0.1-2.0	0.8	4.0
2.0-10.0	2.5	12.5
10.0-80.0	8.0	40

Table 5 Sampling and evaluation lengths for the measurement of periodic profiles

Sm (mm)	Sampling length (mm)	Evaluation length (mm)
0.01-0.032	0.08	0.4
0.032-0.1	0.25	1.25
0.1-0.32	0.8	4.0
0.32-1	2.5	12.5
1-3.2	8.0	40

Table 6 Roughness profile parameters, equations and definitions from ISO 4287

Parameters	Equation	Definition
Ra	$\frac{1}{l}\int_0^l \lvert Z(x)\rvert dx$	Arithmetic mean deviation of the assessed profile

Rt	$max(Z(Rp)_i)+ min(Z(Rv)_i)$	Total height of the profile
Rp	$max(Z(x))$	Maximum profile peak height
Rv	$\lvert min(Z(x))\rvert$	Maximum profile valley depth
Rz	$Rp+Rv$	Maximum height of the profile
Rq	$\sqrt{\frac{1}{l}\int_0^l Z^2(x)dx}$	Root mean square deviation of the assessed profile
Rsk	$\frac{1}{Rq^3}\left[\frac{1}{l}\int_0^l Z^3(x)dx\right]$	Skewness of the assessed profile
Rku	$\frac{1}{Rq^4}\left[\frac{1}{l}\int_0^l Z^4(x)dx\right]$	Kurtosis of the assessed profile
Rc	$\frac{1}{m}\sum_1^m Z(Rt)_i$	Mean height of profile elements
Rsm	$\frac{1}{m}\sum_1^m X_i$	Mean spacing of profile elements
Rdq	$\sqrt{\frac{1}{l}\int_0^l \left[\frac{d}{dx}Z(x)\right]^2 dx}$	Root mean square slope of the assessed profile
RPc	/	Peak count number
Rmr	$\frac{1}{ln}\sum_{i=1}^m Ml(c)_i$	Material ratio at a given depth
Rdc	c(Rmr1)-c(Rmr2)	Profile section height between two material ratios

2.8.2 Areal parameters

Similar to the profile parameters, areal parameters can be divided into three groups: primary parameters, waviness parameters and roughness parameters. However, all of them were expressed as S-parameters and V-parameters such as Sa, Sv, Sp, Sz, Sq, etc., where the first letter did not reflect the nature of surfaces. The meaning of the parameters depended on the surfaces obtained and measured. Figure 34 shows the analysis workflow for general surfaces from ISO 25178-2. S filter was to eliminate small wavelength components from primary surfaces, after which the primary surface can be obtained. F operation was to eliminate the specific forms of the components. The primary areal parameters can be calculated based on the surfaces after being processed by the S filter and F operation. Then, the waviness and roughness parameters can be calculated, respectively, by further applying another S filter or L

filter on the S-F surfaces. L filter was to eliminate large wavelength components from the surfaces. The surface evolution with different filters and operations is shown in Figure 35.

The terms, definitions and surface texture parameters were defined in ISO 25178 and revised in ISO 25178-2, which are summarised in Table 7. *A* was the test area of samples, and *Z(x, y)* was the height at the coordinate of *(x, y)*.

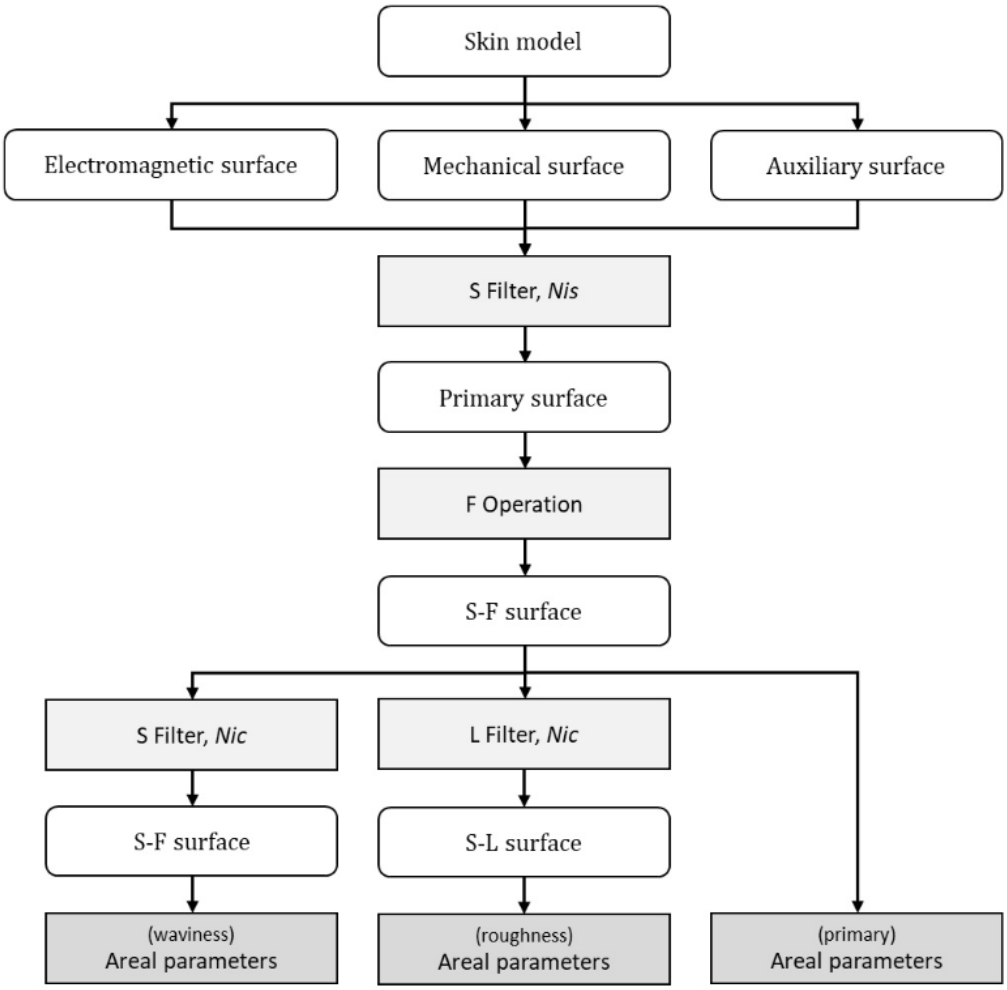

Figure 34 Analysis workflow and surface categories for surfaces

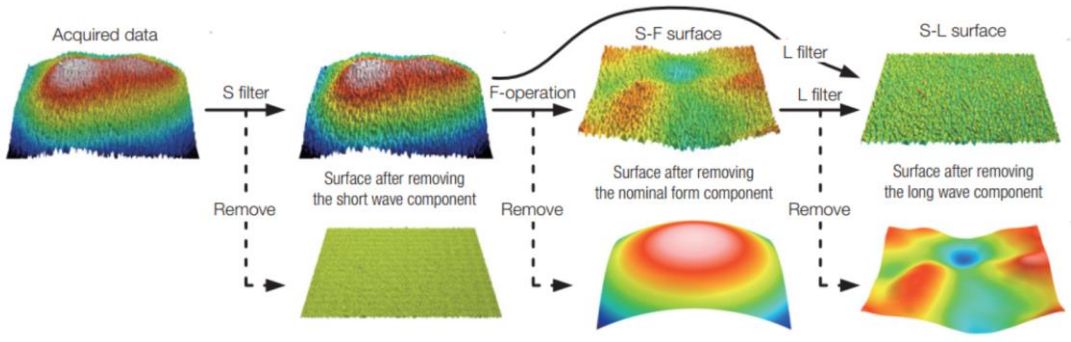

Figure 35 Surface evolution with different operations

Table 7 Areal texture parameters, equations and definitions from ISO 4287

Parameters	Equation	Definition
Sa	$\frac{1}{A}\iint Z(x,y)dxdy$	Arithmetic mean deviation
Sq	$\sqrt{\frac{1}{A}\iint Z^2(x,y)dxdy}$	Root mean square deviation
Sp	*max(Z(x,y))*	Maximum peak height
Sv	*|min(Z(x,y))|*	Maximum valley depth
Sz	*Sp+Sv*	Maximum height
Ssk	$\frac{1}{Sq^3}\left[\frac{1}{A}\iint Z^3(x,y)dxdy\right]$	Skewness
Sku	$\frac{1}{Sq^4}\left[\frac{1}{A}\iint Z^4(x,y)dxdy\right]$	Kurtosis
Str	/	Texture aspect ratio
Sal	/	Fastest decay autocorrelation length
Std	/	Texture direction
Sdq	$\sqrt{\frac{1}{A}\iint \left[(\frac{\partial z(x,y)}{\partial x})^2+(\frac{\partial z(x,y)}{\partial y})^2\right]dxdy}$	Mean quadratic slope
Sdr	$\frac{1}{A}\iint(\sqrt{\left[1+\left(\frac{\partial z(x,y)}{\partial x}\right)^2+\left(\frac{\partial z(x,y)}{\partial y}\right)^2\right]}-1)dxdy$	Eveloped Area

2.8.3 Operations and Filtrations

F operation was the form removal of samples using the least square method while filters include morphological, outlier removal and smoothing filters. The morphological filter was generally applied in the stylus profilometry while the outlier filter was applied in the optical microscope. The smoothing filters such as S-filter, L-filter, etc. were used to separate the surface in different scales and compare data obtained from a different instrument.

Spline and Gaussian filters were the main methods used as the smoothing filters in the profilometry equipment. Theoretically, the Spline filter was better than the Gaussian filter in processing structural and stratified surfaces while the difference in the results was not evident. Additionally, the Gaussian filter was much simpler to implement and could save time,

becoming the preferred choice over the former. The calculation process of the Gaussian filter can be expressed as follows.

In general, the extraction of long-wave components through a filter operation can be mathematically described using equation *(9)*.

$$z(x,y) \xrightarrow{filter} w(x,y) \quad (9)$$

The residual short-wave component, denoted as *r(x,y)*, can be obtained by subtracting the long-wave components from the original surface, as shown in equation (*10*).

$$r(x,y) = z(x,y) - w(x,y) \quad (10)$$

When a Gaussian function is introduced to calculate the weight moving average, the filter with the weight moving average is called the Gaussian filter. The averaging process involves different weights assigned to the moving averages, which are determined by the weighting function *s(x,y)* of the filter. Regarding areal filtering, the weight moving average can be expressed as a double integral of the product of two functions *s(x,y)* and *z(u, v)*, as shown in equation (*11*).

$$w(x,y) = \iint s(x-\mu, y-v) z(\mu, v) d\mu dv \quad (11)$$

where μ and v represent the integral variants for the x and y axes, respectively. By progressively calculating the value of weight moving average around the coordinate *(x,y)* based on the function *s(x,y)*, the weighting function with a cut-off value λc can be obtained, as shown in equation (*12*) (cut-off value is defined as threshold wavelength for profile filters. Wavelength indicates 50% transmission of profile characteristics).

$$s(x,y) = \frac{1}{\alpha\lambda_c} e^{-\pi(\frac{x}{\alpha\lambda_c})^2} \frac{1}{\alpha\lambda_c} e^{-\pi(\frac{y}{\alpha\lambda_c})^2} \quad (12)$$

The filter constant $\alpha = \sqrt{\frac{ln2}{\pi}} \cong 0.4697$ determines the amplitude damping of the planar filter at 50%. However, the Gaussian weighting function used in the filter has no compact support and is unbounded in the x and y directions. To apply the filter practically, the weighting function must be limited to a defined radius of influence. Points outside of this radius are excluded from the calculation, which is achieved by setting the weighting function to zero for $\sqrt{x^2+y^2} > L_c\lambda_c$ (Lc is commonly set as 0.5 or 0.6). This modification ensures that the filtered surface value is based only on the surface values within the range of influence of the filter, resulting in improved surface roughness.

Using the Fourier transform with the correlation $\lambda = \lambda_x cos\varphi$ and $\lambda = \lambda_y sin\varphi$, as shown in Figure 36, and adding the complex-valued exponential function to the equation *w(x,y)* above, the filter transfer function can be obtained.

$$S(\lambda_x, \lambda_y) = \iint s(\mu, v) e^{-i\pi\left(\frac{x}{\lambda_x} + \frac{y}{\lambda_y}\right)} d\mu dv \qquad (13)$$

By utilising the equation for the filter transfer function and the Gaussian weighting function and considering the wavefront depicted in Figure 36, we can determine the filter transfer function as follows.

$$S(\lambda, \varphi) = e^{-\pi\left(\alpha\frac{\lambda_c}{\lambda}\right)^2} = \left(\frac{1}{2}\right)^{\left(\frac{\lambda_c}{\lambda}\right)^2} \qquad (14)$$

The filter transfer function for the short-wave and long-wave components is shown in Figure 37, where the quotient $\frac{\lambda_c}{\lambda}$ determines the cut-off wavelength for the filter. The wave with wavelength λ equalling λc only has 50% transmission and with longer wavelengths has a higher transmission.

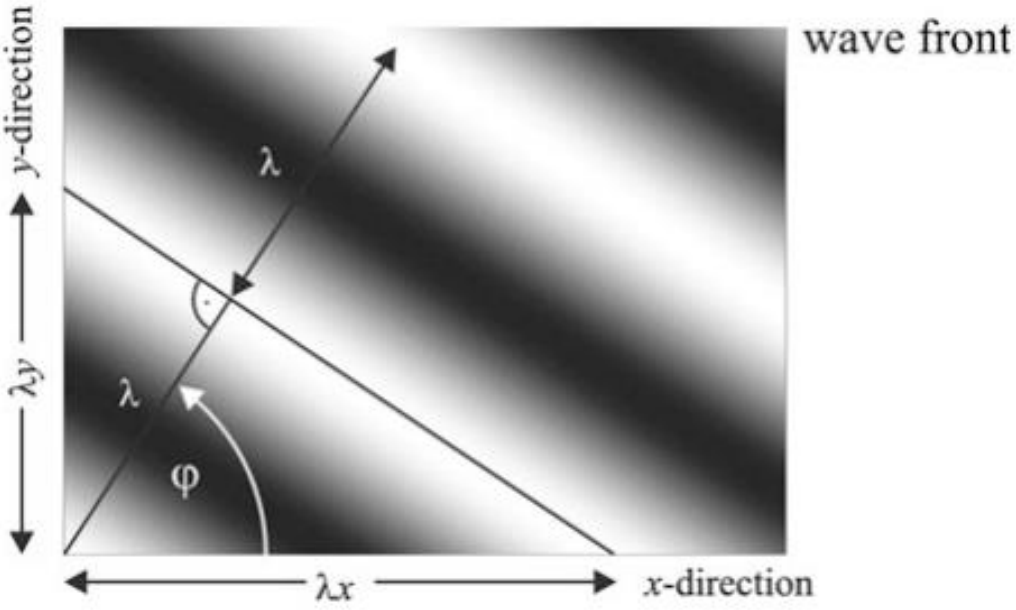

Figure 36 Wavefront to calculate the transmission characteristic for sinusoidal topographies

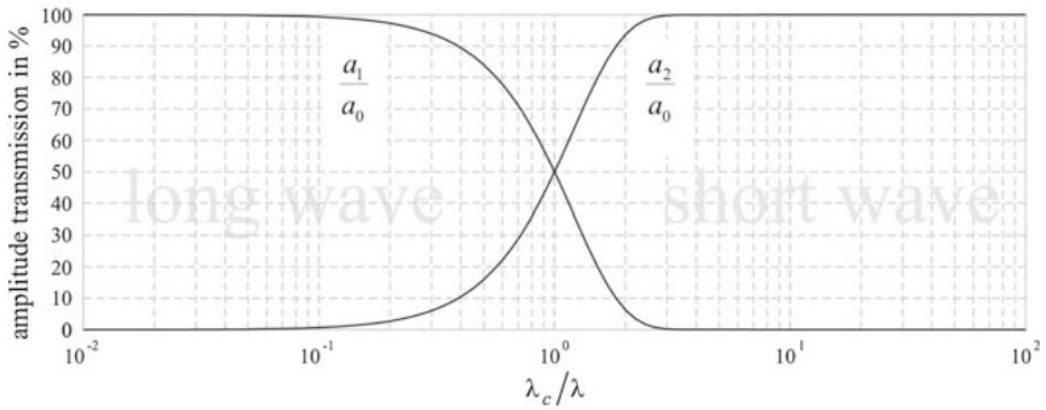

Figure 37 Filter transfer function of the Gaussian planar filter for long- and short-wave components ($\frac{a_1}{a_0} = S(\lambda_x, \lambda_y), \frac{a_2}{a_0} = 1 - \frac{a_1}{a_0}$, $a_0, a_1, and\ a_2$ *are amplitude of the primary, filtered and roughness exponential functions)*

2.9 Summary

This chapter summarised the mechanism, theories, and parameters of the EP process, and the characterisation techniques. According to the previous studies and the application on polishing L-PBF steel and Ti alloys, researchers keep investigating effective and green electrolytes for the EP process and optimise the polishing parameters.

However, there are still some limitations of previous electrolytes and parameters, and some limitations on research methods, such as large experiment workload, low polishing efficiency, low current efficiency, poor polishing capability, poor geometry control, lack of general relationship between parameters and roughness, etc. Therefore, combining the numerical simulation, experiment, and computer prediction method to systematically study the EP L-PBF components, proposing and controlling the EP process is attractive.

Chapter 3 Materials and Characterisation Techniques

This chapter will introduce materials, experiment setup, and the devices used for the electrochemical analysis and surface characterisation including the potentiostat, optical microscope and field emission SEM. The surface index and metrology for characterisation in this research will also be presented.

3.1 Simulation model and parameters

3.1.1 Problem Definition

Figure 38 (a) shows the 2D model of the EP system, including an anode, a cathode, a DC power supply and flowing electrolytes with an initial velocity and concentration. To simplify the simulation model, the region of interest between the electrodes is extracted from the EP system and shown in Figure 38 (b). The model contains an anode surface (number 1), a cathode surface (number 3), and inlet and outlet electrolyte boundaries (numbers 2 and 4). The anode and cathode surfaces were set as wall boundaries. The parameters L and W represent the length of the electrodes and the inter-electrode distance, respectively.

Since the L-PBF component surface profile is complicated, it was categorised into two groups: waviness profile and residual profile[5,255]. The composition and the production mechanism of the surface features are presented in Table 8. The surface roughness of the anode is considered as an average height over the measured length of the area enclosed by the

entire profile height characteristics, which can be represented by the surface index Ra. The cathode surface is considered to be an ideally smooth and flat boundary.

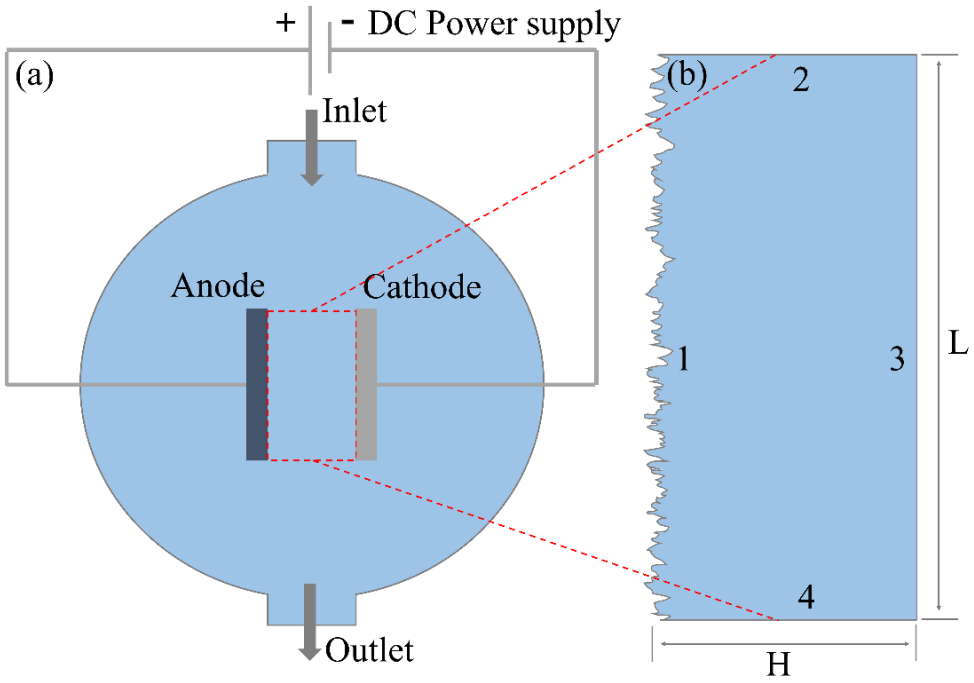

Figure 38 (a) Schematic digraph and (b) simulation model of the EP system

Table 8 Components and their production mechanism of surface features

Surface types		Components	Production mechanism
Primary surface	Waviness	Melted tracks	Formed by the flow of melted liquid
		Form error	Formed by thermal effect
		Pores	Low power or local overheat, wavelength larger than melted tracks
	Residual	Micro-asperity	Formed by the interaction between the melting process and metal powder
		Globules	Unmelted/partial melted powder
		Pores	Low power or local overheat, wavelength smaller than melted tracks

During the EP process, a uniformly flat and highly resistive viscous layer was formed on the anode surface, as shown in Figure 39 (a). The resistance at the protrusion was lower than the valley of the anode surface, leading to a higher current density and materials removal rate in the protrusion region. However, when the layer thickness was smaller than the anode surface profile height, the viscous layer became non-uniform, as shown in Figure 39 (b). The

difference in local materials removal rates on the anode surface became smaller, leading to poorer polishing efficiency and effect. The viscous layer composed of dissolved metal ions and electrolytic ions would be generated during the EP process, whose concentration would reach the maximum adjacent to the anode surface and be reduced towards the bulk electrolyte at the steady state[38,46]. Therefore, the ions were assumed as an entire group and their mass transport process under the diffusion and convection conditions on the rough L-PBF component surfaces are investigated.

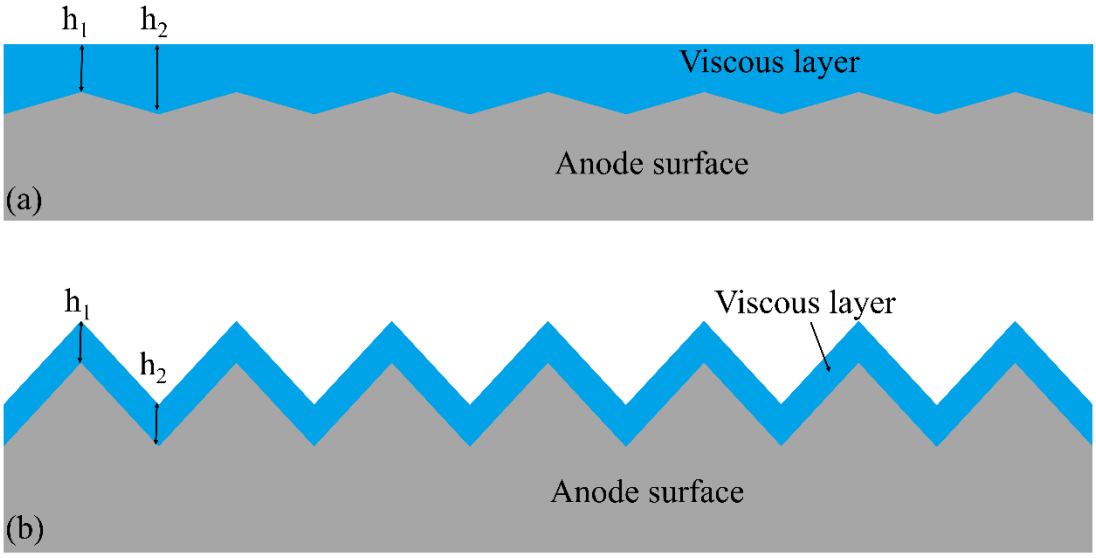

Figure 39 Profile of the viscous layer on the anode surface when the thickness is (a) larger or (b) smaller than the height of the anode surface profile.

3.1.2 Governing Equations

An appropriate model is essential for the simulation of electrochemically polished additive manufacturing metals. General rough surfaces can be modelled using the Spatial Frequencies Method as the equations *(15)*[192].

$$y = A\int_{-N}^{N}\left(n^{2\times\left(-\frac{b}{2}\right)}\times g1(n)\times cos\left(\omega\pi nx + u1(n)\right)\right) \quad (15)$$

where N is the spatial frequency resolution, b is the spectral exponent, A is the scale parameter in y coordinate, ω is the average spatial frequency, $g1$ is the Gaussian random function, and $u1$ is the uniform random function. Regarding the metal-PBF component surface, which can be divided into waviness and residual surface, two elements are introduced to formulate the final model.

$$y = A_W\int_{-N}^{N}\left(n^{2\times\left(-\frac{b}{2}\right)}g1(n)\,cos\left(\omega_W\pi nx + u1(n)\right)\right) + A_R\int_{-N}^{N}\left(n^{2\times\left(-\frac{b}{2}\right)}g1(n)\,cos\left(\omega_R\pi nx + u1(n)\right)\right) \quad (16)$$

where A_W, A_R, ω_W, and ω_R are scale parameters and spatial frequency of waviness and residual surface characteristics. Hereafter, the surface roughness of the generated profile can be calculated using equation *(17)*.

$$Ra = \frac{\int_0^L |y - \bar{y}| dx}{L} \quad (17)$$

In the simulation, the temperature is always considered to be ambient. To address the electrolyte flow characteristics subject to external forces, the electrolyte is considered an incompressible Newtonian fluid. Furthermore, the electrolyte is in laminar mode and gravity is neglected. Therefore, the Navier-Stokes equations *(18)* and the continuity equation *(19)* can be applied.

$$\rho \frac{\partial u}{\partial t} + \rho(\nabla \cdot u)u + \nabla p - \nabla[\eta(\nabla u + (\nabla u)^T)] = F \quad (18)$$

$$\nabla u = 0 \quad (19)$$

where u is the velocity (*m/s*), ρ is the electrolyte density (kg/m^3), p is the pressure (*Pa*), F is the body force (N/m^3), and η is the dynamic viscosity *(Pa*s)*. In addition to convection, diffusion and electromigration also contribute to the mass transport of the substances in the electrolyte. This process can be described using the Nernst-Planck equation given the assumption of mass conservation conditions.

$$\frac{\partial c_i}{\partial t} + \nabla(-D_i \nabla c_i - Z_i \mu_i c_i \nabla \Phi + \bar{u} c_i) = R_i \quad (20)$$

Where D_i, c_i, Z_i, μ_i and R_i are diffusion coefficient (cm^2/s), concentration (mol/m^3), charge number, ionic migration rate and electrochemical reaction rate of species i. ϕ is the electric potential (*V*). The three terms in the brackets to the left of the equation represent diffusion, migration and convection contributing to mass transport, respectively. Therefore, the concentration and mass fluxes of inherent electrolyte substances and reacted substances can be calculated by solving equation *(20)* for different metal surfaces, diffusion coefficients and boundary conditions. However, the influence of the hydrodynamics on the formation of the diffusion layer is considerably greater than that of the migration and therefore assumes that no electrochemical reaction occurs at the steady state. Therefore, the governing equation *(21)* can be obtained.

$$\frac{\partial c_i}{\partial t} + \nabla(-D_i \nabla c_i + \bar{u} c_i) = 0 \quad (21)$$

3.1.3 Boundary Conditions

To solve the Navier-Stokes equation, the density (ρ) and dynamic viscosity (η) of the electrolyte are specified. The inlet boundary (number 2, Figure 38) is set to normal velocity

with u_0, and the outlet condition is zero-gauge pressure. Other surfaces are in non-slip wall condition.

Regarding the diffusion model, the viscous layer forms on the anode surface and grows toward the bulk electrolyte with a diffusion coefficient of *D* (from number 1 to 3, Figure 38). To simplify the mass transport process, the concentration of the integral substances composing the viscous layer on the anode surface is normalised to 1 and the concentration of the other domains to 0. Noticeably, no inlet concentration boundary is applied as the concentration values are normalised, and the inlet boundary (number 2, Figure 38) is set to no mass flux. At the outlet boundary (number 4, Figure 38), the convection flow conditions are applied. The detailed boundary conditions for the convection and diffusion model are shown in Table 9.

Table 9 Boundary conditions and applied equations for the EP model

Boundary (Figure 38)	Boundary conditions	Equations
1	Wall, no-slip	$u = 0$
	Concentration	$c = c_0$
2	Inlet, the velocity of the electrolyte	$u = u_0$
	No Flux	$-n \cdot (N + uc) = 0$
3	Wall, no-slip	$u = 0$
	No Flux	$-n \cdot (N + uc) = 0$
4	Outlet, pressure = 0	$p = 0$
	convective flux	$n \cdot D\nabla c = 0$

Density: 1075 (kg/m^3), dynamic viscosity: 0.001 (*Pa*s*), Diffusion coefficient: *D* (m^2/s)

3.1.4 Data Analysis and Model Validation

As shown in equation *(15)*, to separate the height and wavelength characteristics, parameters ω are introduced to the equation. Therefore, the equation can be expressed as the wavelength distribution of the generated surface is $[\frac{1}{\omega N}, +\infty]$. The anode surface profile model was validated by comparing the surface roughness of the simulated surface profile with the practical surface profile of L-PBF 316L SS. Detailed characterisation procedure and corresponding theory were introduced in section 3.4.

The parameters used for calculating the profiles are listed in Table 10 and Table 11. Three sets of simulated profiles were generated, for example, the profile set1 composed of line W_1

and line R_1. Simultaneously, three steel samples were picked and their profiles were measured to compare with the simulated profiles, respectively.

Table 10 Parameters used for simulating the L-PBF component waviness profile.

Profiles	N	b	A_w	ω_w
Line W_1	2000	0.5	0.0012	0.08
Line W_2	2000	0.5	0.010	0.08
Line W_3	2000	0.5	0.010	0.08

Table 11 Parameters used for simulating the L-PBF component residual profile.

Profiles	N	b	A_R	ω_R
Line R1	2000	0.5	0.007	0.15
Line R2	2000	0.5	0.0065	0.15
Line R3	2000	0.5	0.008	0.15

The convection and diffusion model was validated as well by comparing the growth process of the viscous layer with the work reported by Lee *et al* and Tailor *et al*[46,256]. The parameters and results are shown in Table 12 and Figure 47. To intuitively compare the diffusion process, the anode was constructed as a smooth surface with a length of 60 mm, and the inter-electrode distance was 10 mm, which corresponds to the work reported by Lee *et al*[256]. The values of the diffusion coefficient ranged from 10^{-7} to 10^{-9} cm/s and from 10^{-6} to 10^{-10} m^2/s in the two articles, meaning that there might be a typing mistake in Lee's work after validation[46,256].

Table 12 Variants and values used for the validation.

Parameters	D (m^2/s)	u_0 (m/s)	H (mm)	A	ω
Values	10^{-7}	0	10	0	0

3.1.5 Simulation Parameters of Viscous Layer Formation

The variables and values utilised for the simulations are listed in Table 13. Since the scale parameters and spatial frequency in equation *(15)* can represent the characteristics of waviness and residual profiles, the surface model was simplified. Additionally, the length of the model was reconstructed to 30 mm to reduce the computation burden.

The viscous layer roughness was calculated utilising equation *(17)* to quantitatively evaluate the uniformity. The value was comparable to the anode surface roughness, meaning that they

shared a similar surface height distribution and were not effective for the EP process. Conversely, the viscous layer was smooth and flat when the roughness value was 0.

Table 13 Variants and values used in the simulation.

Parameters		Values	Surface Parameters
Polishing Parameters	D (m^2/s)	10^{-7} - 10^{-10}	A_w=0.012, ω_w=0.08 A_R=0.007, ω_R=0.15
	u_0 (m/s)	0.001 - 0.009	
	H (mm)	1 - 5	
Surface Parameters	A	0.006 - 0.022	ω=0.12
	ω	0.04 - 0.2	A=0.014

3.2 Materials and Experiment Setup

3.2.1 Materials and electrolytic solutions

The nominal composition and concentration of the 316L SS and TC4 with powder (Bright Laser Technologies, China, https://www.xa-blt.com/) size ranging between 15 - 53 μm are shown in Table 14. The L-PBF samples were manufactured using the EOS M290 from Germany. The parameters used in the L-PBF process include laser power of 220 W, scanning speed of 100 mm/s, hatch distance of 0.11 mm and layer thickness of 0.04 mm. After fabrication, 100 each of 316L stainless steel and TC4 specimens with a nominal size of 15 mm × 15 mm × 3 mm and the initial surface roughness *Sa* ranges from 10 μm to 25 μm were obtained. Figure 40 shows the equipment and working platform.

The concentration and composition of the electrolytes are listed in Table 16. Four types of electrolytes including 65 % and 85 % phosphoric acid, a mixture solution of NaCl, Ethylene glycol (EG), and ethanol and a commercial electrolyte A2 were introduced. The phosphoric acid was made by mixing with deionised water. The concentration of the NaCl was 1 M/L for polishing both metals. The EG functioned as the solvent and the ethanol as an additive with a concentration of 10% for polishing both metals. The commercial electrolyte A2 was purchased from Struers Ltd (Rotherham, United Kingdom) which was fabricated by mixing the total electrolyte A2-I and A2-II, and finally, was composed of 4.7 % perchloric acid, 60.0 % -78.4 % ethanol, 9.2 % - 13.8 % 2-butoxyethanol and 4.6 % – 13.8 % water.

Table 14 Chemical composition of the initial feedstock steel powder in wt%.

Materials	Fe	Cr	Ni	Mo	Mn	Si	Others
316L SS	Bal	16.0-18.0	10.0-14.0	2.0-3.0	< 2.0	<1.0	< 0.1

Table 15 Chemical composition of the initial feedstock TC4 powder in wt%.

Materials	Ti	Al	V	Fe	O	C	Others
TC4	Bal	5.5 - 6.75	3.5 - 4.5	< 0.3	0.08-0.15	< 0.08	< 0.07

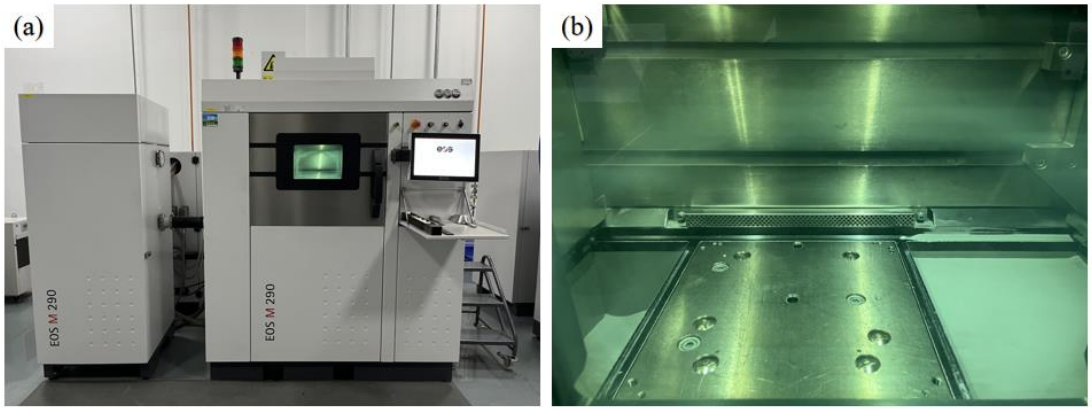

Figure 40 L-PBF equipment for manufacturing 316L SS and TC4 (EOS M290, Germany). (a) the equipment and (b) the working platform.

Table 16 The concentration and composition of the electrolytes

Electrolytes		Composition	Concentration
65% H_3PO_4		65% H_3PO_4 + 35 % H_2O	
85% H_3PO_4		85% H_3PO_4 + 15 % H_2O	
NaCl-EG-Ethanol		NaCl	0.5/1 mol/L
		Ethylene glycol	90 %
		Ethanol	10%
Electrolyte A2	A2-I 92 ml	Perchloric acid	60 %
		Ethanol	65 % - 85 %
	A2-II 920 ml	2-Butoxyethanol	10%- 15 %
		Water	5 % - 15 %

3.2.2 Experiment setup and characterisation techniques

Figure 41 (a) showed the anode fixture used to contain and control the polishing area of the L-PBF workpiece. The top and bottom covers were made of PEEK (polyetheretherketone) material and were tightly sealed with six stainless steel screws. A copper strip was utilised as the conductor between the power supply and the 316L SS/TC4. An elastic gasket was placed under the copper plate to allow both good conductivity and tightness among the copper, specimen and fixture. On the top cover, there was a circular hole with a diameter of 10 mm for the exposure of the steel to the electrolyte. Figure 41 (b) showed the experimental setup for the EP process. It was performed in a two-electrode system because the reference electrode will be damaged under a high current density. Additionally, the removal of the reference electrode has no impact on the investigation of the polishing effect under the current density above the limiting current density. The system includes an anodic working electrode and a cathodic platinum mesh. The beaker with the electrolyte was placed into a water bath to allow temperature control. A high-power direct current supply (type pe86CB-20-5-25-S/GD, Plating Electronic GmbH (Sexau, Germany)) was used to apply current between the electrodes. The local magnification graph in the polishing beaker was also provided.

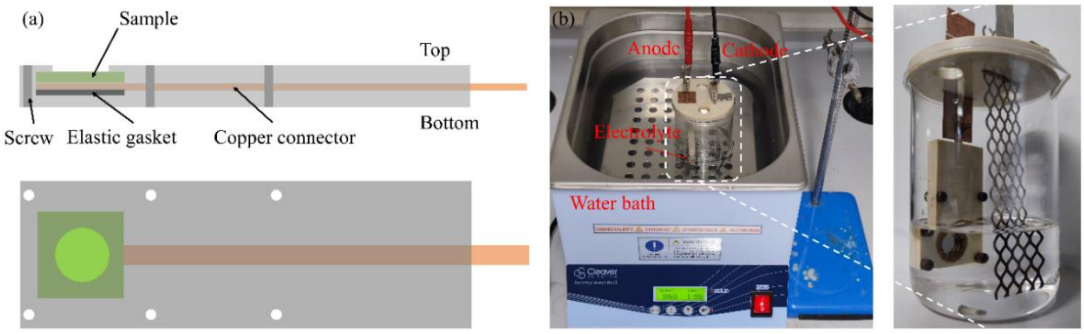

Figure 41 (a) Anode fixture and (b) experimental setup for the EP process

3.3 Experiment Strategy and Parameters

3.3.1 Parameters for the One-step EP method

Firstly, the polishing duration was determined by investigating the roughness changes with the polishing time. The parameters used were as listed in Table 17, where the parameters including agitation, electrolyte flowing, and inter-electrode distance were decided based on the simulation in chapter 4. According to the polarisation curve shown in Figure 55 and Figure 56, the current density ranges of the transpassive region for the eight EP systems were different and were unclear for polishing TC4. Therefore, a high current density of 1 A/cm^2 was adopted to guarantee the EP was carried out at the transpassive region. Then, high current

densities ranging from 0.25 A/cm^2 to 2 A/cm^2 were adopted to investigate the influence of the current density on the polishing effect. Detailed parameters were listed in Table 18. Noticeably, the product of the current density and polishing time was kept the same for all the EP processes to ensure the same amount of charges flowing through the unit area during the polishing process. The H_3PO_4 electrolyte was not used in the further experiment because it cannot provide ideal roughness reduction in the experiment of polishing duration determination.

The surface morphology of the workpiece was characterised by the Olympus Microscope and SEM. The thickness reduction of the AM steel after polishing was measured by the Olympus Microscope with MPLAPON10xLEXT objectives from 15000 μm length profiles. The material removal weight was calculated by weight changes with a precise balance with an accuracy of ±0.00001 g.

Table 17 EP process parametric for polishing duration determination

Electrolyte	*i (A/cm^2)*	*T (°C)*	Inter-electrode distance	Others
65% H_3PO_4 85% H_3PO_4 A2 electrolyte NaCl-EG-ethanol	1 A/cm^2	ambient	5 mm	No agitation No convection

Table 18 EP process parametric changes

Electrolyte	i (A/cm^2)	t (s)	T (°C)
A2 electrolyte NaCl-EG-ethanol	0.25	4t	ambient
	0.5	2t	
	1.0	t	
	1.5	t/1.5	
	2.0	t/2	

3.3.2 Parameters for the Two-step EP method

In the past, Deguchi and Chikamori discovered that a two-step EP process with different polishing potential led to smoother surfaces than a one-step EP process[257]. Han and Fengzhou discovered that a two-step EP process with different water concentrations in phosphoric glycerol-water electrolyte led to higher EP efficiency than a one-step EP process with low

water concentration and lower roughness than that with high water concentration[39]. The reported processes consisted of the first step with 25 V potential or 43 % water concentration and the second step with 10 V potential or 0 % water concentration. However, the polishing potential/current density is quite small in the study and the electrolytes in the two-step process are aqueous solutions. Therefore, considering the experiment results of the one-step EP method and the environment (perchloride acid in the A2 electrolyte was not friendly to the environment), a two-step EP method was also proposed to utilise the EP characterisations with the electrolytes at the best operating current density to get an improvement of the EP effect and reduce the usage amount of the acid solution. The proposed two-step polishing process was different from the previous studies, where: 1) the two-step EP process is carried out at the transpassive region where the current density is high, at the hundreds or thousands of amps per square centimetre because the material removal rate is proportional to the total charges flowing through the system according to Faraday's law[197]; 2) A large amount of materials should be removed because the polishing targets are manufactured by AM processes with an average roughness greater than 15 μm, while in the previous work, the initial sample roughness was in the nanometre-scale; 3) Non-aqueous and aqueous electrolytes are introduced in the first and second-step polishing process, respectively, to improve the polishing effect and geometry accuracy.

The applied current density in the first- and second steps was 1.5 A/cm^2 and 0.25 A/cm^2, where the NaCl-EG-ethanol electrolyte was used in the first step as the pre-polishing process. The EP duration for the two steps is listed in Table 19 and the corresponding groups were nominated as S_{N1}, S_{N2} and S_{N3}, respectively. The product of the current density and the polishing time for the two-step EP processes were still kept the same as the one-step EP process. When the first step was completed, the sample was cleaned using distilled water before the second step. Similarly, EP conditions for polishing TC4 were shown in Table 20. The polishing current density and duration also depended on the polishing effect obtained in the one-step EP experiment.

Table 19 Conditions used for the two-step EP process of 316L SS.

Sample	1M NaCl-EG-10% ethanol		A2 electrolyte	
	i (A/cm^2)	t (s)	i (A/cm^2)	t (s)
S_{N1}		160		2400
S_{N2}	1.5	320	0.25	1440
S_{N3}		480		480

Table 20 Conditions used for the two-step EP process of TC4.

Sample	A2 electrolyte		1M NaCl-EG-10% ethanol	
	i (A/cm^2)	t (s)	i (A/cm^2)	t (s)
T_{N1}		120		320
T_{N2}	1.0	240	1.5	240
T_{N3}		480		80

3.4 Roughness Prediction Strategy of the EP Process

After the one-step and two-step experiments, all the parameters and polishing results including the parameters of initial primary roughness, polishing duration, current density, materials, electrolyte, and primary roughness after polishing will be collected for the prediction process. The sorted data (150 data in total) will be kept in an Excel document, as shown in Figure 42, where the materials of 316L SS and TC4 were represented by 0 and 1, respectively, and the electrolytes of the commercial A2 and NaCl-EG-Ethanol were represented by 0 and 1. The parameters ranged between the first and fifth columns were used as the input values and the last column was used as the output values in the training and test datasets.

Six algorithms based on different calculation strategies were selected, as shown in Table 21, including the Adaptive Boosting algorithm (AdaBoost), Random Forest (RF), Multilayer Perceptron Regression (MPL), Ridge Regression (RR), Support Vector Regression (SVR), and Classification and Regression Trees (CART). The workflow of the regression prediction was shown in Figure 43 and the prediction process was carried out in the Python software. The Dataset will be messed up in order first. 70 % of the data will be used as the training dataset and 30 % will be the test dataset. All the data will be normalised to range [0, 1] and features of the initial primary roughness, polishing time, current density, materials and electrolytes will be extracted to be the input parameters. Then, the training dataset will be used to train the models using the algorithms and the test data will be input to the trained models for prediction. The predictive results will be output and compared with the test results, and the coefficient of determination R^2 will be adopted to evaluate the prediction accuracy. The workflow will be run ten times and the variance of the R^2 will be calculated to evaluate the stability of the algorithms.

Initial Roughness (um)	Polishing time (s)	Current Density (mA/cm2)	Materials	Electrolyte	Psa (um)
25.75	3360	250	0	0	10.2
25.69	3360	250	0	0	12.76
24.69	3360	250	0	0	11.76
23.24	1680	500	0	0	8.2373
20.26	1680	500	0	0	8.22
19.26	1680	500	0	0	7.22
21.75	840	1000	0	0	9.157
21.8	840	1000	0	0	8.29
20.8	840	1000	0	0	7.29
25.16	560	1500	0	0	7.384
23.5	560	1500	0	0	7.101
22.5	560	1500	0	0	6.101
22.55	420	2000	0	0	5.46
21.58	420	2000	0	0	4.695
20.58	420	2000	0	0	3.695
19.16	160	1500	0	0	9.438
18.12	160	1500	0	0	8.974
18.12	320	1500	0	0	8.341
18.42	160	1500	0	0	10.26
18.42	320	1500	0	0	7.708
18.42	480	1500	0	0	8.355
15.55	0	1000	0	0	15.55
15.55	120	1000	0	0	13.7
15.55	240	1000	0	0	12.16
15.55	360	1000	0	0	11.74
15.55	600	1000	0	0	10.33
15.55	840	1000	0	0	9.08
15.55	1200	1000	0	0	10.45
15.37	0	1000	0	0	15.37
15.37	120	1000	0	0	13.23

Figure 42 Dataset of the experiment parameters and results.

Table 21 Base learner selection.

Category	Algorithm
Ensemble-based	Adaptive boosting algorithm (AdaBoost)
	Random Forest (RF)
Neural network-based	Multilayer Perceptron Regression (MPL)
Regularisation-based	Ridge Regression (RR)
	Support Vector Regression (SVR)
Decision tree-based	Classification and Regression Trees (CART)

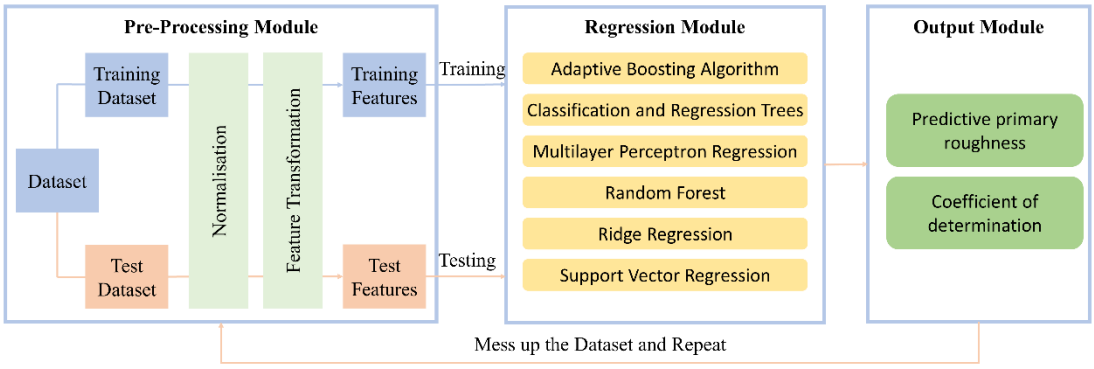

Figure 43 Framework and workflow of the multi-algorithms regression prediction.

3.5 Electrochemical Analysis and Surface Metrology

3.5.1 Potentiostat

The electrochemical analysis of the EP cell was carried out with a PGSTAT302N Potentiostat/Galvanostat (Metrohm Autolab). A saturated calomel electrode (SCE, EDT direction, UK) was utilised as the reference electrode. The setup of the device is shown in Figure 44. The red electrode is the positive, blue negative and green reference electrode. Since the maximum values of the current and potential of the potentiostat are 1000 mA and 10 V, a voltage multiplier (Metrohm) was introduced to increase the maximum potential to 30 V. The current can be controlled by adjusting the measurement area of the sample.

Figure 45 shows the Nova software interface used for controlling and monitoring the potentiostat, which can be divided into four regions: commands database, working area, parameters controlling area, and diagram plotting area. In the Autolab control section, potentiostatic mode was selected with a 1000 mA current range and high stable bandwidth. A potential of 0 V (vs (SCE)) will be applied first and after the cell is turned on, the system will wait for 5 seconds to confirm the whole system was in a stable state. Then a scanning potential from 0 V to 29 V (vs SCE) at a speed of 20 mV/s, and the values of the potential and current will be recorded and plotted. Noticeably, due to the voltage multiplier being introduced, the voltage will be magnified 10 times. For example, the setting value is 1.0 V while the real output value will be 10 V.

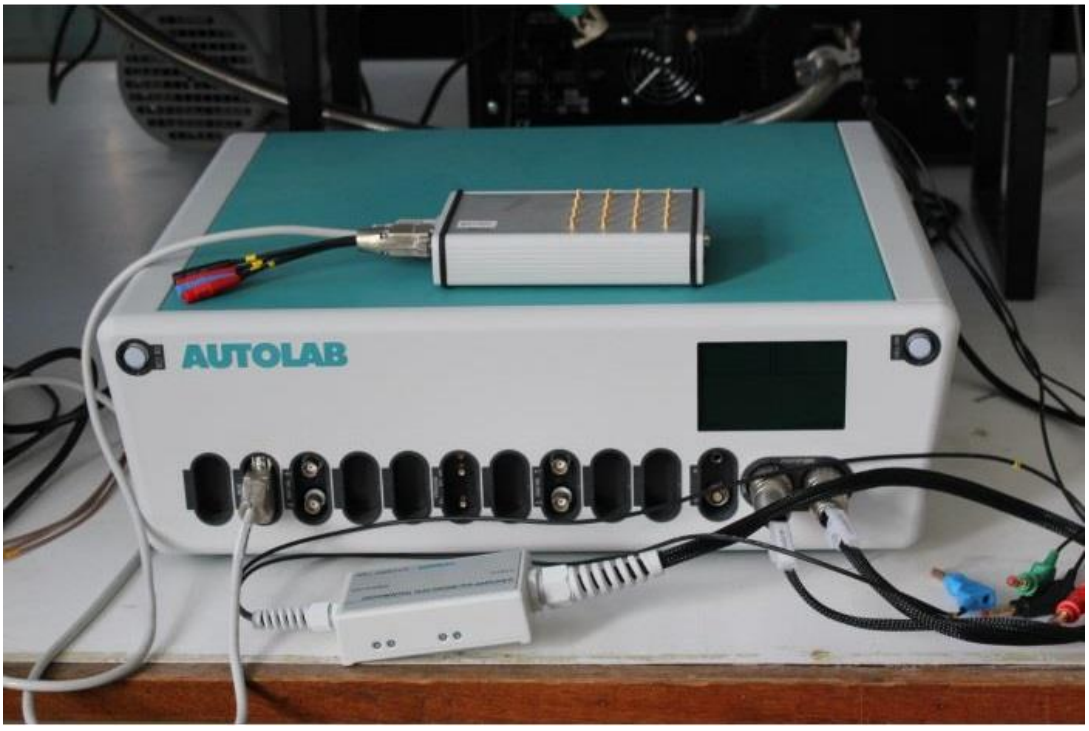

Figure 44 Setup of the potentiostat

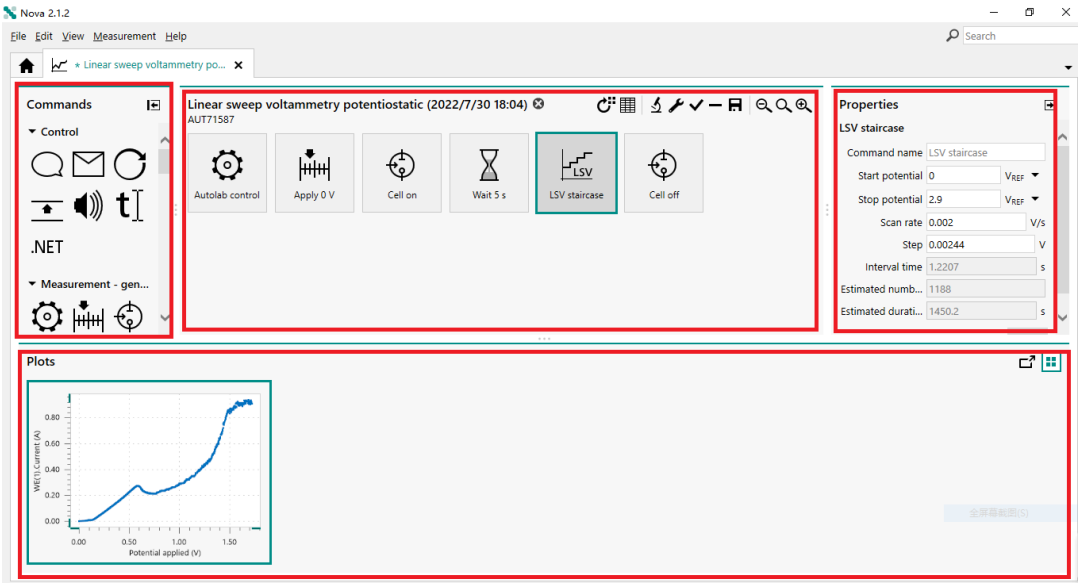

Figure 45 Interface of the Nova software

3.5.2 Olympus Microscope and ProfilmOnline

The surface morphology of the workpiece before and after the EP process was characterised by an Olympus LEXT 5000 Laser Microscope with MPLAPON20xLEXT objectives. During the data acquisition process, the size of each field was 640 × 640 μm and 4 × 4 fields were measured and stitched to form a large map. To quantitatively characterise the changes in surface condition, the tool ProfilmOnline (https://www.profilmonline.com/gallery) which can read the uncompressed Spatial Data File (*.sdf file format) exported from the microscope was applied to calculate the areal roughness *Sa*. The acquired data from the microscope was flattened by a 3-order polynomial to remove the inherent shape of the sample before a Gaussian filter was applied. According to the ISO 4288 and ISO 25178 standards, a high-pass filter (L-filter) was applied to extract the waviness from the primary surface and a low-pass filter (S-filter) was to extract the rough surfaces.

However, as mentioned in section 2.5, there was no guidance on what cut-off values were appropriate for the rough AM components. Many researchers have adopted different cut-off values such as 0.8, 1.0, 1.1, 2.0 and 2.5 mm, which were meaningless for extracting the waviness from AM surfaces[258–261]. Nagalingam *et al* advised that the maximum size of surface textures (partially melted particles, beam path, etc.) can be used as the cut-off values and the measurement area should be at least five times the cut-off values[40]. Lou *et al* and Agustin summarised the surface topographical features of L-PBF components and suggested that the Gaussian filter could be applied to the separate surface of L-PBF components[5,255]. Therefore, to avoid confusion, the roughness surface was referred to as the residual surface in this

research, meaning that the primary surface of the L-PBF components was categorised into waviness and residual surfaces. The corresponding component and production mechanism of surface features are listed in Table 22. Surface roughness for the primary surface *Psa*, waviness surface *Wsa* and residual surface *Rsa* were calculated based on their height distribution and area, as the equation shown in Table 7 (*Sa*).

Table 22 Components and their production mechanism of the surface features

Surface types		Components	Production mechanism
Primary surface	Waviness	Melted tracks	Formed by the flow of melted liquid
		Form error	Formed by thermal effect
		Pores	Low power or local overheating, wavelength larger than melted tracks
	Residual	Micro-asperity	Formed by the interaction between the melting process and metal powder
		Globules	Unmelted/partially melted powder
		Pores	Low power or local overheating, wavelength smaller than melted tracks

3.5.3 Scanning Eletron Microscope

A Field Emission Scanning Electron Microscope (FESEM, JEOL JSM-7800F) was utilised to measure the surface texture below 1 μm. It has a magnification range of 25 × to 1000000 ×, an accelerating voltage of 10 V to 30 kV, a probe with a current range of a few pA to 200 nA and a resolution of 0.8 nm @ 15 kV.

3.6 Summary

(1) The polarisation curves of the EP cells with four types of electrolytes: 65 % and 85 % H_3PO_4, a mixture of NaCl-EG-Ethanol, and commercial A2 electrolytes were measured. Systems for polishing 316L SS showed evident polishing regions while no hint of polishing TC4.

(2) Surface metrology including the texture parameters (profile and areal parameters), the operation and filtration to process the raw data was introduced.

(3) To appropriately characterise the surface texture of the L-PBF components, the primary surface was separated into waviness and residual surface based on the surface morphology. A gaussian filter with 150 μm cut-off values was applied for separation.

(4) The initial surface conditions of L-PBF 316L SS characterised by the optical microscope and SEM were presented.

Chapter 4 Numerical Simulation of the Viscous Layer Formation

As mentioned in section 2.5, the viscous layer generated on the anode surface during the electrochemical polishing process is essential for obtaining a smooth and mirror-like surface. However, the growth of the viscous layer for polishing Laser-Powder Bed Fusion (L-PBF) components having rough surface features with a height and wavelength difference range of several hundred microns differs from the surface finish at the micro/nanometre level. In this chapter, an L-PBF surface profile model was proposed using the Spatial Frequency Method and the Navier-Stokes equation was solved to simulate the influence of the diffusion coefficient, inlet velocity, inter-electrode distance, and workpiece surface profile on the thickness and geometry of the viscous layer. The surface roughness index Ra was employed to characterise the uniformity of the viscous layer for the first time. Results show that the moderate values of 10^{-8} m^2/s diffusion coefficient and 4 to 5 mm inter-electrode distance facilitate the establishment of a moderately thick and uniform viscous layer while the flow field in the present case led to non-uniform thickness at the inlet and outlet boundaries. Surfaces with a large height distribution demand a thicker viscous layer, while surfaces with shorter wavelength distribution characteristics are conducive to lower initial surface roughness and improved uniformity of the viscous layer.

4.1 Results of the Model Validation

The results of the schematic profile and roughness values are shown in Figure 46. The scale parameters and spatial frequencies utilised to simulate waviness and residual profile were

adjusted according to the measured steel surface roughness. In this case, the roughness of the original profiles, simulated by combining the waviness and residual profiles, can be compared with the measured roughness. Figure 46 (c) showed the primary roughness of the simulated and measured profiles, corresponding to 20.48 μm and 22.75 μm, 16.92 μm and 18.13 μm, 20.35 μm and 22.55 μm. respectively for the three sets. The corresponding errors were 9.97%, 6.67% and 9.76%, respectively. The reasons for the deviation were calculation method and accuracy, meaning that (a) the simulated original profile employed the addition method while the measured profile employed the Gaussian filter, and (b) the waviness and residual profile can be further represented in equations with different characteristic wavelengths. Although the multi-level expansion of equation 15 could improve the accuracy of the surface model, the computation burden would increase. Therefore, in the chapter, equation 15 was adopted for investigating the impact of the height and wavelength distribution on the viscous layer formation process.

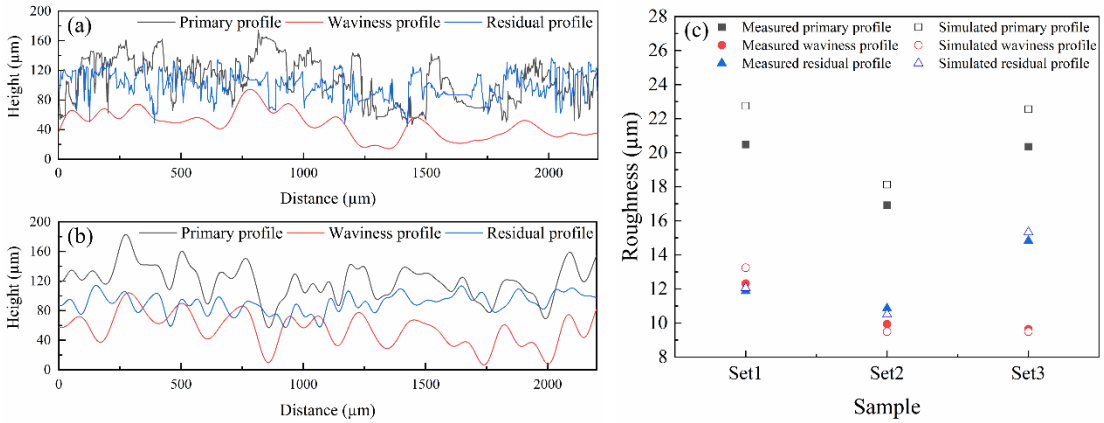

Figure 46 (a) Measured L-PBF steel surface profile, (b) simulated profile and (c) their roughness comparison.

The growth process of the diffusion layer is shown in Figure 47. The present results showed that the mass transport process and concentration distribution of the diffusion layer were similar to the reported work. The process did not reach equilibrium at 300 s, meaning that no steady viscous layer was formed and the EP process at the conditions could not provide a uniform polishing effect. The simulation results of Tailor's work were also presented here for comparison. The mass transport process and concentration distribution within the 300s were quite similar, proving that the model was correct.

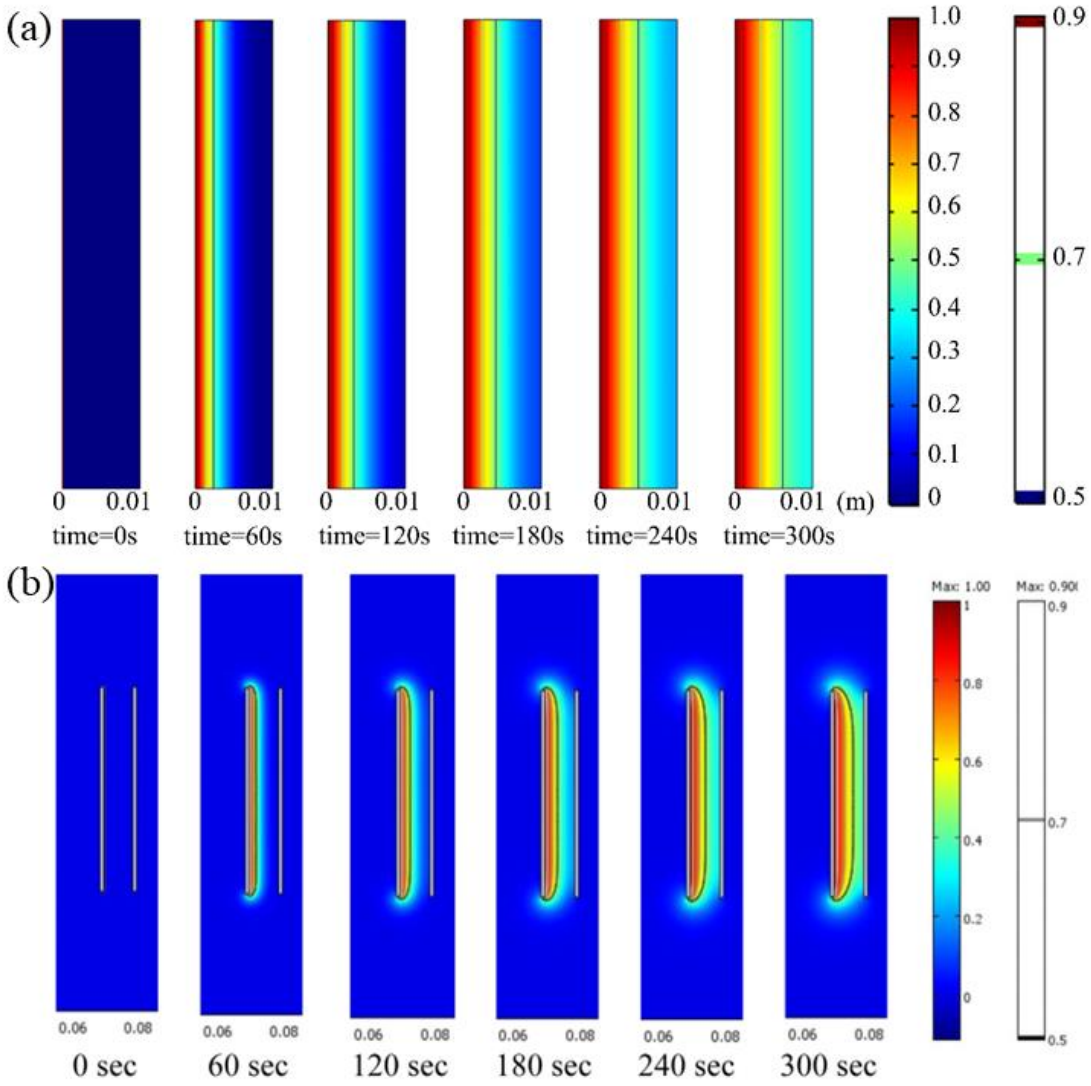

Figure 47 Growth process of the diffusion layer with time at the diffusion coefficient of 10^{-7} m^2/s (a) in this work and (b) in Tailor's work.

4.2 Impact of the Diffusion Coefficient of the Electrolyte

Figure 48 showed the profile, uniformity, thickness and concentration distribution of the viscous layer variation with the diffusion coefficient after 300s simulation. The thickness was calculated from the difference between the average height of the viscous layer and the anode surface. It was understandable and reasonable that the thickness increased with the diffusion coefficient. However, on one hand, when the diffusion coefficient was excessively high (1×10^{-7} m^2/s), the viscous layer disappeared because of the rapid diffusion process. As shown in Figure 48 (c) ($D=10^{-7}$ m^2/s), the concentration distribution of the dissolved metals and electrolyte composition nearly reached uniformity and there is no concentration gradient from the anode to the cathode surfaces, meaning that polished surfaces cannot be produced in such

a condition. Conversely, the viscous layer thickness was too small to polish rough L-PBF components at low diffusion coefficients. With the diffusion coefficients of 1×10^{-9} m^2/s and 1×10^{-9} m^2/s, the viscous layer thickness was only approximately 50 and 100 µm while the height difference between the protrusion and valley region on the anode surface can exceed 150 µm. The viscous layer geometry was similar to that of the anode surface, especially in the protrusion region, leading to low polishing efficiency, as shown in Figure 48 (a) and (b). Moreover, the viscous layer roughness also indicated that the layer became less uniform with the decreasing diffusion coefficient. Therefore, the viscosity should be considered for the choice of the electrolyte and be adjusted in the EP process. Common methods included adjusting the solvent concentration, temperature, magnetic stirring, or employing pulse current etc. to fulfil the requirements[38,44,262–266].

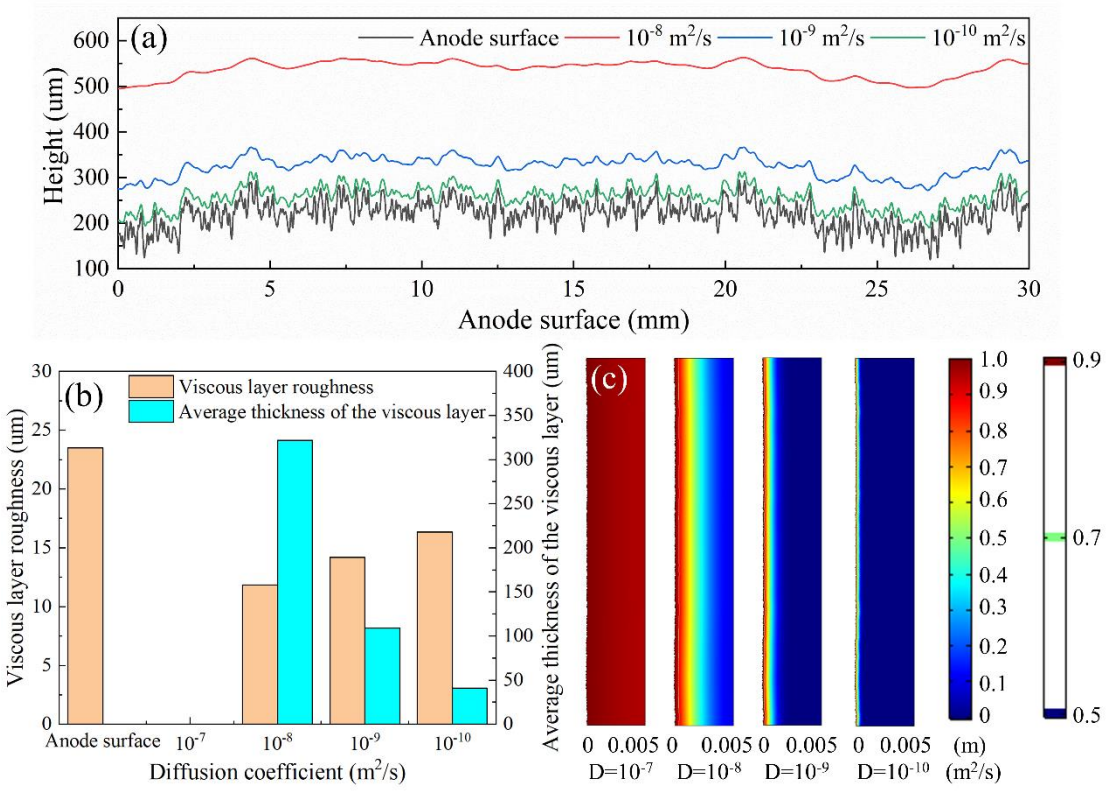

Figure 48 (a) the profile, (b) uniformity and thickness variant and (c) the concentration field of the viscous layer at the different diffusion coefficients.

4.3 Impact of the Inlet Velocity

Figure 49 shows the profile, uniformity, thickness and concentration distribution of the viscous layer variation with the inlet velocity. The viscous layer thickness was smaller than the thickness without inlet velocity in Figure 48, reducing from approximately 325 µm to below 100 µm. The thickness of the viscous layer was lowest at the inlet and highest at the

outlet, leading to non-uniform material removal rates and polishing efficiency. Noticeably, the thickness was almost zero at the inlet side, which could result in an unpolished surface in this case.

When the inlet velocity was 0.001 m/s, the viscous layer roughness exceeded the values of the anode surface, corresponding to 23.5 μm and 26.6 μm, respectively. The viscous layer roughness decreased and then increased slightly with the inlet velocity, indicating that the viscous layer uniformity improved but then deteriorated. This is because the thickness difference between the inlet and outlet boundary became smaller with the inlet velocity and this process was the dominant factor at the beginning. However, as the velocity increased further, the viscous layer thickness reduced, and the geometry became similar to that of the anode surface, leading to an increase in roughness values.

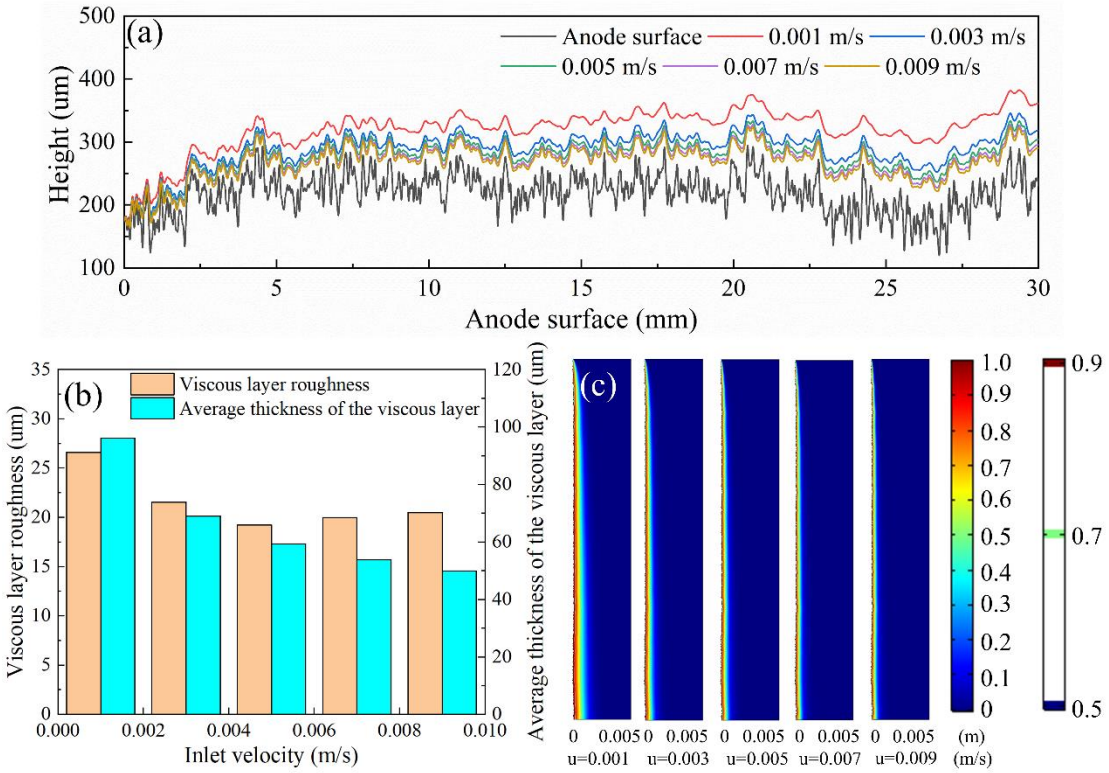

Figure 49 (a) the profile, (b) uniformity and average thickness variant and (c) the concentration field of the viscous layer under the different inlet velocities of the electrolyte.

4.4 Impact of the Inter-electrode Distance

Figure 50 (a) and (b) show the viscous layer profile, roughness, and thickness for different inter-electrode distances without inlet velocity. The profile for the 1 mm distance is not shown on the graph as the thickness exceeded the inter-electrode distance, and the thickness was hereby considered as 1000 μm. When the inter-electrode increased, the thickness

decreased and reached a constant of approximately 120 μm. Noticeably, the viscous layer roughness decreased with the inter-electrode distance, indicating that the uniformity improved. This was because the diffusion rate was proportional to the concentration gradient, which decreased as the domain of the electrodes was too small for the dissolved metals to diffuse. Therefore, the uniformity deteriorated although the thickness of the viscous layer increased. On the contrary, when the inter-electrode distance was large enough, the dissolved metals can diffuse sufficiently to form a thin and smooth viscous layer, which can enhance the polishing efficiency and provide a smooth polished surface.

Because applying inlet velocity will seriously deteriorate the viscous layer uniformity, comparing the results in Figure 48 and Figure 49, it is not recommended to apply the inlet velocity. The value of 0.01 m/s was just chosen for investigating the difference in the viscous layer formation process under different conditions. Figure 50 (c) and (d) show the viscous layer profile, roughness, and thickness for different inter-electrode distances with the 0.001 m/s inlet velocity. Similarly, the viscous layer thickness was smaller than the values without flow fields, below 100 μm. However, the thickness increased with increasing inter-electrode distance, which was contrary to the result without inlet velocity. This is because, in one respect, the dissolved metal was removed by the flowing electrolyte, leading to a sufficient domain for the substances to diffuse. Conversely, the effect of the flow field on the electrode surface became more pronounced with a smaller inter-electrode distance, leading to a smaller layer thickness. Additionally, the viscous layer roughness increased with the inter-electrode distance, which is because of the increased thickness difference at the inlet and outlet boundaries, despite the improved fluctuation.

The smallest value of the viscous layer roughness increased from 12.0 μm (5 mm inter-electrode distance) to 22.3 μm (1 mm inter-electrode distance) after applying 0.01 m/s inlet velocity, meaning that the viscous layer uniformity was deteriorated seriously, as mentioned above. Therefore, this flow method was not appropriate for polishing L-PBF component surfaces in the present case although a large amount of metal was dissolved into electrolytes. Additionally, a large inter-electrode distance can be adapted in the stationary electrolyte to provide a flat viscous layer with small thickness, and thus a fast-polishing rate and improved polishing surface.

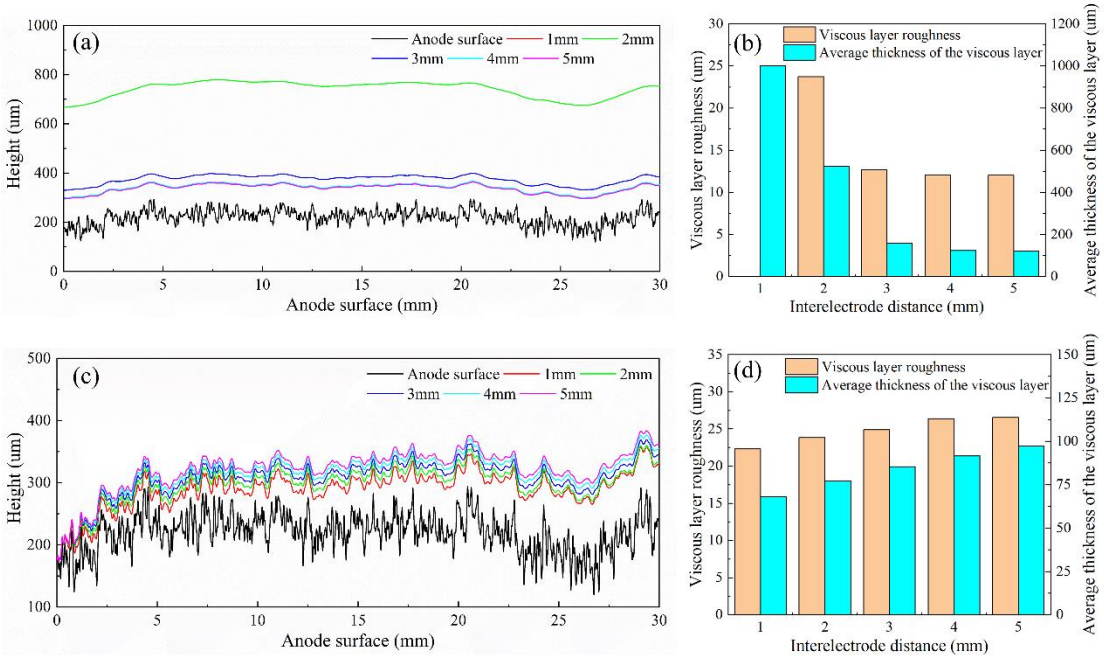

Figure 50 (a, c) Profiles of anode surfaces and viscous layer, (b, d) uniformity and thickness of viscous layer under the (a-b) 0 and (c-d) 0.001 m/s inlet velocity.

4.5 Impact of the Height and Wavelength Distribution

L-PBF component surfaces varied according to the particle size, melting parameters (speed, power, etc.) and building orientation and have a non-negligible influence on the polishing effect[42]. Therefore, the effect of height and wavelength distributions on viscous layer formation was investigated. The results of the profile and roughness are shown in Figure 51.

Figure 51 (a) showed the anode surfaces (solid lines) and the corresponding viscous layer (dotted lines) when the anode surfaces have different height distributions (parameters A in equation 15). By positioning the highest and lowest points, the height difference of the anode surface and viscous layer can be obtained. By calculating the average height distribution, the distance between the anode surfaces and the viscous layer (viscous layer thickness) can be obtained, as shown in Figure 51 (c). Results showed that the height difference of the anode surface and the viscous layer increased from 74.2 μm to 272.3 μm, and from 48.9 μm to 176.0 μm, respectively, with increasing scale parameters. The thicknesses of the viscous layer were 33.6, 37.9, 43.0, 48.7, and 54.9 μm, respectively. The height difference of the anode surface and viscous layer showed a linear relationship (R^2 = 1) while the viscous layer thickness showed an approximately linear relationship (R^2 = 0.995) with the scale parameter. The fitted equations are shown as follows:

$$y_{anode} = 12383.1A - 0.10976 \quad (22)$$

$$y_{viscous} = 7943.55A + 1.2534 \quad (23)$$

$$y_{thickness} = 1335.38A + 24.9553 \quad (24)$$

where y_{anode} and $y_{viscous}$ represented the height difference of the anode surface and viscous layer, $y_{thickness}$ represented the viscous layer thickness, and A represented the scale parameters. According to the slope of the equation, the increase of height difference of the anode surface is faster than that of the viscous layer, indicating that the anode surface roughness might be more sensitive than the viscous layer uniformity to the scale parameters. This can be proved by Figure 51 (e), although the roughness of the viscous layer and anode surface both increased with the increasing scale parameters (the number 0.006 - 0.022 above the green line), the roughness difference between the anode surface and the viscous layer was more evident at larger scale parameters, indicating that the roughness reduction might be more pronounced on surfaces with larger height distribution.

The average spatial frequency parameters (parameters ω in equation 15) had no impact on the height distribution of the anode surface, with a height difference of approximately 173 μm while the height difference of the viscous layer decreased from 73.8 μm to 43.2 μm. The thickness of the viscous layer was not affected by the wavelength distribution in the current case, corresponding to 45.9 μm, 41.1 μm, 43.1 μm, 45.0 μm and 47.0 μm, as shown in Figure 51 (d). However, the spatial frequency had a smaller impact on the anode surface roughness than on the viscous layer uniformity, as shown in Figure 51 (e). With the decreasing spatial frequency (from 0.2 to 0.04), the anode surface roughness increased from 21.5 μm to 25.6 μm, while the viscous layer roughness increased from 8.6 μm to 13.2 μm. This means that surfaces with shorter-wavelength distribution could reduce the initial surface roughness and generate a uniform viscous layer with moderate thickness.

To conclude, the fitted equations for the viscous layer roughness under different scale and spatial parameters in Figure 51 (e) are as follows, with the corresponding R2 values of 0.99 and 0.79.

$$y_{scale\_10-8} = 0.9897x + 0.4614 \quad (25)$$

$$y_{spatial\_10-8} = 1.2376x - 18.0383 \quad (26)$$

where y_{scale_10-8} and $y_{spatial\_10-8}$ represented the viscous layer roughness under the diffusion coefficient of 10^{-8} m^2/s, and x represented the anode surface roughness. Noticeably, the slope of y_{scale_10-8} is smaller than 1 while the slope of $y_{spatial\_10-8}$ is larger than 1, meaning that rougher surfaces caused by height distribution alteration would generate a more uniform viscous layer than surfaces caused by wavelength distribution alteration. Additionally, smaller height (small scale parameter) and shorter wavelength (large spatial frequency) distribution could provide a

viscous layer with smaller roughness values (better uniformity), and thus better polishing effect.

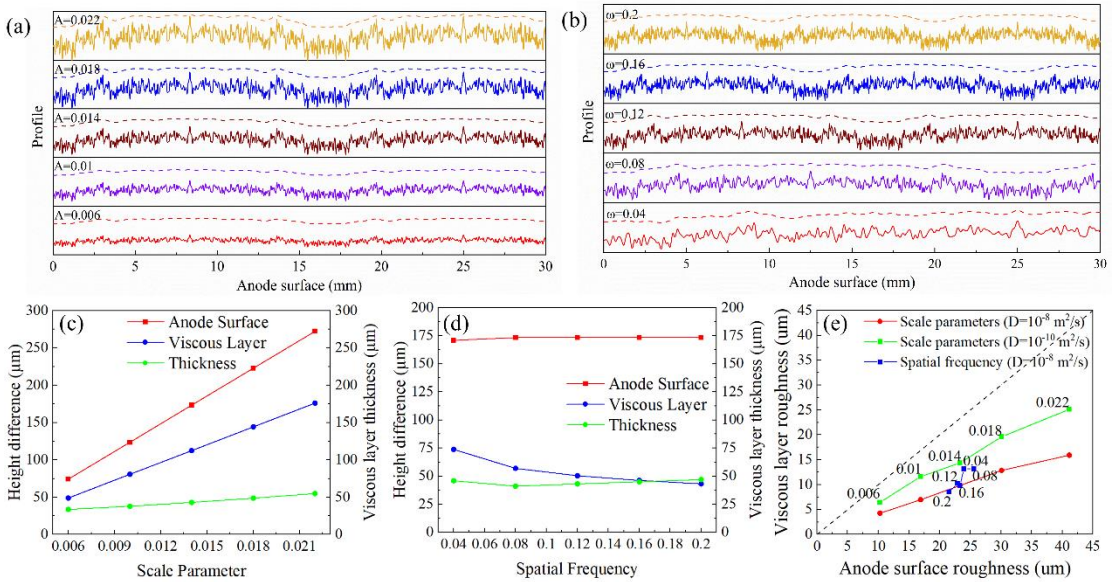

Figure 51 (a and b) Profiles, (c and d) height difference, thickness and (e) roughness of the anode surfaces and viscous layers with different height and wavelength characteristics, the solid and dotted lines in (a) and (b) are anode surfaces and viscous layers under different conditions.

4.6 Summary

The Spatial Frequencies Method was applied to model the rough L-PBF component surface and the growth process of the viscous layer with several inherent and external parameters was investigated. Based on the results, the following conclusions can be drawn.

(1) The Spatial Frequencies Method can be employed to model the L-PBF component surface with different height distribution and wavelength features by adjusting the scale parameters and spatial frequency.

(2) External parameters of diffusion coefficient, inlet velocity and inter-electrode distance had negligible influence on the viscous layer thickness and geometry. The diffusion coefficient should be chosen appropriately based on the metal surface conditions. The inlet velocity can reduce the viscous layer thickness while increasing the non-uniformity of polishing rough L-PBF components. Inter-electrode distance should be chosen based on the flow field and the generator sufficient diffusion space.

(3) The inherent parameters of the height distribution and wavelength affected the anode surface roughness, viscous layer uniformity and thickness. These three indexes showed linear relationships with the height distribution, while small wavelength features can reduce the anode surface roughness and improve the uniformity of the viscous layer.

Chapter 5 One-Step Electrochemical Polishing SLM 316L SS and TC4

L-PBF fabricated 316L SS and TC4 components were electrochemically polished in four types of electrolytes including 65 % and 85 % phosphoric acid, a non-aqueous electrolytic solution consisting of sodium chloride, ethylene glycol, and ethanol, and an aqueous commercial electrolyte A2. The influence of high current densities ranging between 250 – 2000 mA/cm^2 on the surface roughness (*Psa*, *Wsa*, and *Rsa*), materials removal weight, and thickness reduction with various morphological characteristics was investigated. It is confirmed that polishing at the tranpassive region was feasible in non-aqueous electrolytes where little pitting occurred.

5.1 Initial surface conditions

Assuming that the shape of trapped powders and partially melted/sintering particles are ideal spheres, their size distribution can be estimated at approximately 0 - 50 μm, as shown in Figure 52 (a), meaning that the cut-off values should be larger than 50 μm. Figure 52 (b) and (c) show the primary, waviness and residual profiles separated with the cut-off values of 50, 150 and 250 μm. The transmittance for the waves with different wavelengths can be calculated by the filter transfer function as the *equation (13)*. Results showed that the transmittance for the waves below 50 μm can reach 50 %, and for the waves with a wavelength of 40 μm was 35.8 %, meaning that many particle features will be extracted to the waviness profile. As the red region in Figure 52 (b) showed, the peak regions on the primary profile should be particle features while part of them was extracted onto the waviness profile

and thus the height of the residual profile in Figure 52 (c) decreased. In contrast, the transmittance for the particle with 50 µm wavelength was only 2.7 %, while the many waviness features remained in the residual profiles. When the cut-off value was 150 µm, the transmittance for the particle with 50 µm wavelength was 7.4 % and for the laser tracks with 200 - 250 um wavelength was 67.7 % - 77.9 %. Since the transmittance values for short and long waves cannot be satisfied simultaneously and the short waves were more sensitive to the EP process than the long waves because of the shape-edge effect. Therefore, general primary L-PBF steel surfaces with their waviness and residual surfaces can be obtained with the 150 µm cut-off values, as shown in Figure 53 (b), (c) and (d).

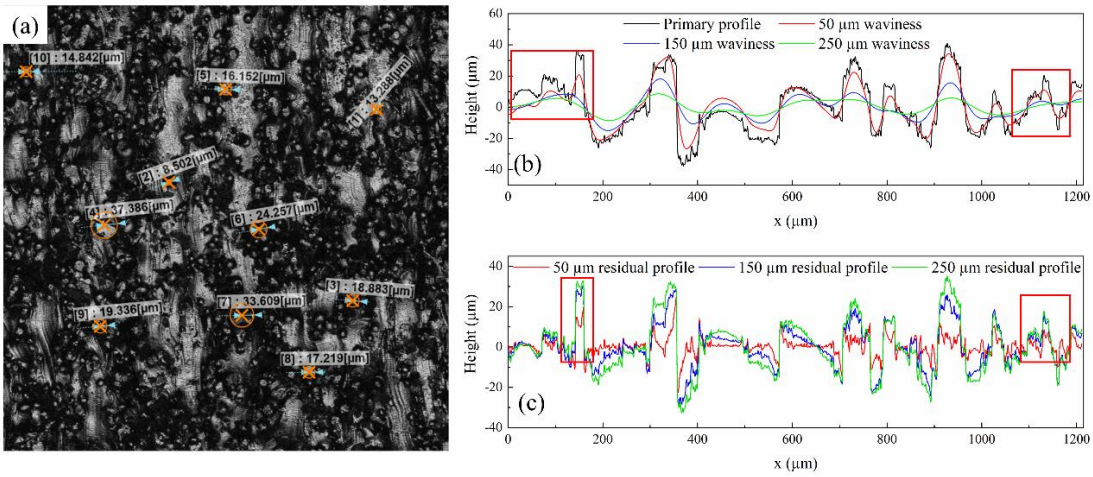

Figure 52 (a) Size distribution of the unmelt and partially melted powders, and separation of the (b) primary, waviness and (c) residual profile using the Gaussian filter with 50, 150 and 250 µm cut-off values.

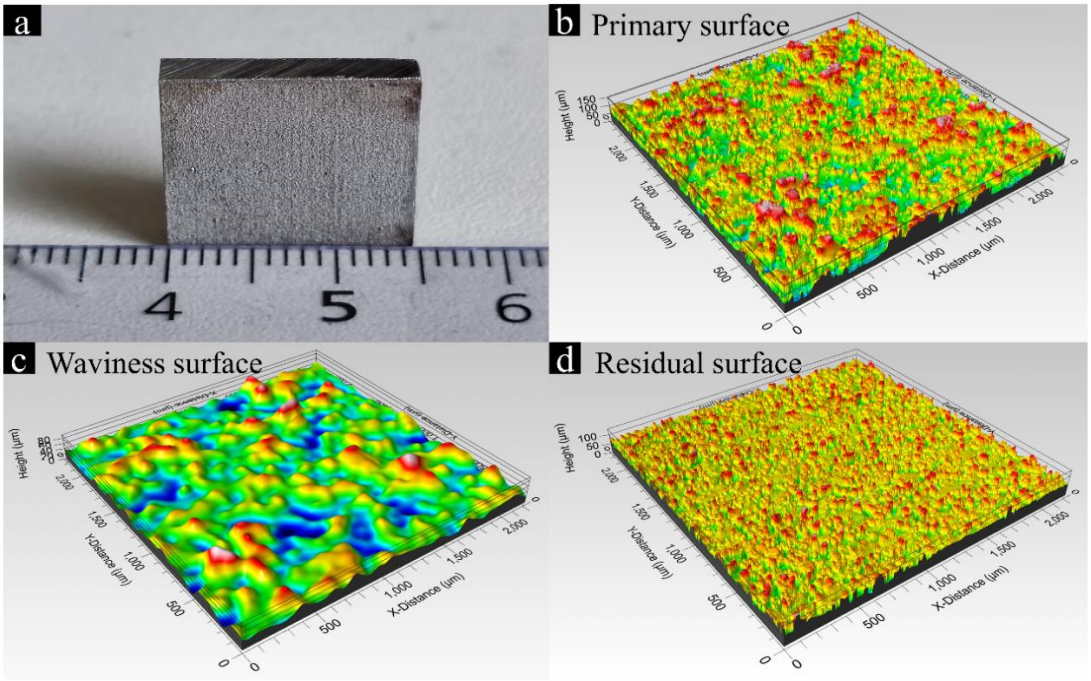

Figure 53 (a) Physical photo, general (b) primary, (c) waviness and (d) residual surface topography of L-PBF AM 316L SS with the cut-off values of 150 µm.

The initial surface condition of L-PBF 316L SS before polishing was obtained using the SEM with 5.0 kV, 100x and 3000x magnification, as shown in Figure 54, where many residual powder particles and partially melted powder are attached to the surfaces.

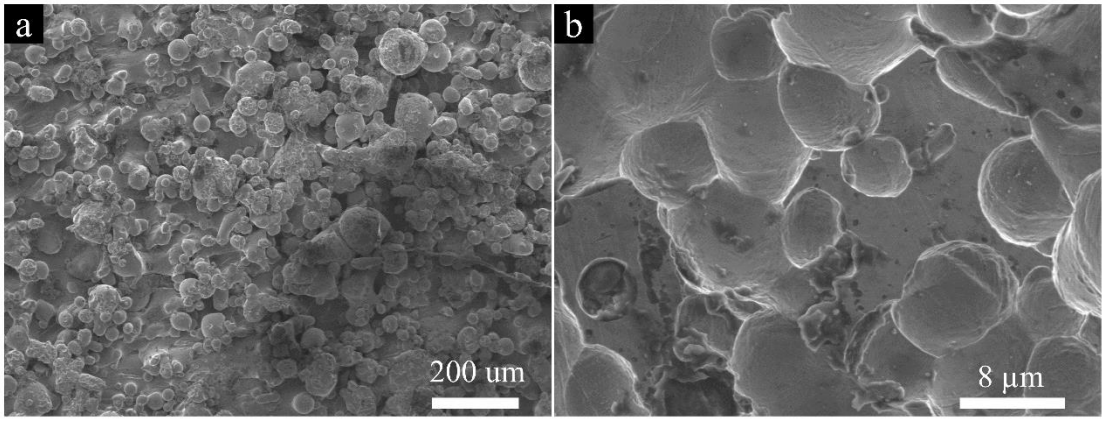

Figure 54 Surface morphology of L-PBF 316L SS obtained by SEM.

5.2 Anodic Polarisation Curve

Figure 55 shows the current density vs. potential curve of the EP system with the phosphoric acid, NaCl-Ethylene Glycol-Ethanol and A2 electrolyte for 316L SS. The measurement was repeated three times for the electrolytes and the corresponding curves were shown by the transparent solid lines. Hereafter, an average curve, represented by the blue line, was calculated and drawn to improve accuracy. As shown in Figure 55 (a), the limiting current density for the electrolyte A2 approximately started from 200 – 240 mA/cm^2, which was greatly higher than that of the other electrolytes. However, the polishing region and the transpassive region were difficult to distinguish as no apparent critical point on the curve. Two plateau regions were shown in Figure 55 (a), corresponding to approximately 1.8 – 2.7 V, and 4.5 – 5.3 V. However, according to the literature, the behaviour in the green rectangle was possibly caused by a brown product generated adjacent to the anode surface, but not representing the polishing phenomenon[38]. The red rectangle was the polishing region where the current density was approximately 30 – 40 mA/cm^2. The limiting current density plateau regions for the phosphoric acid with different concentrations ranged between 1.5 - 2.0 V. The difference was that the current density in 85% H_3PO_4 was a little higher than that in 65% H_3PO_4 solution because more H^+ and PO_4^{2-} can be ionised in the former solution.

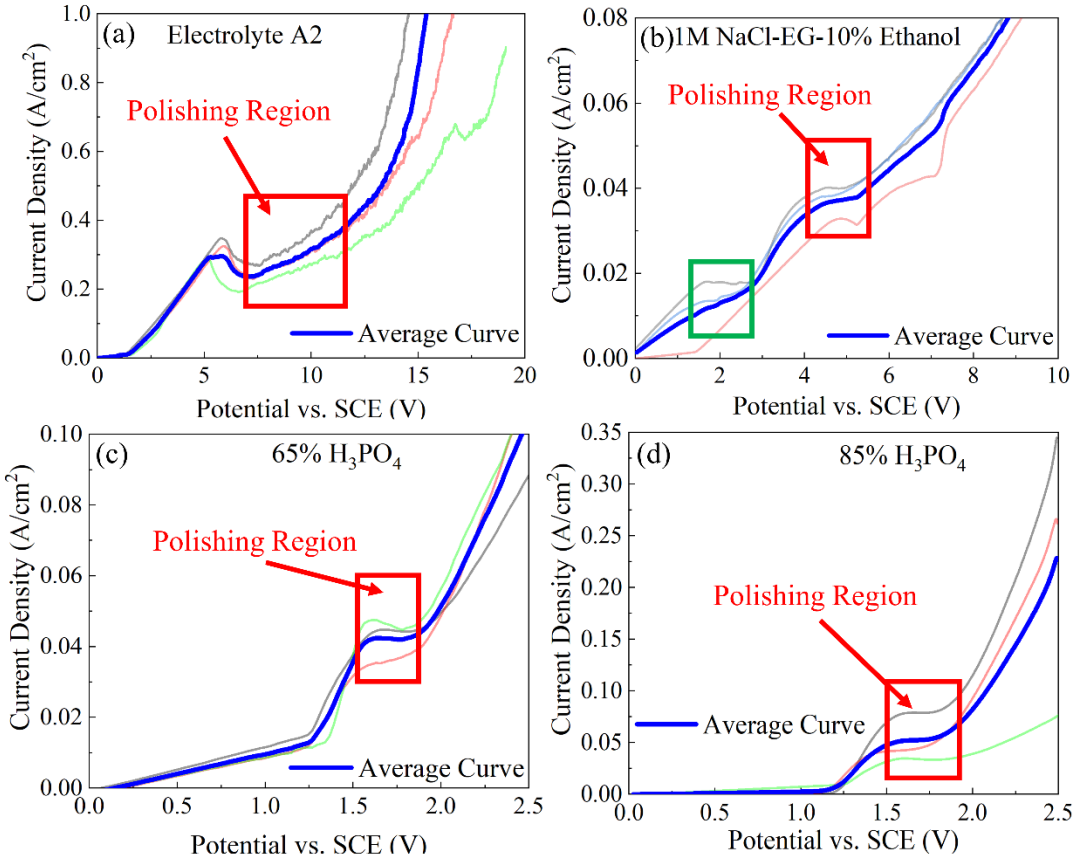

Figure 55 polarisation curve of the EP system with the electrolytes of (a) A2, (b)1M NaCl-Ethylene Glycol-Ethanol (c) 65% H_3PO_4 and (d) 85 % H_3PO_4 electrolytes for 316L SS.

Figure 56 shows the current density vs. potential curve of the EP system with the phosphoric acid, NaCl-Ethylene Glycol-Ethanol and A2 electrolyte for TC4. The current density increased suddenly at the potential of approximately 18 V for the A2 electrolyte while showing no evident inflexion point for the other electrolytes. The polarisation curve for the H_3PO_4 electrolyte showed serious fluctuations at the high potential, indicating the electrochemical cells became unstable. The viscous layer or the distribution of the current density at the anode surface might be un-uniform, deteriorating the polishing effect.

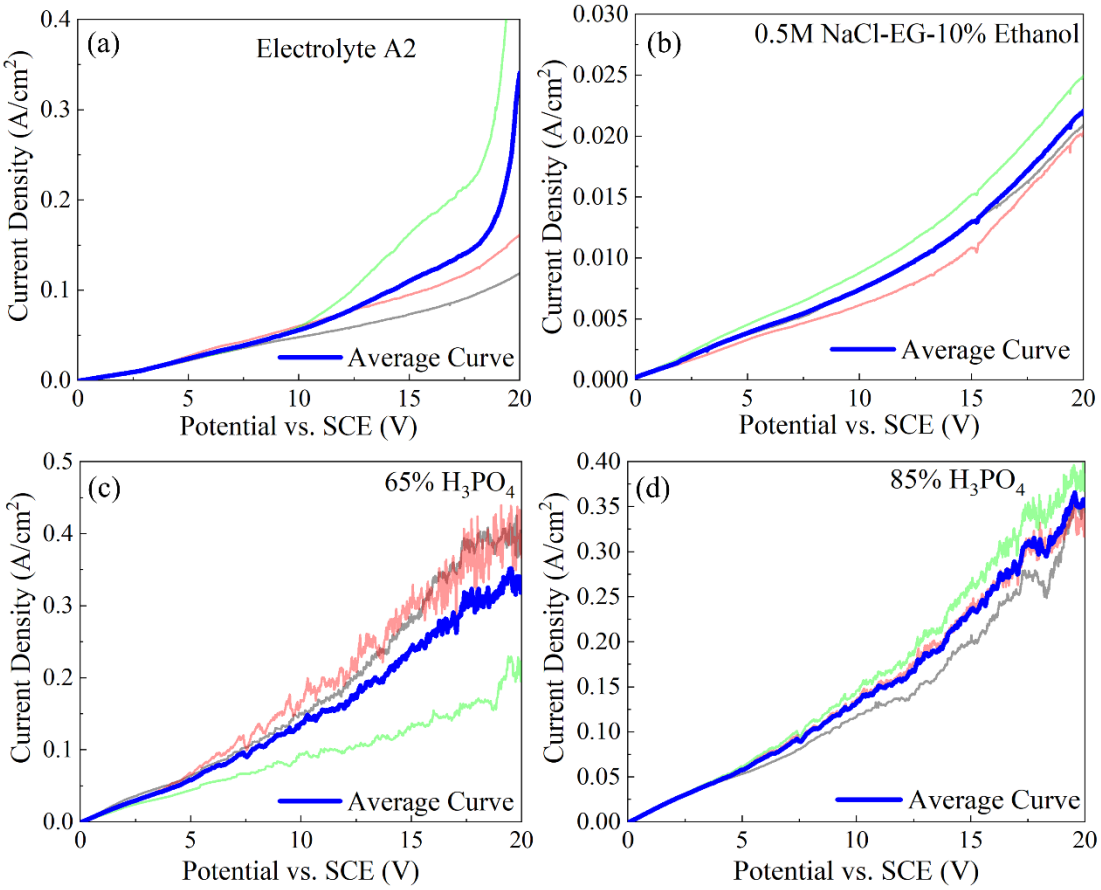

Figure 56 polarisation curve of the EP system with the electrolytes of (a) A2, (b)1M NaCl-Ethylene Glycol-Ethanol (c) 65% H_3PO_4 and (d) 85 % H_3PO_4 electrolytes for TC4.

5.3 Electrochemical Polishing 316L SS

5.3.1 Polishing duration determination

Figure 57 showed the primary roughness changes with the polishing time for polishing 316L SS in the EP systems with the electrolytes of 65 % and 85 % H_3PO_4, 1M NaCl-EG-10% Ethanol, and commercial A2. The roughness values of the 316L SS increased from 13 - 16 μm to 17 μm after 400 s polishing in the phosphoric acid solutions, indicating that the electrolyte cannot provide a good polishing effect at the transpassive region. The roughness values reduced from 15 ± (0.55, 0.92) μm to 8.4 ± (2.45, 4.5) μm and 5.2 ± (0.68, 0.73) μm, respectively, using the electrolytes 1M NaCl-EG-Ethanol and commercial A2 when being polished for 840 s, and then increased with polishing time. Therefore, the best polishing duration should be 840 s when the current density was 1 A/cm^2.

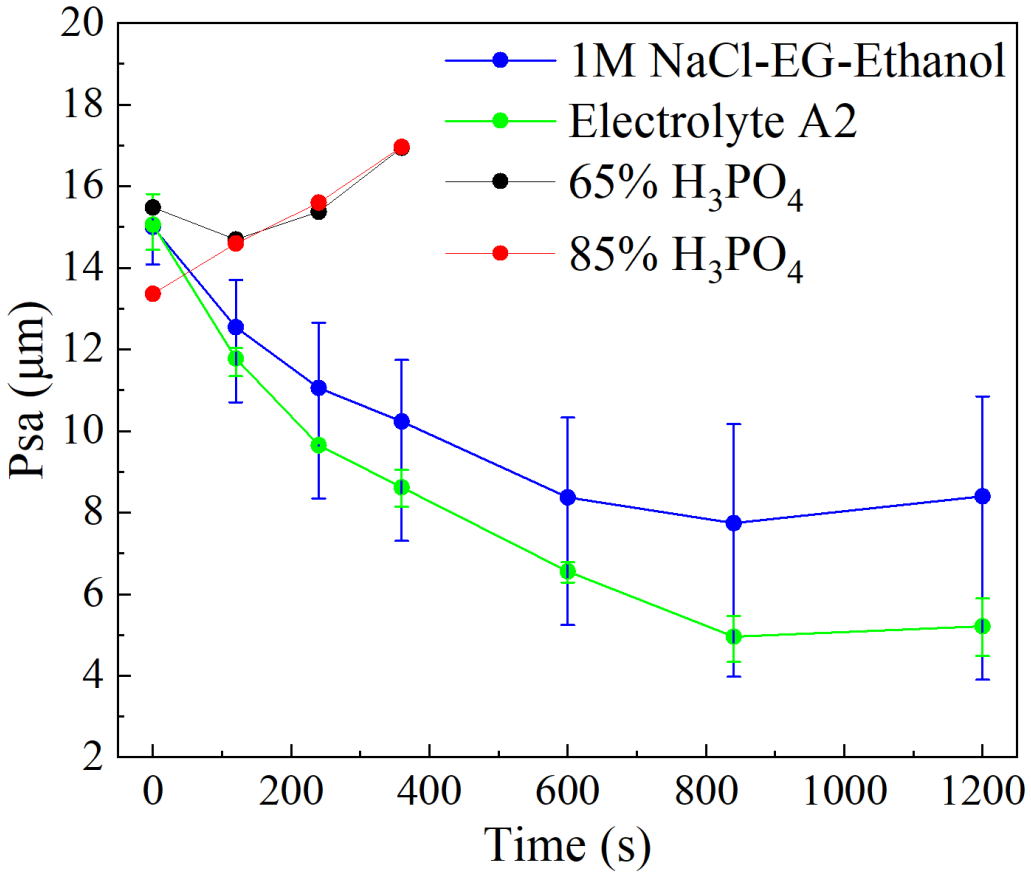

Figure 57 Roughness changes with the EP duration in the systems for polishing 316L SS with the four types of electrolytes.

5.3.2 Surface topography analysis

Figure 58 and Figure 59 show the three types of polished surface topographies at the current densities from 0.25 to 2.0 A/cm^2 polished by the A2 electrolyte. Regarding the primary surface, the maximum height difference between peak and valleys can reach to 150 μm for the unpolished components, as shown in Figure 53 (b), for instance. The values have a reduction of 84 ± (26, 34) μm after polishing. Additionally, the sharp peaks disappeared and only several long waves remained on the surface. Regarding the waviness surface shown in Figure 59 (a) – (e), there was also a reduction of around 41 ± (14, 11) μm in the height difference between the peak and valleys. The surface became smoother than before, because in one respect, the peak regions were flattened, and conversely, short waves were connected to form long waves. Regarding the residual surface, the small particles disappeared, and the reduction in height difference was 65 ± (25, 25) μm. However, large amounts of pores smaller than 10 μm were observed on the sample residual surface polished with the current density of 0.25 A/cm^2. The phenomenon of the pitting corrosion became weak first with the increased current density, as shown in Figure 59 (f) – (h), while became serious when the current density was

over 1.0 mA/cm^2, as shown in Figure 59 (h) – (j). Two reasons would cause the pitting corrosion during the polishing process: an acidic environment and oxygen bubbles[267,268]. Because the current density of 0.25 mA/cm^2 was still in the limiting current density plateau region according to Figure 55 (a), where less gas bubble will be generated on the anode surface, the pores on the sample surface can be attributed to prolonged polishing time in the acidic environment. With the increased current density, the number of pores should decrease due to the reduction in polishing duration. However, because the polishing current density of above 0.5 mA/cm^2 was in the transpassive region, as Figure 55 (a) showed, the water in the solution was electrolysed and the viscous layer was broken. Therefore, oxygen bubbles would generate and grow on the anode surface. Figure 59 (g) and (h) did not have many pores on the surfaces which assumed that the bubble effect was not serious, while the amount and growth rate of the oxygen bubbles increased with the increasing current density and therefore the pores became evident again on Figure 59 (h) and (i)[45,269]. The amount of pores on the samples was also positioned and counted with numbers (24 - 12 - 4 - 5 - 17).

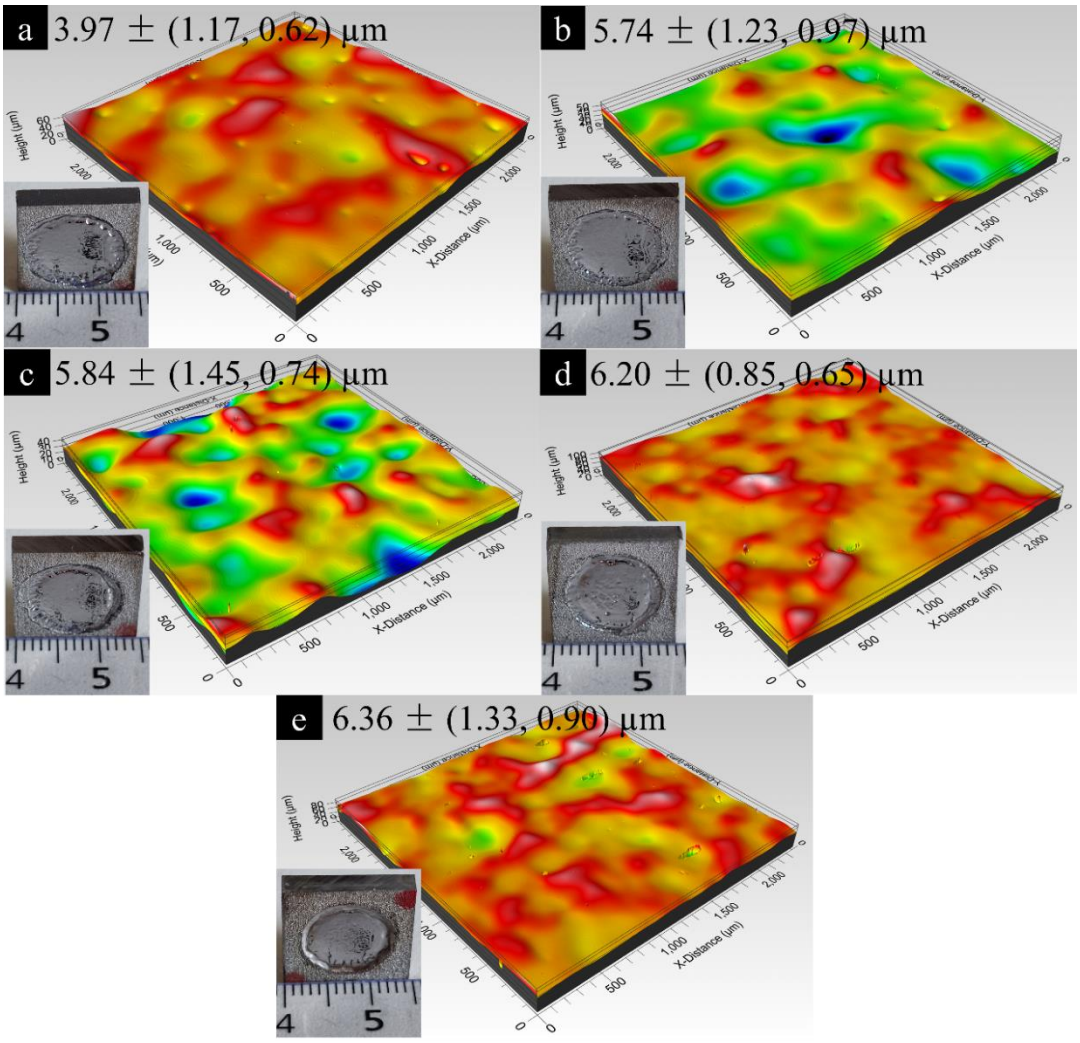

Figure 58 Physical photos, topographies and mean roughness values of the primary surfaces of the 316L SS polished with the A2 electrolyte at the (a) 0.25, (b) 0.5, (c) 1.0, (d) 1.5 and (e) 2.0 A/cm^2 current densities.

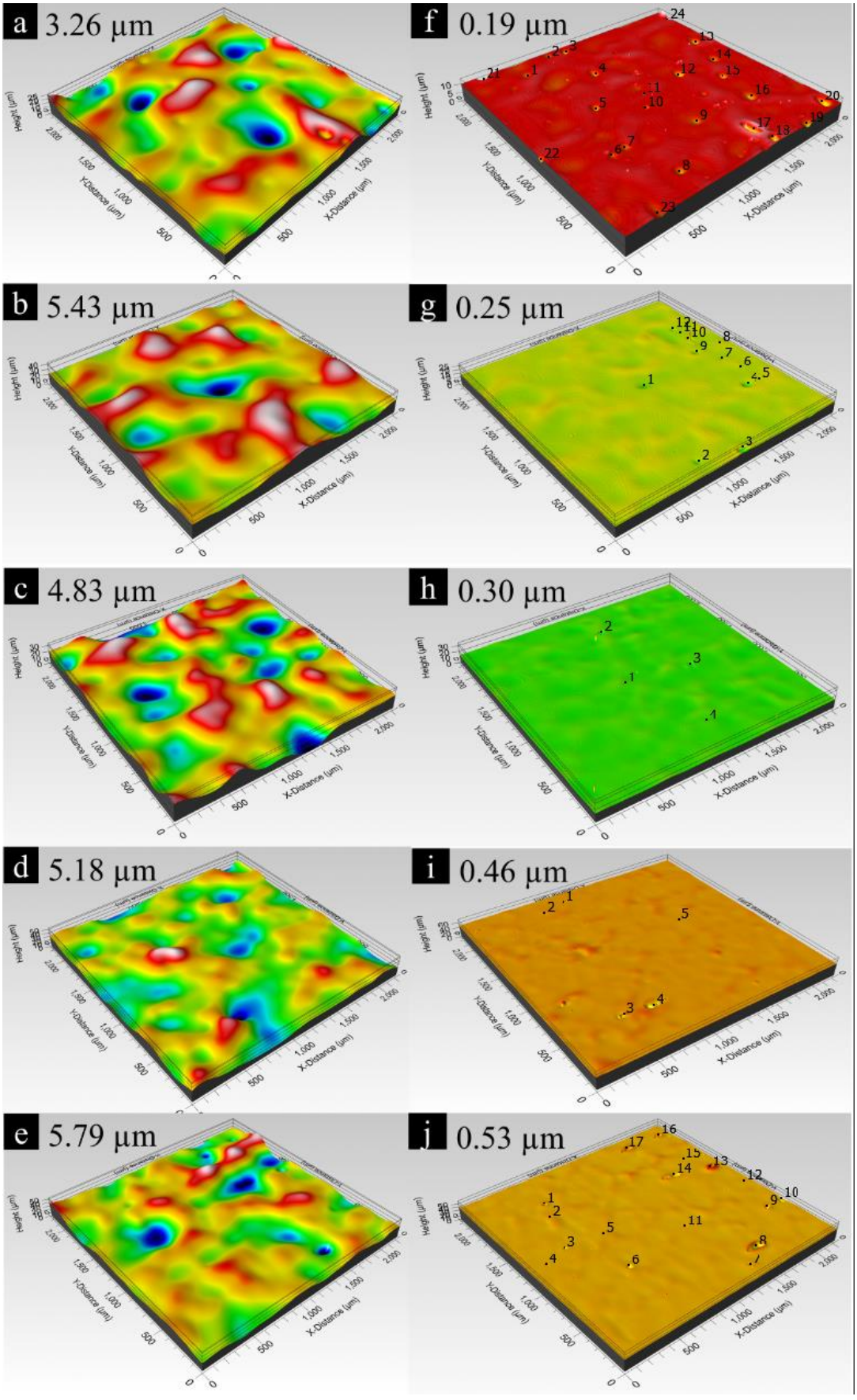

Figure 59 Topographies and mean roughness values of the (a-e) waviness and (f-j)) residual surfaces of the 316L SS after polishing with the A2 electrolyte at the (a-e) (f-j) 0.25 - 2.0 A/cm^2 current densities.

Figure 60 and Figure 61 showed the three types of polished surface topographies with the 1M NaCl-EG-10% ethanol electrolyte at the current densities from 0.25 to 2.0 A/cm^2. The surfaces after polishing did not present much porosity as no water was added to the electrolyte, however, polygonal patterns were exhibited at the low current densities and flocculent tearing at the high current densities, especially on the residual surfaces. Several deep pores emerged on the steel surface at 0.25 A/cm^2, which may be due to prolonged exposure to the Cl^- environment[38]. The polished surfaces were not as smooth as those of the samples polished with the electrolyte A2 in terms of waviness and residual surfaces. For instance, at the 0.5 A/cm^2 current density, the samples polished with the different electrolytes had similar height scales corresponding to 25 and 15 µm, however, the latter had more pronounced surface undulation. Additionally, the roughness values after polishing with the NaCl-EG-ethanol electrolyte were higher than those of the surfaces with the A2 electrolyte.

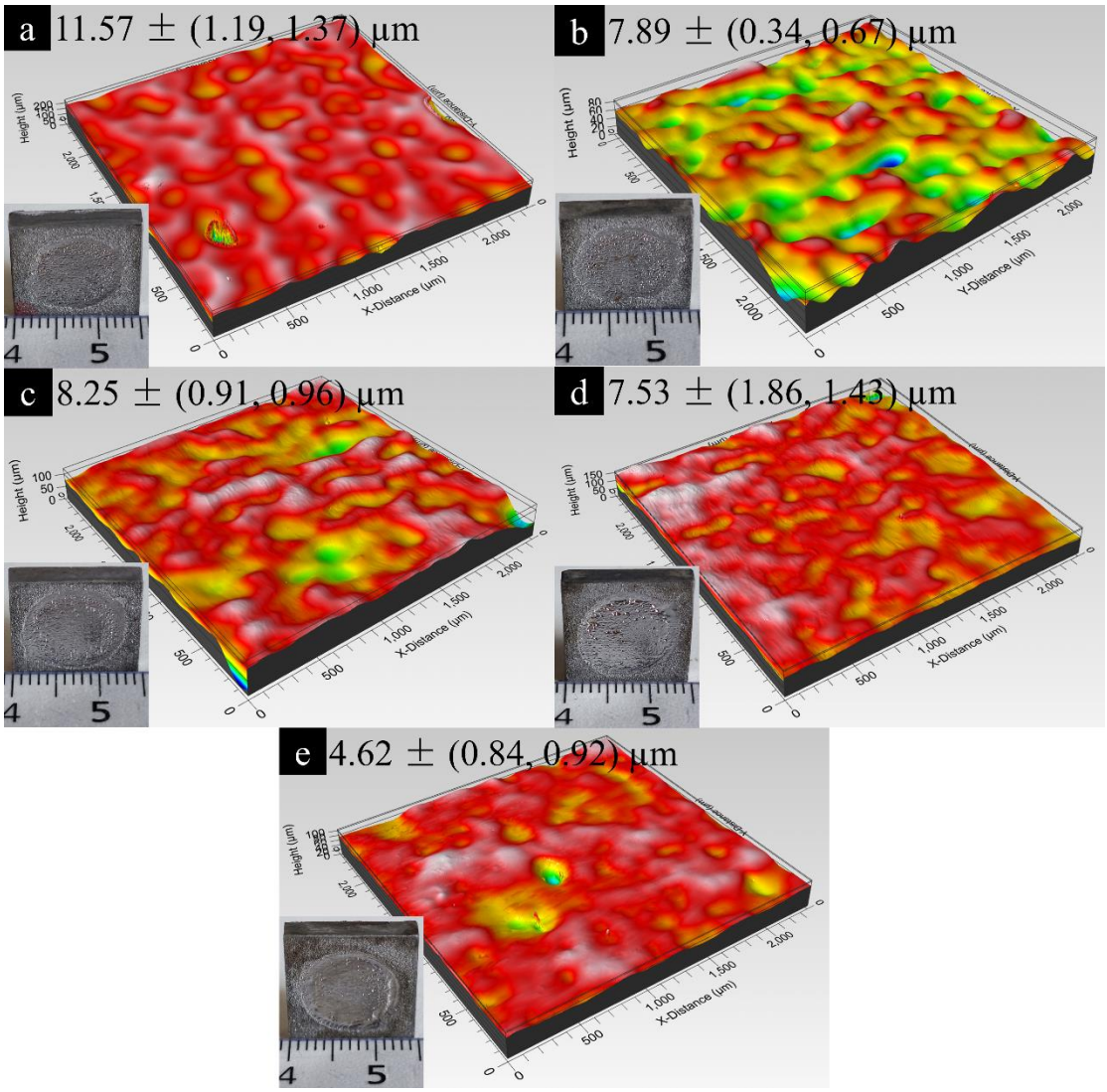

Figure 60 Physical photos, topographies, and mean roughness values of the primary surfaces of the 316L SS polished with the 1M NaCl-EG-10% Ethanol at the (a) 0.25, (b) 0.5, (c) 1.0, (d) 1.5 and (e) 2.0 A/cm^2 current densities.

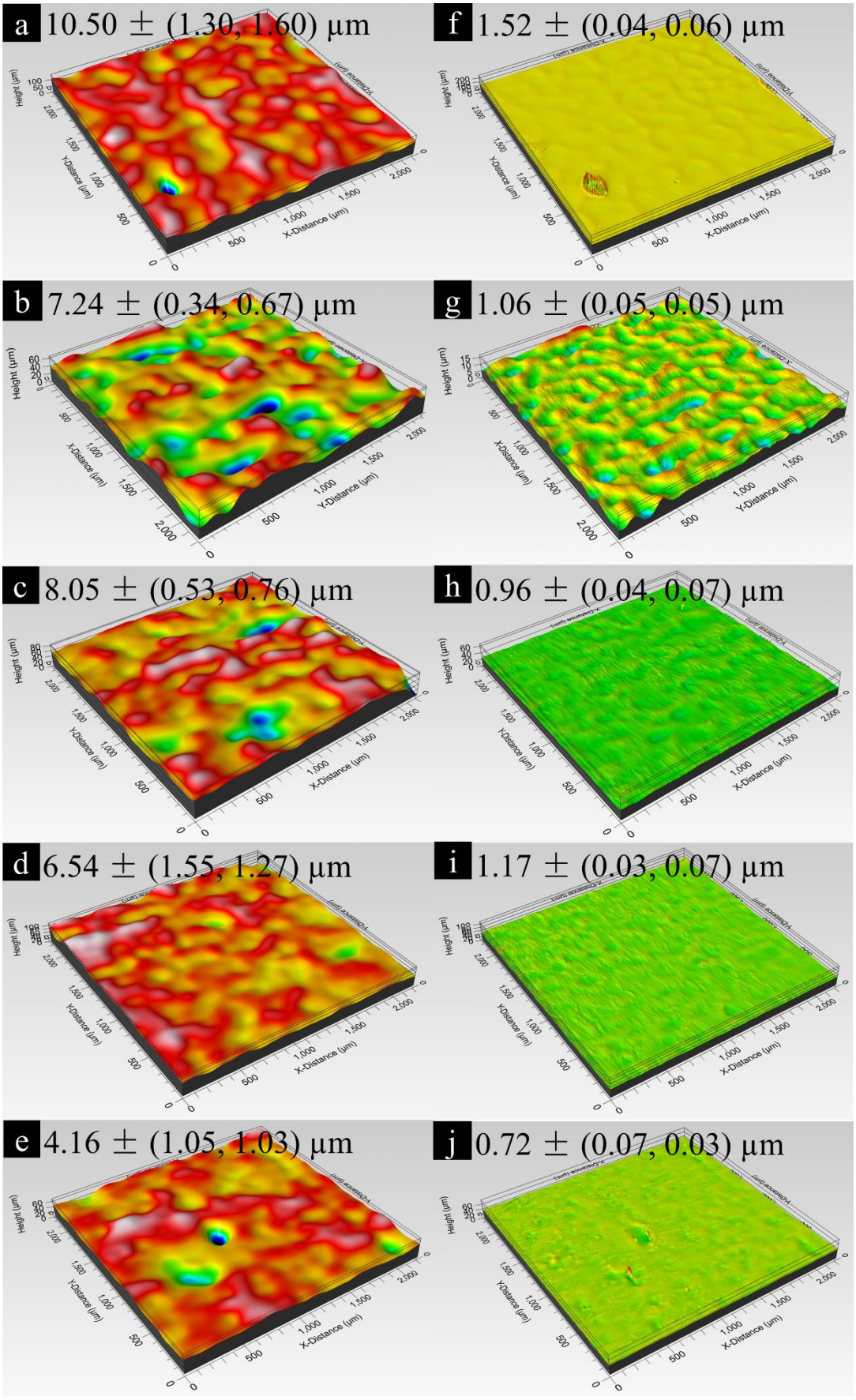

Figure 61 Topographies and mean roughness values of the (a-e) waviness and (f-j)) residual surfaces of the 316L SS after polishing with the 1M NaCl-EG-10% Ethanol at the (a-e) (f-j) 0.25 - 2.0 A/cm^2 current densities.

Figure 62 (a) and (b) showed the morphologies of the 316L SS after polishing with the A2 electrolyte under the current densities of 0.25 and 1.5 A/cm^2. The surfaces were flat after polishing while some scratches and holes with widths below 1 μm existed on the sample surfaces, which might be caused by the broken bubbles tunnelling effect[45]. The scratches became more evident and complicated (as the red line showed) under the 1.5 A/cm^2 current density, and more white dots which might be elements not being polished existed on the surface, as shown in Figure 62 (b).

Figure 62 (c) and (d) showed the morphologies of the 316L SS after polishing with the 1M NaCl-EG-10% Ethanol electrolyte under the current densities of 0.25 and 1.5 A/cm^2. Results for the sample with 0.25 A/cm^2 showed a flat surface with many dark regions that might be etched by the Cl^-. Some unpolished elements and large particles exceeding 1 μm existed on the surface. The dark regions and large particles disappeared with 1.5 A/cm^2 while many raised filamentous textures and holes with inserted particles were generated on the surface.

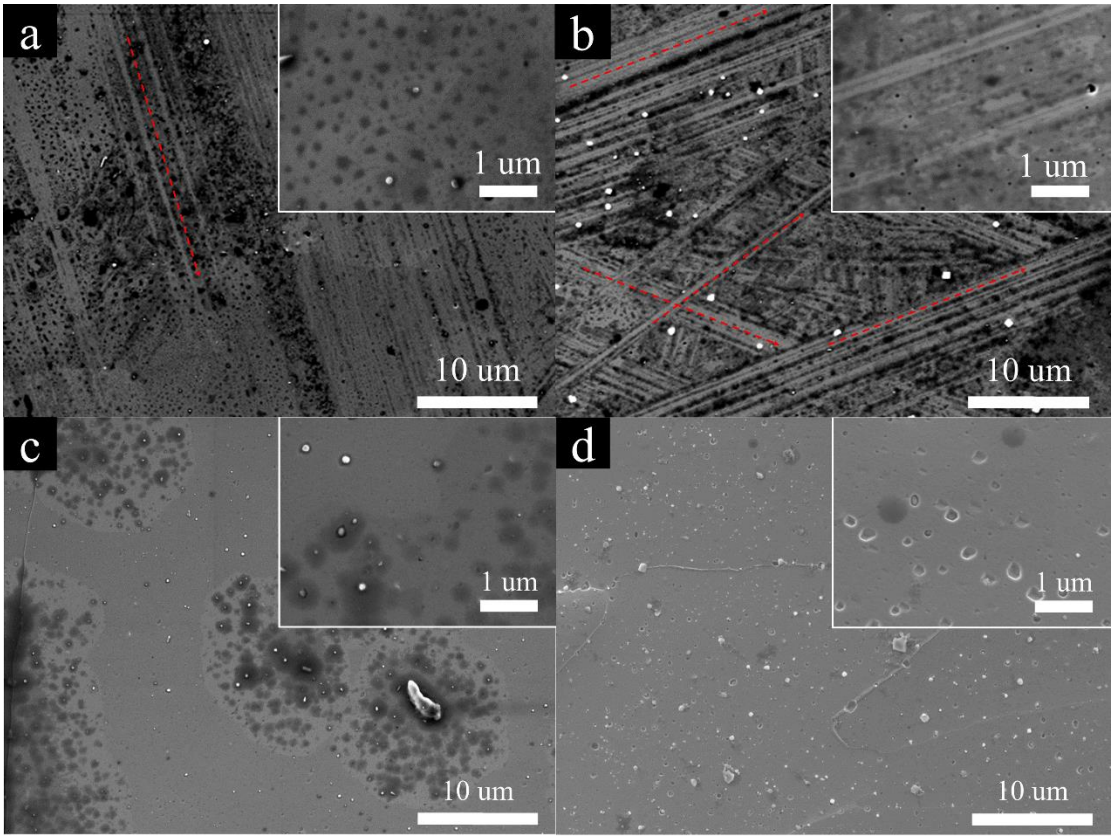

Figure 62 SEM morphologies of the 316L SS polished with (a) A2 electrolyte, 0.25 A/cm^2; (b) A2 electrolyte, 1.5 A/cm^2; (c) 1M NaCl-EG-10% Ethanol, 0.25 A/cm^2; and (d) 1M NaCl-EG-10% Ethanol, 1.5 A/cm^2.

5.3.3 Current density on surface roughness

Figure 63 (a) and (b) showed the surface roughness after polishing with the two electrolytes. Since the polishing effect of the electrolytes was related to the initial surface conditions, the initial surface roughness values were normalised for the three types of surfaces. The surface roughness polished with the electrolyte A2 appeared to increase with higher current density, while the surface roughness polished with NaCl-EG-ethanol electrolyte decreased. This trend was most evident in the *Rsa* values. This was because, a brown product would generate on the anode surface and hinder the diffusion process in the NaCl-EG-Ethanol, which deteriorates the polishing effect[38]. Han et al found that the brown product was mainly composed of Cl, O, Fe and Na elements and speculated that it might be $[Fe(C_2O_4)(OH)(OH_2)]_n \cdot 0.3nH_2O$, proposing that the addition of ethanol could improve the solubilities of the ions contained in the brown product and decrease the adherent ability[38]. In addition, they also found that the small current density peak on the polarisation curve, as shown in Figure 55 (b) was mainly caused by the brown product, which disappeared at a high stirrer speed[38]. The oscillation under the high current density might have a similar function as the stirring to destroy the brown product, and therefore, the roughness after polishing decreased with the increased current density although some side effects happened during the process. On the contrary, no obstructing layer formed when polishing with A2 electrolyte, while the current became more unstable with the increased current density, leading to a bad polishing effect.

In addition, because of the different polishing behaviours under the different current densities such as local heating, current density distribution, viscous layer uniformity, etc., polished surfaces will have different textures such as large waviness and small pitting etc., resulting in different roughness values[60,269]. As the amplitude and wavelength of defects (residual peaks, holes, pitting, etc.) were far smaller than the waviness, the defects would not have an apparent impact on the measured and waviness roughness values. For example, the roughness difference and proportion for the primary surfaces were 2.52 µm, 4.74 µm, 42.4 %, and 46.5 % (vs. max roughness value), respectively. Regarding the residual surfaces, although the difference in the roughness reduction only reached 0.34 µm and 0.86 µm, the proportion can reach 64.2 % and 55.8 %. Additionally, the residual surface roughness after polishing had an average reduction of more than 90 %, meaning that most granular features have been removed, whilst conversely, the surface roughness of the waviness was only 40 % – 70 % lower than the unpolished surface. Finally, the primary surface roughness was reduced by 50 % – 80 %. The corresponding roughness values are shown in Figure 58 to Figure 61, *Rsa* values can be reduced to approximately 1 µm or below, while *Wsa* values can only be reduced to approximately 3 µm or above which also limited the *Psa* values. The difference between *Wsa* and *Psa* values was considerable on the initial surface, which however became somewhat

smaller as the polishing time progressed. This is because the surface feature became long wave-dominated and the difference in current density distribution between the peak and valley regions became smaller as the polishing time progressed.

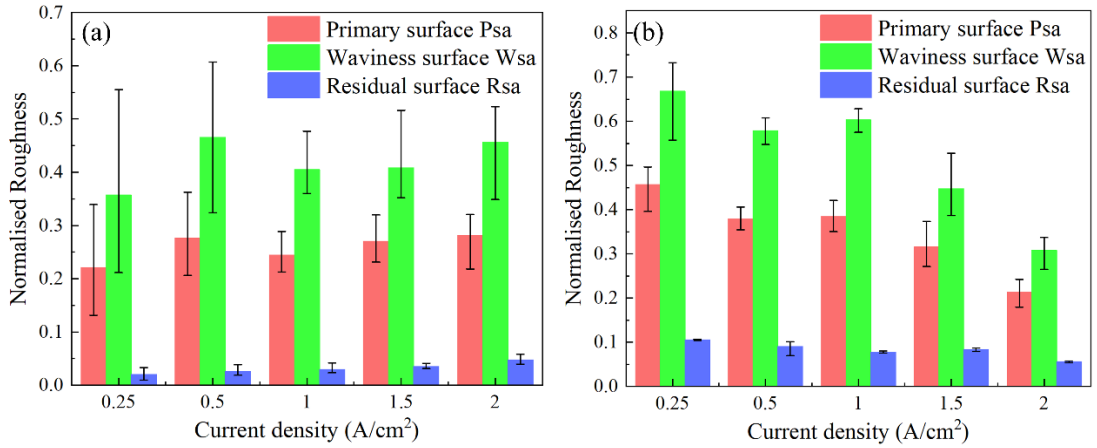

Figure 63 Normalised surface roughness of the 316L SS polished with the (a) A2 electrolyte and (b) 1M NaCl-EG-10% Ethanol electrolyte under different current densities.

5.3.4 Dimensional and geometric accuracy analysis

Figure 64 (a) and (b) show the materials removal weight and the thickness reduction for the EP process with the A2 and the NaCl-EG-ethanol electrolyte at the current densities of 0.25 – 2.0 A/cm^2. Regarding the A2 electrolyte, the total weight of the material being removed remained similar as the current density increased, meaning that no obvious reduction in the current efficiency was observed. However, the roughness values shown in Figure 63 (a) increased and the average reduction in thickness decreased. This was because the current density distribution became non-uniform and unstable as the current density increased, resulting in a rough surface with significant material removal weight in the edge region. Regarding the NaCl-EG-Ethanol electrolyte, the total materials removal weight decreased with the increasing current density, reaching a minimum of 98.2 mg at the current density of 1.5 A/cm^2. Both the weight and thickness reductions decreased with the current density and reached the minimum values at the current density of 1.5 A/cm^2, which was attributed to the reduction in materials removal weight and depth at the edge region. In this case, the removal of the reduced material can be divided into two portions: the normal removal of the surface and the depth of the edge regions, which can be estimated through equations *(22)* and *(23)* based on the total weight and height removal.

$$m_{normal} = \rho\pi r^2 h_{reduction} \quad (22)$$

$$m_{depth} = m_{reduction} - m_{normal} \quad (23)$$

where the m_{normal}, m_{depth} and $m_{reduction}$ are the material removal weight from the part above the flat polished surface, the edge region, and the total material removal weight, ρ is the density of 316L SS which is 7.93 g⁄cm^3, r is the diameter of the polishing region, and $h_{reduction}$ is the thickness reduction of the flat polished region. The calculated results are shown in Table 23. The normal materials removal in the central region decreased with the increasing current density, while the edge region showed the opposite trend, implying an improvement in the dimensional accuracy but worse geometric accuracy at the high current densities. The increment in materials removal weight and thickness reduction at 2.0 A/cm^2 may be due to the localised overheating of the sample surface. In addition, although these two indices were relatively higher for the NaCl-EG-ethanol polished samples at low current densities, the roughness values *Psa*, *Wsa*, and *Rsa* were higher. This could be explained by the erosive effect of inert particles from the sample surface, the extent of which decreased as the polishing time decreased.

Table 23 Materials removal weight and the height changes in the one-step EP process

Electrolytes	i (A/cm^2)	$m_{reduction}$ [mg]	m_{center} [mg]	m_{edge} [mg]
A2 electrolyte	0.25	115.1 ± (17.7, 18.9)	82.5 ± (13.3, 23.2)	32.7 ± (8.7, 14.1)
	0.5	135.0 ± (12.2, 20.6)	73.5 ± (12.1, 22.5)	61.5 ± (5.9, 13.4)
	1.0	121.9 ± (22.7, 20.9)	65.0 ± (12.5, 21.4)	56.9 ± (20.3, 14.4)
	1.5	118.2 ± (17.0, 31.8)	62.1 ± (13.5, 15.6)	56.2 ± (6.0, 20.5)
	2.0	120.9 ± (13.5, 19.6)	70.1 ± (11.2, 9.1)	50.8 ± (4.3, 17.2)
NaCl-EG-ethanol	0.25	122.4 ± (2.8, 2.2)	85.0 ± (1.6, 3.0)	37.4 ± (1.4, 2.7)
	0.5	123.2 ± (0.8, 1.0)	70.5 ± (8.6, 4.3)	52.6 ± (3.3, 2.9)
	1.0	111.3 ± (4.7, 6.2)	56.5 ± (6.6, 3.7)	54.8 ± (3.4, 3.7)
	1.5	98.2 ± (2.7, 3.4)	42 ± (6.4, 3.4)	56.5 ± (4.6, 5.6)
	2.0	103.0 ± (2.4, 1.6)	54.8 ± (1.2, 1.1)	48.2 ± (2.8, 1.5)

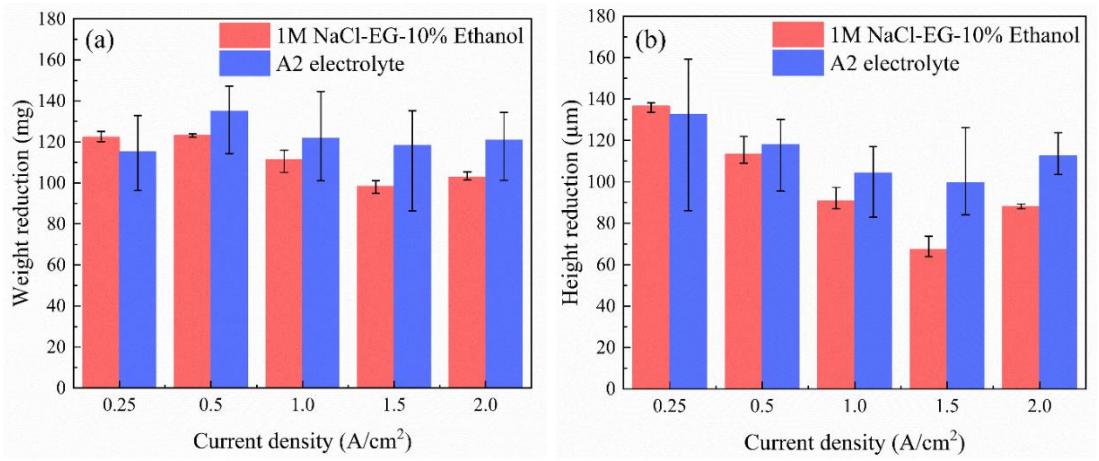

Figure 64 (a) Weight and (b) height reduction of the 316L SS polished with the A2 and 1M NaCl-EG-10% Ethanol electrolyte under different current densities

5.4 Electrochemical Polishing TC4

5.4.1 Polishing duration determination

Figure 65 shows the primary roughness changes with the polishing time for polishing TC4 in the EP systems with the electrolytes of 65 % and 85 % H_3PO_4, 1M NaCl-EG-10% Ethanol, and commercial A2. The roughness values of the TC4 remained unchanged or had little reduction after 360 s polishing, indicating that the electrolyte cannot provide a good polishing effect at the transpassive region. The roughness values reduced from 9.5 μm to approximately 3.5 μm and 3 μm, respectively, using the electrolytes 1M NaCl-EG-Ethanol and commercial A2 when being polished for 600 s, and then increased with polishing time. Therefore, the best polishing duration should be 600 s when the current density was 1 A/cm^2.

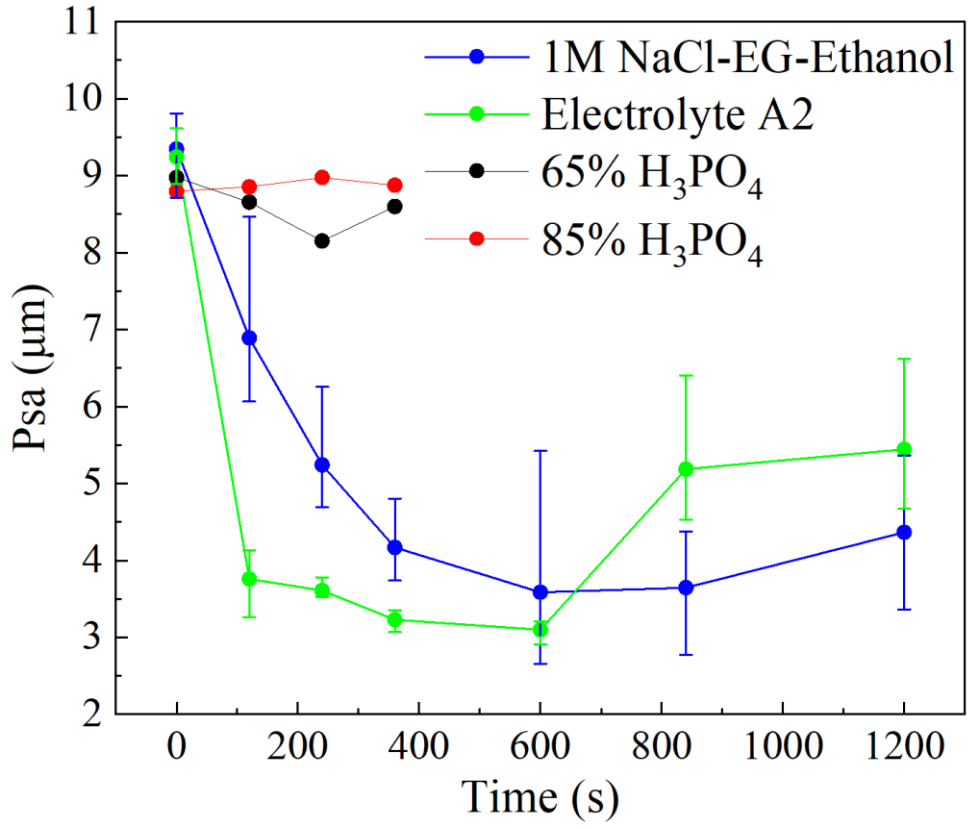

Figure 65 Roughness changes with the EP duration in the systems for polishing TC4 with the four types of electrolytes.

5.4.2 Surface topography analysis

Figure 66 and Figure 67 show the three types of polished surface topographies of TC4 at the current densities from 0.25 to 2.0 A/cm^2 polished by the A2 electrolyte. The surfaces became quite rough after polishing at 0.25 A/cm^2, especially on the primary and residual surfaces, as shown in Figure 66 (a) and Figure 67 (f). Because the potentiostat has a maximum measuring potential of 20 V, it cannot give the potential and current density of the EP system, as shown in Figure 56 (b). However, according to Kim's work of polishing Ti in the NaCl-EG-Ethanol electrolytes, the polishing current density might be higher than 0.3 A/cm^2 [56]. Therefore, the low current density and the stable oxide layer on the TC4 surface were assumed as the main reasons for the poor polishing effect. With the increased current densities, the surfaces became smoother and reached the best at 1.0 A/cm^2 for the primary and waviness surface while at 1.5 A/cm^2 for the residual surfaces, and then increased again. The evolution of the waviness surfaces was similar to the 316L SS in that the peak regions were flattened, and short waves were connected to form long waves. However, many micro particle-like features appeared on the residual surface polished under the current densities of 1.0 - 2.0 A/cm^2 and the features became more evident under the higher current density. This might be because of

the generation of the gas bubbles on the anode surface which functioned as agitation for the viscous layer, leading to the un-uniform distribution of the current density.

Compared to the surfaces of 316L SS shown in Figure 58 and Figure 59, the TC4 did not have pores on the surfaces after polishing. Since the formation and growth of the pores depend on the acidic environment and release of the broken bubble tunnelling effect, a stable oxide layer could protect the TC4 surface and raise the requirement of the polishing current density [45,176,197]. Therefore, at the same current density, the broken bubble tunnelling effect in the EP system of TC4 might be weaker than in the EP system of 316L SS. A large amount of small gas bubbles are generated in the viscous layer while most of them cannot grow and move to the bulk electrolytes. Therefore, the pores would be quite small even if they were generated. Additionally, a large amount of small gas bubbles would influence the distribution of the current density, leading to rough surfaces.

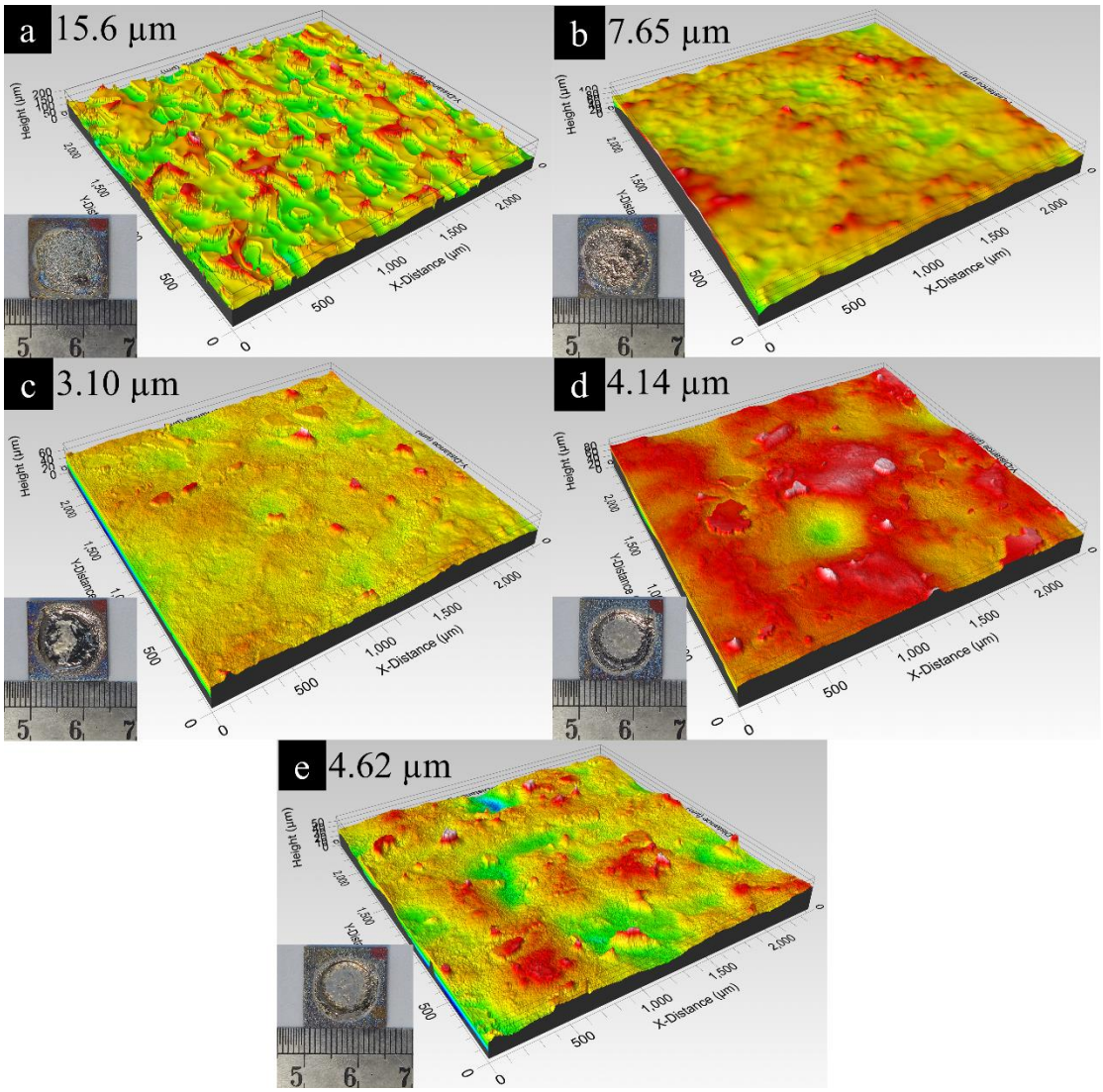

Figure 66 Physical photos and topographies of the primary surfaces of the TC4 polished with the A2 electrolyte at the (a) 0.25, (b) 0.5, (c) 1.0, (d) 1.5 and (e) 2.0 A/cm^2 current densities.

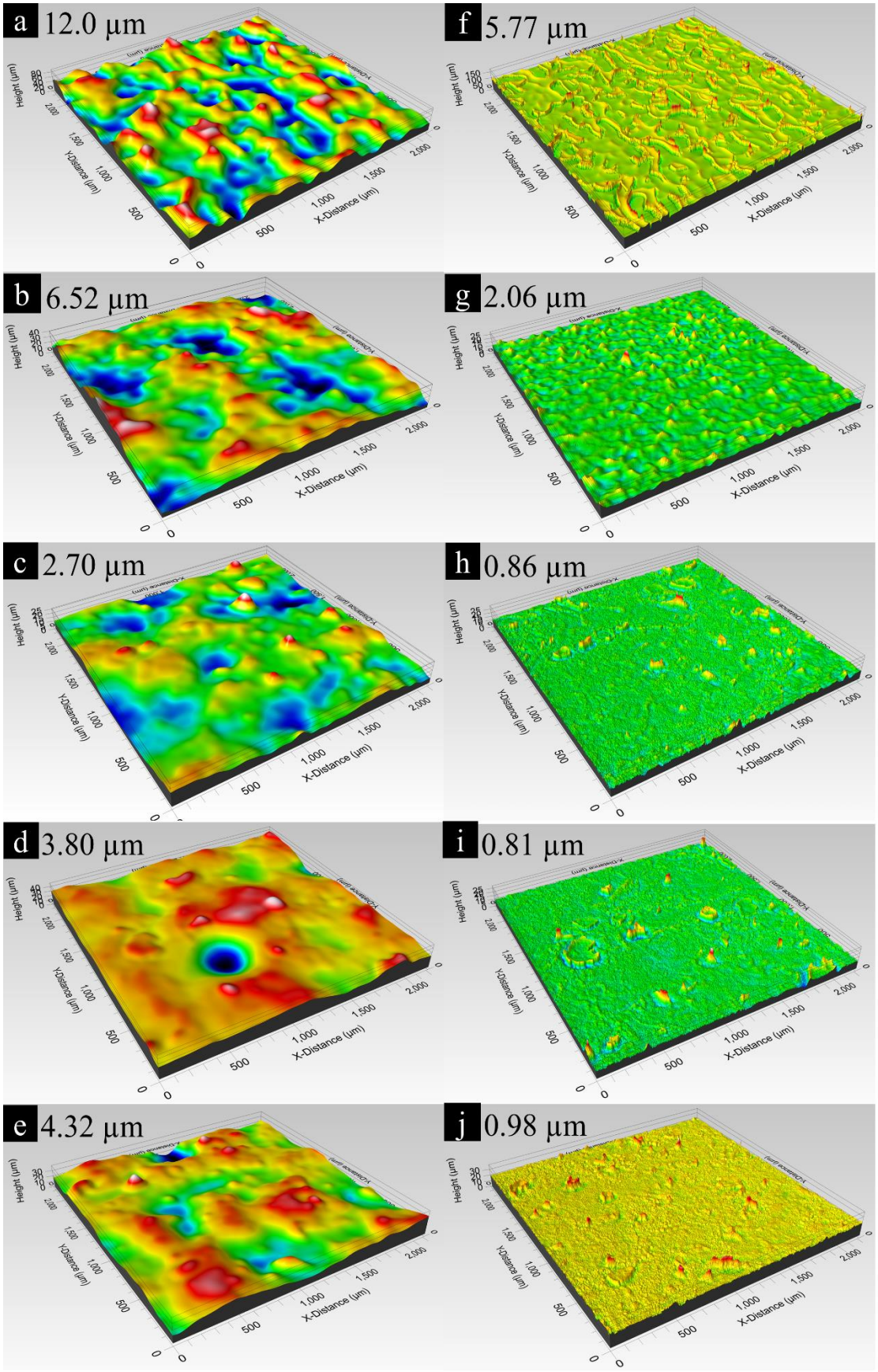

Figure 67 Topographies of the (a-e) waviness and (f-j)) residual surfaces of the TC4 after polishing with the A2 electrolyte at the (a-e) (f-j) 0.25 - 2.0 A/cm^2 current densities.

Figure 68 and Figure 69 showed the surface topographies of TC4 polished with the 1M NaCl-EG-10% ethanol electrolyte at the current densities from 0.25 to 2.0 A/cm^2. The surfaces polished at the 0.25 A/cm^2 still showed micro-roughness features whose size ranged from tens of microns. The micro-features should be residual powder particles that remained because of the high viscosity of the viscous layer and low polishing efficiency. The particles disappeared with the increased current density and the surface became smoother while pores started emerging on the anode surface. According to the polarisation curve shown in Figure 56, the current density for polishing TC4 in the 1M NaCl-EG-10% Ethanol electrolyte would be low because of the high viscosity of the electrolyte. Therefore, the pores will generate and grow when the viscous layer is broken under the high current density. Additionally, contrary to the results of polishing 316L SS, the 1M NaCl-EG-10% Ethanol electrolyte showed a better polishing effect than the A2 electrolytes.

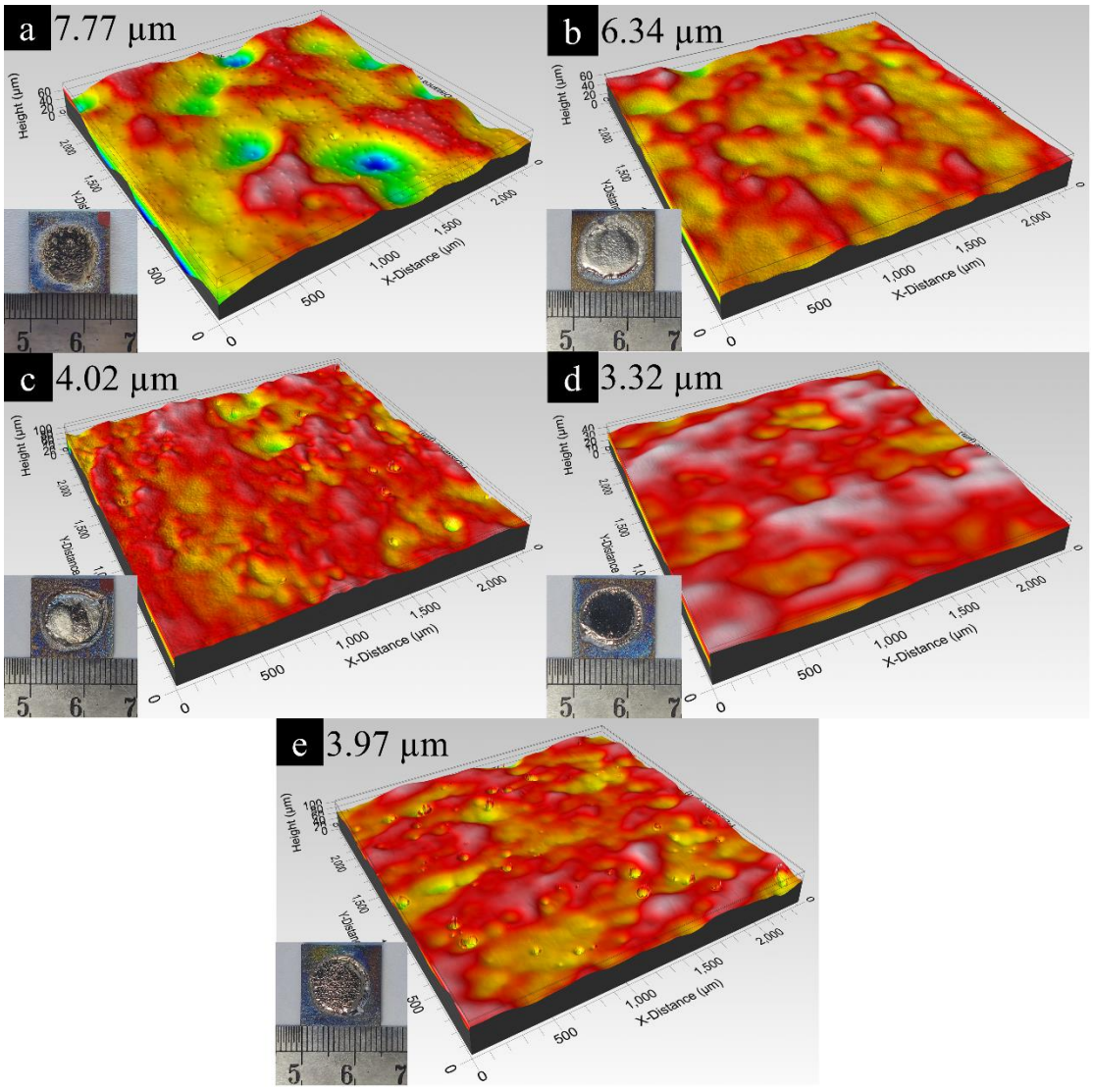

Figure 68 Physical photos and topographies of the primary surfaces of the TC4 polished with the 1M NaCl-EG-10% Ethanol at the (a) 0.25, (b) 0.5, (c) 1.0, (d) 1.5 and (e) 2.0 A/cm^2 current densities.

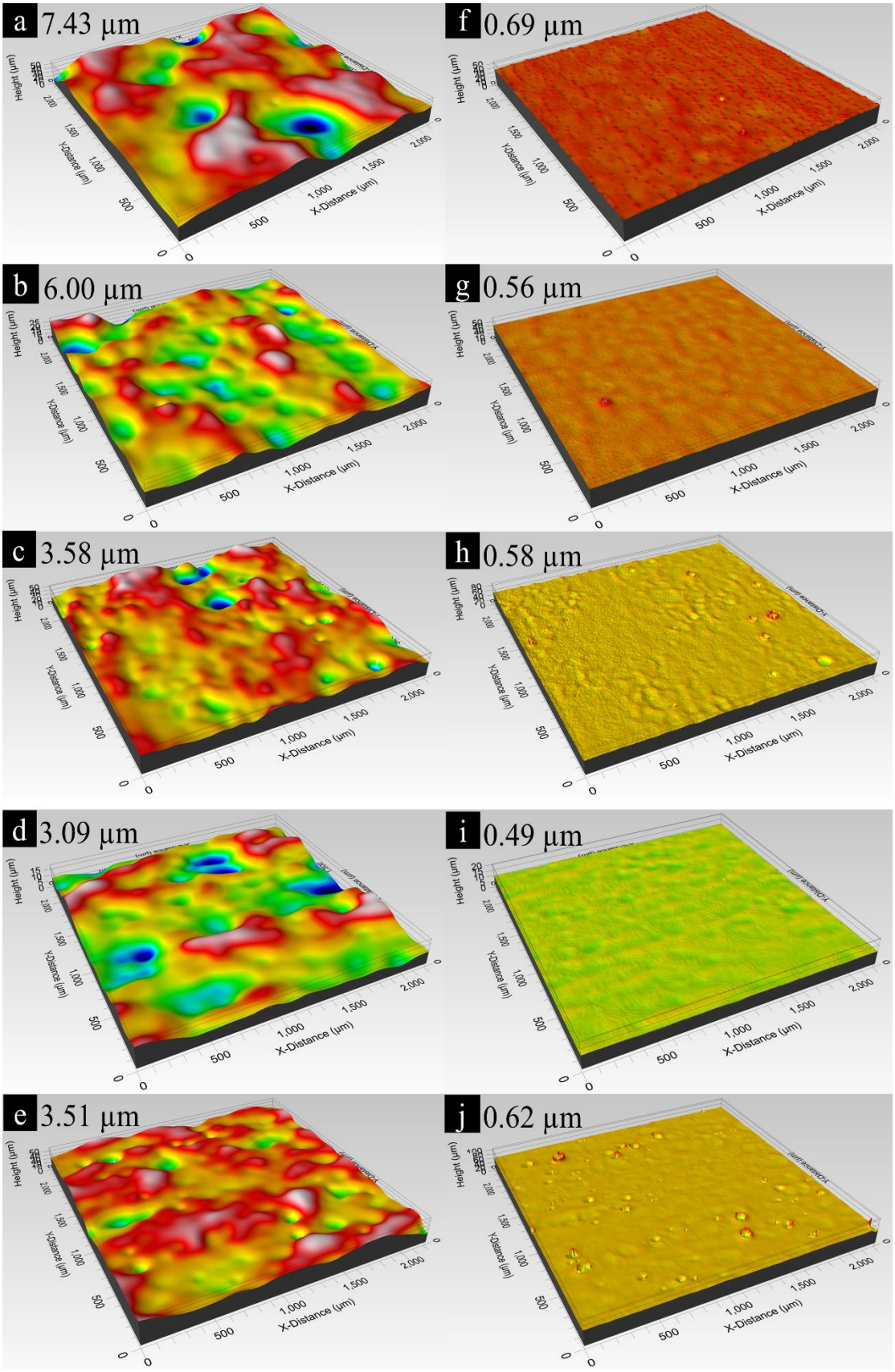

Figure 69 Topographies of the (a-e) waviness and (f-j)) residual surfaces of the TC4 after polishing with the 1M NaCl-EG-10% Ethanol at the (a-e) (f-j) 0.25 - 2.0 A/cm^2 current densities.

Figure 70 (a) and (b) show the morphologies of the TC4 after polishing with the A2 electrolyte under the current densities of 1.0 and 1.5 A/cm^2. The surfaces have many irregular raised regions in Figure 70 (a) and broken powder particles in Figure 70 (b), which also reflect the serious effect of the agitation from the gas bubble and the non-uniform distribution of the current density.

Figure 70 (c) and (d) show the morphologies of the TC4 after polishing with the 1M NaCl-EG-10% Ethanol electrolyte under the current densities of 1.0 and 1.5 A/cm^2. Results for the sample with 1.0 A/cm^2 showed a flat surface with several wrinkles features and some unpolished elements. The wrinkle features disappeared with 1.5 A/cm^2 while more small unpolished elements emerged on the surface, indicating that the polishing effect was improved.

Compared to the SEM morphologies of 316L SS shown in Figure 62, the TC4 polished with A2 electrolyte has many partially melted powders and broken powders adhered on the surfaces, especially under the 1.5 A/cm^2 current density. On the contrary, the 1M NaCl-EG-10% Ethanol electrolyte had a better polishing effect on the TC4 surface than the 316L SS as smooth surfaces without pores and small particles can be provided.

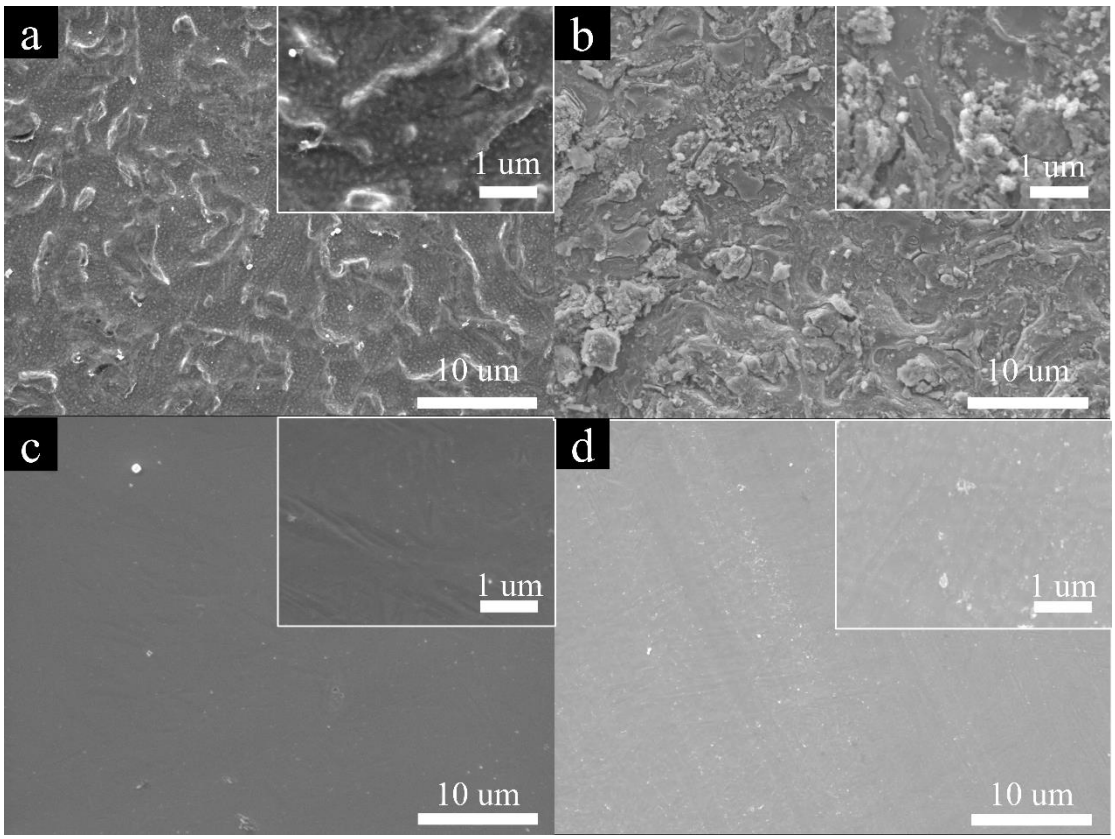

Figure 70 SEM morphologies of the TC4 polished with (a) A2 electrolyte, 1.0 A/cm^2; (b) A2 electrolyte, 1.5 A/cm^2; (c) 1M NaCl-EG-10% Ethanol, 1.0 A/cm^2; and (d) 1M NaCl-EG-10% Ethanol, 1.5 A/cm^2.

5.4.3 Current density on surface roughness

Figure 71 (a) and (b) showed the normalised surface roughness after polishing with the two electrolytes. The surface roughness polished with the electrolyte A2 at 0.25 A/cm^2 current density became larger than the initial surface because of the serious etching effect. Then the values appeared to decrease with higher current density and reach the minimum at 1.0 A/cm^2 for the primary and waviness surfaces and 1.5 A/cm^2 for the residual surface. The roughness would increase again when the current density increased to 2.0 A/cm^2. The samples polished with 1M NaCl-EG-10% Ethanol electrolyte showed a similar trend in that the roughness decreased with the current density and reached the minimum at 1.5 A/cm^2 and then increased again at 2.0 A/cm^2. This was because the polishing process was not happening at the low current density due to the highly dense oxide layer on the TC4 surface. With the increased current density, the oxide layer was destroyed, and the viscous layer could be formed on the surface for the polishing process. Therefore, the samples polished with the two electrolytes showed a reduction in roughness with the increased current density. Conversely, because the current density became unstable and the viscous layer might be broken under the high current density such as 2.0 A/cm^2, the roughness values increased again. Noticeably, the current density of 1.0 A/cm^2 or 1.5 A/cm^2 might be above the limiting current density plateau region because the thickness of the viscous layer would increase with the potential at the limiting current density plateau region, leading to a small current density. For example, the current density for polishing Ti-6Al-4V in 0.1 - 0.5 M/L NaCl-EG electrolyte was only 0.5 A/cm^2 [27].

Compared to the 316L SS, the TC4 has a lower roughness after polishing on the primary and waviness surfaces while a higher value on the residual surface roughness. However, the roughness reduction rates of the TC4 were higher than that of the 316L SS because the TC4 had a better initial surface condition. For example, when being polished with the A2 electrolyte, the maximum roughness reduction proportion for the 316L SS were 79.64 ± (7.22, 13.59) %, 67.11 ± (11.74, 22.64) % and 98.16 ± (0.84, 1.49) % while only 66.47 ± (7.94, 9.01) %, 50.97 ± (14.22, 11.35) % and 87.95 ± (4.85, 4.27) % for TC4, respectively, for the primary, waviness and residual surfaces. Similarly, when being polished with the 1M NaCl-EG-10% Ethanol electrolyte, the roughness reduction proportion were 78.60 ± (3.45, 2.81) %, 68.94 ± (4.62, 2.64) %, and 94.41 ± (2.26, 1.12) % for the 316L SS while only 66.56 ± (14.34, 10.64) %, 44.21 ± (21.66, 21.01) %, and 93.24 ± (4.46, 6.02) % for TC4, respectively. Noticeably, the A2 electrolyte had a better polishing effect than the NaCl-EG-Ethanol electrolyte on the primary and residual surfaces for the 316L SS and a worse polishing effect on the waviness surface, while the result was contrary to the TC4.

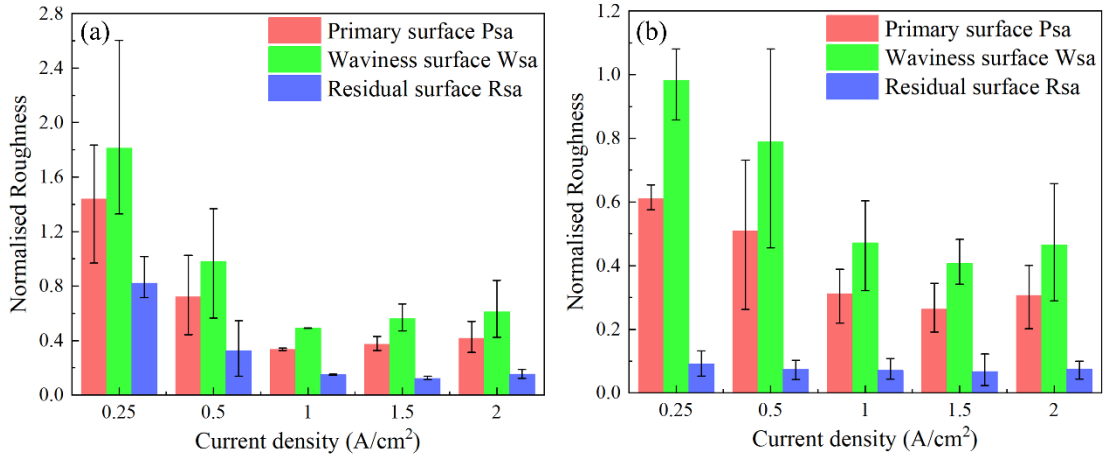

Figure 71 Normalised surface roughness of the TC4 polished with the (a) A2 electrolyte and (b) 1M NaCl-EG-10% Ethanol electrolyte under different current densities.

5.4.4 Dimensional and geometric accuracy analysis

Figure 72 (a) and (b) showed the materials removal weight and the thickness reduction for the EP process with the A2 and the NaCl-EG-ethanol electrolyte at the current densities of 0.25 – 2.0 A/cm^2. Regarding the A2 electrolyte, the total weight of the material being removed was small at 0.25 A/cm^2 because no polishing process happened. Then the weight loss reduced with the increased current density because more side reactions happened and there was more heat generation. However, the height reduction increased sharply with the increased current density, as shown in Figure 72 (b). Noticeably, the height reduction was not the average value but the values at the centre region because a large hole feature was formed and it was meaningless to measure the average height reduction, as shown in Figure 73. The profile feature of TC4 polished with A2 electrolyte was different to the profiles of 316L SS and the TC4 polished with the NaCl-EG-Ethanol electrolyte. Regarding the NaCl-EG-Ethanol electrolyte, the total materials removal weight increased with the increasing current density, reaching a maximum of 65.5 ± (1.40, 0.90) mg at the current density of 2.0 A/cm^2, compared to 127.7 ± (3.23, 6.37) mg for the surface polished with A2 electrolyte. Additionally, although the height reduction also increased with the increased current density, they were much smaller than the surfaces polished with the A2 electrolyte. Therefore, the NaCl-EG-Ethanol electrolyte had a higher polishing efficiency than the A2 electrolyte.

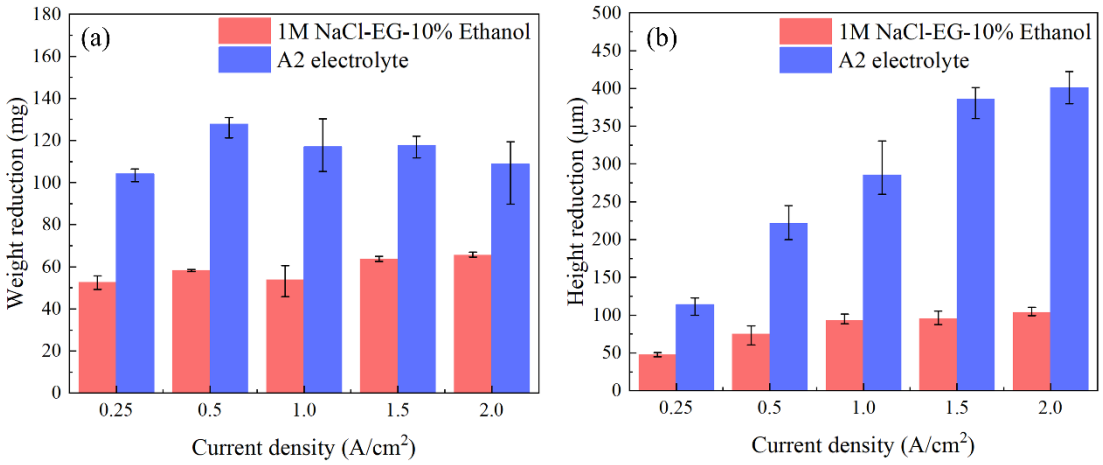

Figure 72 (a) Weight and (b) height reduction of the TC4 polished with the A2 and 1M NaCl-EG-10% Ethanol electrolyte under different current densities.

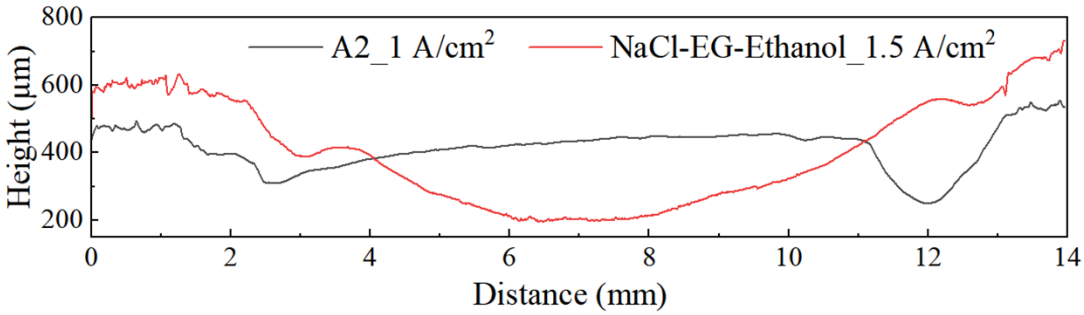

Figure 73 Line profiles of the TC4 polished with the A2 and NaCl-EG-Ethanol electrolytes.

5.5 Summary

Four types of electrolytes including 65 % H3PO4, 85 % H3PO4, commercial A2 and 1M NaCl-EG-Ethanol electrolytes were introduced into the experiment. The roughness changes with the polishing duration for the four electrolytes and the influence of current density on the EP process of L-PBF 316 L stainless steel and TC4 components in the A2 and NaCl-EG-Ethanol electrolytes were investigated. The following conclusions can be drawn:

(1) The phosphoric acid cannot be used to polish rough L-PBF 316L stainless and TC4 with the current densities at the transpassive region because of the low current efficiency and high-water content. The surface roughness increased with the polishing duration under the 1A/cm^2 current density.

(2) The A2 electrolyte has a better polishing effect than the NaCl-EG-Ethanol electrolyte on the 316L SS while it was contrary to the TC4. The optimised primary surface roughness could reach 3.42 μm, 5.46 μm, 3.10 μm, and 3.32 μm for 316L SS and TC4 polished with the A2

and NaCl-EG-Ethanol electrolytes, the corresponding reduction rates were 79.64 %, 78.60 %, 66.47 %, and 68.70 % respectively.

(3) The total material removal amount for 316L SS polished with the electrolyte A2 remained consistent with the current density, while decreased for those polished with the NaCl-EG-ethanol electrolyte due to increased side chemical reactions at higher current densities. The NaCl-EG-ethanol electrolyte has a higher current efficiency for polishing TC4 than the commercial electrolyte because the materials removal weight was only approximately half of that polished with the A2 electrolyte.

(4) The 316L SS had similar profile features after being polished with the electrolytes and the material removal amount above the flat surface decreased with increasing current density while at the edges increased, which corresponded to variations in dimensional accuracy and shape. However, the profiles for polished TC4 are different in that the central region had the most height reduction when being polished by A2 electrolyte while maximum height reduction was at the edge for the surfaces polished by NaCl-EG-ethanol electrolyte.

Chapter 6 EP Optimisation and Prediction

A two-step EP method for polishing L-PBF 316L SS and TC4 components was proposed based on the previous results using the NaCl-EG-Ethanol and commercial A2 electrolytes. The influence of high current densities ranging between 250 – 2000 mA/cm^2 on the surface roughness, materials removal weight, and thickness reduction with various morphological characteristics was investigated. Six algorithms including the Adaptive Boosting algorithm, Random Forest, Multilayer Perceptron Regression, Ridge Regression, Support Vector Regression, and Classification and Regression Trees were introduced for training and predicting the results obtained from the one-step and two-step EP experiment.

6.1 Two-step EP Effect of 316L SS

Figure 74 and Figure 75 showed the topographies of the primary, waviness and residual surfaces of 316L SS after two-step polishing at different conditions. The optimal roughness can be reduced to 4.40 ± (0.57, 0.88) μm, 3.73 ± (0.15, 0.13) μm and 0.21 ± (0.02, 0.03) μm when the polishing duration of the A2 electrolyte dominated the EP process. When the polishing duration of the NaCl-EG-Ethanol electrolyte gradually dominated the EP process, the polishing effect became worse, as the sample S_{N3} showed. The worst roughness values after polishing were 7.64 ± (0.97, 0.86) μm, 6.88 ± (0.29, 0.29) μm and 0.58 ± (0.02, 0.02) μm. However, both surfaces of S_{N1} and S_{N3} became smooth without etching, pitting and scratches, as the SEM graphs shown in Figure 76.

Figure 77 showed the normalised surface roughness, weight and height reduction utilising the two-step method. The polishing effect deteriorated as the polishing proportion of the NaCl-

EG-ethanol electrolyte increased, while the weight and thickness reduction decreased. Similarly, the materials removal and thickness reduction values of the two-step EP process were in the middle of those obtained with the one-step EP process in the A2 electrolyte and NaCl-EG-Ethanol electrolytes.

Compared to the one-step EP process, the polishing effect of the two-step EP method was much better than the samples polished with the NaCl-EG-Ethanol electrolyte. The roughness after polishing could decrease to below 7.64 ± (0.97, 0.86) μm and even 4.40 ± (0.57, 0.88) μm (Figure 74) while most of the surface roughness was larger than 8 μm after one-step polishing with the NaCl-EG-Ethanol electrolyte (Figure 60). Although the polishing effect cannot be as good as the sample polished with the A2 electrolyte, the roughness showed little difference for the three types of surfaces, especially for the S_{N1} sample. For example, the primary, waviness and residual roughness of the 316L SS polished with the A2 electrolyte at 0.25 A/cm^2 for 56 mins were 3.97 ± (1.17, 0.62) μm, 3.71 ± (1.09, 0.64) μm, and 0.22 ± (0.09, 0.0.06) μm, while the values of the sample S_{N1} were 4.40 ± (0.57, 0.88) μm, 3.73 ± (0.15, 0.13) μm and 0.21 ± (0.02, 0.03) μm. The comparison of the normalised surface roughness and the weight loss of the 316L stainless steel after polishing with the one-step and two-step EP processes were shown in Figure 79. The surface roughness and weight loss of the S_{N1} were quite similar to the sample polished in the A2 electrolyte under 0.25 mA/cm^2. Moreover, the total polishing time was reduced from 56 min to 42.7 mins and the polishing time in the commercial A2 electrolyte was 16 mins less than the one-step EP process which benefited the environment.

In conclusion, although the two-step EP process of 316L process cannot provide a better polishing effect than the commercial A2 electrolyte, it can either reduce the usage of the perchloride acid or improve the polishing effect of the NaCl-EG-Ethanol electrolytes.

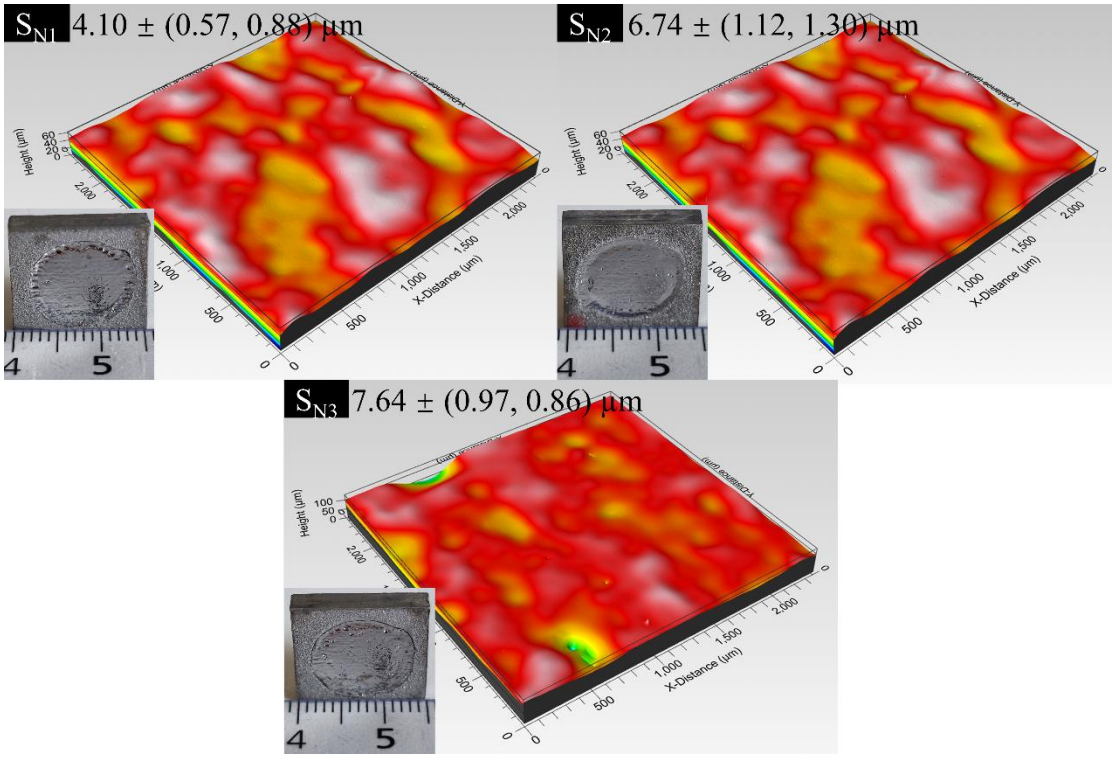

Figure 74 Physical photos, surface topographies and roughness values of the primary surfaces of the 316L SS polished at different conditions.

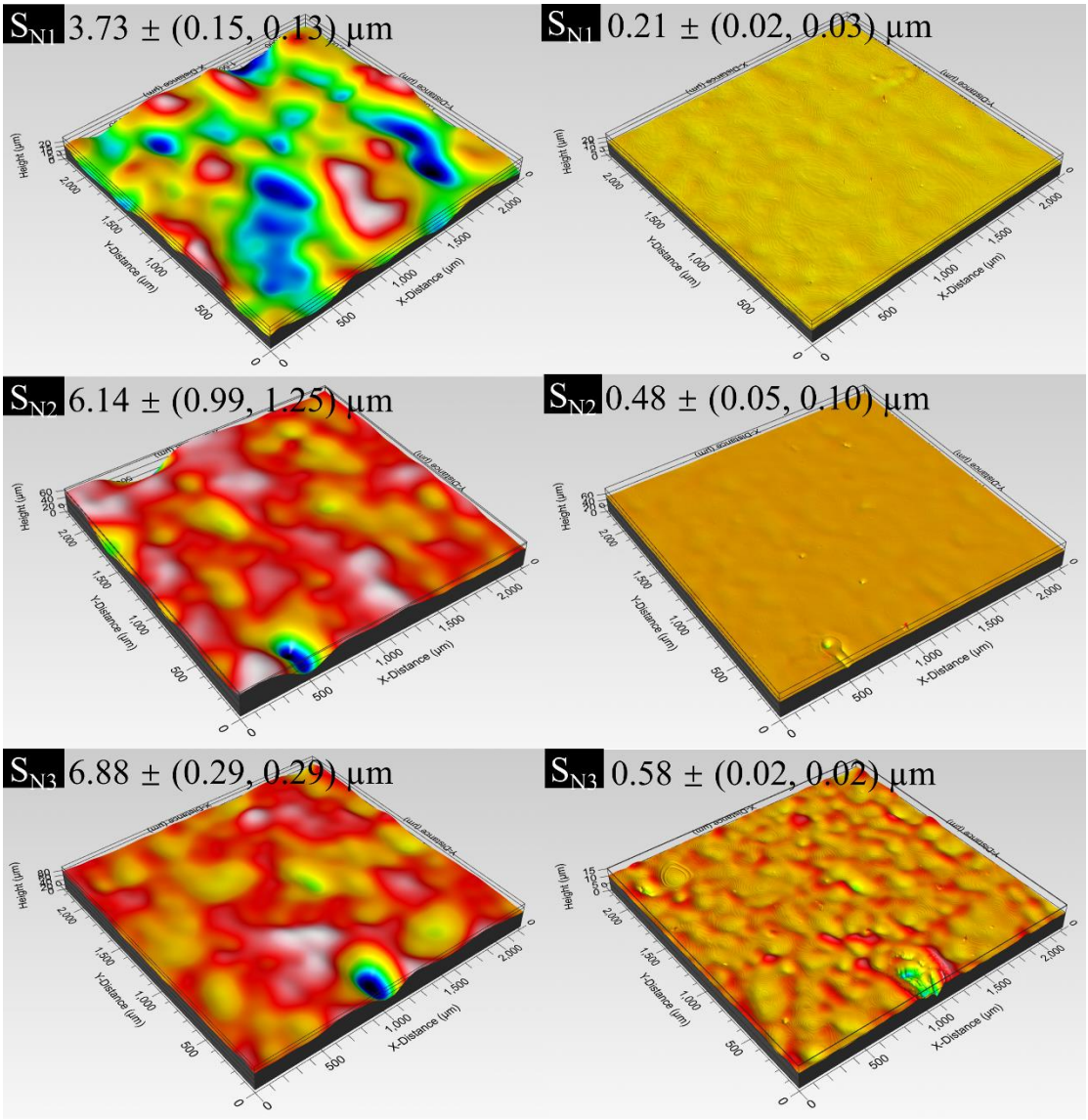

Figure 75 Surface topographies and roughness values of the (left) waviness and (right)) residual surfaces of the 316L SS after polishing at different conditions.

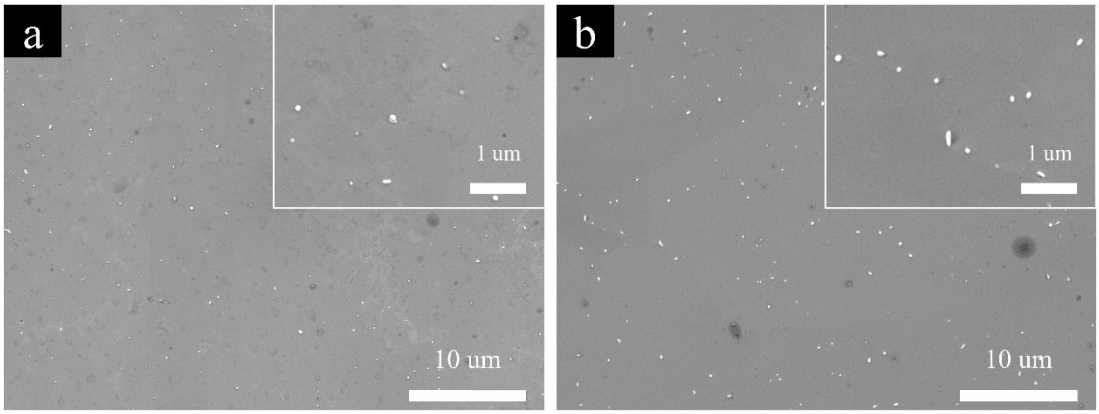

Figure 76 SEM morphologies of the 316L SS polished at different conditions (a: S_{N1} and b: S_{N3})

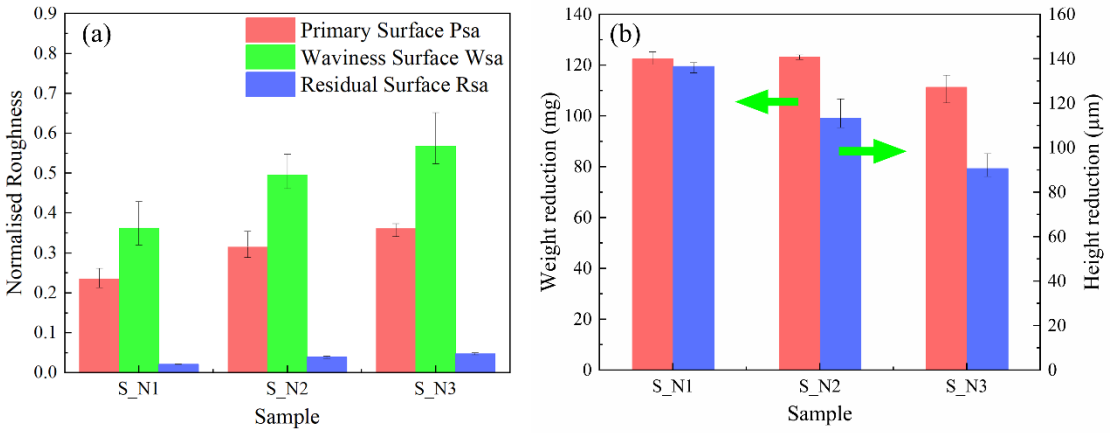

Figure 77 (a) Normalised surface roughness, (b) weight and height reduction of 316L SS polished with the two-step EP method.

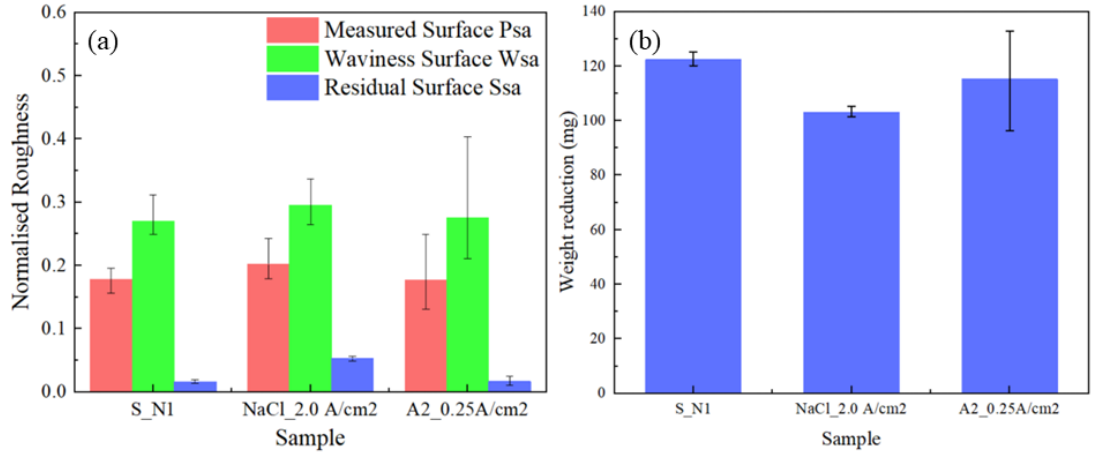

Figure 78 Comparison of the optimal (a) Normalised surface roughness, (b) weight and height reduction of 316L SS polished after polishing with the one-step and two-step EP method.

6.2 Two-step EP Effect of TC4

Figure 79 and Figure 80 show the topographies of the primary, waviness and residual surfaces of 316L SS after polishing at different conditions. Different to the 316L SS, the optimal roughness can be reduced to 2.72 ± (0.90, 0.74) μm, 2.51 ± (0.79, 0.61) μm and 0.29 ± (0.22, 0.18) μm when the polishing duration of the NaCl-EG-Ethanol electrolyte dominated the EP process. When the polishing duration of the A2 electrolyte gradually dominated the EP process, the polishing effect became worse, as the sample T_{N3} showed. The worst roughness values after polishing were 5.67 ± (0.95, 1.00) μm, 5.07 ± (0.69, 0.74) μm and 0.94 ± (0.80, 0.54) μm. However, both surfaces of S_{N1} and S_{N3} became smooth without etching, pitting and scratches, as the SEM graphs shown in Figure 81.

Figure 82 shows the normalised surface roughness, weight and height reduction of TC4 utilising the two-step method. The roughness reduction decreased as the polishing proportion of the A2 electrolyte increased, while the weight and thickness reduction decreased. Compared to the one-step EP process, the optimised roughness reduction in the two-step EP process was better while the values of materials removal weight and thickness reduction were in the middle of those polished in the one-step EP process. The mechanism was similar to the roughness changes in that the electrolytes have a much different influence on the material removal weight and thickness reduction for polishing TC4.

Compared to the one-step EP method, the two-step EP method for polishing TC4 provided a better polishing result than the one-step EP process, which is also different to the 316L SS. The minimum primary, waviness and residual surface roughness can reach 2.72 ± (0.91, 0.74) μm, 2.51 ± (0.79, 0.61) μm, and 0.29 ± (0.22, 0.18) μm, while the minimum values in the one-step EP process were only 3.1 ± (0.11, 0.19) μm, 2.7 ± (0.16, 0.20) μm, and 0.49 ± (0.35, 0.26) μm (Figure 66 (c), Figure 67 (c) and Figure 69 (i)). The roughness reduction rate for the primary, waviness and residual surface reached 70.8 ± (7.4, 11.5) %, 53 ± (11.2, 14.7) %, and 95 ± (3.1, 4.3) %. Figure 83 also showed that the optimal polishing effect of the two-step EP method was much better than the one-step EP method, especially on the residual surface although the weight loss in the EP process with NaCl-EG-Ethanol electrolyte was much lower. This might be because 1) the dissolved metals would be removed from the anode surface during the change of the electrolytes and therefore, the dissolved metals would not influence the polishing effect in the second step; 2) the two types of electrolytes had a comparative polishing effect for polishing TC4 while the commercial A2 electrolyte had a much better polishing effect than the NaCl-EG-Ethanol electrolyte on polishing 316L SS. Additionally, as the SEM graphs shown in Figure 70 and Figure 81, the surface polished with the A2 electrolyte had a large amount of micro unevenness (the broken particles on the surface) while the unevenness disappeared and smooth surfaces without scratches were presented in the two-step EP process.

In conclusion, the two-step EP process could improve the roughness reduction for polishing TC4 and present a smooth surface without pitting and scratches while the material removal weight and thickness reduction should be controlled appropriately.

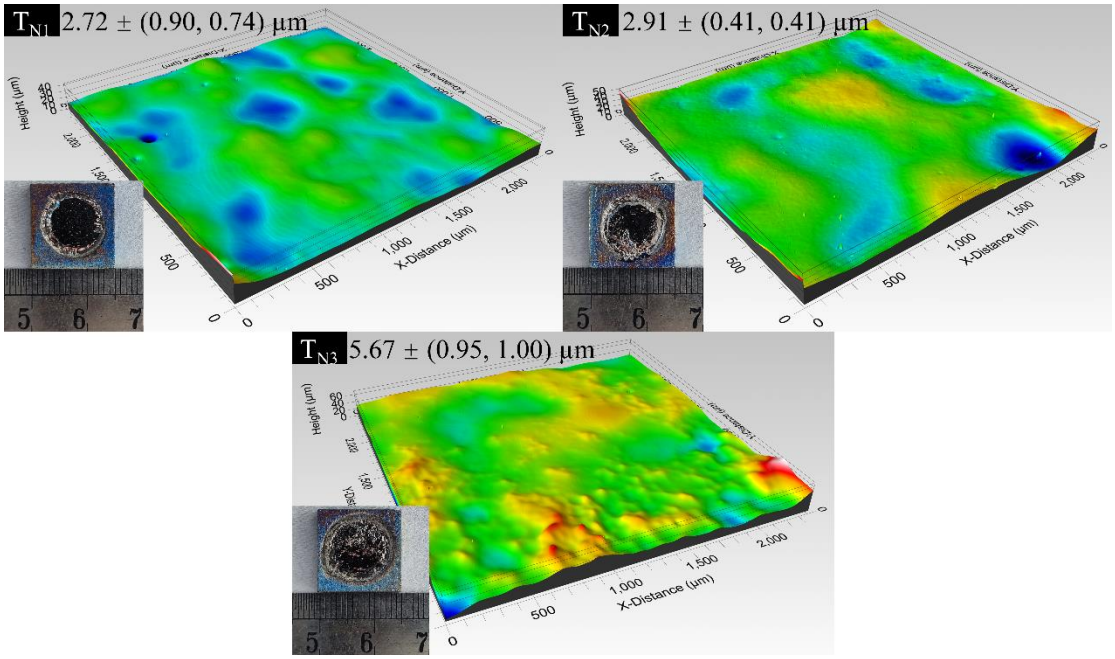

Figure 79 Physical photos, surface topographies and roughness values of the primary surfaces of the TC4 polished at different conditions.

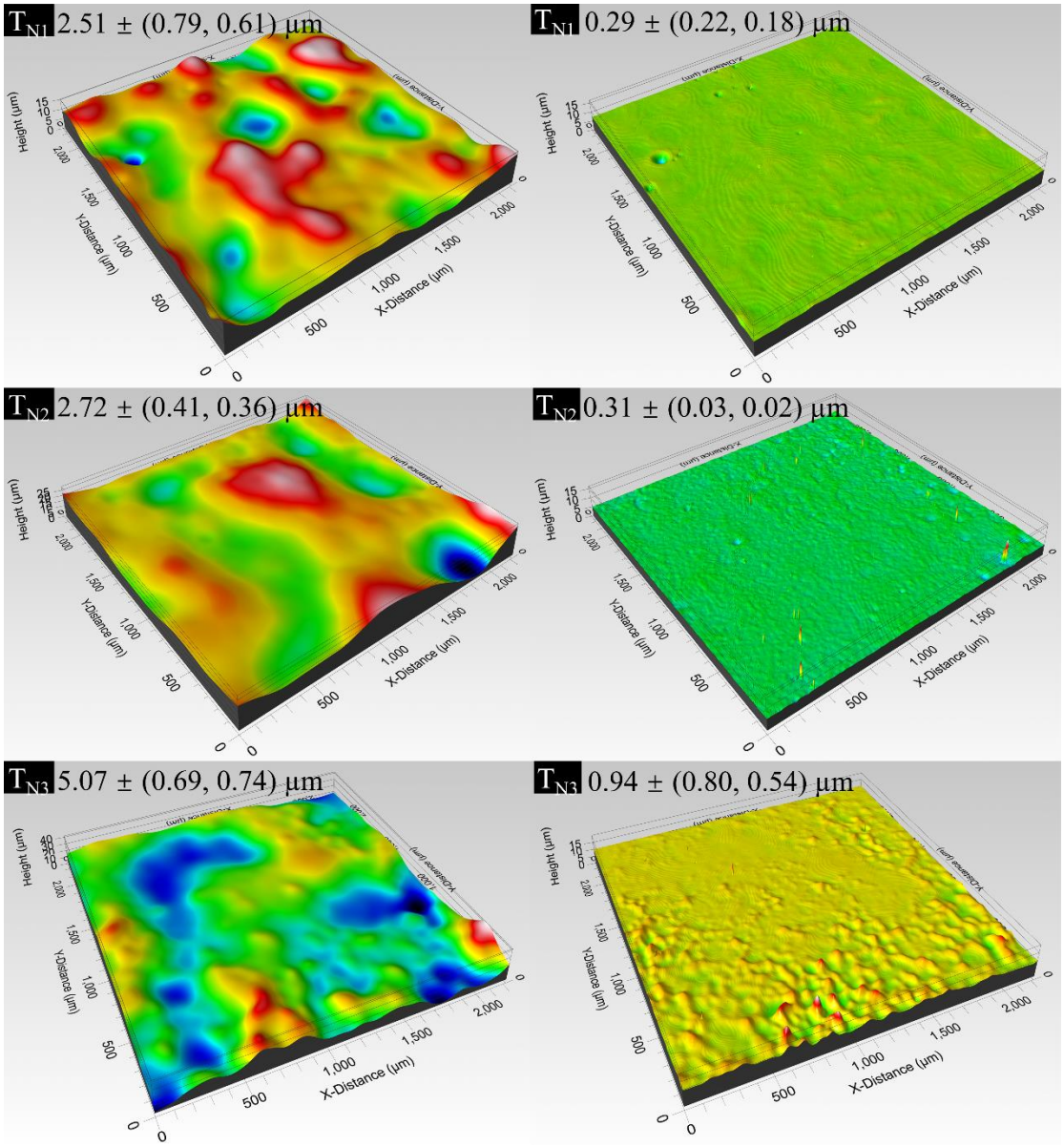

Figure 80 Surface topographies and roughness values of the (left) waviness and (right)) residual surfaces of the TC4 after polishing at different conditions.

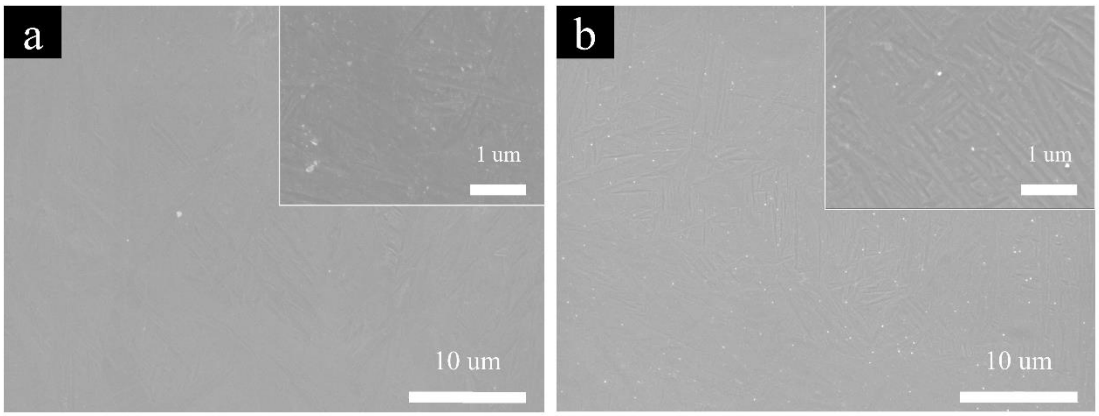

Figure 81 SEM morphologies of the 316L SS polished at different conditions (a: T_{N1} and b: T_{N3})

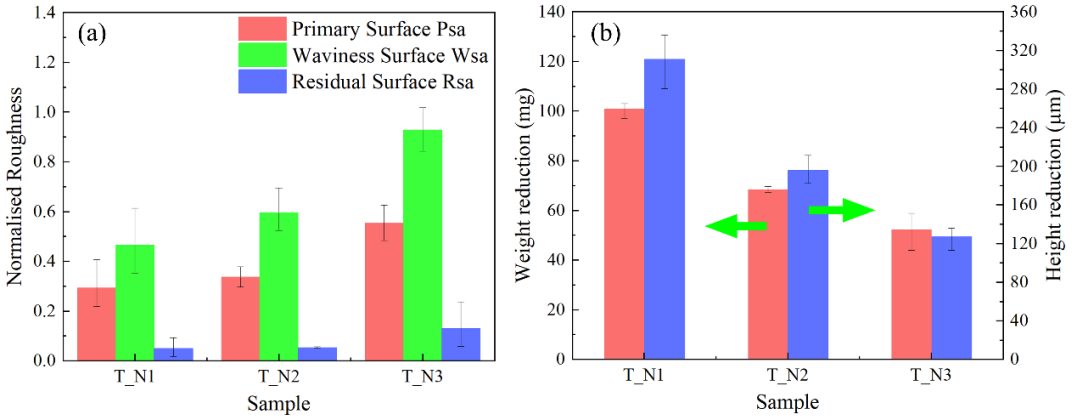

Figure 82 (a) Normalised surface roughness, (b) weight and height reduction of TC4 polished with the two-step EP method.

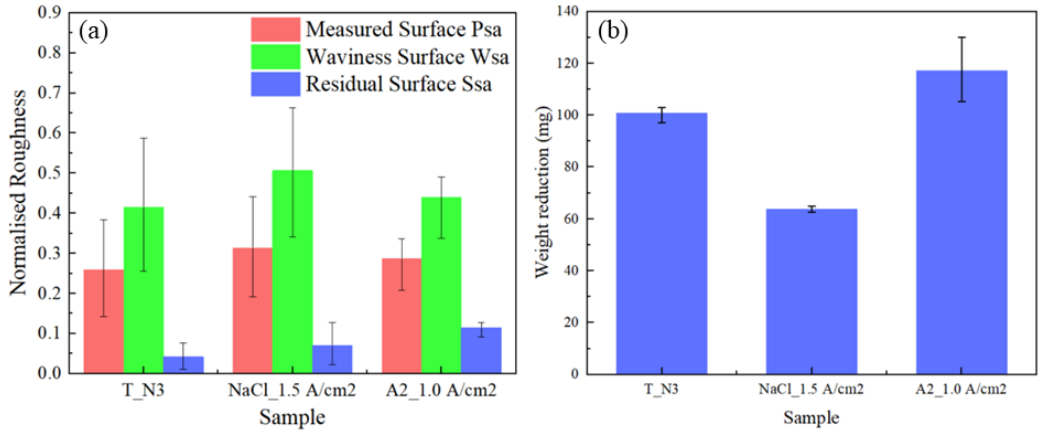

Figure 83 Comparison of the optimal (a) Normalised surface roughness, (b) weight and height reduction of TC4 polished after polishing with the one-step and two-step EP method.

6.3 Prediction Accuracy and Stability

Figure 84 shows one example of predictive surface roughness obtained by the algorithms. Ensemble, neural network, and decision tree-based algorithms could present better results while the predictive results obtained by regularisation-based methods have a large difference from the true values. The highest R^2 values could reach 0.89 and the lowest was 0.31. To avoid the deviation caused by the small scale of the dataset, 10 sets of R^2 values for the algorithms were presented in Figure 85 (a). The MLP have the best prediction accuracy and the R^2 values ranged between 0.73 and 0.92. Second is the RF method and the R^2 values ranged between 0.73 and 0.88. The worst was the RR method whose R^2 values only ranged between 0.27 and 0.47. Figure 85 (b) showed the mean values and the variance of the R^2. The MPL method had the highest prediction accuracy with the mean R^2 values of 0.85 while the variance ranked fifth, corresponding to 0.0039, which may be caused by the small amount of data (only 150 data) and less amount of data would increase the fluctuation of the prediction

results. Although the mean R^2 of the ensemble-based methods of AdaBoost and RF were lower than the MPL method, corresponding to 0.76 and 0.80, respectively, the variance of the R^2 was lower, corresponding to 0.0028 and 0.0017. Therefore, the AdaBoost and RF methods had better stability in predicting the dataset, particularly for the RF method which had the lowest variance values among the 6 algorithms. As the dataset had two properties: 1) the scale was quite small and 2) the dataset might contain some abnormal data caused by the experiment errors, the variance of R^2 of the CART method reached 0.0121, indicating that it cannot be used for predicting the dataset. Similarly, the RR and SVR cannot be used for prediction because of the low mean R^2 values, corresponding to 0.39 and 0.62.

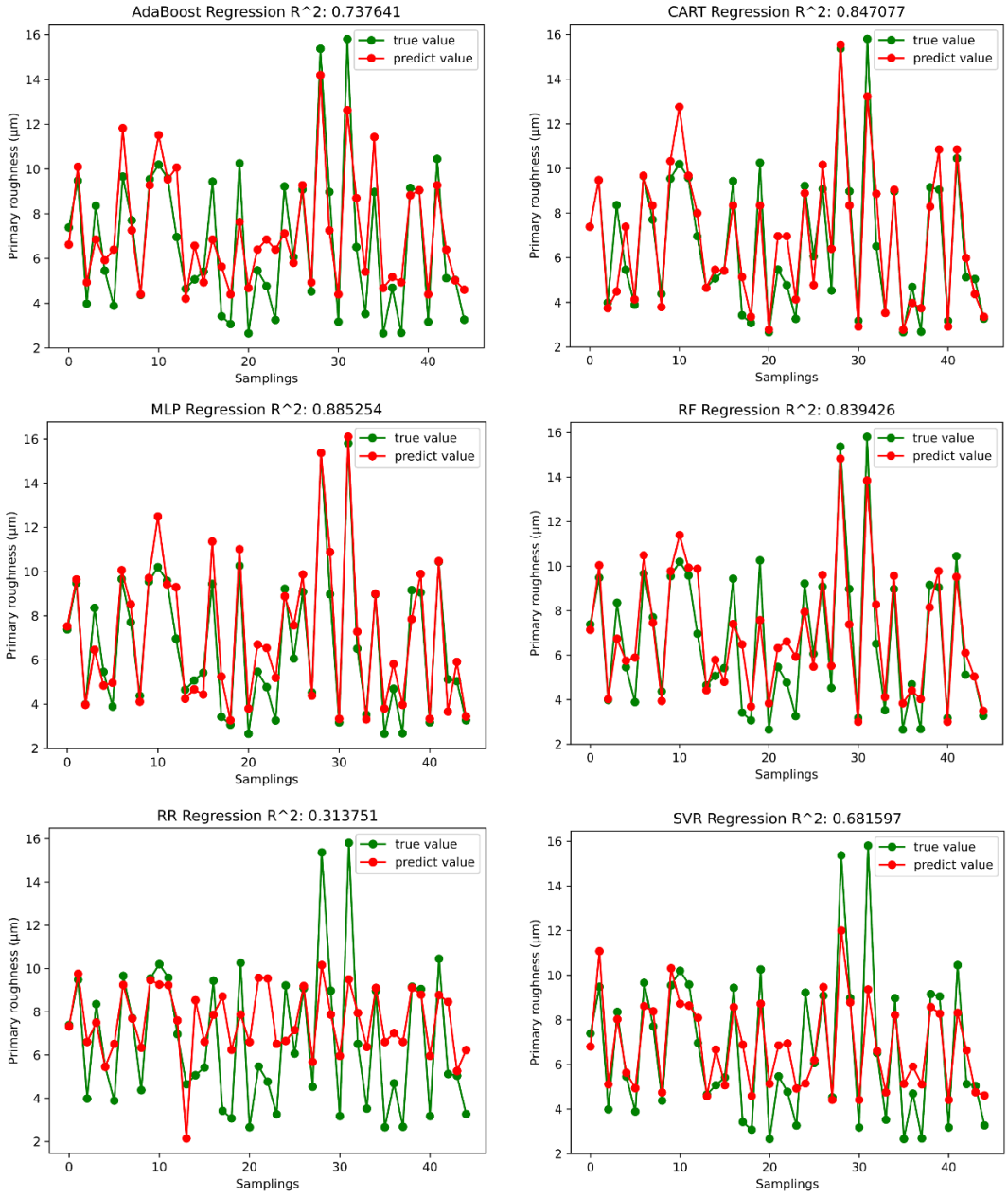

Figure 84 Comparison between the true values of the test dataset and the predictive results obtained from the different algorithms.

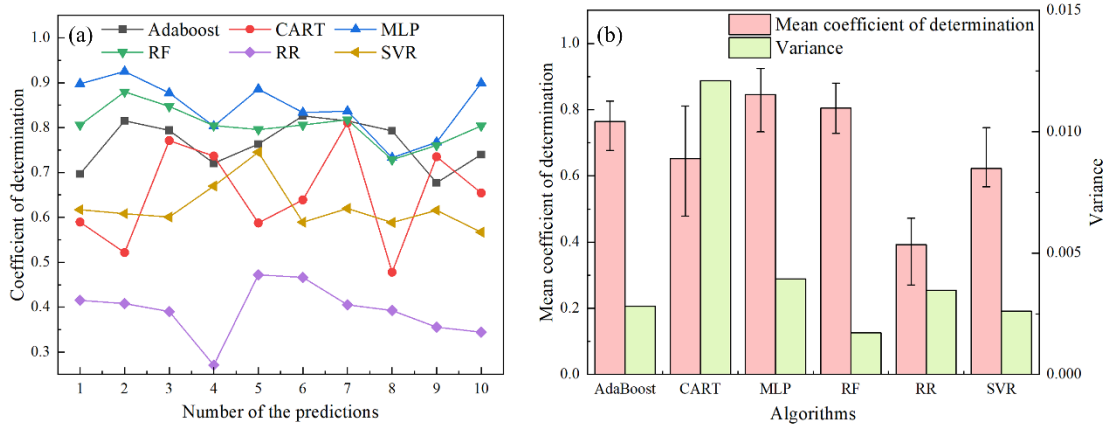

Figure 85 (a) Coefficient of determination change with the number of the prediction; (b) Mean value and variance of the coefficient of determination of different algorithms.

6.4 Summary

A two-step EP method was proposed to improve polishing effects by utilising the polishing characteristics with different current densities and electrolytes. The experimental data including the parameters and results were adopted for prediction using the machine learning algorithms including the Adaptive Boosting algorithm, Random Forest, Multilayer Perceptron Regression, Ridge Regression, Support Vector Regression, and Classification and Regression Trees. The following conclusions can be drawn:

(1) Regarding polishing the 316L SS, the proposed two-step EP process showed an improvement in surface roughness and edge depth at 1.5 A/cm^2 current density compared to the one-step EP process with the NaCl-EG-Ethanol electrolyte. Polishing efficiency and thickness reduction were improved compared to the one-step EP process with the commercial electrolyte A2 at 0.25 A/cm^2 current density. In addition, the two-step method reduced the usage of acid.

(2) Regarding polishing the TC4, the proposed two-step EP process showed an improvement in maximum surface roughness reduction compared to the one-step EP process with the A2 and NaCl-EG-Ethanol electrolytes. The weight and thickness reduction were smaller than the sample polished with the A2 electrolyte.

(3) The neural network and the ensemble-based methods are preferable for predicting the small-scale dataset with errors. The Multilayer Perceptron Regression have the best prediction accuracy while the Random Forest had the best prediction stability.

Chapter 7 Conclusion and Future Work

7.1 Conclusions

This research systematically investigates the EP process of L-PBF 316L SS and TC4 to improve the polishing effect and reduce the experimental workload. The research contents include the FEM simulation of the viscous layer formation process, the determination of the separation method for the surface texture, electrochemical analysis of the EP systems, one-step and two-step EP of 316L SS and TC4, and prediction of the surface roughness using the machine learning method. Results showed that the proposed two-EP process can improve the polishing efficiency and surface roughness, and the MLP and RF methods can be used to predict the polished surfaces with high accuracy and stability.

EP method was a promising tool for polishing L-PBF components, but there are many limitations, such as the low polishing efficiency, low polishing capability, geometry deformation, large workload on experiment attempts, etc. Therefore, in this thesis, numerical simulation and machine learning were introduced to assist in polishing L-PBF components at higher current densities.

Due to the complexity of the EP process, many factors will influence the polishing effect and these factors will also have impacts on each other. In order to reduce the experimental workload, a FEM model composed of rough surfaces obtained by the Spatial Frequency Method was established, and the parameters of the diffusion coefficient of ions, inter-electrode distance, electrolyte flowing rate, and the height and the wavelength distribution on the L-PBF component surfaces were investigated. By comparing the surface roughness of the simulation with that of the physical samples, and the mass transport process with the results in

the previous studies, the accuracy of the model was verified. By simulation, a diffusion coefficient of 10^{-8} m^2/s, an inter-electrode distance of 5 mm, electrolyte flowing rate of 0 mm/s were obtained. However, the numerical simulation was not quite accurate because it was impossible to consider all factors and appropriate assumptions were compulsory. Additionally, the simulation results depended on the mechanism of the EP process while the detailed mechanisms were still controversial. Therefore, the FEM methods were only used to reduce the variants in this thesis and the real polishing effect will be illustrated by experiments.

Many types of electrolytes can be used for polishing while many of them can only work for several specific metals. 316L SS and TC4 are common metals used in the AM process and they have different requirements for the polishing electrolytes. The most electrolyte can be used for polishing 316L SS while in general, perchloric acid or hydrofluoric acid was needed for polishing TC4. Recently, the proposed NaCl-based solution was a promising electrolyte for polishing 316L SS and TC4 while the limiting current density was low, leading to a low polishing efficiency for rough L-PBF components surfaces. Therefore, the influence of the high current density ranging between 0.25 A/cm^2 to 2 A/cm^2 with the phosphoric acid, commercial A2 and NaCl-based electrolytes on polishing 316L SS and TC4 was investigated. A two-step EP process was proposed based on the polishing effect with the electrolytes under different current densities. Results showed that the EP process at the high current density for polishing 316L SS and TC4 with the A2 and NaCl electrolyte can improve the polishing efficiency, and the two-step EP process could improve the polishing effect and the geometry deformation. However, the polishing effect of other current densities, electrolytes and metals was still unknown, and it was impossible to experiment on all the combinations. Therefore, the machine learning method was introduced to generate models for EP prediction.

Generally, machine learning requires a large-scale dataset for training to obtain a model that can accurately predict results. Since experimenting with data collection is time-consuming and costly, six types of algorithms including AdaBoost, RF, MPL, RR, and CART were introduced to generate models for predictions. The prediction accuracy and stability were evaluated using the mean values and variance of the coefficient of determination. Results showed that MPL could present the most accurate prediction results and the RF had the most stable prediction result. Therefore, the polishing effect of the samples with different initial surface roughness, at different current densities, etc. can be obtained by the trained models.

By now, a clear logic line of EP L-PBF 316L SS and TC4 has been drawn:

- Numerical simulation to reduce the experimental variants.

- Experiment to investigate the influence of the high current density and types of electrolytes and collection of data.
- Using machine learning method to predict the surface roughness polished under other conditions.

In conclusion, a systematic investigation through numerical simulation, experiment and machine learning prediction on the EP process of L-PBF components had been studied to allow an improved polishing effect with low experiment workload and cost.

7.2 Future Works

Based on the research presented in this thesis, if more time and resources were available, the study on the EP of L-PBF components could be further improved and expanded in the following aspects:

- The surface topography of the L-PBF components can be scanned and imported into the simulation model to restore the sample surface conditions. The electrochemical reaction process and the dynamically moving mesh can be added to the numerical simulation process to simulate the materials removal process during the EP process. By this method, the simulation results can be verified by the experiment and the requirement of large-scale data used in machine learning can be fulfilled by collecting data from the simulation results.
- More parameters can be investigated in the EP experiment such as the type of power source: direct current, pulse current and pulse reverse current. The surface texture evolution of the L-PBF components with the parameters during the EP process can be further studied using advanced in-situ characterisation techniques.
- Advanced machine learning methods such as transformer, federated learning, or combining using two or more algorithms could generate more accurate and stable prediction results. Moreover, the model can be further improved by the optimisation of the data structures and super-parameters. The prediction system can also be revised for the purpose of predicting the EP parameters, for example, predicting the current density, inter-electrode distance, etc. based on initial surface roughness and expected surface roughness.

References

(1) Monzón, M. D.; Ortega, Z.; Martínez, A.; Ortega, F. Standardization in Additive Manufacturing: Activities Carried out by International Organizations and Projects. *Int. J. Adv. Manuf. Technol.* **2015**, *76* (5), 1111–1121. https://doi.org/10.1007/s00170-014-6334-1.

(2) Yadroitsev, I.; Yadroitsava, I.; Plessis, A. D.; MacDonald, E. *Fundamentals of Laser Powder Bed Fusion of Metals - 1st Edition*, 1st ed.; Elsevier, 2021.

(3) Gibson, I.; Rosen, D.; Stucker, B.; Khorasani, M. *Additive Manufacturing Technologies*; Springer International Publishing: Cham, 2021. https://doi.org/10.1007/978-3-030-56127-7.

(4) Habibzadeh, S.; Li, L.; Shum-Tim, D.; Davis, E. C.; Omanovic, S. Electrochemical Polishing as a 316L Stainless Steel Surface Treatment Method: Towards the Improvement of Biocompatibility. *Corros. Sci.* **2014**, *87*, 89–100. https://doi.org/10.1016/j.corsci.2014.06.010.

(5) Lou, S.; Jiang, J.; Sun, W.; Zeng, W.; Pagani, L.; Scott, P. Characterisation Methods for Powder Bed Fusion Processed Surface Topography. *Precis. Eng.* **2019**, *57*, 1–15. https://doi.org/10.1016/j.precisioneng.2018.09.007.

(6) Chaghazardi, Z.; Wüthrich, R. Electropolishing of Additive Manufactured Metal Parts. *J. Electrochem. Soc.* **2022**, *169* (4), 043510. https://doi.org/10.1149/1945-7111/ac6450.

(7) Krishna, A. V.; Flys, O.; Reddy, V. V.; Berglund, J.; Rosen, B.-G. Areal Surface Topography Representation of As-Built and Post-Processed Samples Produced by Powder Bed Fusion Using Laser Beam Melting. *Surf. Topogr. Metrol. Prop.* **2020**, *8* (2), 024012. https://doi.org/10.1088/2051-672X/ab9b73.

(8) Yasa, E.; Poyraz, O.; Solakoglu, E. U.; Akbulut, G.; Oren, S. A Study on the Stair Stepping Effect in Direct Metal Laser Sintering of a Nickel-Based Superalloy. *Procedia CIRP* **2016**, *45*, 175–178. https://doi.org/10.1016/j.procir.2016.02.068.

(9) Young, Z. A.; Guo, Q.; Parab, N. D.; Zhao, C.; Qu, M.; Escano, L. I.; Fezzaa, K.; Everhart, W.; Sun, T.; Chen, L. Types of Spatter and Their Features and Formation Mechanisms in Laser Powder Bed Fusion Additive Manufacturing Process. *Addit. Manuf.* **2020**, *36*, 101438. https://doi.org/10.1016/j.addma.2020.101438.

(10) Guo, Q.; Zhao, C.; Escano, L. I.; Young, Z.; Xiong, L.; Fezzaa, K.; Everhart, W.; Brown, B.; Sun, T.; Chen, L. Transient Dynamics of Powder Spattering in Laser Powder Bed Fusion Additive Manufacturing Process Revealed by In-Situ High-Speed

High-Energy X-ray Imaging. *Acta Mater.* **2018**, *151*, 169–180. https://doi.org/10.1016/j.actamat.2018.03.036.

(11) Zhao, C.; Guo, Q.; Li, X.; Parab, N.; Fezzaa, K.; Tan, W.; Chen, L.; Sun, T. Bulk-Explosion-Induced Metal Spattering During Laser Processing. *Phys. Rev. X* **2019**, *9* (2), 021052. https://doi.org/10.1103/PhysRevX.9.021052.

(12) Khairallah, S. A.; Martin, A. A.; Lee, J. R. I.; Guss, G.; Calta, N. P.; Hammons, J. A.; Nielsen, M. H.; Chaput, K.; Schwalbach, E.; Shah, M. N.; Chapman, M. G.; Willey, T. M.; Rubenchik, A. M.; Anderson, A. T.; Wang, Y. M.; Matthews, M. J.; King, W. E. Controlling Interdependent Meso-Nanosecond Dynamics and Defect Generation in Metal 3D Printing. *Science* **2020**, *368* (6491), 660–665. https://doi.org/10.1126/science.aay7830.

(13) Zhao, C.; Qu, N.; Tang, X. Removal of Adhesive Powders from Additive-Manufactured Internal Surface via Electrochemical Machining with Flexible Cathode. *Precis. Eng.* **2021**, *67*, 438–452. https://doi.org/10.1016/j.precisioneng.2020.11.003.

(14) Ansari, P.; Rehman, A. U.; Pitir, F.; Veziroglu, S.; Mishra, Y. K.; Aktas, O. C.; Salamci, M. U. Selective Laser Melting of 316L Austenitic Stainless Steel: Detailed Process Understanding Using Multiphysics Simulation and Experimentation. *Metals* **2021**, *11* (7), 1076. https://doi.org/10.3390/met11071076.

(15) Wei, H. L.; Mukherjee, T.; Zhang, W.; Zuback, J. S.; Knapp, G. L.; De, A.; DebRoy, T. Mechanistic Models for Additive Manufacturing of Metallic Components. *Prog. Mater. Sci.* **2021**, *116*, 100703. https://doi.org/10.1016/j.pmatsci.2020.100703.

(16) Larimian, T.; Kannan, M.; Grzesiak, D.; AlMangour, B.; Borkar, T. Effect of Energy Density and Scanning Strategy on Densification, Microstructure and Mechanical Properties of 316L Stainless Steel Processed via Selective Laser Melting. *Mater. Sci. Eng. A* **2020**, *770*, 138455. https://doi.org/10.1016/j.msea.2019.138455.

(17) Scime, L.; Beuth, J. Melt Pool Geometry and Morphology Variability for the Inconel 718 Alloy in a Laser Powder Bed Fusion Additive Manufacturing Process. *Addit. Manuf.* **2019**, *29*, 100830. https://doi.org/10.1016/j.addma.2019.100830.

(18) Khairallah, S. A.; Anderson, A. T.; Rubenchik, A.; King, W. E. Laser Powder-Bed Fusion Additive Manufacturing: Physics of Complex Melt Flow and Formation Mechanisms of Pores, Spatter, and Denudation Zones. *Acta Mater.* **2016**, *108*, 36–45. https://doi.org/10.1016/j.actamat.2016.02.014.

(19) Skalon, M.; Meier, B.; Leitner, T.; Arneitz, S.; Amancio-Filho, S. T.; Sommitsch, C. Reuse of Ti6Al4V Powder and Its Impact on Surface Tension, Melt Pool Behavior and Mechanical Properties of Additively Manufactured Components. *Materials* **2021**, *14* (5), 1251. https://doi.org/10.3390/ma14051251.

(20) Chouhan, A.; Aggarwal, A.; Kumar, A. Role of Melt Flow Dynamics on Track Surface Morphology in the L-PBF Additive Manufacturing Process. *Int. J. Heat Mass Transf.* **2021**, *178*, 121602. https://doi.org/10.1016/j.ijheatmasstransfer.2021.121602.

(21) Kazemi, Z.; Soleimani, M.; Rokhgireh, H.; Nayebi, A. Melting Pool Simulation of 316L Samples Manufactured by Selective Laser Melting Method, Comparison with Experimental Results. *Int. J. Therm. Sci.* **2022**, *176*, 107538. https://doi.org/10.1016/j.ijthermalsci.2022.107538.

(22) Zhao, C.; Parab, N. D.; Li, X.; Fezzaa, K.; Tan, W.; Rollett, A. D.; Sun, T. Critical Instability at Moving Keyhole Tip Generates Porosity in Laser Melting. *Science* **2020**, *370* (6520), 1080–1086. https://doi.org/10.1126/science.abd1587.

(23) Thomas, D. S.; Gilbert, S. W. Costs and Cost Effectiveness of Additive Manufacturing. *NIST* **2014**.

(24) Khan, H. M.; Karabulut, Y.; Kitay, O.; Kaynak, Y.; Jawahir, I. S. Influence of the Post-Processing Operations on Surface Integrity of Metal Components Produced by Laser Powder Bed Fusion Additive Manufacturing: A Review. *Mach. Sci. Technol.* **2020**, *25* (1), 118–176. https://doi.org/10.1080/10910344.2020.1855649.

(25) Charles, A.; Elkaseer, A.; Müller, T.; Thijs, L.; Torge, M.; Hagenmeyer, V.; Scholz, S. A Study of the Factors Influencing Generated Surface Roughness of Downfacing Surfaces in Selective Laser Melting. In *Proceedings of the World Congress on Micro and Nano Manufacturing*; Portorož, Slovenia, 2018; Vol. 3, p 5.

(26) Gora, W. S.; Tian, Y.; Cabo, A. P.; Ardron, M.; Maier, R. R. J.; Prangnell, P.; Weston, N. J.; Hand, D. P. Enhancing Surface Finish of Additively Manufactured Titanium and Cobalt Chrome Elements Using Laser Based Finishing. *Phys. Procedia* **2016**, *83*, 258–263. https://doi.org/10.1016/j.phpro.2016.08.021.

(27) Zhang, Y.; Li, J.; Che, S.; Tian, Y. Electrochemical Polishing of Additively Manufactured Ti–6Al–4V Alloy. *Met. Mater. Int.* **2020**, *26* (6), 783–792. https://doi.org/10.1007/s12540-019-00556-0.

(28) Wysocki, B.; Idaszek, J.; Buhagiar, J.; Szlązak, K.; Brynk, T.; Kurzydłowski, K. J.; Święszkowski, W. The Influence of Chemical Polishing of Titanium Scaffolds on Their Mechanical Strength and In-Vitro Cell Response. *Mater. Sci. Eng. C* **2019**, *95*, 428–439. https://doi.org/10.1016/j.msec.2018.04.019.

(29) Chmielewska, A.; Jahadakbar, A.; Wysocki, B.; Elahinia, M.; Święszkowski, W.; Dean, D. Chemical Polishing of Additively Manufactured, Porous, Nickel–Titanium Skeletal Fixation Plates. *3D Print. Addit. Manuf.* **2021**. https://doi.org/10.1089/3dp.2020.0209.

(30) Tyagi, P.; Goulet, T.; Riso, C.; Stephenson, R.; Chuenprateep, N.; Schlitzer, J.; Benton, C.; Garcia-Moreno, F. Reducing the Roughness of Internal Surface of an Additive

Manufacturing Produced 316 Steel Component by Chempolishing and Electropolishing. *Addit. Manuf.* **2019**, *25*, 32–38. https://doi.org/10.1016/j.addma.2018.11.001.

(31) Walther, B.; Schilm, J.; Michaelis, A.; Lohrengel, M. M. Electrochemical Dissolution of Hard Metal Alloys. *Electrochimica Acta* **2007**, *52* (27), 7732–7737. https://doi.org/10.1016/j.electacta.2006.12.038.

(32) Ferchow, J.; Hofmann, U.; Meboldt, M. Enabling Electropolishing of Complex Selective Laser Melting Structures. In *Procedia CIRP*; 2020; Vol. 91, pp 472–477. https://doi.org/10.1016/j.procir.2020.02.201.

(33) Tyagi, P.; Goulet, T.; Riso, C.; Klein, K.; Garcia-Moreno, F. *ELECTROPOLISHING OF ADDITIVELY MANUFACTURED HIGH CARBON GRADE 316 STAINLESS STEEL*; preprint; engrXiv, 2018. https://doi.org/10.31224/osf.io/5dn49.

(34) Han, W.; Fang, F. Fundamental Aspects and Recent Developments in Electropolishing. *Int. J. Mach. Tools Manuf.* **2019**, *139*, 1–23. https://doi.org/10.1016/j.ijmachtools.2019.01.001.

(35) Chen, C.; Chen, J.; Chao, C.; Say, W. C. Electrochemical Characteristics of Surface of Titanium Formed by Electrolytic Polishing and Anodizing. *J. Mater. Sci.* **2005**, *40* (15), 4053–4059. https://doi.org/10.1007/s10853-005-2802-1.

(36) Rotty, C.; Mandroyan, A.; Doche, M.-L.; Hihn, J. Y. Electropolishing of CuZn Brasses and 316L Stainless Steels: Influence of Alloy Composition or Preparation Process (ALM vs. Standard Method). *Surf. Coat. Technol.* **2016**, *307*, 125–135. https://doi.org/10.1016/j.surfcoat.2016.08.076.

(37) Rahman, Z. ur; Deen, K. M.; Cano, L.; Haider, W. The Effects of Parametric Changes in Electropolishing Process on Surface Properties of 316L Stainless Steel. *Appl. Surf. Sci.* **2017**, *410*, 432–444. https://doi.org/10.1016/j.apsusc.2017.03.081.

(38) Han, W.; Fang, F. Eco-Friendly NaCl-Based Electrolyte for Electropolishing 316L Stainless Steel. *J. Manuf. Process.* **2020**, *58*, 1257–1269. https://doi.org/10.1016/j.jmapro.2020.09.036.

(39) Han, W.; Fang, F. Two-Step Electropolishing of 316L Stainless Steel in a Sulfuric Acid-Free Electrolyte. *J. Mater. Process. Technol.* **2020**, *279*, 116558. https://doi.org/10.1016/j.jmatprotec.2019.116558.

(40) Nagalingam, A. P.; Vohra, M. S.; Kapur, P.; Yeo, S. H. Effect of Cut-Off, Evaluation Length, and Measurement Area in Profile and Areal Surface Texture Characterization of As-Built Metal Additive Manufactured Components. *Appl. Sci.* **2021**, *11* (11), 5089. https://doi.org/10.3390/app11115089.

(41) Haïdopoulos, M.; Turgeon, S.; Sarra-Bournet, C.; Laroche, G.; Mantovani, D. Development of an Optimized Electrochemical Process for Subsequent Coating of 316

Stainless Steel for Stent Applications. *J. Mater. Sci.-Mater. Med.* **2006**, *17* (7), 647–657. https://doi.org/10.1007/s10856-006-9228-4.

(42) Han, W.; Fang, F. Orientation Effect of Electropolishing Characteristics of 316L Stainless Steel Fabricated by Laser Powder Bed Fusion. *Front. Mech. Eng.* **2021**. https://doi.org/10.1007/s11465-021-0633-7.

(43) Palmieri, V.; Rampazzo, V. *AUTOMATED ELECTROPOLISHING*; CARE; CARE-Report-07-010-SRF; ISTITUTO NAZIONALE DI FISICA NUCLEARE, 2007; p 10. https://cds.cern.ch/record/1089001/files/care-report-07-010.pdf.

(44) Tyagi, P.; Brent, D.; Saunders, T.; Goulet, T.; Riso, C.; Klein, K.; Moreno, F. G. Roughness Reduction of Additively Manufactured Steel by Electropolishing. *Int. J. Adv. Manuf. Technol.* **2020**, *106* (3–4), 1337–1344. https://doi.org/10.1007/s00170-019-04720-z.

(45) Lee, S.-J.; Chen, Y.-H.; Hung, J.-C. The Investigation of Surface Morphology Forming Mechanisms in Electropolishing Process. *Int. J. Electrochem. Sci.* **2012**, *7*, 12495–12506.

(46) Tailor, P. B.; Agrawal, A.; Joshi, S. S. Numerical Modeling of Passive Layer Formation and Stabilization in Electrochemical Polishing Process. *J. Manuf. Process.* **2015**, *18*, 107–116. https://doi.org/10.1016/j.jmapro.2015.02.001.

(47) Zhang, Z.; Cheung, C. F.; Wang, C.; Guo, J. Modelling of Surface Morphology and Roughness in Fluid Jet Polishing. *Int. J. Mech. Sci.* **2023**, *242*, 107976. https://doi.org/10.1016/j.ijmecsci.2022.107976.

(48) Yaseer, A.; Chen, H. Machine Learning Based Layer Roughness Modeling in Robotic Additive Manufacturing. *J. Manuf. Process.* **2021**, *70*, 543–552. https://doi.org/10.1016/j.jmapro.2021.08.056.

(49) Huang, P. B.; Inderawati, M. M. W.; Rohmat, R.; Sukwadi, R. The Development of an ANN Surface Roughness Prediction System of Multiple Materials in CNC Turning. *Int. J. Adv. Manuf. Technol.* **2023**, *125* (3), 1193–1211. https://doi.org/10.1007/s00170-022-10709-y.

(50) Singh, A.; Gu, Z.; Hou, X.; Liu, Y.; Hughes, D. J. Design Optimisation of Braided Composite Beams for Lightweight Rail Structures Using Machine Learning Methods. *Compos. Struct.* **2022**, *282*, 115107. https://doi.org/10.1016/j.compstruct.2021.115107.

(51) Gu, Z.; Liu, Y.; Hughes, D. J.; Ye, J.; Hou, X. A Parametric Study of Adhesive Bonded Joints with Composite Material Using Black-Box and Grey-Box Machine Learning Methods: Deep Neuron Networks and Genetic Programming. *Compos. Part B Eng.* **2021**, *217*, 108894. https://doi.org/10.1016/j.compositesb.2021.108894.

(52) Rotty, C.; Mandroyan, A.; Doche, M.-L.; Monney, S.; Hihn, J.-Y.; Rouge, N. Electrochemical Superfinishing of Cast and ALM 316L Stainless Steels in Deep

Eutectic Solvents: Surface Microroughness Evolution and Corrosion Resistance. *J. Electrochem. Soc.* **2019**, *166* (13), C468. https://doi.org/10.1149/2.1211913jes.

(53) Lyczkowska-Widlak, E.; Lochynski, P.; Nawrat, G.; Chlebus, E. Comparison of Electropolished 316L Steel Samples Manufactured by SLM and Traditional Technology. *Rapid Prototyp. J.* **2018**, *25* (3), 566–580. https://doi.org/10.1108/rpj-03-2018-0060.

(54) Rottya, C.; Dochea, M.-L.; Mandroyana, A.; Hihna, J.-Y.; Montavonb, G.; Moutarliera, V. Electropolishing of Thermal Spray Coating and Laser Additive Manufacturing of 316L Stainless Steel in Strong Acidic Media. In *Proceedings of the International Conference on Surface Modification Technologies (SMT30)*; 2016.

(55) Alrbaey, K.; Wimpenny, D. I.; Al-Barzinjy, A. A.; Moroz, A. Electropolishing of Re-Melted SLM Stainless Steel 316L Parts Using Deep Eutectic Solvents: 3$\times$ 3 Full Factorial Design. *J. Mater. Eng. Perform.* **2016**, *25* (7), 2836–2846. https://doi.org/10.1007/s11665-016-2140-2.

(56) Kim, D.; Son, K.; Sung, D.; Kim, Y.; Chung, W. Effect of Added Ethanol in Ethylene Glycol–NaCl Electrolyte on Titanium Electropolishing. *Corros. Sci.* **2015**, *98*, 494–499. https://doi.org/10.1016/j.corsci.2015.05.057.

(57) Tsoeunyane, G. M.; Mathe, N.; Tshabalala, L.; Makhatha, M. E. Electropolishing of Additively Manufactured Ti-6Al-4V Surfaces in Nontoxic Electrolyte Solution. *Adv. Mater. Sci. Eng.* **2022**, *2022*, e6987353. https://doi.org/10.1155/2022/6987353.

(58) Landolt, D. Fundamental Aspects of Electropolishing. *Electrochimica Acta* **1987**, *32* (1), 1–11. https://doi.org/10.1016/0013-4686(87)87001-9.

(59) Datta, M.; Landolt, D. Fundamental Aspects and Applications of Electrochemical Microfabrication. *Electrochimica Acta* **2000**, *45* (15), 2535–2558. https://doi.org/10.1016/s0013-4686(00)00350-9.

(60) Yang, G.; Wang, B.; Tawfiq, K.; Wei, H.; Zhou, S.; Chen, G. Electropolishing of Surfaces: Theory and Applications. *Surf. Eng.* **2017**, *33* (2), 149–166. https://doi.org/10.1080/02670844.2016.1198452.

(61) Bhattacharyya, B. Electrochemical Machining. *Electrochem. Micromach. Nanofabrication MEMS Nanotechnol.* **2015**, 25–52. https://doi.org/10.1016/b978-0-323-32737-4.00002-5.

(62) Jacquet, P. A. On the Anodic Behavior of Copper in Aqueous Solutions of Orthophosphoric Acid. *Trans. Electrochem. Soc.* **1936**, *69* (1), 629. https://doi.org/10.1149/1.3498234.

(63) Hoar, T. P.; Mowat, J. a. S. Mechanism of Electropolishing. *Nature* **1950**, *165* (4185), 64–65. https://doi.org/10.1038/165064a0.

(64) Elmore, W. C. Electrolytic Polishing. *J. Appl. Phys.* **1939**, *10* (10), 724–727. https://doi.org/10.1063/1.1707257.

(65) Elmore, W. C. Electrolytic Polishing. II. *J. Appl. Phys.* **1940**, *11* (12), 797–799. https://doi.org/10.1063/1.1712738.

(66) Rowland, P. R. Mechanism of Electropolishing. *Nature* **1953**, *171* (4360), 931–931. https://doi.org/10.1038/171931a0.

(67) Jacquet, P. A. Electrolytic Method for Obtaining Bright Copper Surfaces. *Nature* **1935**, *135* (3426), 1076–1076. https://doi.org/10.1038/1351076c0.

(68) Gilbertson, L. I.; Fortner, O. W. Electrolytic Polishing of Silver. *Trans. Electrochem. Soc.* **1942**, *81* (1), 199. https://doi.org/10/b7g974.

(69) Feancis, H. T.; Colner, W. H. Cyclic Phenomena Observed in Electropolishing of Silver. *J. Electrochem. Soc.* **1950**, *97* (8), 237. https://doi.org/10.1149/1.2778001.

(70) Fan, Z.-W.; Hourng, L.-W.; Wang, C.-Y. Fabrication of Tungsten Microelectrodes Using Pulsed Electrochemical Machining. *Precis. Eng.* **2010**, *34* (3), 489–496. https://doi.org/10.1016/j.precisioneng.2010.01.001.

(71) Wang, G.; Liu, Z.; Niu, J.; Huang, W.; Wang, B. Effect of Electrochemical Polishing on Surface Quality of Nickel-Titanium Shape Memory Alloy after Milling. *J. Mater. Res. Technol.* **2020**, *9* (1), 253–262. https://doi.org/10.1016/j.jmrt.2019.10.053.

(72) Wang, F.; Zhang, X.; Deng, H. A Comprehensive Study on Electrochemical Polishing of Tungsten. *Appl. Surf. Sci.* **2019**, *475*, 587–597. https://doi.org/10.1016/j.apsusc.2019.01.020.

(73) Lebedeva, O.; Kultin, D.; Zakharov, A.; Kustov, L. Advantages of Electrochemical Polishing of Metals and Alloys in Ionic Liquids. *Metals* **2021**, *11* (6), 959. https://doi.org/10.3390/met11060959.

(74) Müller, M. J.; Löw, E. *Elektrochem 39*, 872.

(75) Hoar, T. P.; Farthing, T. W. Solid Films on Electropolishing Anodes. *Nature* **1952**, *169* (4295), 324–325. https://doi.org/10.1038/169324b0.

(76) Williams, E. C.; Barrett, M. A. The Nature of the Film Formed on Copper during Electropolishing. *J. Electrochem. Soc.* **1956**, *103* (7), 363. https://doi.org/10.1149/1.2430357.

(77) Kolthoff, I. M.; Miller, C. S. Anodic Waves Involving Electroöxidation of Mercury at the Dropping Mercury Electrode. *J. Am. Chem. Soc.* **1941**, *63* (5), 1405–1411. https://doi.org/10.1021/ja01850a077.

(78) Halfaway, M. Experientia. **1951**, *7*, 175.

(79) Edwards, J. The Mechanism of Electropoiishing of Copper in Phosphoric Acid Solutions: I . Processes Preceding the Establisment of Polishing Conditions. *J. Electrochem. Soc.* **1953**, *100* (7), 189C. https://doi.org/10.1149/1.2781122.

(80) Edwards, J. The Mechanism of Electropolishing of Copper in Phosphoric Acid Solutions: II . The Mechanism of Smoothing. *J. Electrochem. Soc.* **1953**, *100* (8), 223C. https://doi.org/10.1149/1.2781129.

(81) Darmois, E.; Epelboin, I.; Amine, D. Resistivite Electrique et Composition Optimum Des Bains de Polissage Electrolytique. *COMPTES RENDUS Hebd. SEANCES Acad. Sci.* **1950**, *230* (4), 386–388.

(82) Metz, F. I. Electropolishing of Metals, Iowa State University Of Science and Technology, 1960.

(83) Lee, S.-J.; Lai, J.-J. The Effects of Electropolishing (EP) Process Parameters on Corrosion Resistance of 316L Stainless Steel. *J. Mater. Process. Technol.* **2003**, *140* (1–3), 206–210. https://doi.org/10.1016/s0924-0136(03)00785-4.

(84) Magaino, S.; Matlosz, M.; Landolt, D. An Impedance Study of Stainless Steel Electropolishing. *J. Electrochem. Soc.* **1993**, *140* (5), 1365. https://doi.org/10.1149/1.2221562.

(85) Jacquet, P. A. Electrolytic and Chemical Polishing. *Metall. Rev.* **1956**, *1* (1), 157–238. https://doi.org/10.1179/mtlr.1956.1.1.157.

(86) Asokan, T.; Sudarshan, T. S. Analysis of the Scanning Electron Microscope Mirror Image Based on the Dielectric Surface Microstructure. *J. Appl. Phys.* **1994**, *75* (8), 3715–3722. https://doi.org/10.1063/1.356043.

(87) P. Abbott, A.; Capper, G.; J. McKenzie, K.; Glidle, A.; S. Ryder, K. Electropolishing of Stainless Steels in a Choline Chloride Based Ionic Liquid : An Electrochemical Study with Surface Characterisation Using SEM and Atomic Force Microscopy. *Phys. Chem. Chem. Phys.* **2006**, *8* (36), 4214–4221. https://doi.org/10.1039/B607763N.

(88) Peters, M.; Kumpfert, J.; Ward, C. H.; Leyens, C. Titanium Alloys for Aerospace Applications. *Adv. Eng. Mater.* **2003**, *5* (6), 419–427. https://doi.org/10.1002/adem.200310095.

(89) Popov, V. V.; Muller-Kamskii, G.; Kovalevsky, A.; Dzhenzhera, G.; Strokin, E.; Kolomiets, A.; Ramon, J. Design and 3D-Printing of Titanium Bone Implants: Brief Review of Approach and Clinical Cases. *Biomed. Eng. Lett.* **2018**, *8* (4), 337–344. https://doi.org/10.1007/s13534-018-0080-5.

(90) Yildirim, T.; Ciraci, S. Titanium-Decorated Carbon Nanotubes as a Potential High-Capacity Hydrogen Storage Medium. *Phys. Rev. Lett.* **2005**, *94* (17), 175501. https://doi.org/10.1103/physrevlett.94.175501.

(91) Duerig, T.; Pelton, A.; Stöckel, D. An Overview of Nitinol Medical Applications. *Mater. Sci. Eng. A* **1999**, *273–275*, 149–160. https://doi.org/10.1016/S0921-5093(99)00294-4.

(92) Wever, D. J.; Veldhuizen, A. G.; de Vries, J.; Busscher, H. J.; Uges, D. R. A.; van Horn, J. R. Electrochemical and Surface Characterization of a Nickel–Titanium Alloy. *Biomaterials* **1998**, *19* (7), 761–769. https://doi.org/10.1016/s0142-9612(97)00210-x.

(93) Wang, K. The Use of Titanium for Medical Applications in the USA. *Mater. Sci. Eng. A* **1996**, *213* (1), 134–137. https://doi.org/10.1016/0921-5093(96)10243-4.

(94) Thierry, B.; Tabrizian, M.; Trepanier, C.; Savadogo, O.; Yahia, L. Effect of Surface Treatment and Sterilization Processes on the Corrosion Behavior of NiTi Shape Memory Alloy. *J. Biomed. Mater. Res.* **2000**, *51* (4), 685–693. https://doi.org/10.1002/1097-4636(20000915)51:4<685::AID-JBM17>3.0.CO;2-S.

(95) Urlea, V.; Brailovski, V. Electropolishing and Electropolishing-Related Allowances for Powder Bed Selectively Laser-Melted Ti-6Al-4V Alloy Components. *J. Mater. Process. Technol.* **2017**, *242*, 1–11. https://doi.org/10.1016/j.jmatprotec.2016.11.014.

(96) Yang, L.; Gu, H.; Lassell, A. Surface Treatment of Ti6Al4V Parts Made by Powder Bed Fusion Additive Manufacturing Processes Using Electropolishing. In *Solid Freeform Fabrication (SFF) Symposium*; 2014; p 10.

(97) Taylor, E. J.; Inman, M. E.; Hall, T. D.; Kagajwala, B. Electropolishing of Passive Materials in HF-Free Low Viscosity Aqueous Electrolytes. *ECS Trans.* **2013**, *45* (8), 13–20. https://doi.org/10.1149/04508.0013ecst.

(98) Mahé, E.; Devilliers, D. Surface Modification of Titanium Substrates for the Preparation of Noble Metal Coated Anodes. *Electrochimica Acta* **2001**, *46* (5), 629–636. https://doi.org/10.1016/s0013-4686(00)00646-0.

(99) Aggarwal, S.; Shah, P.; Duggal, R.; Jain, H. Electrodeposition of Milligram Amounts of Uranium on Electropolished Stainless Steel Disks. *J. Radioanal. Nucl. Chem.* **2005**, *154* (2), 103–110. https://doi.org/10.1007/bf02162668.

(100) Sedahmed, G. H.; Iskander, S. S.; Mansour, I. A. S.; Fawzy, M. A. Electropolishing of Vertical Copper Cylinders in Phosphoric Acid under Natural Convection Conditions. *Surf. Technol.* **1980**, *11* (1), 67–71. https://doi.org/10.1016/0376-4583(80)90020-5.

(101) Drensler, S.; Neelakantan, L.; Somsen, C.; Eggeler, G.; Hassel, A. W. Electropolishing of a Nickel–Titanium–Copper Shape Memory Alloy in Methanolic Sulfuric Acid. *Electrochem. Solid State Lett.* **2008**, *12* (2), C1. https://doi.org/10.1149/1.3025889.

(102) Alanis, I. L.; Schiffrin, D. J. The Influence of Mass Transfer on the Mechanism of Electropolishing of Nickel in Aqueous Sulphuric Acid. *Electrochimica Acta* **1982**, *27* (7), 837–845. https://doi.org/10.1016/0013-4686(82)80205-3.

(103) Zhang, X. G.; Collins, S. D.; Smith, R. L. Porous Silicon Formation and Electropolishing of Silicon by Anodic Polarization in HF Solution. *J. Electrochem. Soc.* **1989**, *136* (5), 1561. https://doi.org/10.1149/1.2096961.

(104) Hocheng, H.; Pa, P. S. Electropolishing of Cylindrical Workpiece of Tool Materials Using Disc-Form Electrodes. *J. Mater. Process. Technol.* **2003**, *142* (1), 203–212. https://doi.org/10.1016/s0924-0136(03)00599-5.

(105) Pa, P. S. Design of Effective Plate-Shape Electrode in Ultrasonic Electrochemical Finishing. *Int. J. Adv. Manuf. Technol.* **2007**, *34* (1–2), 70–78. https://doi.org/10.1007/s00170-006-0567-6.

(106) Hocheng, H.; Pa, P. S. Effective Form Design of Electrode in Electrochemical Smoothing of Holes. *Int. J. Adv. Manuf. Technol.* **2003**, *21* (12), 995–1004. https://doi.org/10.1007/s00170-002-1422-z.

(107) Jin, S.; Wu, A. T.; Lu, X. Y.; Rimmer, R. A.; Lin, L.; Zhao, K.; Mammosser, J.; Gao, J. Effect of Cathode Shape on Vertical Buffered Electropolishing for Niobium SRF Cavities. *Appl. Surf. Sci.* **2013**, *280*, 93–103. https://doi.org/10.1016/j.apsusc.2013.04.102.

(108) Mohan, S.; Kanagaraj, D.; Sindhuja, R.; Vijayalakshmi, S.; Renganathan, N. G. Electropolishing of Stainless Steel—a Review. *Trans. IMF* **2001**, *79* (4), 140–142. https://doi.org/10.1080/00202967.2001.11871382.

(109) Maciąg, T.; Wieczorek, J.; Węcki, B. Parameters Selection for Electropolishing Process of Products Made of Copper and Its Alloys. *Arch. Metall. Mater.* **2017**, *62* (3), 1443–1447. https://doi.org/10.1515/amm-2017-0223.

(110) Lee, E. S.; Shin, T. H. An Evaluation of the Machinability of Nitinol Shape Memory Alloy by Electrochemical Polishing. *J. Mech. Sci. Technol.* **2011**, *25* (4), 963.

(111) Qu, N. S.; Chan, K. C.; Zhu, D. Surface Roughening in Pulse Current and Pulse Reverse Current Electroforming of Nickel. *Surf. Coat. Technol.* **1997**, *91* (3), 220–224. https://doi.org/10.1016/S0257-8972(96)03184-2.

(112) Satoh, A. Mechanism and Characteristics of Through-Hole Formation on Si Wafer by Optical Excitation Electropolishing Method. *Jpn. J. Appl. Phys.* **2000**, *39* (4R), 1612. https://doi.org/10.1143/JJAP.39.1612.

(113) Ramasawmy, H.; Blunt, L. 3D Surface Topography Assessment of the Effect of Different Electrolytes during Electrochemical Polishing of EDM Surfaces. *Int. J. Mach. Tools Manuf.* **2002**, *42* (5), 567–574. https://doi.org/10.1016/s0890-6955(01)00154-7.

(114) Tailor, P. B.; Agrawal, A.; Joshi, S. S. Evolution of Electrochemical Finishing Processes through Cross Innovations and Modeling. *Int. J. Mach. Tools Manuf.* **2013**, *66*, 15–36. https://doi.org/10.1016/j.ijmachtools.2012.11.005.

(115) Huang, C. A.; Hsu, F.-Y.; Yu, C. H. Electropolishing Behavior of Pure Titanium in Sulfuric Acid–Ethanol Electrolytes with an Addition of Water. *Corros. Sci.* **2011**, *53* (2), 589–596. https://doi.org/10.1016/j.corsci.2010.10.002.

(116) Nazneen, F.; Galvin, P.; Arrigan, D. W. M.; Thompson, M.; Benvenuto, P.; Herzog, G. Electropolishing of Medical-Grade Stainless Steel in Preparation for Surface Nano-Texturing. *J. Solid State Electrochem.* **2012**, *16* (4), 1389–1397. https://doi.org/10.1007/s10008-011-1539-9.

(117) Lappin, D.; Mohammadi, A. R.; Takahata, K. An Experimental Study of Electrochemical Polishing for Micro-Electro-Discharge-Machined Stainless-Steel Stents. *J. Mater. Sci.-Mater. Med.* **2012**, *23* (2), 349–356. https://doi.org/10.1007/s10856-011-4513-2.

(118) Sueptitz, R.; Tschulik, K.; Becker, C.; Stoica, M.; Uhlemann, M.; Eckert, J.; Gebert, A. Micropatterning of Fe-Based Bulk Metallic Glass Surfaces by Pulsed Electrochemical Micromachining. *J. Mater. Res.* **2012**, *27* (23), 3033–3040. https://doi.org/10.1557/jmr.2012.347.

(119) Datta, M.; Landolt, D. Electrochemical Machining under Pulsed Current Conditions. *Electrochimica Acta* **1981**, *26* (7), 899–907. https://doi.org/10.1016/0013-4686(81)85053-0.

(120) Wagner, T. High Rate Electrochemical Dissolution of Iron-Based Alloys in NaCl and NaNO3 Electrolytes. *Schnelle elektrochemische Auflösung von Eisen-basierenden Legierungen in NaCl- und NaNO3-Elektrolyten* **2002**. https://doi.org/10.18419/opus-741.

(121) Lee, J. M.; Kim, Y. B.; Park, J. W. Pulse Electrochemical Meso/Micro/Nano Ultraprecision Machining Technology. *J. Nanosci. Nanotechnol.* **2013**, *13* (11), 7741–7744. https://doi.org/10.1166/jnn.2013.7716.

(122) Ramasawmy, H.; Blunt, L. Investigation of the Effect of Electrochemical Polishing on EDM Surfaces. *Int. J. Adv. Manuf. Technol.* **2007**, *31* (11–12), 1135–1147. https://doi.org/10.1007/s00170-005-0302-8.

(123) Xu, W.; Wei, Z.; Sun, J.; Wei, L.; Yu, Z. Surface Quality Prediction and Processing Parameter Determination in Electrochemical Mechanical Polishing of Bearing Rollers. *Int. J. Adv. Manuf. Technol.* **2012**, *63* (1–4), 129–136. https://doi.org/10.1007/s00170-011-3891-4.

(124) Yi, J. J.; Chen, C. M.; Tian, X. Q.; Ji, B. Y. Basic Experimental Investigation of Pulsed Electrochemical Mechanical Polishing Process. *Surf. Eng.* **2009**, *25* (7), 535–540. https://doi.org/10.1179/174329409X397796.

(125) Tang, L.; Gan, W. M. Experiment and Simulation Study on Concentrated Magnetic Field-Assisted ECM S-03 Special Stainless Steel Complex Cavity. *Int. J. Adv. Manuf. Technol.* **2014**, *72* (5–8), 685–692. https://doi.org/10.1007/s00170-014-5701-2.

(126) Skrabalak, G.; Stwora, A. Electrochemical, Electrodischarge and Electrochemical-Discharge Hole Drilling and Surface Structuring Using Batch Electrodes. *Procedia CIRP* **2016**, *42*, 766–771. https://doi.org/10.1016/j.procir.2016.02.316.

(127) Hocheng, H.; Sun, Y. H.; Lin, S. C.; Kao, P. S. A Material Removal Analysis of Electrochemical Machining Using Flat-End Cathode. *J. Mater. Process. Technol.* **2003**, *140* (1–3), 264–268. https://doi.org/10.1016/s0924-0136(03)00791-x.

(128) Weber, O.; Natter, H.; Bähre, D. Pulse Electrochemical Machining of Cast Iron: A Layer-Based Approach for Modeling the Steady-State Dissolution Current. *J. Solid State Electrochem.* **2015**, *19* (5), 1265–1276. https://doi.org/10.1007/s10008-014-2735-1.

(129) Gomez-Gallegos, A. A.; Mill, F.; Mount, A. R. Surface Finish Control by Electrochemical Polishing in Stainless Steel 316 Pipes. *J. Manuf. Process.* **2016**, *23*, 83–89. https://doi.org/10.1016/j.jmapro.2016.05.010.

(130) Masuzawa, T.; Kimura, M. Electrochemical Surface Finishing of Tungsten Carbide Alloy. *CIRP Ann.* **1991**, *40* (1), 199–202. https://doi.org/10.1016/s0007-8506(07)61967-2.

(131) Lochynski, P.; Kowalski, M.; Szczygiel, B.; Kuczewski, K. Improvement of the Stainless Steel Electropolishing Process by Organic Additives. *Pol. J. Chem. Technol.* **2016**, *18* (4), 76–81. https://doi.org/10.1515/pjct-2016-0074.

(132) Jäckel, N.; Weingarth, D.; Zeiger, M.; Aslan, M.; Grobelsek, I.; Presser, V. Comparison of Carbon Onions and Carbon Blacks as Conductive Additives for Carbon Supercapacitors in Organic Electrolytes. *J. Power Sources* **2014**, *272*, 1122–1133. https://doi.org/10.1016/j.jpowsour.2014.08.090.

(133) Hanna, F.; Hamid, Z. A.; Aal, A. A. Controlling Factors Affecting the Stability and Rate of Electroless Copper Plating. *Mater. Lett.* **2004**, *58* (1), 104–109. https://doi.org/10.1016/S0167-577X(03)00424-5.

(134) Piotrowski, O.; Madore, C.; Landolt, D. The Mechanism of Electropolishing of Titanium in Methanol-Sulfuric Acid Electrolytes. *J. Electrochem. Soc.* **1998**, *145* (7), 2362. https://doi.org/10.1149/1.1838644.

(135) Christophersen, M.; Carstensen, J.; Voigt, K.; Föll, H. Organic and Aqueous Electrolytes Used for Etching Macro- and Mesoporous Silicon. *Phys. Status Solidi A* **2003**, *197* (1), 34–38. https://doi.org/10.1002/pssa.200306464.

(136) Tajima, S.; Baba, N. Anodic Polishing and Passivation of Iron in the Non-Aqueous Sulphamic-Acid-Formamide System. *Electrochimica Acta* **1962**, *7* (3), 355–367. https://doi.org/10.1016/0013-4686(62)87010-8.

(137) Turner, D. R. Electropolishing Silicon in Hydrofluoric Acid Solutions. *J. Electrochem. Soc.* **1958**, *105* (7), 402. https://doi.org/10.1149/1.2428873.

(138) Abdel-Fattah, T. M.; Loftis, D.; Mahapatro, A. Nanosized Controlled Surface Pretreatment of Biometallic Alloy 316L Stainless Steel. *J. Biomed. Nanotechnol.* **2011**, *7* (6), 794–800. https://doi.org/10.1166/jbn.2011.1346.

(139) Ghanavati, S.; Shishesaz, M. R.; Farzam, M.; Danaee, I. Effects of Surface Treatment on Corrosion Resistance of 304L and 316L Stainless Steel Implants in Hank's Solution. **2016**, *5* (1), 8.

(140) Alrbaey, K.; Wimpenny, D. I.; Al-Barzinjy, A. A.; Moroz, A. Electropolishing of Re-Melted SLM Stainless Steel 316L Parts Using Deep Eutectic Solvents: 3 × 3 Full Factorial Design. *J. Mater. Eng. Perform.* **2016**, *25* (7), 2836–2846. https://doi.org/10.1007/s11665-016-2140-2.

(141) Kuhn, A. The Electropolishing of Titanium and Its Alloys. *Met. Finish.* **2004**, *102* (6), 80–86. https://doi.org/10.1016/S0026-0576(04)82510-8.

(142) Yi, J.; Ding, Y.; Zhao, S.; Ji, B.; Zhou, J. A Novel Technique of Polishing Gear Working Surface Using PECMP. *Int. J. Precis. Eng. Manuf.* **2009**, *10* (4), 57–62. https://doi.org/10.1007/s12541-009-0071-7.

(143) Simka, W.; Mosiałek, M.; Nawrat, G.; Nowak, P.; Żak, J.; Szade, J.; Winiarski, A.; Maciej, A.; Szyk-Warszyńska, L. Electrochemical Polishing of Ti–13Nb–13Zr Alloy. *Surf. Coat. Technol.* **2012**, *213*, 239–246. https://doi.org/10.1016/j.surfcoat.2012.10.055.

(144) Chang, S.-C.; Shieh, J.-M.; Huang, C.-C.; Dai, B.-T.; Feng, M.-S. Pattern Effects on Planarization Efficiency of Cu Electropolishing. *Jpn. J. Appl. Phys.* **2002**, *41* (12R), 7332. https://doi.org/10.1143/JJAP.41.7332.

(145) Chen, S. C.; Tu, G. C.; Huang, C. A. The Electrochemical Polishing Behavior of Porous Austenitic Stainless Steel (AISI 316L) in Phosphoric-Sulfuric Mixed Acids. *Surf. Coat. Technol.* **2005**, *200* (7), 2065–2071. https://doi.org/10.1016/j.surfcoat.2005.06.008.

(146) Fushimi, K.; Stratmann, M.; Hassel, A. W. Electropolishing of NiTi Shape Memory Alloys in Methanolic H2SO4. *Electrochimica Acta* **2006**, *52* (3), 1290–1295. https://doi.org/10.1016/j.electacta.2006.07.030.

(147) Ramasawmy, H.; Blunt, L. 3D Surface Topography Assessment of the Effect of Different Electrolytes during Electrochemical Polishing of EDM Surfaces. *Int. J. Mach. Tools Manuf.* **2002**, *42* (5), 567–574. https://doi.org/10.1016/S0890-6955(01)00154-7.

(148) Pa, P. S. Effective Form Design of Electrode in Electrochemical Smoothing of End Turning Surface Finishing. *J. Mater. Process. Technol.* **2008**, *195* (1–3), 44–52. https://doi.org/10.1016/j.jmatprotec.2007.04.107.

(149) Zaytsev, A.; Agafonov, I.; Gimaev, N.; Moukhoutdinov, R.; Belogorsky, A. Precise Pulse Electrochemical Machining by Bipolar Current: Aspects of Effective Technological Application. *J. Mater. Process. Technol.* **2004**, *149* (1–3), 419–425. https://doi.org/10.1016/j.jmatprotec.2003.10.054.

(150) Burstein, G. T.; Hutchings, I. M.; Sasaki, K. Electrochemically Induced Annealing of Stainless-Steel Surfaces. *Nature* **2000**, *407* (6806), 885–887. https://doi.org/10.1038/35038040.

(151) Nazneen, F.; Galvin, P.; Arrigan, D. W. M.; Thompson, M.; Benvenuto, P.; Herzog, G. Electropolishing of Medical-Grade Stainless Steel in Preparation for Surface Nano-Texturing. *J. Solid State Electrochem.* **2012**, *16* (4), 1389–1397. https://doi.org/10.1007/s10008-011-1539-9.

(152) Park, J. W.; Lee, D. W. Pulse Electrochemical Polishing for Microrecesses Based on a Coulostatic Analysis. *Int. J. Adv. Manuf. Technol.* **2009**, *40* (7–8), 742–748. https://doi.org/10.1007/s00170-008-1391-y.

(153) Yi, J.; Ding, Y.; Zhao, S.; Ji, B.; Zhou, J. A Novel Technique of Polishing Gear Working Surface Using PECMP. *Int. J. Precis. Eng. Manuf.* **2009**, *10* (4), 57–62. https://doi.org/10.1007/s12541-009-0071-7.

(154) Yin, L.; Zhang, W. M.; Yan, Y.; Tu, Q. S.; Zhang, Z. J. Study of Electrochemical Finishing with Magnetic Field and High-Frequency Group Pulse. *Proc. - 2010 Int. Conf. Digit. Manuf. Autom. ICDMA 2010* **2010**, *2*, 440–443. https://doi.org/10.1109/ICDMA.2010.77.

(155) Haisch, T.; Mittemeijer, E.; Schultze, J. W. Electrochemical Machining of the Steel 100Cr6 in Aqueous NaCl and NaNO3 Solutions: Microstructure of Surface Films Formed by Carbides. *Electrochimica Acta* **2001**, *47* (1), 235–241. https://doi.org/10.1016/S0013-4686(01)00561-8.

(156) Sueptitz, R.; Tschulik, K.; Becker, C.; Stoica, M.; Uhlemann, M.; Eckert, J.; Gebert, A. Micropatterning of Fe-Based Bulk Metallic Glass Surfaces by Pulsed Electrochemical Micromachining. *J. Mater. Res.* **2012**, *27* (23), 3033–3040. https://doi.org/10.1557/jmr.2012.347.

(157) CoteaţĂ, M.; Pop, N.; Schulze, H. P.; SlĂtineanu, L.; Dodun, O. Investigation on Hybrid Electrochemical Discharge Drilling Process Using Passivating Electrolyte. *Procedia CIRP* **2016**, *42* (Isem Xviii), 778–782. https://doi.org/10.1016/j.procir.2016.02.318.

(158) Yao, Y.; Qiao, L. J.; Volinsky, A. A. Hydrogen Effects on Stainless Steel Passive Film Fracture Studied by Nanoindentation. *Corros. Sci.* **2011**, *53* (9), 2679–2683. https://doi.org/10.1016/j.corsci.2011.05.025.

(159) Abdel-Fattah, T. M.; Loftis, D.; Mahapatro, A. Nanosized Controlled Surface Pretreatment of Biometallic Alloy 316L Stainless Steel. *J. Biomed. Nanotechnol.* **2011**, *7* (6), 794–800. https://doi.org/10.1166/jbn.2011.1346.

(160) Alrbaey, K.; Wimpenny, D. I.; Al-Barzinjy, A. A.; Moroz, A. Electropolishing of Re-Melted SLM Stainless Steel 316L Parts Using Deep Eutectic Solvents: 3 × 3 Full

Factorial Design. *J. Mater. Eng. Perform.* **2016**, *25* (7), 2836–2846. https://doi.org/10.1007/s11665-016-2140-2.

(161) Hryniewicz, T.; Rokosz, K.; Rokicki, R.; Prima, F. Nanoindentation and XPS Studies of Titanium TNZ Alloy after Electrochemical Polishing in a Magnetic Field. *Materials* **2015**, *8* (1), 205–215. https://doi.org/10.3390/ma8010205.

(162) Jiang, G. U. O.; Goh, M. H.; Pan, W.; Huang, R.; Xiaohua, L. E. E.; Bin, W.; Nai, S. M. L.; Jun, W. E. I. Investigation on Surface Integrity of Electron Beam Melted Ti-6Al-4 V by Precision Grinding and Electropolishing. *Chin. J. Aeronaut.* **2021**, *34* (12), 28–38. https://doi.org/10.1016/j.cja.2020.08.014.

(163) García-Blanco, M. B.; Díaz-Fuentes, M.; Espinosa, E.; Mancisidor, A. M.; Vara, G. Comparative Study of Different Surface Treatments Applied to Ti6Al4V Parts Produced by Selective Laser Melting. *Trans. Inst. Met. Finish.* **2021**, *99* (5), 274–280. https://doi.org/10.1080/00202967.2021.1898171.

(164) Kiyoshi, T.; Masahisa, H.; Ker-Kong, C.; Yuki, N.; Hiroshi, K.; Yoshio, K. Electropolishing of CP Titanium and Its Alloys in an Alcoholic Solution-Based Electrolyte. *Dent. Mater. J.* **2008**, *27* (2), 258–265. https://doi.org/10.4012/dmj.27.258.

(165) Fayazfar, H.; Rishmawi, I.; Vlasea, M. Electrochemical-Based Surface Enhancement of Additively Manufactured Ti-6Al-4V Complex Structures. *J. Mater. Eng. Perform.* **2021**, *30* (3), 2245–2255. https://doi.org/10.1007/s11665-021-05512-x.

(166) Dong, G.; Marleau-Finley, J.; Zhao, Y. F. Investigation of Electrochemical Post-Processing Procedure for Ti-6Al-4V Lattice Structure Manufactured by Direct Metal Laser Sintering (DMLS). *Int. J. Adv. Manuf. Technol.* **2019**, *104* (9–12), 3401–3417. https://doi.org/10.1007/s00170-019-03996-5.

(167) Zhang, Y.; Jianzhong, L. I.; Che, S. Electropolishing Mechanism of Ti-6Al-4V Alloy Fabricated by Selective Laser Melting. *Int. J. Electrochem. Sci.* **2018**, *13* (5), 4792–4807. https://doi.org/10.20964/2018.05.79.

(168) Mingear, J.; Zhang, B.; Hartl, D.; Elwany, A. Effect of Process Parameters and Electropolishing on the Surface Roughness of Interior Channels in Additively Manufactured Nickel-Titanium Shape Memory Alloy Actuators. *Addit. Manuf.* **2019**, *27*, 565–575. https://doi.org/10.1016/j.addma.2019.03.027.

(169) Longhitano, G. A.; Larosa, M. A.; Munhoz, A. L. J.; Zavaglia, C. A. de C.; Ierardi, M. C. F. Surface Finishes for Ti-6Al-4V Alloy Produced by Direct Metal Laser Sintering. *Mater. Res.* **2015**, *18*, 838–842. https://doi.org/10.1590/1516-1439.014415.

(170) Wu, Y.-C.; Kuo, C.-N.; Chung, Y.-C.; Ng, C.-H.; Huang, J. C. Effects of Electropolishing on Mechanical Properties and Bio-Corrosion of Ti6Al4V Fabricated by Electron Beam Melting Additive Manufacturing. *Materials* **2019**, *12* (9), 1466. https://doi.org/10.3390/ma12091466.

(171) Asgari, V.; Noormohammadi, M.; Ramazani, A.; Kashi, M. A. A New Approach to Electropolishing of Pure Ti Foil in Acidic Solution at Room Temperature for the Formation of Ordered and Long TiO2 Nanotube Arrays. *Corros. Sci.* **2018**, *136*, 38–46. https://doi.org/10.1016/j.corsci.2018.02.040.

(172) Pyka, G.; Burakowski, A.; Kerckhofs, G.; Moesen, M.; Van Bael, S.; Schrooten, J.; Wevers, M. Surface Modification of Ti6Al4V Open Porous Structures Produced by Additive Manufacturing. *Adv. Eng. Mater.* **2012**, *14* (6), 363–370. https://doi.org/10.1002/adem.201100344.

(173) Liu, L.; Wu, S. Q.; Gu, H. F.; Yang, Y.; Wang, H.; Huang, A. J. Effect of The Number of Hydroxyls and Carbons on the Solubility of Sodium Chloride in Alcohol and The Electropolishing Behavior of Ti-6Al-4V Alloy in Alcohol-Salt System. *J. Electrochem. Soc.* **2021**, *168* (9), 093503. https://doi.org/10.1149/1945-7111/ac24b3.

(174) Nicholas C, F.; Daniel J, S.; Marko, K. Non-Acid, Alcohol-Based Electropolishing Enables High-Quality Electron Backscatter Diffraction Characterization of Titanium and Its Alloys: Application to Pure Ti and Ti-6Al-4V. *Mater. Charact.* **2020**, *166*, 110406. https://doi.org/10.1016/j.matchar.2020.110406.

(175) Karim, W. O. Electropolishing of Pure Metallic Titanium in a Deep Eutectic Solvent. *Arab. J. Chem.* **2021**, *14* (1), 102906. https://doi.org/10.1016/j.arabjc.2020.11.012.

(176) Barnes, P.; Savva, A.; Dixon, K.; Bull, H.; Rill, L.; Karsann, D.; Croft, S.; Schimpf, J.; Xiong, H. Electropolishing Valve Metals with a Sulfuric Acid-Methanol Electrolyte at Low Temperature. *Surf. Coat. Technol.* **2018**, *347*, 150–156. https://doi.org/10.1016/j.surfcoat.2018.04.082.

(177) Jung, J.-H.; Park, H.-K.; Lee, B. S.; Choi, J.; Seo, B.; Kim, H. K.; Kim, G. H.; Kim, H. G. Study on Surface Shape Control of Pure Ti Fabricated by Electron Beam Melting Using Electrolytic Polishing. *Surf. Coat. Technol.* **2017**, *324*, 106–110. https://doi.org/10.1016/j.surfcoat.2017.05.061.

(178) Bard, A. J.; Faulkner, L. R. *Electrochemical Methods: Fundamentals and Applications*; Wiley, 2001.

(179) Hou, Y.; Li, R.; Liang, J.; Su, P.; Ju, P. Electropolishing of Al and Al Alloys in AlCl 3 /Trimethylamine Hydrochloride Ionic Liquid. *Surf. Coat. Technol.* **2018**, *335*, 72–79. https://doi.org/10.1016/j.surfcoat.2017.12.028.

(180) Li, D.; Li, N.; Xia, G.; Zheng, Z.; Wang, J.; Xiao, N.; Zhai, W.; Wu, G. An In-Situ Study of Copper Electropolishing in Phosphoric Acid Solution. *Int J Electrochem Sci* **2013**, *8*, 6.

(181) Zhao, H.; Humbeeck, J. V.; Sohier, J. Electrochemical Polishing of 316L Stainless Steel Slotted Tube Coronary Stents: An Investigation of Material Removal and Surface Roughness. **2003**, *8* (2), 12.

(182) Teixeira, A. F. Development of an Electropolishing Method for Titanium Materials. 91.

(183) Yin, L.; Zhang, W.; Yan, Y.; Tu, Q.; Zhang, Z. Study of Electrochemical Finishing with Magnetic Field and High-Frequency Group Pulse. In *2010 International Conference on Digital Manufacturing & Automation*; 2010; pp 440–443. https://doi.org/10.1109/icdma.2010.77.

(184) Davydov, A. D.; Shaldaev, V. S.; Malofeeva, A. N.; Savotin, I. V. Electrochemical Dissolution of Tungsten under Pulsed Conditions. 4.

(185) Jeong, H.-J.; Park, J.; Jeong, K. J.; Hwang, N. M.; Hong, S.-T.; Han, H. N. Effect of Pulsed Electric Current on TRIP-Aided Steel. *Int. J. Precis. Eng. Manuf.-Green Technol.* **2019**, *6* (2), 315–327. https://doi.org/10.1007/s40684-019-00060-1.

(186) Taylor, E. J.; Inman, M. Electrochemical Surface Finishing. *Electrochem. Soc. Interface* **2014**, 5. https://doi.org/10.1149/2.f05143if.

(187) Inman, M.; Hall, T.; Garich, H.; Taylor, E. J. Environmentally Benign Electropolishing of Biomedical Alloys. In *Volume 2: Processing*; American Society of Mechanical Engineers: Detroit, Michigan, USA, 2014; p V002T02A027. https://doi.org/10.1115/MSEC2014-4035.

(188) Vara, G. A.; Butrón, E. J.; BelénGarcía-Blanco, M. Challenges and Opportunities in next Generation of Electropolishing Surfaces. *Surf. Eng.* **2015**, *31* (6), 397–398. https://doi.org/10.1179/0267084415z.000000000624.

(189) Lin, C.-C.; Hu, C.-C.; Lee, T.-C. Electropolishing of 304 Stainless Steel: Interactive Effects of Glycerol Content, Bath Temperature, and Current Density on Surface Roughness and Morphology. *Surf. Coat. Technol.* **2009**, *204* (4), 448–454. https://doi.org/10.1016/j.surfcoat.2009.08.005.

(190) Zhao, X.; Corcoran, S. G.; Kelley, M. J. Sulfuric Acid–Methanol Electrolytes as an Alternative to Sulfuric–Hydrofluoric Acid Mixtures for Electropolishing of Niobium. *J. Appl. Electrochem.* **2011**, *41* (6), 633–643. https://doi.org/10.1007/s10800-011-0276-1.

(191) Eliaz, N.; Nissan, O. Innovative Processes for Electropolishing of Medical Devices Made of Stainless Steels. *J. Biomed. Mater. Res. A* **2007**, *83A* (2), 546–557. https://doi.org/10.1002/jbm.a.31429.

(192) Danilov, I.; Hackert-Oschätzchen, M.; Zinecker, M.; Meichsner, G.; Edelmann, J.; Schubert, A. Process Understanding of Plasma Electrolytic Polishing through Multiphysics Simulation and Inline Metrology. *Micromachines* **2019**, *10* (3), 214. https://doi.org/10.3390/mi10030214.

(193) Brent, D.; Saunders, T. A.; Garcia Moreno, F.; Tyagi, P. Taguchi Design of Experiment for the Optimization of Electrochemical Polishing of Metal Additive Manufacturing Components. In *Proceedings of the ASME 2016 International Mechanical Engineering*

Congress and Exposition; 2016; p V002T02A014. https://doi.org/10.1115/imece2016-67492.

(194) Rotty, C.; Doche, M.-L.; Mandroyan, A.; Hihn, J.-Y.; Montavon, G.; Moutarlier, V. Comparison of Electropolishing Behaviours of TSC, ALM and Cast 316L Stainless Steel in H 3 PO 4 /H 2 SO 4. *Surf. Interfaces* **2017**, *6*, 170–176. https://doi.org/10.1016/j.surfin.2017.01.008.

(195) Ali, U.; Fayazfar, H.; Ahmed, F.; Toyserkani, E. Internal Surface Roughness Enhancement of Parts Made by Laser Powder-Bed Fusion Additive Manufacturing. *Vacuum* **2020**, *177*, 109314. https://doi.org/10.1016/j.vacuum.2020.109314.

(196) Chang, J.-K.; Lee, C.-Y.; Tzeng, Y.-C.; Lin, M.-H.; Ger, M.-D.; Kao, C.-H.; Chen, C.-P.; Jen, K.-K.; Jian, S.-Y. Electropolishing of Additive Manufactured 17-4 PH Stainless Steel Using Sulfuric Acid. *Int. J. Electrochem. Sci.* **2021**, *16* (3).

(197) Han, W.; Fang, F. Fundamental Aspects and Recent Developments in Electropolishing. *Int. J. Mach. Tools Manuf.* **2019**, *139*, 1–23. https://doi.org/10.1016/j.ijmachtools.2019.01.001.

(198) Mahardika, M.; Setyawan, M. A.; Sriani, T.; Miki, N.; Prihandana, G. S. Electropolishing Parametric Optimization of Surface Quality for the Fabrication of a Titanium Microchannel Using the Taguchi Method. *Machines* **2021**, *9* (12), 325. https://doi.org/10.3390/machines9120325.

(199) Choi, S.-G.; Kim, S.-H.; Choi, W.-K.; Lee, E.-S. The Optimum Condition Selection of Electrochemical Polishing and Surface Analysis of the Stainless Steel 316L by the Taguchi Method. *Int. J. Adv. Manuf. Technol.* **2016**, *82* (9), 1933–1939. https://doi.org/10.1007/s00170-015-7404-8.

(200) Huang, P.; Lai, J.; Han, L.; Yang, F.-Z.; Jiang, L.-M.; Su, J.-J.; Tian, Z.-W.; Tian, Z.-Q.; Zhan, D. Electropolishing of Titanium Alloy under Hydrodynamic Mode. *Sci. China Chem.* **2016**, *59* (11), 1525–1528. https://doi.org/10.1007/s11426-016-0211-y.

(201) Kityk, A. A.; Danilov, F. I.; Protsenko, V. S.; Pavlik, V.; Boča, M.; Halahovets, Y. Electropolishing of Two Kinds of Bronze in a Deep Eutectic Solvent (Ethaline). *Surf. Coat. Technol.* **2020**, *397*, 126060. https://doi.org/10.1016/j.surfcoat.2020.126060.

(202) Dickinson, E. J. F.; Ekström, H.; Fontes, E. COMSOL Multiphysics®: Finite Element Software for Electrochemical Analysis. A Mini-Review. *Electrochem. Commun.* **2014**, *40*, 71–74. https://doi.org/10.1016/j.elecom.2013.12.020.

(203) Jemmely, P.; Mischler, S.; Landolt, D. Electrochemical Modeling of Passivation Phenomena in Tribocorrosion. *Wear* **2000**, *237* (1), 63–76. https://doi.org/10.1016/s0043-1648(99)00314-2.

(204) Lee, S.-J.; Lai, J.-J.; Lin, Y.-T. Simulation Of The Formation Mechanism Of A Viscous Layer For The Electropolishing Process. *WIT Trans. Eng. Sci.* **2005**, *48*. https://doi.org/10.2495/ECOR050201.

(205) Tang, L.; Gan, W. M. Utilization of Flow Field Simulations for Cathode Design in Electrochemical Machining of Aerospace Engine Blisk Channels. *Int. J. Adv. Manuf. Technol.* **2014**, *72* (9), 1759–1766. https://doi.org/10.1007/s00170-014-5814-7.

(206) Tailor, P. B.; Agrawal, A.; Joshi, S. S. Numerical Simulation and Experimentation on Electrochemical Buffing. *J. Manuf. Sci. Eng.* **2016**, *138* (6). https://doi.org/10.1115/1.4032087.

(207) Mosavat, M.; Rahimi, A. Simulation and Experimental Study on the Effect of Abrasive Size, Rotational Speed, and Machining Gap during Ultra-Precision Polishing of Monocrystalline Silicon. *Colloids Surf. Physicochem. Eng. Asp.* **2019**, *575*, 50–56. https://doi.org/10.1016/j.colsurfa.2019.05.005.

(208) Chen, Y.; Zhou, X.; Chen, P.; Wang, Z. Electrochemical Machining Gap Prediction with Multi-Physics Coupling Model Based on Two-Phase Turbulence Flow. *Chin. J. Aeronaut.* **2020**, *33* (3), 1057–1063. https://doi.org/10.1016/j.cja.2019.03.006.

(209) Liu, G.; Zhang, Y.; Natsu, W. Influence of Electrolyte Flow Mode on Characteristics of Electrochemical Machining with Electrolyte Suction Tool. *Int. J. Mach. Tools Manuf.* **2019**, *142*, 66–75. https://doi.org/10.1016/j.ijmachtools.2019.04.010.

(210) Cao, W.; Wang, D.; Zhu, D. Modeling and Experimental Validation of Interelectrode Gap in Counter-Rotating Electrochemical Machining. *Int. J. Mech. Sci.* **2020**, *187*, 105920. https://doi.org/10.1016/j.ijmecsci.2020.105920.

(211) Zhu, D.; Gu, Z.; Xue, T.; Liu, A. Simulation and Experimental Investigation on a Dynamic Lateral Flow Mode in Trepanning Electrochemical Machining. *Chin. J. Aeronaut.* **2017**, *30* (4), 1624–1630. https://doi.org/10.1016/j.cja.2017.02.020.

(212) Liu, W.; Ao, S.; Li, Y.; Liu, Z.; Zhang, H.; Manladan, S. M.; Luo, Z.; Wang, Z. Effect of Anodic Behavior on Electrochemical Machining of TB6 Titanium Alloy. *Electrochimica Acta* **2017**, *233*, 190–200. https://doi.org/10.1016/j.electacta.2017.03.025.

(213) Jordan, M. I.; Mitchell, T. M. Machine Learning: Trends, Perspectives, and Prospects. *Science* **2015**, *349* (6245), 255–260. https://doi.org/10.1126/science.aaa8415.

(214) Mahesh, B. *Machine Learning Algorithms -A Review*; 2019. https://doi.org/10.21275/ART20203995.

(215) Oladipupo, T. Types of Machine Learning Algorithms. In *New Advances in Machine Learning*; Zhang, Y., Ed.; InTech, 2010. https://doi.org/10.5772/9385.

(216) Grzesik, W. A Revised Model for Predicting Surface Roughness in Turning. *Wear* **1996**, *194* (1), 143–148. https://doi.org/10.1016/0043-1648(95)06825-2.

(217) Zhou, X.; Xi, F. Modeling and Predicting Surface Roughness of the Grinding Process. *Int. J. Mach. Tools Manuf.* **2002**, *42* (8), 969–977. https://doi.org/10.1016/s0890-6955(02)00011-1.

(218) Li, Z.; Zhang, Z.; Shi, J.; Wu, D. Prediction of Surface Roughness in Extrusion-Based Additive Manufacturing with Machine Learning. *Robot. Comput.-Integr. Manuf.* **2019**, *57*, 488–495. https://doi.org/10.1016/j.rcim.2019.01.004.

(219) Wang, R.; Cheng, M. N.; Loh, Y. M.; Wang, C.; Fai Cheung, C. Ensemble Learning with a Genetic Algorithm for Surface Roughness Prediction in Multi-Jet Polishing. *Expert Syst. Appl.* **2022**, *207*, 118024. https://doi.org/10.1016/j.eswa.2022.118024.

(220) *McGeough: Principles of electrochemical machining - Google Scholar*. https://scholar.google.com/scholar_lookup?title=Principles%20of%20Electrochemical%20Machining&publication_year=1974&author=J.A.%20McGeough (accessed 2020-07-23).

(221) Schaller, T.; Bohn, L.; Mayer, J.; Schubert, K. Microstructure Grooves with a Width of Less than 50 Mm Cut with Ground Hard Metal Micro End Mills. *Precis. Eng.* **1999**, *23* (4), 229–235. https://doi.org/10.1016/S0141-6359(99)00011-2.

(222) Datta, M.; Vercruysse, D. Transpassive Dissolution of 420 Stainless Steel in Concentrated Acids under Electropolishing Conditions. *J. Electrochem. Soc.* **1990**, *137* (10), 3016. https://doi.org/10.1149/1.2086151.

(223) Vidal, R.; West, A. C. Copper Electropolishing in Concentrated Phosphoric Acid: I . Experimental Findings. *J. Electrochem. Soc.* **1995**, *142* (8), 2682. https://doi.org/10.1149/1.2050074.

(224) Elmalah, N. M.; Elhaliem, S. M. A.; Ahmed, A. M.; Ghozy, S. M. Effect of Some Organic Aldehydes on the Electropolishing of Copper in Phosphoric Acid. *Int J Electrochem Sci* **2012**, *7*, 20.

(225) Dai, G.; Hu, X.; Degenhardt, J. Bottom-up Approach for Traceable Calibration of Tip Geometry of Stylus Profilometer. *Surf. Topogr. Metrol. Prop.* **2022**, *10* (1), 015018. https://doi.org/10.1088/2051-672x/ac4f36.

(226) Choi, D.-J.; Choi, J.-S.; Choi, I.-M.; Kim, S.-H. A Newly Designed Contact Profiler for Microstructure. *J. Korean Soc. Precis. Eng.* **2002**, *19* (3), 39–45.

(227) Poon, C. Y.; Bhushan, B. Comparison of Surface Roughness Measurements by Stylus Profiler, AFM and Non-Contact Optical Profiler. *Wear* **1995**, *190* (1), 76–88. https://doi.org/10.1016/0043-1648(95)06697-7.

(228) Ren, N.; Yu, Y.; Li, H. Improved Roughness Measurement Method Using Fiber Bragg Gratings and Machine Learning. *Sens. Actuators Phys.* **2021**, *332*, 113161. https://doi.org/10.1016/j.sna.2021.113161.

(229) Kissling, S.; Bade, K.; Börner, M.; Klymyshyn, D. M. Electropolishing as a Method for Deburring High Aspect Ratio Nickel RF MEMS. *Microsyst. Technol.* **2010**, *16* (8–9), 1361–1367. https://doi.org/10.1007/s00542-010-1075-z.

(230) Shin, T. H.; Baek, S. Y.; Lee, E. S. Micro Electrochemical Polishing of TiNi Alloy for Medical Stent. *Adv. Mater. Res.* **2009**, *79–82*, 155–158. https://doi.org/10.4028/www.scientific.net/AMR.79-82.155.

(231) Berestovskyi, D.; Soriaga, M.; Lomeli, P.; James, J.; Sessions, B.; Xiao, H.; Hung, W. Electrochemical Polishing of Microcomponents; 8th International Conference on MicroManufacturing (ICOMM 2013), 2013.

(232) Yuzhakov, V. V.; Chang, H.-C.; Miller, A. E. Pattern Formation during Electropolishing. *Phys. Rev. B* **1997**, *56* (19), 12608–12624. https://doi.org/10.1103/physrevb.56.12608.

(233) Yuzhakov, V. V.; Takhistov, P. V.; Miller, A. E.; Chang, H.-C. Pattern Selection during Electropolishing Due to Double-Layer Effects. *Chaos Interdiscip. J. Nonlinear Sci.* **1999**, *9* (1), 62–77. https://doi.org/10.1063/1.166380.

(234) Guo, W.; Johnson, D. T. Pattern Selection with Anisotropy during Aluminum Electropolishing. *J. Cryst. Growth* **2004**, *268* (1), 258–271. https://doi.org/10.1016/j.jcrysgro.2004.04.039.

(235) Zhao, G.-Y.; Xu, C.-L.; Guo, D.-J.; Li, H.; Li, H.-L. Patterning Polycrystalline Aluminum by Electropolishing at Low Voltages. *J. Solid State Electrochem.* **2006**, *10* (5), 266–269. https://doi.org/10.1007/s10008-005-0681-7.

(236) Bandyopadhyay, S.; Miller, A. E.; Chang, H. C.; Banerjee, G.; Yuzhakov, V.; Yue, D.-F.; Ricker, R. E.; Jones, S.; Eastman, J. A.; Baugher, E.; Chandrasekhar, M. Electrochemically Assembled Quasi-Periodic Quantum Dot Arrays. *Nanotechnology* **1996**, *7* (4), 360–371. https://doi.org/10.1088/0957-4484/7/4/010.

(237) Vignal, V.; Roux, J. C.; Flandrois, S.; Fevrier, A. Nanoscopic Studies of Stainless Steel Electropolishing. *Corros. Sci.* **2000**, *42* (6), 1041–1053. https://doi.org/10.1016/s0010-938x(99)00094-3.

(238) Kido, H.; Fujita, K.; Osaki, K.; Sakurai, T.; Inoue, A. Spiral Pattern Formation on Bulk Metallic Glass by Electropolishing. *Chem. Lett.* **2011**, *40* (2), 191–193. https://doi.org/10.1246/cl.2011.191.

(239) Slimani, A.; Iratni, A.; Chazalviel, J.-N.; Gabouze, N.; Ozanam, F. Experimental Study of Macropore Formation in P-Type Silicon in a Fluoride Solution and the Transition between Macropore Formation and Electropolishing. *Electrochimica Acta* **2009**, *54* (11), 3139–3144. https://doi.org/10.1016/j.electacta.2008.11.052.

(240) Christophersen, M.; Carstensen, J.; Rönnebeck, S.; Jäger, C.; Jäger, W.; Föll, H. Crystal Orientation Dependence and Anisotropic Properties of Macropore Formation of P- and

n-Type Silicon. *J. Electrochem. Soc.* **2001**, *148* (6), E267. https://doi.org/10.1149/1.1369378.

(241) Hinds, G.; Spada, F. E.; Coey, J. M. D.; Ní Mhíocháin, T. R.; Lyons, M. E. G. Magnetic Field Effects on Copper Electrolysis. *J. Phys. Chem. B* **2001**, *105* (39), 9487–9502. https://doi.org/10.1021/jp010581u.

(242) Hryniewicz, T.; Rokicki, R.; Rokosz, K. Surface Characterization of AISI 316L Biomaterials Obtained by Electropolishing in a Magnetic Field. *Surf. Coat. Technol.* **2008**, *202* (9), 1668–1673. https://doi.org/10.1016/j.surfcoat.2007.07.067.

(243) US7632390B2 - Apparatus and Method for Enhancing Electropolishing Utilizing Magnetic Fields - Google Patents. https://patents.google.com/patent/US7632390B2/en (accessed 2020-07-20).

(244) Hryniewicz, T.; Rokosz, K.; Filippi, M. Biomaterial Studies on AISI 316L Stainless Steel after Magnetoelectropolishing. *Materials* **2009**, *2* (1), 129–145. https://doi.org/10.3390/ma2010129.

(245) Hryniewicz, T.; Rokicki, R.; Rokosz, K. METAL SURFACE MODIFICATION BY MAGNETOELECTROPOLISHING. In *16th International Metallurgical & Materials Conference METAL*; 2007; p 8. https://doi.org/10.1179/174591907x246537.

(246) Hryniewicz, T.; Rokosz, K.; Rokicki, R. Electrochemical and XPS Studies of AISI 316L Stainless Steel after Electropolishing in a Magnetic Field. *Corros. Sci.* **2008**, *50* (9), 2676–2681. https://doi.org/10.1016/j.corsci.2008.06.048.

(247) Hryniewicz, T.; Rokosz, K. Analysis of XPS Results of AISI 316L SS Electropolished and Magnetoelectropolished at Varying Conditions. *Surf. Coat. Technol.* **2010**, *204* (16), 2583–2592. https://doi.org/10.1016/j.surfcoat.2010.02.005.

(248) Hryniewicz, T.; Rokicki, R.; Rokosz, K. Corrosion and Surface Characterization of Titanium Biomaterial after Magnetoelectropolishing. *Surf. Coat. Technol.* **2009**, *203* (10), 1508–1515. https://doi.org/10.1016/j.surfcoat.2008.11.028.

(249) Hryniewicz, T.; Rokosz, K.; Valíček, J.; Rokicki, R. Effect of Magnetoelectropolishing on Nanohardness and Young's Modulus of Titanium Biomaterial. *Mater. Lett.* **2012**, *83*, 69–72. https://doi.org/10.1016/j.matlet.2012.06.010.

(250) Cissé, O.; Savadogo, O.; Wu, M.; Yahia, L. Effect of Surface Treatment of NiTi Alloy on Its Corrosion Behavior in Hanks' Solution. *J. Biomed. Mater. Res.* **2002**, *61* (3), 339–345. https://doi.org/10.1002/jbm.10114.

(251) Seddon, K. R. Ionic Liquids for Clean Technology. *J. Chem. Technol. Biotechnol.* **1997**, *68* (4), 351–356. https://doi.org/10.1002/(SICI)1097-4660(199704)68:4<351::AID-JCTB613>3.0.CO;2-4.

(252) Lin, C.-C.; Hu, C.-C. Electropolishing of 304 Stainless Steel: Surface Roughness Control Using Experimental Design Strategies and a Summarized Electropolishing

Model. *Electrochimica Acta* **2008**, *53* (8), 3356–3363. https://doi.org/10.1016/j.electacta.2007.11.075.

(253) Abbott, A. P.; Capper, G.; Davies, D. L.; Rasheed, R. K.; Tambyrajah, V. Novel Ambient Temperature Ionic Liquids for Zinc and Zinc Alloy Electrodeposition. *Trans. IMF* **2001**, *79* (6), 204–206. https://doi.org/10.1080/00202967.2001.11871395.

(254) Abbott, A. P.; Capper, G.; McKenzie, K. J.; Ryder, K. S. Voltammetric and Impedance Studies of the Electropolishing of Type 316 Stainless Steel in a Choline Chloride Based Ionic Liquid. *Electrochimica Acta* **2006**, *51* (21), 4420–4425. https://doi.org/10.1016/j.electacta.2005.12.030.

(255) Diaz, A. Surface Texture Characterization and Optimization of Metal Additive Manufacturing-Produced Components for Aerospace Applications. In *Additive Manufacturing for the Aerospace Industry*; Froes, F., Boyer, R., Eds.; Elsevier, 2019; pp 341–374. https://doi.org/10.1016/B978-0-12-814062-8.00018-2.

(256) Lee, S.-J.; Lai, J.-J.; Lin, Y.-T. Simulation of the Formation Mechanism of a Viscous Layer for the Electropolishing Process. *WIT Trans. Eng. Sci.* **2005**, *48*.

(257) Deguchi, T.; Chikamori, K. Development of Electropolishing Method of Titanium Materials. In *Proceedings of the 2003 Annual Meeting of the Japan Society for Precision Engineering*; 2003; Vol. 338.

(258) Grimm, T.; Wiora, G.; Witt, G. Characterization of Typical Surface Effects in Additive Manufacturing with Confocal Microscopy. *Surf. Topogr.-Metrol. Prop.* **2015**, *3* (1), 014001. https://doi.org/10.1088/2051-672x/3/1/014001.

(259) Triantaphyllou, A.; Giusca, C. L.; Macaulay, G. D.; Roerig, F.; Hoebel, M.; Leach, R. K.; Tomita, B.; Milne, K. A. Surface Texture Measurement for Additive Manufacturing. *Surf. Topogr.-Metrol. Prop.* **2015**, *3* (2). https://doi.org/10.1088/2051-672x/3/2/024002.

(260) Fox, J. C.; Moylan, S. P.; Lane, B. M.; Whitenton, B. M. Preliminary Study toward Surface Texture as a Process Signature in Laser Powder Bed Fusion Additive Manufacturing. In *2016 Summer Topical Meeting: Dimensional Accuracy and Surface Finish in Additive Manufacturing*; 2016.

(261) Vetterli, M.; Schmid, M.; Wegener, K. Comprehensive Investigation of Surface Characterization for Laser Sintered Parts. In *DDMC 2014: Fraunhofer Direct Digital Manufacturing Conference: proceedings*; Fraunhofer Verlag, 2014.

(262) Shrivastava, A.; Anand Kumar, S.; Nagesha, B. K.; Suresh, T. N. Electropolishing of Inconel 718 Manufactured by Laser Powder Bed Fusion: Effect of Heat Treatment on Hardness, 3D Surface Topography and Material Ratio Curve. *Opt. Laser Technol.* **2021**, *144*, 107448. https://doi.org/10.1016/j.optlastec.2021.107448.

(263) Antsikhovich, I.; Chernik, A. Using Pulse Modes in Non-Chromium Electrolytes for Electropolishing. *Promis. Mater. Process. Appl. Electrochem.* **2017**, 7.

(264) Inman, M.; Taylor, E. J.; Hall, T. D. Electropolishing of Passive Materials in HF-Free Low Viscosity Aqueous Electrolytes. *J. Electrochem. Soc.* **2013**, *160* (9), E94–E98. https://doi.org/10.1149/2.044309jes.

(265) Lee, C.-Y.; Ger, M.-D.; Hung, J.-C.; Yang, P.-J.; Ferng, Y.-C.; Jen, K.-K.; Jian, S.-Y. Effect of Phosphoric Acid and Perchloric Acid on Electropolishing of Additive Manufactured 17-4 PH Stainless Steel and Its Characterization. *Int. J. Electrochem. Sci.* **2022**, *17* (220315), 2.

(266) Hryniewicz, T.; Rokosz, K.; Rokicki, R. Magnetic Fields for Electropolishing Improvement: Materials and Systems. *Int. Lett. Chem. Phys. Astron.* **2014**, *Vol. 4*.

(267) Loto, R. T. Pitting Corrosion Evaluation of Austenitic Stainless Steel Type 304 in Acid Chloride Media. **2013**.

(268) Alonso-Falleiros, N.; Hakim, A.; Wolynec, S. Comparison Between Potentiodynamic and Potentiostatic Tests for Pitting Potential Measurement of Duplex Stainless Steels. *Corrosion* **1999**, *55* (5), 443–448. https://doi.org/10.5006/1.3284005.

(269) Haisch, T.; Mittemeijer, E. J.; Schultze, J. W. High Rate Anodic Dissolution of 100Cr6 Steel in Aqueous NaNO3Solution. *J. Appl. Electrochem.* **2004**, *34* (10), 997–1005. https://doi.org/10.1023/B:JACH.0000042675.15101.ff.